

University of Zagreb  
Faculty of Science

Tomislav Vuletić

**COLLECTIVE ELECTRONIC  
STATES OF NEW  
QUASI-ONE-DIMENSIONAL  
MATERIALS**

Dissertation

Zagreb, 2004.

# Contents

<b>Preface</b>	<b>4</b>
<b>1 q1D materials</b>	<b>5</b>
1.1 q1D Bechgaard salt $(\text{TMTSF})_2\text{PF}_6$ - still a new material . . .	5
1.1.1 Structure . . . . .	7
1.1.2 Electronic structure and transport properties in metallic regime of $\text{TMTSF}_2\text{X}$ . . . . .	10
1.1.3 SDW phase transition in $(\text{TMTSF})_2\text{PF}_6$ . . . . .	12
1.1.4 Phase transitions in $(\text{TMTSF})_2\text{PF}_6$ under pressure . .	16
1.2 q1D cuprates $(\text{La, Sr, Ca})_{14}\text{Cu}_{24}\text{O}_{41}$ - a complex system . . . .	23
1.2.1 Models of spin and charge arrangements applicable to cuprate structures . . . . .	23
1.2.2 Crystallographic structure of q1D cuprates $(\text{La, Sr, Ca})_{14}\text{Cu}_{24}\text{O}_{41}$ . . . . .	27
1.2.3 Electronic structure of q1D cuprates $(\text{La, Sr, Ca})_{14}\text{Cu}_{24}\text{O}_{41}$ . . . . .	30
1.2.4 Hole distribution . . . . .	33
1.2.5 Chains subsystem . . . . .	42
1.2.6 Ladders subsystem . . . . .	50
<b>2 One-dimensional systems - theoretical overview</b>	<b>58</b>
2.1 Phase diagram of weakly interacting 1D Fermi gas - the <i>g-ology</i> model . . . . .	58
2.1.1 Noninteracting Hamiltonian . . . . .	59
2.1.2 Interacting part of the Hamiltonian . . . . .	60
2.1.3 Instabilities in the 1D system . . . . .	61
2.1.4 Weak coupling limit of the extended 1D Hubbard model	63
2.2 Strongly interacting 1D electron system . . . . .	65
2.2.1 Strong coupling limit for cuprates . . . . .	65
2.2.2 $t - J$ model for two-leg ladders . . . . .	67
2.2.3 1D EHM in strong coupling limit . . . . .	69

2.3	Reexamined phase diagram of 1D EHM at half-filling . . . . .	72
2.4	CDW phason response to ac field . . . . .	76
<b>3</b>	<b>Experimental techniques</b>	<b>87</b>
3.1	$(\text{TMTSF})_2\text{PF}_6$ . . . . .	87
3.1.1	$(\text{TMTSF})_2\text{PF}_6$ samples and high pressure measurements protocol . . . . .	87
3.2	$(\text{La, Sr, Ca})_{14}\text{Cu}_{24}\text{O}_{41}$ . . . . .	90
3.2.1	Samples and contacts preparation . . . . .	90
3.2.2	dc resistivity measurements . . . . .	91
3.2.3	Complex conductivity measurements- low frequency dielectric spectroscopy (LFDS) . . . . .	95
<b>4</b>	<b><math>(\text{TMTSF})_2\text{PF}_6</math> phase diagram</b>	<b>98</b>
4.1	Experimental observations . . . . .	98
4.1.1	Metallic state : $T > T_{\text{SDW}}, T > T_{\text{SC}}$ . . . . .	98
4.1.2	SDW region: $p < 8.6$ kbar, $T \lesssim T_{\text{SDW}}$ . . . . .	100
4.1.3	SC region: $p > 9.43$ kbar, $T \lesssim T_{\text{SC}}$ . . . . .	100
4.1.4	Coexistence region: $8.6 < p < 9.43$ kbar . . . . .	100
4.1.5	Detailed $p, T$ phase diagram of $(\text{TMTSF})_2\text{PF}_6$ . . . . .	110
4.2	Quantification of domain fraction in coexistence region . . . . .	112
4.3	Phase segregation scenario . . . . .	115
4.4	Discussion: DW and SC coexist in Bechgaard-Fabre salts $(\text{TM})_2\text{X}$ . . . . .	120
<b>5</b>	<b>q1D cuprates phase diagram</b>	<b>123</b>
5.1	Evidence for CDW along legs of ladders in $\text{Sr}_{14}\text{Cu}_{24}\text{O}_{41}$ . . . . .	123
5.1.1	Correspondence of dc transport and LFDS . . . . .	123
5.1.2	Nonlinear conductivity . . . . .	128
5.1.3	Standard features of CDW ground state in $\text{Sr}_{14}\text{Cu}_{24}\text{O}_{41}$ . . . . .	134
5.1.4	Conclusions . . . . .	137
5.2	Localization of holes in chains of $\text{La}_y\text{Sr}_{14-y-x}\text{Ca}_x\text{Cu}_{24}\text{O}_{41}$ . . . . .	138
5.2.1	dc conductivity indicates hopping charge transport mechanism . . . . .	138
5.2.2	Frequency dependent measurements also indicate hopping transport mechanism . . . . .	140
5.2.3	Hopping transport is due to localized holes in chains . . . . .	142

5.2.4	A comparison between $\text{Sr}_{14-x}\text{Ca}_x\text{...}$ and $\text{La}_y\text{Sr}_{14-y-x}\text{Ca}_x\text{...}$ materials . . . . .	143
5.2.5	Conclusions . . . . .	147
5.3	Suppression of CDW, in ladders of $\text{Sr}_{14-x}\text{Ca}_x\text{Cu}_{24}\text{O}_{41}$ , by Ca-substitution, $x=0, 3, 6, 8, 9, 11.5$ . . . . .	148
5.3.1	dc transport $E  c$ , $0 \leq x \leq 11.5$ . . . . .	148
5.3.2	ac response $E  c$ , $0 \leq x \leq 9$ . . . . .	151
5.3.3	Features of CDW phason response in $\text{Sr}_{14-x}\text{Ca}_x\text{Cu}_{24}\text{O}_{41}$ , $0 \leq x \leq 9$ , $E  c$ . . . . .	154
5.4	Evidence for anisotropic CDW in ladder planes . . . . .	156
5.4.1	dc transport $E  c$ , $E  a$ , $E  b$ , $0 \leq x \leq 11.5$ . . . . .	156
5.4.2	ac response $E  c$ , $E  a$ , $0 \leq x \leq 9$ . . . . .	160
5.4.3	Dimensionality <i>vs.</i> $x$ - correspondence of dc and ac results . . . . .	165
5.4.4	Within $(c,a)$ ladder plane CDW develops 2D LRO . . . . .	166
5.5	Discussion: Competing and coexisting ground states in ladders and chains . . . . .	167
5.5.1	Phase diagram for ladders . . . . .	167
5.5.2	Origin of HT insulating phase and CDW ground state and mechanism that governs their suppression . . . . .	169
5.5.3	Correspondence of phase diagrams of ladders and chains	172
5.5.4	Nature of CDW ground state in ladders . . . . .	174
5.5.5	Superconductivity in the ladders . . . . .	177
<b>6</b>	<b>Summary and Concluding Remarks</b>	<b>178</b>
	<b>Bibliography</b>	<b>183</b>
	<b>List of publications</b>	<b>195</b>

# Preface

# 1 Investigated quasi-one-dimensional materials

## 1.1 q1D Bechgaard salt $(\text{TMTSF})_2\text{PF}_6$ - still a new material

A common feature of many strongly correlated electron systems is a proximity of a superconducting state to some kind of magnetically ordered insulating state. Examples include low-dimensional organic materials, [1, 2], heavy fermion superconductors [3], and layered high- $T_c$  copper oxide superconductors (HTSC), [4]. Particularly, the close proximity of antiferromagnetic (AF) or spin-density wave (SDW) phases with the onset of organic superconductivity (SC) in the temperature and pressure phase diagram of organic compounds, indicated at an early stage, that the apparent difficulty to describe both phenomena emerges from their mutual interaction, [5]. It needs to be pointed out that the proximity of the two phases poses the question whether the two order parameters interact (support each other) or compete (repulse each other), Fig. 1.1.

An AF – SC coexistence region has been observed recently in the layered organic  $\kappa$ -(BEDT-TTF) $_2$ X compounds under well controlled pressure [2, 6]. Even better characterised system featuring the coexistence of AF (or SDW) and SC (or normal state) is formed in the quasi-one dimensional organic superconductors, *i.e.* the Bechgaard-Fabre salts. This family of materials features a unified phase diagram, Fig. 1.1, lower right panel. Different members of the family are positioned at different points in the diagram, as indicated by arrows. Applying enough pressure stabilizes any of the ground states found to the right of the arrow which denotes respective material. A recent observation of the whole spectrum of states from this diagram for  $(\text{TMTTF})_2\text{PF}_6$ , where SC was reached at 43.5 kbar, confirmed this, [7]. Even after 25 years of investigation the nature of the transition from magnetism, *i.e.* SDW to superconductivity, and the respective part of the unified phase diagram has

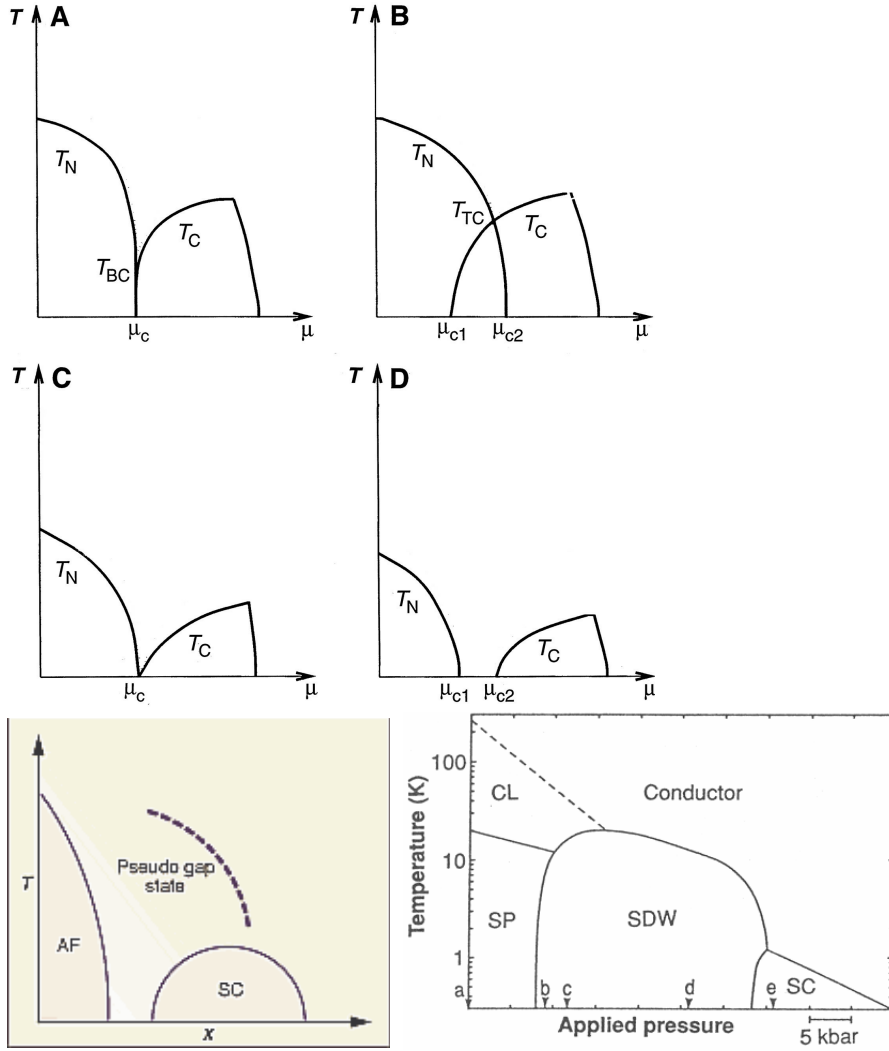


Fig. 1.1: Upper panel: Theoretically possible phase diagrams for the case of proximity between the magnetic (AF or SDW) and SC ground states.  $T_N$  and  $T_c$  are the respective transition temperatures. There are four possible types of transitions from the magnetic to SC state, [8]. (A) a direct first-order transition terminating at a bicritical point  $T_{bc}$ . (B) two second-order phase transitions with an intermediate phase. The second-order lines merge at a tetracritical point  $T_{tc}$ . (C) a single second-order phase transition at a quantum critical point. (D) two second-order quantum phase transitions with an intermediate quantum-disordered phase. These possibilities may be compared to the well known experimental phase diagrams: Lower left panel, HTSC layered cuprates. At low doping  $x$ , an AF ordering is established. At higher doping, a SC phase is created with the pseudo gap state above it, [9]. Lower right panel, the Bechgaard-Fabre salts. The SC state has a common boundary with the SDW state. The ambient pressure locations in the generalized phase diagram for  $(\text{TMTTF})_2\text{PF}_6$ (a),  $(\text{TMDTDSF})_2\text{PF}_6$ (b),  $(\text{TMTTF})_2\text{Br}$ (c),  $(\text{TMTSF})_2\text{PF}_6$ (d),  $(\text{TMTSF})_2\text{ClO}_4$ (e) is indicated. The dashed line delimits the charge-localized (CL) behavior. SP refers to spin-Peierls state, [10].

remained unclear, [10, 17, 19, 20]. In particular, the prototype and most studied compound,  $(\text{TMTSF})_2\text{PF}_6$ , has an ideal position in this phase diagram and an improved experimental setup now allows for investigation of this transition. This justifies for the title of this Section-  $(\text{TMTSF})_2\text{PF}_6$  is still a new material worth investigating due to its rich (especially when magnetic field is introduced as a third axis) and still not completely explored phase diagram [10, 18]. This phase diagram, in the low temperature region, features all known electronic transport mechanisms. Besides metallic conductivity and superconductivity (observed 25 years ago, [21]), the other two, theoretically dissipationless transport mechanisms, occur in the spin-density wave phase and the quantum Hall effect (QHE) state, [11, 12, 16, 17, 18]. Finally, it may be noted that the role of Bechgaard-Fabre salts, as the most explored q1D systems, is also very well appreciated. The Thesis also benefits from this, since any work on other q1D materials is much more instructive if compared to the results obtained on  $(\text{TMTSF})_2\text{PF}_6$ , the principal compound of the family.

### 1.1.1 Structure

All members of Bechgaard,  $(\text{TMTSF})_2\text{X}$  and Fabre salts  $(\text{TMTTF})_2\text{X}$ , in general  $\text{TM}_2\text{X}$ , are isostructural compounds. TMTSF/TMTTF, tetramethyltetra(selena /thia) fulvalene is a derivative of an organic molecule, fulvalene, where four carbon atoms are substituted by four selenium /sulphur atoms, and four methyl ( $\text{CH}_3$ ) groups have been added. Fulvalene (pentafulvalene) structure is basically two pentafulvene (derivative of cyclopentadiene) molecules joined by a double bond between two ring carbons, Fig. 1.2. The double-bonds within and between the rings make the fulvalene a planar molecule, [13]. TMTSF/TMTTF form salts with inorganic anions, where the charge is transferred from the fulvalene molecules to the inorganic anions. There are many possible anions:  $\text{X} = \text{PF}_6, \text{AsF}_6, \text{SbF}_6, \text{BF}_4, \text{ClO}_4, \text{Re}_4, \text{NO}_3\dots$  The anions are placed into centrosymmetrical cavities delimited by methyl groups. Therefore, the most important property of these anions is their symmetry, *i.e.*, the compounds with the centrosymmetric anions have very similar experimental properties, which are quite different from those with noncentrosymmetric ones, where a substantial disorder is introduced, and anion ordering plays a role. The selenium based salts were first synthesized in 1979., by the electrochemical method, by Bechgaard *et al.* [14], Fig. 1.2. The crystal structure was obtained by X-ray diffraction (XRD) and found to be triclinic, [15]. The parameters of the unit cell are  $a=3.65 \text{ \AA}$ ,  $b=7.711 \text{ \AA}$ ,  $c=13.522 \text{ \AA}$ ,  $\alpha=83.39^\circ$ ,  $\beta=86.27^\circ$  and  $\gamma=71.01^\circ$ . The planar shape of TMTSF/TMTTF molecules and their respective stack-

---

ing (in a somewhat zig-zag pattern) along crystal  $a$ -axis are responsible for the highly anisotropic electronic structure of  $\text{TM}_2\text{X}$ . In  $b$ -direction (inter-stack) TMTSF/TMTTF molecules are separated by a slightly larger distance than in  $a$ -direction (intrastack). Adding to the anisotropy, TMTSF/TMTTF stacks are in the  $c$ -direction separated by the anions  $X$ , Fig. 1.2. A tendency towards dimerization between the molecules in the stack is observed, especially for sulphur based compounds.

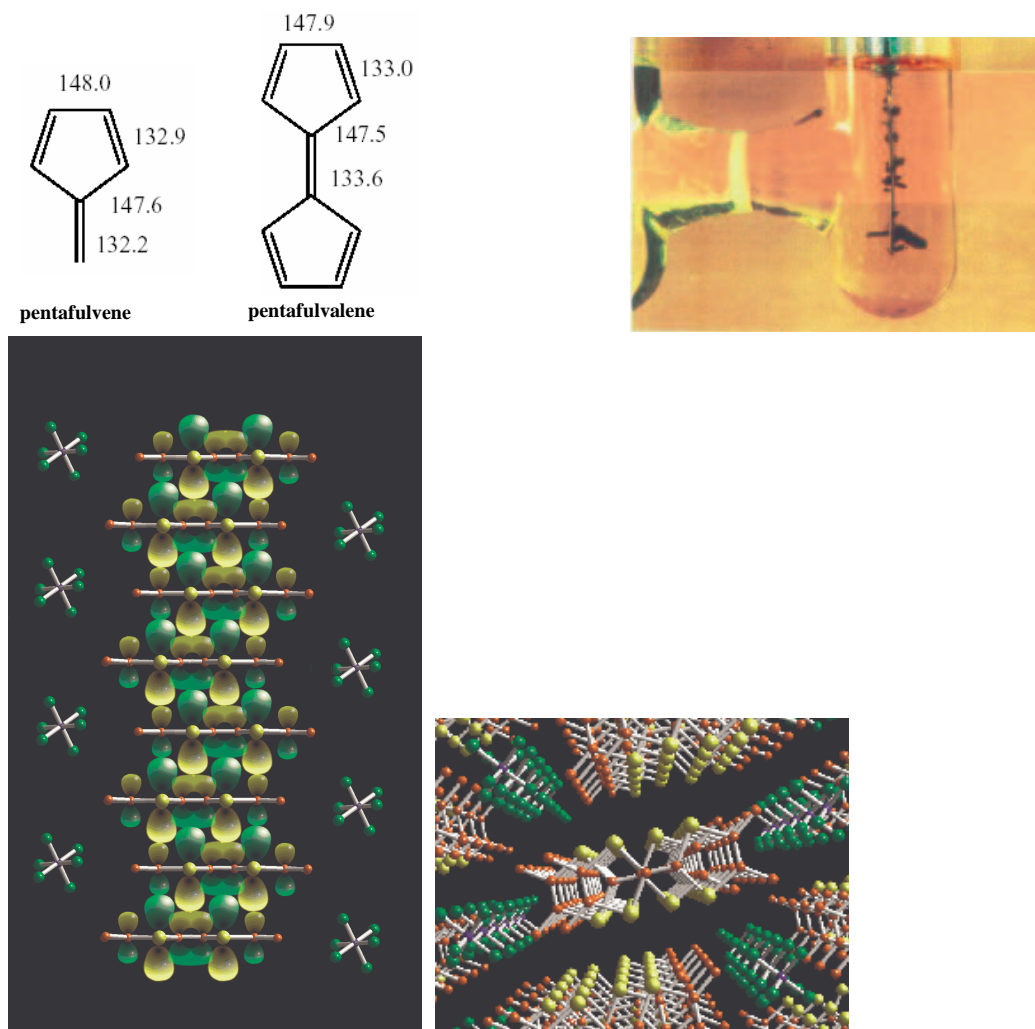


Fig. 1.2: Upper left: Hartree-Fock geometries of fulvene and fulvalene molecules. Bond lengths in picometers. Upper right: The elongated, black crystals of  $(\text{TMTSF})_2\text{PF}_6$  grow on the electrodes during an electrochemical synthesis. Lower left: The structure of  $(\text{TMTSF})_2\text{PF}_6$  can be generated by stacking TMTSF molecules in a somewhat zig-zag pattern along the  $a$ -axis (the view is along the  $b$ -axis). The p-orbitals of the atoms within TMTSF molecule are shown. Lower right: Along the  $c$ -axis stacks are separated by  $\text{PF}_6$  anions (the view is along the  $a$ -axis). yellow - Se, red - C, blue - P, green - F. Model: Institut des Materiaux Jean Rouxel.

### 1.1.2 Electronic structure and transport properties in metallic regime of TMTSF<sub>2</sub>X

The charge transfer results in the excess of holes within the TMTSF stacks. A quarter filled tight-binding band (1 electron transferred per two molecules) is formed within the first Brillouin zone, leading to metallic properties. This band may be altered in case of dimerization, but this review concentrates on TMTSF compounds where this is not crucial. The band formation is due to the superposition of the p-orbitals of the selenium atoms of the neighbouring TMTSF molecules, Fig. 1.2, right picture. The overlap, characterized with the transfer integrals  $t_i$ , is by far the largest along the stacking direction  $a$ - and quite smaller along  $b$ -direction. Along  $c$ -, due to the anions in-between TMTSF molecules, it is almost negligible. The transfer integrals  $t_i$  for TMTSF<sub>2</sub>X materials, were calculated within the tight binding approximation to be  $t_a \approx 0.2\text{eV} : t_b \approx 0.02\text{eV} : t_c < 0.001\text{eV}$ , [22], Fig. 1.3. These theoretical values are also in good agreement with the RT optical and magnetic measurements, [23, 24].

Experimentally, the electronic structure anisotropy reflects in room temperature (RT) conductivity anisotropy for (TMTSF)<sub>2</sub>PF<sub>6</sub>,  $\sigma_a : \sigma_b : \sigma_c \sim 300 : 1 : 0.03$ . Therefore, this and other materials from the family, are regarded as quasi-one-dimensional conductors. The RT conductivity is high  $\sigma_a(300\text{K} \approx 600)\Omega^{-1}\text{cm}^{-1}$  [25], and metallic properties are observed in the electronic transport down to very low temperatures, [27]. The longitudinal resistance decrease follows a power law  $T^{1.5}$  down to  $\approx 100$  K, [26]. Below 35 K, resistivity follows the residual resistivity law  $\rho_{res} + AT^2$  down to metal-to-insulator transition, Fig. 1.4. The ratio RR between the room temperature and the minimum resistance just above the metal-to-insulator is very sample dependent, ranging from 30 to 1000 for the highest quality samples. For high quality samples, the residual resistivity  $\rho_{res}$  appears to be 0, [27], suggesting that the inelastic electron scattering term  $AT^2$  is dominant in the conducting state at low temperature. Conductivity anisotropy seems to be temperature independent, [25] down to  $\approx 25$  K, with the values confirming the theoretical prediction  $\frac{\sigma_a}{\sigma_b} \approx \frac{t_a^2 a}{t_b^2 b}$ .

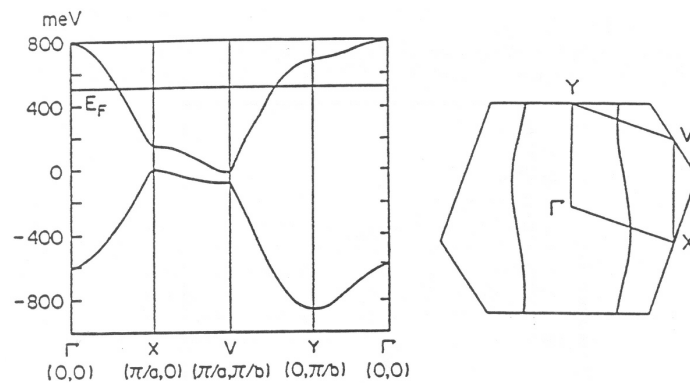


Fig. 1.3: The calculated band structure for  $(\text{TMTSF})_2\text{X}$  materials. From Ref. [22]

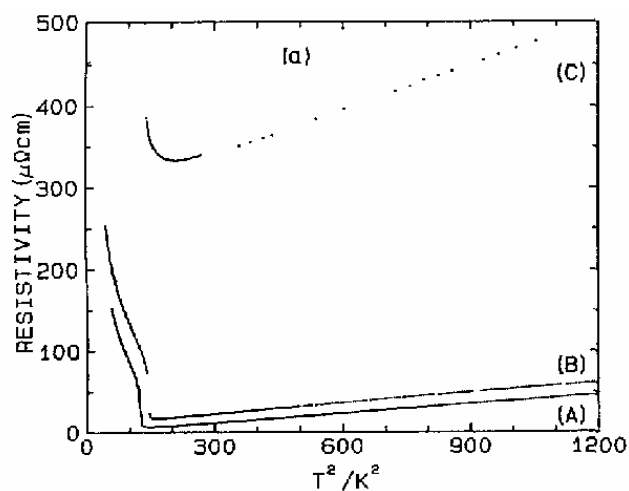


Fig. 1.4: Resistivity *vs.* temperature squared for  $(\text{TMTSF})_2\text{PF}_6$  below 35 K behaves according to the residual resistivity law  $\rho_{res} + AT^2$  down to metal-to-insulator transition. Samples from different batches show different residual resistivities,  $\rho_{res}$ , which even attains zero value for the batch A. A sharp rise of resistance is the onset of the metal-to-insulator transition (12 K for the high quality batch A). From Ref. [27]

### 1.1.3 SDW phase transition in (TMTSF)<sub>2</sub>PF<sub>6</sub>

A very sharp metal-to-insulator transition corresponds to the occurrence of the spin-density wave (SDW) ground state at  $T_{\text{SDW}} = 12$  K. The low field susceptibility of the SDW phase behaves very much like the susceptibility of a regular antiferromagnet, Fig. 1.5. These results for the analogous compound (TMTSF)<sub>2</sub>AsF<sub>6</sub> show that the easy axis is aligned along  $b$ - and that a spin-flip transition arises around 5 kOe, [28]. The magnetic nature of the ground state has also been confirmed by the observation of AF resonance [30] and the measurement of a local field by NMR and  $\mu$ SR [31]. A sinusoidal SDW modulation of wave vector  $\mathbf{Q}_{\text{SDW}} = (0.5, 0.20-0.24, -0.06 \pm 0.20)$  and of amplitude  $0.08 \mu_B$  was suggested by two independent proton NMR experiments [24, 29]. A two component charge modulation (of the electronic system, not the lattice), was observed by X-ray diffuse scattering. One was characterized by a similar wave vector  $\mathbf{Q}_1 = (0.5 \pm 0.05, 0.25 \pm 0.05, 0.25 \pm 0.20)$  as in the magnetic sector, the other had  $\mathbf{Q}_2 = 2\mathbf{Q}_1$ . The amplitude of the charge modulation was 0.1 electron per TMTSF molecule, *i.e.*, it was comparable to the amplitude of the SDW, [33, 34].

The transition to the SDW phase is driven by a specific *nesting* property of the Fermi surface (FS) of (TMTSF)<sub>2</sub>PF<sub>6</sub>, and of some other materials from the family, which have centrosymmetric anions. The characteristic vector of the spin modulation is defined by this FS property, indeed. The FS of an ideal 1D conductor would be composed of two flat opposing sheets. In Bechgaard salts, especially (TMTSF)<sub>2</sub>PF<sub>6</sub>, due to finite  $t_b$  FS is formed of two warped opposing sheets, Fig. 1.6, characterized by a feeble modulation along the  $b$ -axis, and negligible one along the  $c$ -axis, see Sec. 1.1.4. These two opposing FS sheets fit one onto another under a translation in the reciprocal space for a nesting vector  $\mathbf{Q} \approx (2k_F, \frac{\pi}{b})$ . This vector links the occupied orbitals close to one FS sheet to the unoccupied orbitals close to the other FS sheet. Since very many orbitals with very little energy difference,  $E(\mathbf{k}) = E(\mathbf{k} + \mathbf{Q})$ , are linked when the nesting is good, this leads to a logarithmic divergence in the spin susceptibility function  $\chi_0(\mathbf{q} \approx \mathbf{Q})$  as  $T \rightarrow 0$ , and eventually to a transition to a spin-modulated ground state: spin-density wave (SDW). Spin density modulation is characterized with  $\mathbf{Q}$  wave vector:  $S(x) = S_0 \cos(\mathbf{Q}\mathbf{x} + \varphi(x)) = S_0 \cos(2k_F x + \varphi(x))$ . This  $2k_F$  SDW was observed experimentally, as already mentioned above [24, 29].

A long time ago Overhauser, [32] suggested that such a spin-density modulation may be understood as a combination of two electronic CDWs of opposite spin:

$$\delta\rho_{\uparrow} = \rho_0 \cos(2k_F x + \varphi(x))$$

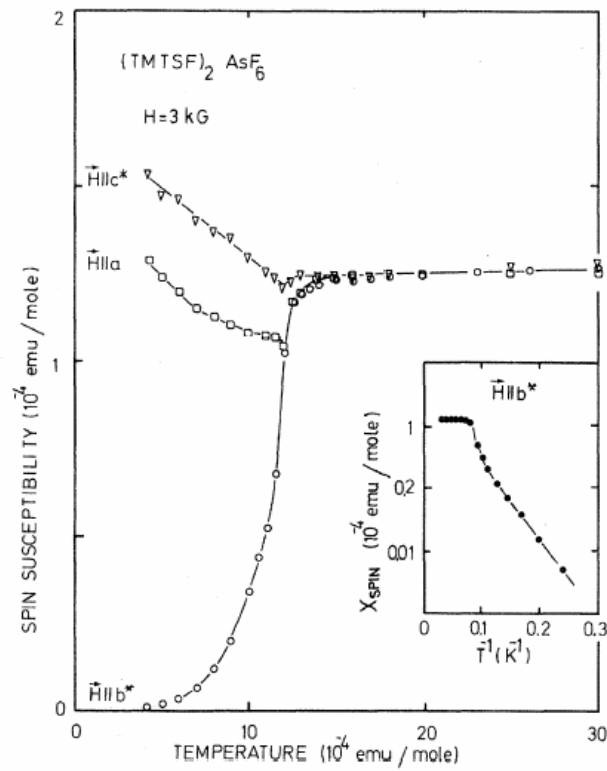


Fig. 1.5: Spin-susceptibility of  $(\text{TMTSF})_2\text{AsF}_6$  as deduced from static measurements with magnetic field along the respective crystal axes. The magnetic field 3 kG, is lower than critical spin-flip field. From Ref. [28].

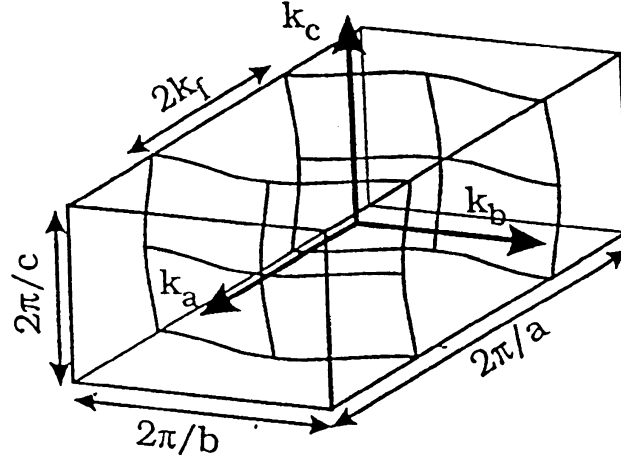


Fig. 1.6: Fermi-surface for q1D materials. A good nesting between the two sheets leads to transition to the spin density wave phase. Warping in the  $b$ -direction is much stronger than the one in the  $c$ -direction, which is neglected and the nesting is considered to be perfect, with the nesting vector  $\mathbf{Q} \approx (2k_F, \frac{\pi}{b})$ . See Sec. 1.1.4.

$$\delta\rho_{\downarrow} = \rho_0 \cos(2k_F x + \varphi(x) + \theta) \quad (1.1)$$

For  $\theta = \pi$  the pure SDW appears, while for  $0 < \theta < \pi$  a mixed  $2k_F$  CDW- $2k_F$  SDW state occurs, as observed by Pouget *et al.* and Kagoshima *et al.* [33, 34, 36]. The mechanism which stabilizes it is unknown.

The development of SDW opens a gap  $2\Delta$  at Fermi surface, leading to the metal-to-insulator transition, [37]. In the SDW phase resistance shows the Arrhenius behaviour,  $R = R_0 e^{\Delta/T}$ , Fig. 1.7. For high quality samples  $\Delta \approx 21$  K, and it has to be noted that the mean-field BCS relation  $2\Delta = 3.52T_{\text{SDW}}$ , is well satisfied for  $(\text{TMTSF})_2\text{PF}_6$  and  $\text{AsF}_6$  materials, [27]. This was also confirmed recently by the direct observation of SDW gap in  $(\text{TMTSF})_2\text{PF}_6$ , Fig. 1.7, by means of the electron tunnelling spectroscopy, using low temperature STM [35].

A mean-field treatment of the Hubbard hamiltonian for a 1D interacting electron gas model of  $(\text{TMTSF})_2\text{PF}_6$ , leads to the exponential dependence of the  $2\Delta_{\text{SDW}}$  gap on the interaction  $U$ . The following illustrates that  $T_{\text{SDW}}$  also shows the same dependence. The BCS relation  $2\Delta = 3.52T_{\text{SDW}}$  is satisfied in this 1D interacting electron gas model, as well as in the experiment.

Firstly, the magnetic susceptibility for a noninteracting electron gas featuring dispersion  $E(\mathbf{k})$ , is given by Lindhard response function

$$\chi_0(\mathbf{q}) \propto \sum_{\mathbf{k}} \frac{f_{\mathbf{k}} - f_{\mathbf{k}+\mathbf{q}}}{E_{\mathbf{k}+\mathbf{q}} - E_{\mathbf{k}}} \quad (1.2)$$

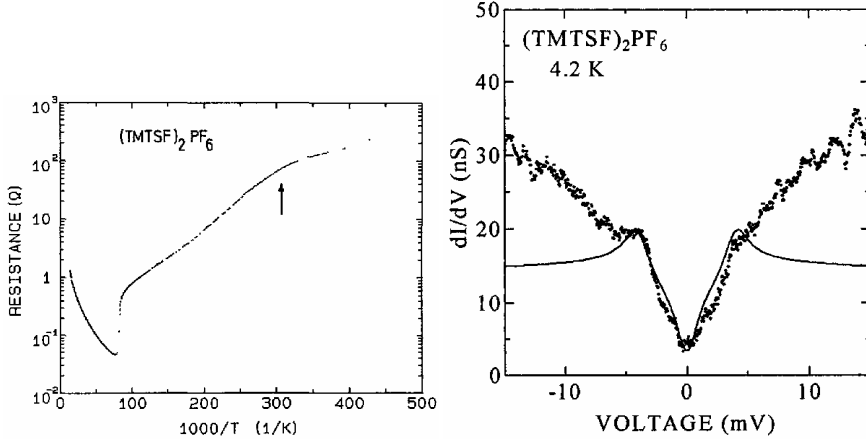


Fig. 1.7: Left panel: Logarithm of resistance *vs.* inverse temperature for  $(\text{TMTSF})_2\text{PF}_6$ . Activation energy  $\Delta_{\text{SDW}}$  is 21 K below  $T_{\text{SDW}} = 12$  K. Note a break in the slope at 3.2 K, indicating a crossover within the SDW phase. From Ref. [27]. Right panel: Direct observation of the gap with STM: Dots represent tunnelling differential conductance at 4.2 K. Solid line represents the calculation from which  $2\Delta_{\text{SDW}} = 35$  K is obtained. From Ref. [35].

where  $f_{\mathbf{k}}$  is Fermi-Dirac statistics at temperature  $T$

$$f_{\mathbf{k}} = \frac{1}{\exp[E_{\mathbf{k}} - E_F] + 1} \quad (1.3)$$

By numerical integration of Eq. 1.2, for the perfect nesting case of 1D dispersion given by Eq. 1.7 (where  $t'_{\perp}$  is neglected), it can be demonstrated that the spin susceptibility diverges logarithmically,  $\chi_0(\mathbf{Q}, T) \propto \ln(1/T)$ . Introduction of interaction  $U$  into this noninteracting electron gas enhances the susceptibility:

$$\chi(\mathbf{Q}, T) = \frac{\chi_0(\mathbf{Q}, T)}{(1 - U\chi_0(\mathbf{Q}, T))} \quad (1.4)$$

When the Stoner criterion  $(1 - U\chi_0(\mathbf{Q}, T))$  is fulfilled the SDW ground state is expected below an ordering temperature  $T_{\text{SDW}} \propto E_F \exp\left[-\frac{1}{N(E_F)U}\right]$ . Below this temperature the electron system responds divergently at the  $\mathbf{Q}$  vector, effectively *freezing* into a spin-modulated state, the spin-density wave.

A prominent feature of this phase is its response to dc and ac electric fields. The response to dc electric field is nonlinear due to SDW condensate sliding above a certain threshold electric field [38]. SDW condensate sliding is accompanied by a phenomenon of narrow band noise, [39]. The response

to ac field is characterized by the enormous dielectric constant of the order of  $10^8$ - $10^9$  [45].

Finally, we would like to mention experiments indicating a complex nature and the possible existence of transition(s) inside the SDW phase of  $(\text{TMTSF})_2\text{PF}_6$ , [44]. A calorimetric transition at 3.5 K with large hysteretic phenomena in the temperature range 2.5K - 4K caused by the sample history has been observed, [41]. In the electrical transport, a break in the slope of logarithm of resistance *vs.* inverse temperature curve for  $(\text{TMTSF})_2\text{PF}_6$  was observed at 3.2 K, indicating a crossover within the SDW phase, Fig. 1.7, [27]. Further, NMR measurements of the spin-lattice relaxation rate ( $1/T_1$ ), have shown a changeover at 3.5K from a temperature independent behaviour at higher temperatures to an activated behaviour at lower temperatures, with an activation energy much lower than the free carrier resistivity one. In addition, another anomaly in  $1/T_1$  was detected at about 2K. Takahashi *et al.* [40] have suggested that the  $1/T_1$  anomalies indicate the existence of successive transitions inside the SDW ground state, adding to the richness of  $(\text{TMTSF})_2\text{PF}_6$  phase diagram. Moreover, the X-ray diffuse scattering showed that SDW ground state is, indeed, mixed  $2k_F$  CDW -  $2k_F$  SDW ground state, (see above) [33, 34]. Other authors showed that CDW disappears below 3-4 K, indicating a possible relation with the subphase structure of SDW in  $(\text{TMTSF})_2\text{PF}_6$ , [36]. Additional magnetoresistance and Hall studies have also indicated changes inside SDW phase, [42, 43]. These authors have also interpreted that an unconventional SDW phase below  $T^* = 4$  K is formed along SDW.

### 1.1.4 Phase transitions in $(\text{TMTSF})_2\text{PF}_6$ under pressure

#### SDW supression under pressure

Here it is appropriate to relate the exposed band structure and corresponding spin susceptibility properties of  $(\text{TMTSF})_2\text{PF}_6$  to dependence of the SDW transition temperature  $T_{\text{SDW}}$  on pressure observed for  $(\text{TMTSF})_2\text{PF}_6$ , in more detail. This dependence is presented within the schematic phase diagram of  $\text{TM}_2\text{X}$  family, Fig. 1.1. The data for this diagram were obtained in numerous electrical transport studies, [47, 12, 48] and also by an elaborate EPR experiment [46], Fig. 1.8. In order to discuss the stability of the SDW phase, it is essential to model the Fermi surface geometry, and the dispersion relation.

The description of the SDW transition and ground state as given in previous Section is based on a strictly one-dimensional model, with  $\mathbf{Q} =$

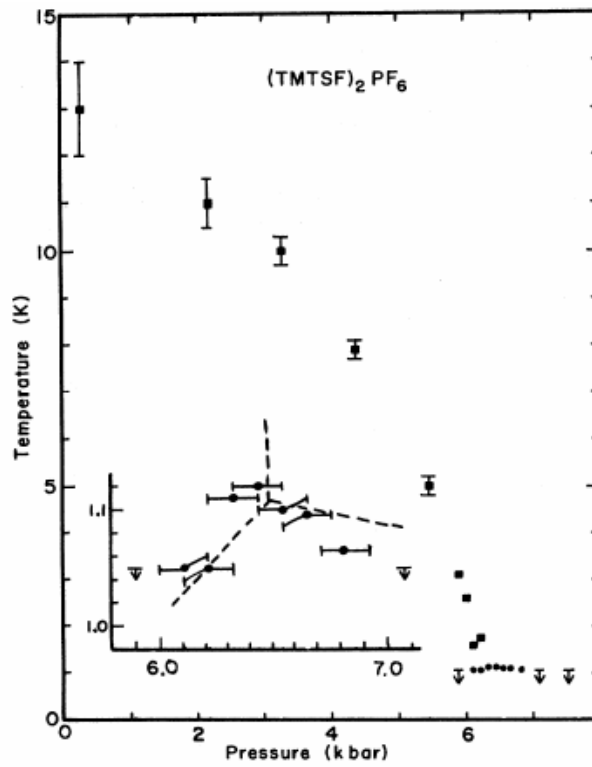


Fig. 1.8: Temperature-pressure phase diagram showing metal-to-SDW transitions (squares) and superconducting transitions. The inset shows the details near the tricritical point. The data were obtained by electron-spin resonance in a single crystal at low magnetic fields. From Ref. [46]

$(2k_F, 0, 0)$ , and it would also apply to the case of perfect nesting,  $\mathbf{Q} \approx (2k_F, \frac{\pi}{b})$ . However, as a realistic material,  $(\text{TMTSF})_2\text{PF}_6$  is characterized by a certain degree of imperfect nesting. This concept is introduced as follows.

Although the symmetry of  $(\text{TMTSF})_2\text{PF}_6$  is triclinic, most physical features can be explained by taking an orthorhombic symmetry (the deviations of the crystalline axes from the axes of the crystallographic coordinate system are neglected) with tight binding energy dispersion given as:

$$E(\mathbf{k}) = -2t_a \cos(k_x a/2) - 2t_b \cos(k_y b) - 2t_c \cos(k_z c) \quad (1.5)$$

Taking the origin of the energy at the Fermi energy  $E_F = 0$ , and staying close to the Fermi level ( $k_B T < t_a$ ) this dispersion may be linearized without significant modifications in the physical properties of the model

$$E(\mathbf{k}) = E_0 - 2t_a (k_F a - |k_x| a) - 2t_b \cos(k_y b) - 2t_b^2/t_a \cos(k_y b) \quad (1.6)$$

Here  $2at_a$  is Fermi velocity  $v_F$ . The band is quarter filled,  $k_F = \pi/4a$ . Only the highest occupied molecular orbital concentrated around Se atoms on the TMTSF molecule is taken into consideration. Commonly the dispersion Eq. 1.6 is written as

$$E(\mathbf{k}) = E_0 + v_F (|k_x| - k_F) - 2t_{\perp} \cos(k_y b) - 2t'_{\perp} \cos(k_y b) \quad (1.7)$$

where a nesting deviation parameter is defined as  $t'_{\perp} = t_{\perp}^2/t_{\parallel} = t_b^2/t_a$ . The dispersion along the  $c$ -direction is neglected. Thus, a Fermi surface of only slightly distorted sinusoidal shape is defined. If  $t'_{\perp}$  is also neglected FS becomes perfectly sinusoidal and perfectly nested with the nesting vector  $\mathbf{Q} = (2k_F, \frac{\pi}{b})$ . But, for  $(\text{TMTSF})_2\text{PF}_6$  we have to note that the FS nesting is already imperfect at ambient pressure and  $t'_{\perp}$  can not be neglected. That is, if transfer integral values calculated by Grant, [22], are taken into account, one gets  $t'_{\perp} \approx 1 - 2$  meV, already at ambient pressure. This is comparable to the energy scale  $\Delta_{\text{SDW}}$ , explaining why only a modest pressure of the order of 10 kbar is enough to suppress the SDW state, [12].

The role of pressure in this model is to increase  $t'_{\perp}$  term in Eq. 1.7. Not surprisingly, the pressure is considered to increase the overlap between the  $p$ -orbitals, and respective transfer integrals. Thus  $t'_{\perp}$  term becomes significant due to its quadratic dependence on  $t_b$  and the FS departs further from perfect nesting.  $\chi_0(\mathbf{Q})$  no longer presents a logarithmic divergence, but only a relative maximum (nondivergent as  $T \rightarrow 0$ ) at a slightly different nesting vector. Then there exists a critical value  $t'_{\perp} = t_{\perp}^{**}$  above which SDW ground state is suppressed and a non-distorted q1D conductor is stabilized at low temperature, Fig. 1.9.

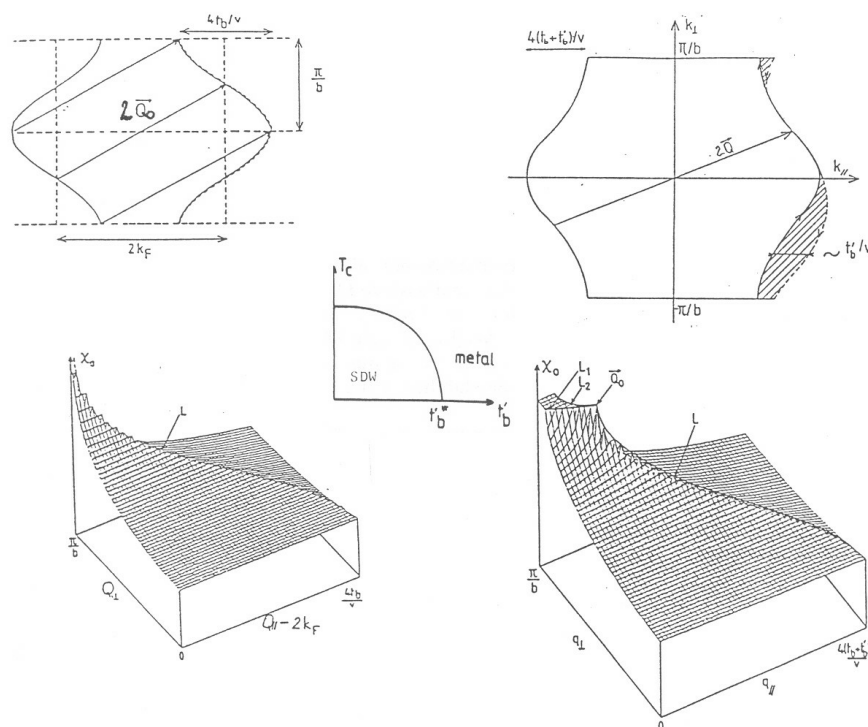


Fig. 1.9: Lower left diagram: a logarithmically divergent  $\chi(\mathbf{Q}=2k_F, \pi/b)$  appears for perfect nesting case (upper left diagram), when  $t'_b = 0$ . Lower right diagram:  $\chi(\mathbf{q})$  is no longer divergent for  $t'_b \neq 0$ . Just a local maximum appears (non-perfect nesting) at a slightly different nesting vector  $\mathbf{Q}_0$ . Nesting is not perfect, un-nested pockets of FS appear (shaded area in the upper right diagram). Central diagram: the SDW ground state of  $(\text{TMTSF})_2\text{X}$  is stable as long as  $t'_b < t_b^{**}$ . Around and above  $t_b^{**}$  other instabilities may prevail. Note:  $t_\perp = t_b$ , see text. From Ref. [49].

### SC transition in $(\text{TMTSF})_2\text{PF}_6$ above 9-10 kbar

When pressure is applied, the nesting properties in  $(\text{TMTSF})_2\text{PF}_6$  are spoiled, which causes a decrease of the ordering temperature  $T_{\text{SDW}}$ , up to a critical pressure  $p_c \approx 9 - 10$  kbar above which the metal-to-SDW transition temperature  $T_{\text{SDW}}$  is totally suppressed, Fig. 1.8. In an isobaric experiment in the pressure range above  $p_c \approx 9 - 10$  kbar, decreasing temperature leads to the observation of a metal-to-SC transition below  $T_{\text{SC}} \approx 1.2$  K [21]. The observation of the Meissner flux expulsion and of specific heat anomaly give the picture of bulk superconductivity, [54, 55].

The experimental temperature - pressure phase diagram of  $(\text{TMTSF})_2\text{PF}_6$ , [47, 46], Fig. 1.1, 1.8 has SC in close proximity to the SDW phase, similar to the theoretical phase diagram for an interacting one-dimensional electron gas [50], where SDW lies adjacent to triplet superconductivity, see also Fig. 2.3. The strong sensitivity of  $T_{\text{SC}}$  to nonmagnetic impurities could point toward the existence of SC phase of  $p$ -wave symmetry, [52]. An absence of a coherence peak [53] and power-law behavior in the temperature dependent proton spin-lattice relaxation rate ( $1/T_1 \propto T^3$ ) were argued [59] for some nodal structure on the Fermi surface indicative of non- $s$ -wave symmetry. On the contrary, thermal measurements such as specific heat [55] and thermal conductivity [56] indicated a finite gap, rather than nodes, on the Fermi surface. None of the above experiments directly probe spin parity and they yield an ambiguous conclusion on the orbital symmetry. Much more attention has been refocused on the issue by upper critical field studies [57] showing that superconductivity persists up to more than 4 times the Pauli limit, a conventional limit for singlet superconductors [58], which strongly support a spin-triplet state. Recently, Lee *et al.*, [60] presented a pulsed NMR Knight shift study of  $^{77}\text{Se}$ , measured in pressurized  $(\text{TMTSF})_2\text{PF}_6$ . This study directly probes the spin susceptibility, which was observed to stay unchanged between the normal state and SC state, giving a strong support to a hypothesis of triplet,  $p$ -wave, superconductivity. The SC phase transition temperature is also suppressed by the application of pressure, at a rate of  $\partial T_{\text{SC}}/\partial p \approx -0.07$  K/kbar, [51].

### SDW - SC boundary region of the phase diagram

A salient feature of superconductivity in  $(\text{TMTSF})_2\text{PF}_6$  is the common boundary between SC and SDW phase. The region of the generalized pressure phase diagram, Fig. 1.1, where this boundary occurs is observed in  $(\text{TMTSF})_2\text{PF}_6$  at pressures around 9-10 kbar. It is not possible to observe SDW-to-SC transition directly in an isothermic, pressure changing experiment, due to

the experimental constraints, which impose isobaric measurements. However, in the first experimental reproduction of organic superconductivity under pressure [61], it was noticed that both metal-to-SDW and an SDW-to-SC transition, appear consecutively upon cooling if applied pressures are from a narrow pressure domain around the SDW - SC boundary. Such investigation of the phase diagram of analogous compound  $(\text{TMTSF})_2\text{AsF}_6$  by Brusetti *et al.* [47] has led to similar observations. Such a competition is also observed in  $(\text{TMTSF})_2\text{ClO}_4$  [62] where anion disorder is the driving parameter. Further, in  $(\text{TMTSF})_2\text{PF}_6$ , using EPR at low field with helium gas pressure technique, Azevedo *et al.* [46], Fig. 1.8 also have reported a consecutive appearance of sharp metal-to-SDW and SDW-to-SC transitions on cooling in at least 200 bar wide pressure domain around the SC - SDW boundary.

Merging of SDW into the SC state around a critical pressure has been extensively studied, from a theoretical point of view. The precursory work of Schulz *et al.* [51], which studied the border between SDW and SC states in  $(\text{TMTSF})_2\text{PF}_6$  has suggested two possible scenarios, namely, the existence of a quantum critical point between SDW and SC or a first order transition line between the insulating and superconducting states, see also Fig.1.1, upper panel. It was also suggested by Yamaji that, at a pressure slightly lower than the critical pressure, a *semi-metallic* SDW phase is formed, with small pockets of unpaired charge carriers, because the SDW gap is not opened on the whole Fermi surface, [63]. In Fig. 1.9, upper right plot shows unnested area (shaded) of FS. These unnested parts of FS may be susceptible to opening of the SC gap. In a way, there is a coexistence of metallic and magnetic phases coming from different parts of the reciprocal space. The possibility of a microscopic coexistence of superconducting and SDW phases at lower temperature, was studied in details by Yamaji in the framework of a phenomenological mean-field theory of the competition between SDW and s-wave SC states in the Bechgaard salts, [64, 65, 66]. The conclusion was negative, because the density of states of the unpaired carrier pockets, left by the SDW ordering in the case of imperfect nesting, is strongly reduced compared to the density of states of the original metallic phase. Such reduction in effective FS size decreases the effective superconducting coupling  $gN(0)$  drastically, which leads to an exponentially small critical temperature. In the case of such microscopical coexistence of phases, there is still the issue of, how could it be translated into the real space, *i.e.* how would the two phases organize in the bulk of the crystal. Would such a segregation be produced on a microscopic scale ( $l \ll \xi$ , where  $\xi$  is the correlation length), on a mesoscopic scale ( $l \sim \xi$ ), or rather on a macroscopic scale ( $l \gg \xi$ ), *i.e.* which would be more energetically favorable? Here it is appropriate to note that Machida was the first to discuss a model of coexisting SC and SDW order parameters

and suggested possible phase diagrams, although he did not refer to the real or reciprocal space separation of phases, [67].

Studies of the border between SDW and SC states in  $(\text{TMTSF})_2\text{PF}_6$  were limited, either due to the experimental constraints, or to the sample quality, while the theoretical studies lack any attempt on quantification of the relationship between the SC and SDW phases. This study was initiated in order to determine the qualitative and quantitative features of this phase space region of  $(\text{TMTSF})_2\text{PF}_6$ . The aim was to give a good basis for successful modelling of the observed coexistence, with a possible wider application in other systems characterized by proximity of SC and magnetic phases.

## 1.2 q1D cuprates (La, Sr, Ca)<sub>14</sub>Cu<sub>24</sub>O<sub>41</sub> - a complex system

Low-dimensional quantum spin systems, q1D cuprates of the formula  $A_{14}Cu_{24}O_{41}$  (A=Sr, Ca, La, Y...) are composite materials. Spins and charges are arranged differently within chain and ladder structural elements. q1D cuprates are under intensive study experimentally, as well as theoretically, [68]. Two independent groups, Siegrist *et al.* and McCarron *et al.* synthesized single crystals in 1988. They also solved the structure, [70, 71]. Only the theoretical suggestions by Dagotto *et al.* [77] in 1992. led the experiment to concentrate on investigating this new family of materials. The studies intensified after the discovery of superconductivity in one of these materials,  $Sr_{0.4}Ca_{13.6}Cu_{24}O_{41}$ , under pressure [69]. Indeed, it was theoretically predicted [77, 72, 73] that compounds, possessing hole doped even-leg ladder structural elements, can produce superconductivity reminiscent of the superconductivity in the underdoped high- $T_c$  cuprates; alternatively, they can undergo a charge-density-wave (CDW) transition.

These ideas seemed applicable to q1D cuprates which contain only the structural element of ladders. Extrinsic hole doping of the pure ladder materials like  $SrCu_2O_3$  did not lead to the discovery of a collective state, [79]. Then, the composite q1D cuprates of (La, Sr, Ca)<sub>14</sub>Cu<sub>24</sub>O<sub>41</sub> family were investigated. (La, Sr, Ca)<sub>14</sub>Cu<sub>24</sub>O<sub>41</sub> structure contains interpenetrating subsystems of  $CuO_2$  chains and  $Cu_2O_3$  two-leg ladders with (Sr, Ca, La) atoms coordinated to the ladder layer [70, 71]. Here, the hole doping of the ladders is intrinsically provided by the chain subsystem [75, 76, 73]. These materials, entering either SC as in  $Sr_{14-x}Ca_xCu_{24}O_{41}$ ,  $10 \leq x \leq 13.6$  or CDW, as in  $Sr_{14-x}Ca_xCu_{24}O_{41}$ ,  $0 \leq x \leq 9$ , [69, 78], proved to be an experimental realisation of a theoretical concept .

We will describe the essence of knowledge on the structure and properties of these materials, at the beginning of our research. We will show (as in the case of  $(TMTSF)_2PF_6$ ) how the design of an artificial structure is related to it's function. Before presenting the experimental framework, it is necessary to clarify the concepts of spin chains and ladders and hole doping.

### 1.2.1 Models of spin and charge arrangements applicable to cuprate structures

A copper site in cuprate materials is experimentally characterized either with a spin  $S = \frac{1}{2}$  of the unpaired  $3d^9$  electron of  $Cu^{2+}$  ion or with a *hole*: an effective  $Cu^{3+}$  site with spin  $S = 0$ . More appropriately,  $Cu^{3+}$  site exists due

to a hole located in the  $2p$  orbitals of the four oxygens coordinated to a  $\text{Cu}^{2+}$  ion. A hole within the  $\text{O}2p$  orbitals of the  $\text{CuO}_4$  square is strongly bound to  $\text{Cu}^{2+}$  ion, due to hybridization of the orbitals. Spin  $S = 0$  is observed due to the combination of the spin  $S = \frac{1}{2}$  of the hole with  $S = \frac{1}{2}$  of the unpaired  $3d^9$  electron in a *Zhang-Rice* singlet, see also Sec. 2.2.1, [74]. Zhang-Rice singlet effectively decouples spin and charge degrees of freedom for a hole. This leads to a complementarity between the spin and charge arrangements in cuprate structures.

HTSC cuprates parent insulator compounds, where the characteristic structural element is a  $\text{CuO}_2$  layer, are the best examples of planar  $S = \frac{1}{2}$  antiferromagnets with isotropic and predominantly nearest-neighbor coupling. They show simple long-range order (LRO) of AF character, in agreement with theory which predicts an ordered ground state for the Heisenberg  $S = \frac{1}{2}$  AF model on a 2D square lattice, Fig. 1.10. This means that spin-spin correlations decay to a non-zero constant as mutual spin distance grows. This non-zero value indicates that there is a LRO in the spin system.

The spin- $\frac{1}{2}$  AF Heisenberg chain with the nearest-neighbor AF coupling is also well understood, Fig. 1.10. A famous exact solution, found by Bethe many years ago, showed that the quantum fluctuations are strong enough to prevent long-range order and that spin-spin correlations decay slowly to zero as a power law of distance. Still they remain dominant over finite length scales, and thus the spin chain is also of AF character. One structural element of q1D cuprates is the  $\text{CuO}_2$  chain. When all copper sites carry spin they become examples of the Heisenberg  $S = \frac{1}{2}$  chain with the nearest-neighbor AF coupling. In both one and two dimensional AF models there is no spin gap, *i.e.* there is no cost in energy to create a spin excitation with  $S = 1$ .

To make the transition from the quasi-LRO in a chain to the true LRO that occurs in a layer, one can assemble chains to make ladders, Fig. 1.10. Apparently, the ladder structures are somewhere inbetween the 1D and 2D case. But the crossover between the 1D and 2D case is not smooth at all. The theoretical investigations indicated that the Heisenberg model on two leg-ladder should show a *spin gap*. That is, a finite energy is necessary to create a spin excitation with  $S = 1$ , making the ladder systems qualitatively different from the chains and layers. The spin gap presence is relatively obvious in the *strong coupling* limit. In this limit coupling along the rung is stronger than along the leg of the ladder,  $J_{\perp} > J_{\parallel}$ . Thus, the ladder ground-state may be regarded as a product of spin singlets, one per rung, Fig. 1.10. The overall spin of the ladder in the ground-state is zero. It costs  $J_{\perp}$  to create a triplet on the rung. If such excitations are created, they may propagate along the ladder, but their correlations decay exponentially, due to the finite spin-gap. Due to the purely short-range correlations this state is also referred

to as a *gapped spin-liquid*.

Final step is the concept of hole-doped ladders, Fig. 1.10. At low hole doping, and in the strong-coupling limit, the system prefers combining two holes in the same rung, in order to save the energy. Otherwise, two holes would break two singlets, producing substantial energy cost. After introducing this concept of pairs' formation, it is only natural to accept the possibility of establishing the superconducting state. Binding pairs of holes gives them a bosonic character, which is a necessary step on the way to superconductivity. However, this alone does not suffice because, in such a low dimensional system, another collective state competes, namely, a charge density wave. The balance between the two and the question which one dominates depends on the parameters of the model and, more generally, on residual interactions between hole pairs, all of which is hard to predict theoretically, [50, 80, 77]. The theoretical overview of the competition between the possible ground states of q1D systems, as well as more detailed concept of ZR singlet and SC in doped ladders, are given in Chapter 2.

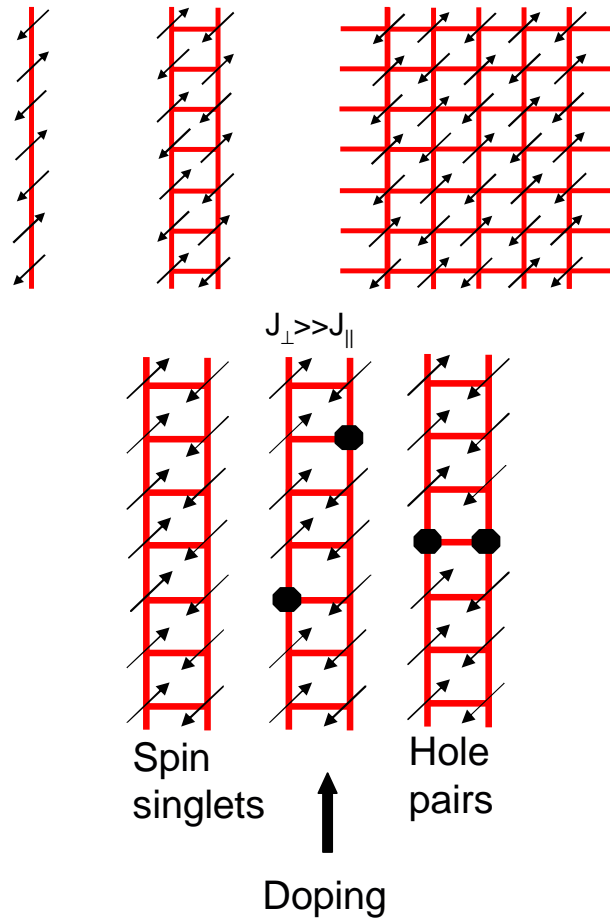


Fig. 1.10: Upper panel: The Heisenberg  $S = \frac{1}{2}$  antiferromagnetic model on chain, two-leg ladder and 2D square lattice. Lower panel: Suggested mechanism of hole-pairing in the two-leg ladders: When the coupling along the ladder rung  $J_{\perp} > J_{\parallel}$  is stronger than along the ladder legs, the ground state is a direct product of spin singlets appearing on the rungs. Doping individual holes to the ladder leads to destroying the singlets, which is energetically unfavorable. Therefore, the holes tend to pair-up on the rungs, [68, 81].

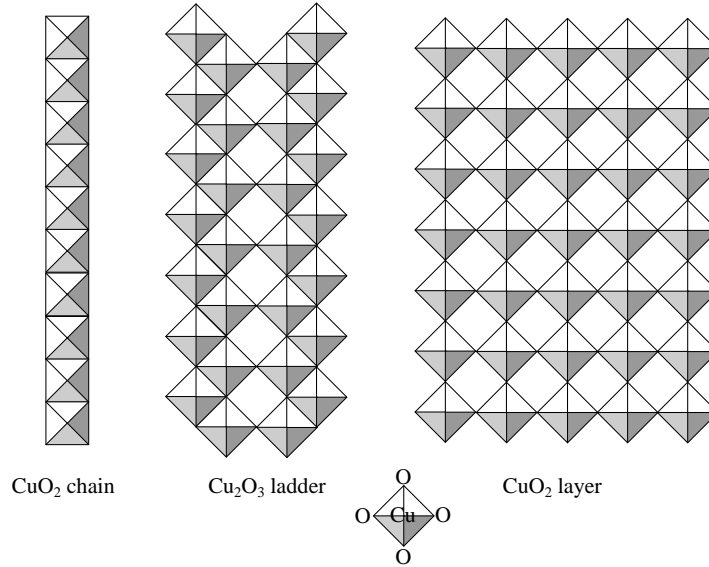


Fig. 1.11: The basic building block of cuprate structures is a  $\text{CuO}_4$  square. Corner and/or edge sharing arrangements of these squares produce different substructures like chains, ladders and layers.

### 1.2.2 Crystallographic structure of q1D cuprates $(\text{La, Sr, Ca})_{14}\text{Cu}_{24}\text{O}_{41}$

Copper and oxygen form the functional structure of the q1D cuprates. They form two different substructures in these composite materials:  $\text{CuO}_2$  chains and  $\text{Cu}_2\text{O}_3$  two-leg ladders. Cu ions are coordinated to four oxygen ions -  $\text{CuO}_4$  square is a basic building block, Fig. 1.11. The layer formed in HTSC cuprates is formed of solely corner sharing (oxygen sharing)  $\text{CuO}_4$  squares. Chains may be regarded as strings of edge sharing  $\text{CuO}_4$  squares. The two-leg ladders are arranged out of zig-zag chains composed of edge sharing  $\text{CuO}_4$  squares, and the zig-zag chains touch at the corners of  $\text{CuO}_4$  squares. The ladders are thus composed of both corner and edge sharing squares.

In Fig. 1.12 the formation of chains and ladders layers is shown, [70, 71]. Strings of (Sr, Ca, La) atoms enter between these layers. Strictly speaking, these atoms are coordinated to the ladder layer. They enter the spaces opened between the zig-zag chains. Thus, Sr, Ca, La atoms strings and the ladder layer form the ladder subsystem, while only  $\text{CuO}_2$  chains in parallel arrangement form the chain subsystem. If the  $\text{CuO}_4$  squares were ideal there would always be  $1 : \sqrt{2}$  incommensurability along the chains and ladders subsystems (this is simply the ratio between a diagonal and a side of an ideal square). In the real q1D cuprate materials all the squares are distorted, but

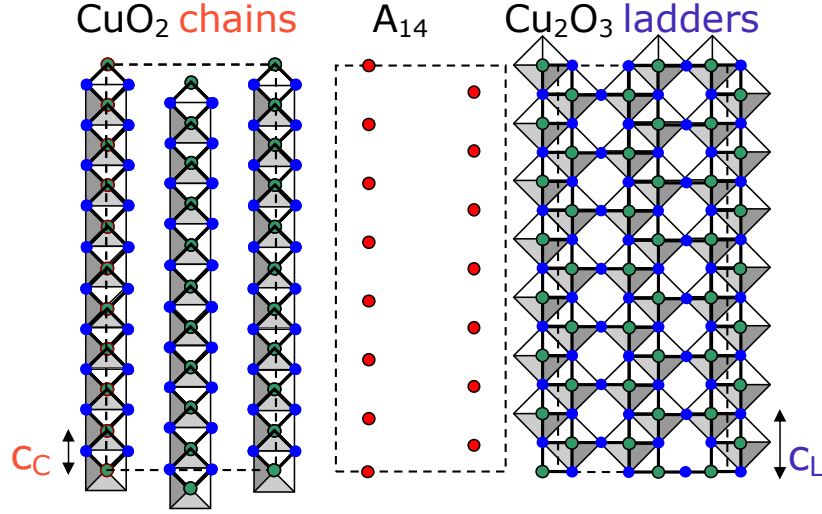


Fig. 1.12: Inbetween every  $\text{Cu}_2\text{O}_3$  ladder and  $\text{CuO}_2$  chain layer (Cu - green, O - blue) enters a layer of strings of Sr, Ca, La atoms (red). These atoms are coordinated to the ladder layer. Thus two subsystems are formed. The  $c$  parameter differs and the subsystems are incommensurate: ladders  $c_L \approx 3.9 \text{ \AA}$ , chains  $c_C \approx 2.75 \text{ \AA}$ . Still, the subsystems are very close to commensurability at  $10 \times c_C = 7 \times c_L$ . Due to this and for practical reasons, an approximate superstructure cell with the parameter  $c' \approx 27.5 \text{ \AA}$  is then used, [70, 71]. This cell is outlined by a dashed line.

chain and ladder subsystems are still incommensurable. These distortions related to incommensurability lead to additional modulations of crystallographic positions, *i.e.* one subsystem is weakly modulated to adjust to the other and *vice versa*. These effects may be regarded as an intrinsic source of disorder, [82]. The unit cells in the  $a - c$  plane of the two subsystems are different along  $c$ -axis: ladders  $c_L \approx 3.9 \text{ \AA}$ , chains  $c_C \approx 2.75 \text{ \AA}$ . For practical purposes, the fact that the subsystems are very close to commensurability at  $10 \times c_C = 7 \times c_L$  leads to an approximate superstructure cell with the parameter  $c' \approx 27.5 \text{ \AA}$ . This cell in the  $a - c$  plane is denoted in Fig. 1.12.

The orthorhombic crystals of  $(\text{La}, \text{Sr}, \text{Ca})_{14}\text{Cu}_{24}\text{O}_{41}$  q1D cuprates are built by alternated stacking of chain and ladder subsystems along the  $b$ -axis, Fig. 1.13. Both  $b$ - and  $a$ - unit cell parameters are common to the subsystems and to the crystal as a whole. The composition of Sr, Ca, La strings dictates the unit cell parameter in  $b$ -direction.

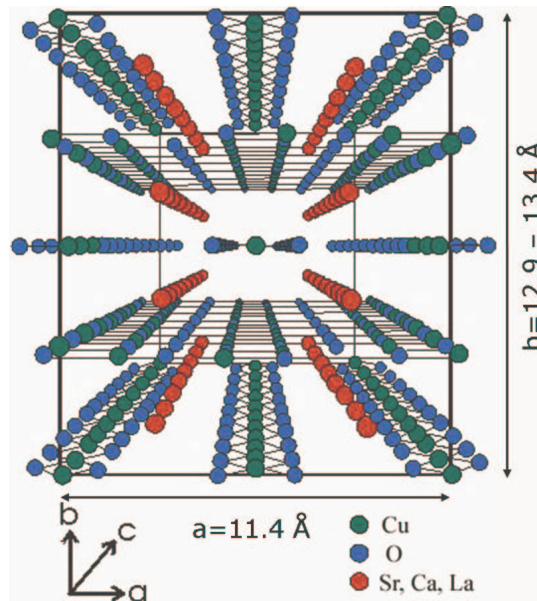


Fig. 1.13: A stereo drawing of  $(\text{La, Sr, Ca})_{14}\text{Cu}_{24}\text{O}_{41}$  structure. The crystal system is orthorombic. The view is along the  $c$ -axis. The alternative stacking of  $\text{CuO}_2$  chain and  $\text{Cu}_2\text{O}_3$  ladder layers along with the included strings of Sr, Ca, La atoms (shown in red) is best understood in this view. Both chain and ladder subsystems and the crystal as a whole have the same  $a \approx 11.5 \text{ \AA}$  and  $b \approx 12.9 - 13.4 \text{ \AA}$  cell parameters. The  $b$ -parameter is the only one that is significantly dependent on the Sr, Ca, La composition. Subsystems are incommensurate along the direction of the  $c$ -axis, [70, 71].

### 1.2.3 Electronic structure of q1D cuprates (La, Sr, Ca)<sub>14</sub>Cu<sub>24</sub>O<sub>41</sub>

The directions of Cu-O bonds characterize the dimensionality of the subsystems. These bonds are shown as lines which connect the atoms in Fig. 1.14. The chains are a structure of pronounced 1D nature where two neighbouring Cu<sup>2+</sup> ions along the chain, are connected via two 90° Cu-O-Cu exchange interaction links of ferromagnetic character. But one chain is completely decoupled from the other. In Fig. 1.12 the pattern of CuO<sub>4</sub> squares and interatomic bonds (black lines) seems to form a continuous ladder layer, of apparent 2D nature. The ladders, as a 1D structure, emerge from this picture as separate entities due to the following: strong antiferromagnetic 180° Cu-O-Cu bonds make a ladder, while the interladder coupling is very weak both because of a very weak ferromagnetic 90° Cu-O-Cu bond and triangular arrangement of Cu atoms between neighboring ladders, which results in frustration. Thus, the ladder layer may be recognized as composed of separate, decoupled ladders, denoted in Fig. 1.14.

180° Cu-O-Cu bond forms due to the following: Cu<sup>2+</sup> ion has a 3d<sup>9</sup> configuration with the single hole occupying an antibonding orbital. This leads to an exceptionally strong ( $J \approx 0.13$  eV) superexchange interaction of two neighboring Cu<sup>2+</sup> ions through *dpσ* overlap with the 2*p* orbital of the oxygen ion inbetween [73]. Here originates a planar structure of CuO<sub>2</sub> layers, composed of CuO<sub>4</sub> squares that are all corner sharing, Fig. 1.11. The 180° Cu-O-Cu bonds are oriented equivalently along both directions within this layer. On the contrary, in the ladders, it should be noted that  $J_{\parallel}$  along the ladder legs is larger than  $J_{\perp}$  along the ladder rungs, thus further pronouncing one-dimensionality of this structure.

The electronic structure of parent compound Sr<sub>14</sub>Cu<sub>24</sub>O<sub>41</sub> was calculated *ab initio* by the linear-muffin-tin-orbital method, [83]. The calculations were performed on a small approximative unit cell containing one formula unit of Sr<sub>14</sub>Cu<sub>24</sub>O<sub>41</sub>. However, this calculation was performed under the assumption that the system was metallic, and that led to finite density of states (DOS) at  $E_F$ , which contradicts the experimentally observed insulating behavior. The total and partial DOS is shown in Fig. 1.15, the Fermi energy is set at  $E_F = 0$ . Still, the total density of states for the valence band is compared with photoemission experiments with fairly good agreement. Around the Fermi energy there exist quasi-one-dimensional bands originating from the ladder and chain subsystems. The bands can be fitted by simple q1D tight-binding dispersions with only nearest-neighbor and next-nearest-neighbor hoppings along and between the ladders (or chains) considered. The nearest-neighbor interladder hoppings are estimated to be 5 - 20 % of the intraladder ones.

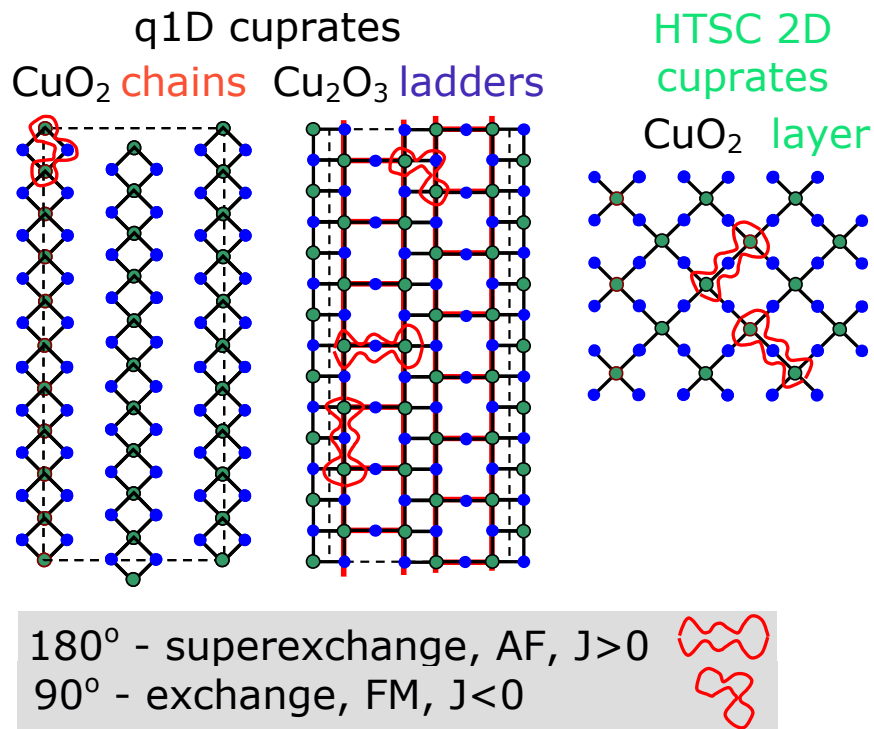


Fig. 1.14: The direction of Cu-O bonds characterizes different cuprate structures: chains, ladders and planes. The 180° Cu-O-Cu bonds are mutually orthogonally oriented within the square lattice layer, thus giving to HTSC cuprates their 2D nature. Chains and ladders also form layers, but the chains are mutually decoupled, which gives the chain subsystem its 1D nature. The pattern of strong antiferromagnetic 180° Cu-O-Cu bonds makes a ladder, and the interladder coupling is very weak both because of a very weak ferromagnetic 90° Cu-O-Cu bond and triangular arrangement of Cu atoms between neighboring ladders, which results in frustration. Therefore, although ladders form layers, the ladder subsystem is also 1D in nature.

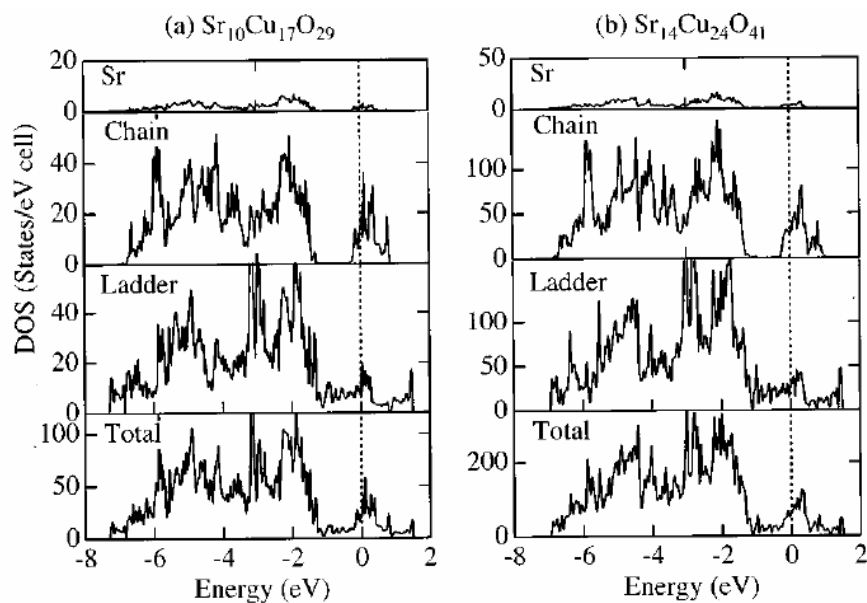


Fig. 1.15: The total and partial density of states, of chains and of ladders, for a small approximative unit cell containing one formula unit of  $\text{Sr}_{14}\text{Cu}_{24}\text{O}_{41}$ .

The obtained interladder hopping seems non-negligible, contradicting the observed room temperature dc conductivity anisotropy, and despite that the strong correlation effects, such as hole-pairing are expected to increase the anisotropy on cooling. At RT these band anisotropy calculations seem to be consistent only with the optical absorption measurements, [84].

### 1.2.4 Hole distribution

The doping in composite  $(\text{La, Sr, Ca})_{14}\text{Cu}_{24}\text{O}_{41}$  materials is completely intrinsic, simple stoichiometry confirms this. In  $\text{Sr}_{14-x}\text{Ca}_x\text{Cu}_{24}\text{O}_{41}$  materials there are 6 holes per formula unit, hole count  $\delta_h = 6$ . Nonisovalent substitution of  $\text{Sr}^{2+}$  or  $\text{Ca}^{2+}$  with  $\text{La}^{3+}$  (or  $\text{Y}^{3+}$ ) reduces  $\delta_h$ . There are 4 formula units per approximative superstructure cell as depicted in Fig. 1.13, so, for  $\text{Sr}_{14-x}\text{Ca}_x\text{Cu}_{24}\text{O}_{41}$  materials there are 24 holes in this cell. This amounts to the hole density of  $6 \times 10^{21}\text{cm}^{-3}$ . The arrangement of these holes in a given subsystem is complementary with the spin arrangement, Fig. 1.16. Simple stoichiometric considerations lead to the arrangement as shown in this figure, where all the holes are found in the chains. Madelung energy calculations lead to the same conclusion for  $x = 0$  material, but Sr-by-Ca substitution leads to the appearance of the hole transfer to the ladders [85]. The tendency of holes to move from chains to ladders is additionally proved by the calculation result for  $x = 14$  (although, this material is not synthesized) where all holes are transferred to ladders. One of the basic assumptions of these calculations is the initial arrangement of the holes whose interactions and rearrangement to the lowest potential state are then calculated. In choosing these initial parameters lies a possibility that the results of these calculations do not refer to the experiment correctly. Still, they do confirm the concept of self-doped holes. This concept is also confirmed by bond-valence-sum (BVS) calculations by Kato *et al.*, [86] based on the crystallographic data for Cu-O bond lengths, [70, 71]. Kato *et al.* calculated, for  $x = 6$  material, a slight increase in hole concentration in the ladder, when compared to  $x = 0$  material.

Various experimentally observable properties of  $(\text{La, Sr, Ca})_{14}\text{Cu}_{24}\text{O}_{41}$  materials are undoubtedly related to the redistribution of the holes and spins in the two subsystems. The parent compound  $\text{Sr}_{14}\text{Cu}_{24}\text{O}_{41}$  has a rather high dc conductivity, which is believed to originate in ladders, along the legs of ladders, of about  $300 (\Omega\text{cm})^{-1}$  at 300 K, showing an anisotropy  $\sigma_c:\sigma_a:\sigma_b \approx 1000:100:1$  [84]. However, starting from the ‘simple’  $\text{Sr}_{14}\text{Cu}_{24}\text{O}_{41}$ , it is not clear what the mechanism of dc conductivity is. The basic question is where the holes at room temperature in  $\text{Sr}_{14}\text{Cu}_{24}\text{O}_{41}$  are, and how are the holes redistributed between chains and ladders when temperature and Ca-content are changed.

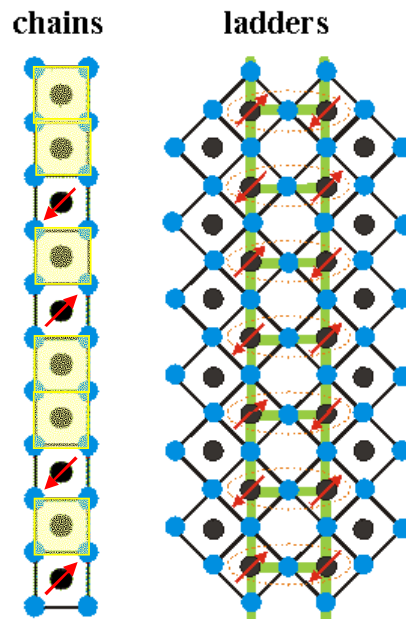


Fig. 1.16: The complementary arrangement of holes and spins in the subsystems of  $\text{Sr}_{14-x}\text{Ca}_x\text{Cu}_{24}\text{O}_{41}$  (shown for one formula unit).  $\text{Cu}^{2+}$  ion of spin  $S = \frac{1}{2}$  is denoted with red arrows, while the holes, which reside in the  $2p$  orbitals of oxygens surrounding  $\text{Cu}^{2+}$  ions (whose spins form Zhang-Rice singlets with the spins of holes) are denoted by yellow squares. For  $\text{Sr}_{14-x}\text{Ca}_x\text{Cu}_{24}\text{O}_{41}$  materials, stoichiometrical considerations indicate that all 6 holes per formula unit reside in the chains. Madelung energy calculations denote the hole transfer upon Sr-by-Ca substitution (see text).

### Evidence for stronger redistribution

The study of possible transfer of holes from chains to ladders was experimentally initiated in the work of Osafune *et al.*, [75]. They report RT optical conductivity  $\sigma(\omega)$  measured along the ladder legs,  $E||c$ . Single crystals of materials  $\text{Sr}_{14-x}\text{Ca}_x\text{Cu}_{24}\text{O}_{41}$ ,  $x = 0, 3, 6, 10, 11$  were studied. They also measured an Yttrium substituted material,  $\text{Y}_3\text{Sr}_{11}\text{Cu}_{24}\text{O}_{41}$ .  $\text{Y}^{3+}$  is nonisovalent to  $\text{Ca}^{2+}$  and  $\text{Sr}^{2+}$ , and thus this material has  $\delta_h = 3$ , lower than  $\delta_h = 6$  of isovalent substituted  $\text{Sr}_{14-x}\text{Ca}_x\text{Cu}_{24}\text{O}_{41}$  materials.

The optical conductivity spectrum of  $\text{Y}_3\text{Sr}_{11}\text{Cu}_{24}\text{O}_{41}$  is typical of insulators, Fig. 1.17. The spectrum is characterized by a peak at 2.0 eV. The most possible origin of this peak is the charge-transfer excitation between  $\text{Cu}3d$  and  $\text{O}2p$  states which is also observed in the parent insulators of HTSC cuprates, [87]. The question for the composite material like  $\text{Y}_3\text{Sr}_{11}\text{Cu}_{24}\text{O}_{41}$  is whether this peak has to be ascribed to the holes in the ladders or in the chains. Taking into account the Madelung energy and BVS calculations, the peak at around 3 eV for  $\text{Sr}_{14-x}\text{Ca}_x\text{Cu}_{24}\text{O}_{41}$  might be attributed to the holes in the chains.

The principal observation of Osafune *et al.* was that for  $\text{Sr}_{14-x}\text{Ca}_x\text{Cu}_{24}\text{O}_{41}$  materials  $\text{Cu}3d\text{-O}2p$  peak spectral-weight (SW) decreases and the conductivity in the low-frequency region below 1.2 eV increases with  $x$ . Such SW transfer is essentially the same as the transfer observed when the parent insulators of HTSC cuprates are doped with carriers. As the substitution of isovalent Ca does not change the hole count in  $\text{Sr}_{14-x}\text{Ca}_x\text{Cu}_{24}\text{O}_{41}$  material, the observed SW transfer should be attributed to a redistribution of holes between chains and ladders.

This transfer may also be quantified as presented in Fig. 1.18. The integrated conductivity  $N_{eff}$  is assumed to be proportional to the hole number;  $\delta_h \propto N_{eff}(\omega) \propto \int_0^\omega \sigma(\omega') d\omega'$ . Since the conductivity below 1.2 eV is attributed to the ladders, the values of  $N_{eff}(\omega = 1.2\text{eV})$  are regarded as proportional to the number of holes in the ladders. Here Osafune *et al.* assumed (correctly, as we will discuss later) that 5 holes reside in chains and one in ladders for  $x = 0$ . SW transfer increases with  $x$  and  $N_{eff}(\omega = 1.2\text{eV})$  reaches 0.20 for  $x = 11$ . This implies  $\delta_h = 2.8$ , *i.e.* almost half of the holes seem to be transferred in the ladders. Number of holes on the copper site in the ladders may be recalculated into the effective valence of copper. In the undoped ladder there are no holes and the average Cu valence is +2, thus coppers in the hole doped ladders have the average valence  $+2 + N_{eff}(\omega = 1.2\text{eV})$ . From the ladder valence the basic stoichiometry gives the chain Cu valence. The respective dependence of Cu valence on Ca substitution is shown in the inset of Fig. 1.18.

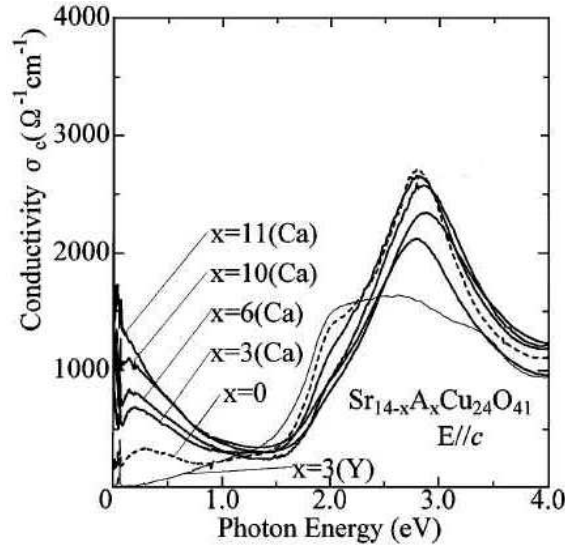


Fig. 1.17: Optical conductivity *vs.* frequency,  $\sigma(\omega)$ , measured at room temperature along the ladder legs,  $E \parallel c$ . Materials  $x = 0, 3, 6, 10, 11$  were studied, as well as Y substituted  $\text{Y}_3\text{Sr}_{11}\text{Cu}_{24}\text{O}_{41}$ . The conductivity was obtained from the Kramers-Kronig transformation of the reflectivity spectra. From Ref. [75].

The conclusion from this analysis is that there is a redistribution of holes from chains to ladders, through the interpretation of the experimentally observed SW transfer process induced by the Ca substitution. However, this analysis provides only information on the relative change in the hole number. The absolute hole counts in the chains and ladders of  $x \neq 0$  were based on the assumption for the hole counts in  $x = 0$ . Another important remark would be that the holes in the chains seem to be well localized, since the charge excitations attributed to the chains start only above 2.0 eV.

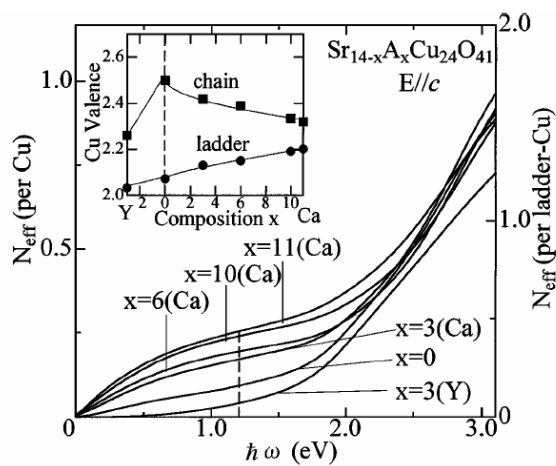


Fig. 1.18: Effective electron number  $N_{eff}$  per Cu site (left-hand scale) from the conductivity sum is plotted as a function of energy for various compositions  $x$ .  $N_{eff}$  per ladder Cu site is indicated on the right-hand scale. The valences of both chain- and ladder-Cu estimated from  $N_{eff}(\omega = 1.2eV)$  for each composition are plotted in the inset. From Ref. [75].

### Evidence for weaker redistribution

The experiment which approached the hole distribution in  $(\text{La}, \text{Sr}, \text{Ca})_{14}\text{Cu}_{24}\text{O}_{41}$  most directly is polarization-dependent near-edge x-ray absorption fine structure (NEXAFS), performed by Nücker *et al.* [76]. The excitation process in NEXAFS involves highly localized O1s core level. Orienting the electric field vector of the incident radiation,  $\mathbf{E}$ , parallel to the crystallographic axes, allows one to investigate specifically the O2p orbitals oriented likewise, and thus gain site-specific information on the hole distribution. Three inequivalent oxygen sites appear in the NEXAFS measurements of O1s core levels spectra. With each of the inequivalent sites, a different Cu-O bond configuration is associated, Fig. 1.19. There is Cu-O-Cu interaction with  $90^\circ$  geometry at the O(c) sites of the chains. There are straight bonds ( $180^\circ$ ) connecting the Cu(l) sites in the two legs of a single ladder via the rung O(2) sites; and there is a different situation for the O(1) sites of the legs, which form bonds to each of the three neighboring Cu(l) atoms. Assuming that, analogous to the situation in HTSCs, only  $\sigma$  bonds formed between Cu3d and O2p states contribute to the spectral weight near the Fermi level,  $E_F$ , there are only five inequivalent O2p orbitals in the  $a, c$  plane which may contribute to spectral weight in O1s NEXAFS.

Nücker *et al.* investigated single crystals of various nonisovalently,  $(\text{La}/\text{Y}, \text{Sr}, \text{Ca})_{14}\text{Cu}_{24}\text{O}_{41}$ , and isovalently,  $\text{Sr}_{14-x}\text{Ca}_x\text{Cu}_{24}\text{O}_{41}$ ,  $x = 0, 5, 9, 11.5, 12$ , substituted materials. The nonisovalent materials have hole count  $\delta_h$  of less than 6 (per formula unit). The observation that for  $\text{La}_3\text{Sr}_3\text{Ca}_8\text{Cu}_{24}\text{O}_{41}$ ,  $\delta_h = 3$ ,  $\text{Y}_3\text{Sr}_{11}\text{Cu}_{24}\text{O}_{41}$ ,  $\delta_h = 3$  and  $\text{La}_2\text{Ca}_{12}\text{Cu}_{24}\text{O}_{41}$ ,  $\delta_h = 4$ , spectra can be attributed to only one type of O sites, which is furthermore almost symmetric within the  $a, c$  plane, is readily understood if the holes in the  $\delta_h < 6$  materials occupy exclusively sites in the chains. In the materials  $\delta_h = 6$ , *i.e.*  $\text{Sr}_{14-x}\text{Ca}_x\text{Cu}_{24}\text{O}_{41}$ , however, this symmetry is obviously broken. NEXAFS spectra unambiguously show that holes are found in all O sites and that distribution is no more symmetric between orbitals aligned along  $a$  and  $c$  axis.

The results are shown in Fig. 1.20. Number of holes refers to the total number of holes found in one of the subsystems in the orbitals oriented either along the  $a$ - or along  $c$ -, *i.e.* along the rungs and legs of ladders, respectively. This number changes with Ca substitution  $x$ . H1 denotes the spectra attributed to the chains subsystem, where distribution is still almost symmetric between  $a$  and  $c$  orientations, and the total number slightly changes from 5.2 to 4.9, that is, approximately 5 holes per formula unit are found in the chains of  $\text{Sr}_{14-x}\text{Ca}_x\text{Cu}_{24}\text{O}_{41}$ , independently of  $x$ . H2 denotes the spectra attributed to the ladders subsystem. Initially, for  $x = 0$ , holes are found in orbitals aligned along  $c$ , along the legs of the ladder, denoted H2  $E||c$ . With

substitution  $x$ , they become transferred into the orbitals, aligned along  $a$ , of the rung oxygen, denoted  $H_2 E||a$ . This transfer within the ladder seems more pronounced than the transfer between the chain and ladder systems.

NEXAFS experiment unambiguously shows that there are holes in ladders already for  $x = 0$ . The number of holes increases from 0.8 for  $x = 0$  to 1.1 for  $x = 12$ . This experiment confirms the assumption of Osafune *et al.*, that one hole resides in the ladders of  $x = 0$ . However, it is somewhat contradictory to their results, regarding the fact that the observed redistribution of holes from chains to ladders is lower. This experiment provides the absolute hole counts in the chains and ladders, while Osafune *et al.* provide only relative numbers. Therefore, we consider the NEXAFS results more reliable. That is, while the hole transfer unambiguously occurs, this is probably not to the extent suggested by Osafune *et al.*.

In the presented outline of the hole distribution between the subsystems at RT, the question whether there is any redistribution at lower temperatures still remains. Studies of the hole/spin patterns within the subsystems provide an additional information on the hole distribution at RT, as well as at low temperatures. They will be presented in the following Sections.

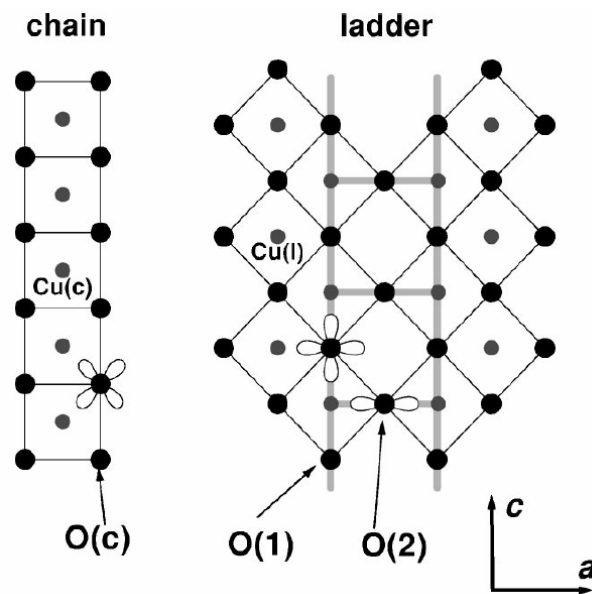


Fig. 1.19: Three inequivalent oxygen sites appear in the NEXAFS measurements. A different Cu-O bond configuration is associated with each site. Chain oxygen orbitals O(c) take part in Cu-O-Cu interaction with about  $90^\circ$  geometry. Ladder oxygens O(1,2) take part in the straight bonds ( $180^\circ$ ), within the *legs* or within the *rungs*. Consequentially, orienting the electric field vector of the incident radiation,  $\mathbf{E}$ , parallel to the crystallographic axes, allows one to investigate specifically the  $O2p$  orbitals oriented likewise, and thus gain site-specific information on the hole distribution. From Ref. [76].

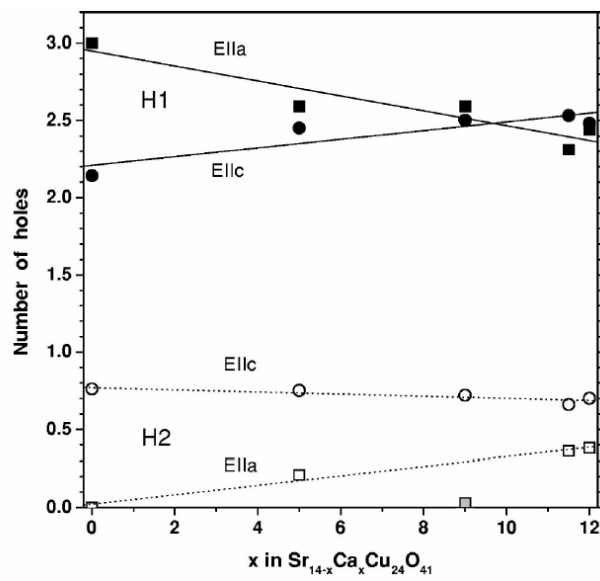


Fig. 1.20: Hole count per formula unit as derived from renormalized spectral weights in NEXAFS for  $\text{Sr}_{14-x}\text{Ca}_x\text{Cu}_{24}\text{O}_{41}$ . Contributions from  $\text{O}2p$  orbitals oriented along the  $a$ - and  $c$ -axes in chain (H1) and ladder (H2) subsystems are shown. From Ref. [76].

## 1.2.5 Chains subsystem

### Magnetic susceptibility

The magnetic susceptibility is a bulk technique which should not be able to discern between the subsystems. Still, the magnetic properties of (La, Sr, Ca)<sub>14</sub>Cu<sub>24</sub>O<sub>41</sub> have been studied by susceptibility, [88, 89, 84], and these results have led to initial results on the arrangement of spins (and complementarily, the holes) in the chains.

In Fig. 1.21 the temperature dependence of susceptibility  $\chi$ , measured by Motoyama *et al.* [84] is shown. Various single crystals of isovalently and nonisovalently substituted materials of different hole counts and different chain/ladder distributions were studied. The susceptibility for the pure two-leg ladder compound SrCu<sub>2</sub>O<sub>3</sub> is shown for comparison. Carter *et al.* [89] argued that, for Cu<sub>2</sub>O<sub>3</sub> ladders found in the composite compounds, the susceptibility should be negligibly small, if it can be approximated by the susceptibility of the isostructural SrCu<sub>2</sub>O<sub>3</sub> that has a spin-gap of 420 K. This immediately leads to the conclusion that only spins in chains contribute to the susceptibility of the composite q1D cuprates, and that susceptibility measurements investigate the chain subsystem. Further, La<sub>6</sub>Ca<sub>8</sub>Cu<sub>24</sub>O<sub>41</sub> material (hole count,  $\delta_h = 0$ ) shows the susceptibility as expected for the Curie paramagnetism of the chain with uncorrelated, free spins on all the ten sites,  $10 - \delta_h = 10$ . Curie paramagnetism of lower magnitude is observed also for Y compounds, Y<sub>3</sub>Sr<sub>11</sub>Cu<sub>24</sub>O<sub>41</sub>,  $\delta_h = 3$ ,  $10 - \delta_h = 7$  free spins and Y<sub>1</sub>Sr<sub>13</sub>Cu<sub>24</sub>O<sub>41</sub>,  $\delta_h = 5$ ,  $10 - \delta_h = 5$  free spins (all the holes are found in the chains in nonisovalently substituted compounds, see previous Section).

Taking into account the results of Nücker *et al.* (previous Section) we note that isovalently substituted compounds Sr<sub>14-x</sub>Ca<sub>x</sub>Cu<sub>24</sub>O<sub>41</sub>,  $\delta_h = 6$ , have one hole transferred to the ladders. Thus, they have 5 spins (Cu<sup>3+</sup> sites) for every ten chain sites. The susceptibility of these 5 spins deviates from the Curie behavior for free spins and shows a decrease in  $\chi$  towards low temperatures. A strong decrease of susceptibility is most pronounced for the parent compound Sr<sub>14</sub>Cu<sub>24</sub>O<sub>41</sub> below 70 K. Thus, the susceptibility data indicate that the ground state of CuO<sub>2</sub> chains is also characterised with a spin gap. The question on the nature of ordering which leads to the spin-gapped state in the chains is still remaining.

Matsuda *et al.* [88] and Carter *et al.* [89] found that a simple AF dimer model gives a good fit to the low temperature part of  $\chi$ . The AF dimer model is based on organizing spins along the chain into isolated antiferromagnetically coupled pairs. The solid line in Fig. 1.22 shows the result of the AF dimer model  $\chi = 2N_D(g\mu_B)^2/kBT [3 + e^{(J/k_B T)}]$  with the number of

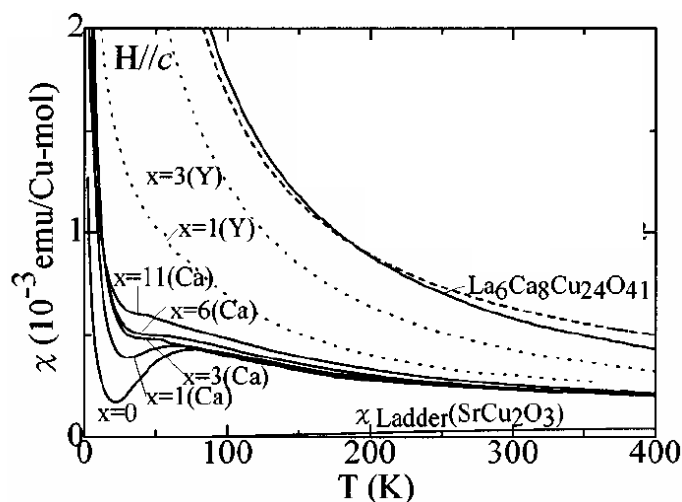


Fig. 1.21: The temperature dependence of the magnetic susceptibility,  $\chi$ , measured with magnetic field oriented along the  $c$ -axis. Various single crystals of isovalently and nonisovalently substituted materials of different hole counts and different chain/ladder distributions were studied. The dashed line is the expected Curie paramagnetism when all spins in the 10 chain Cu sites are free. From Ref. [84].

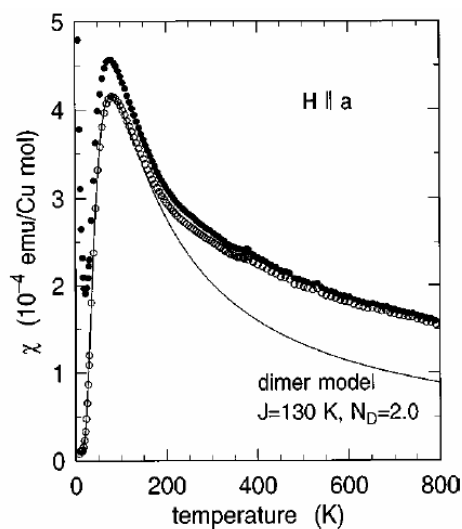


Fig. 1.22: Comparison for  $x = 0$ , of the experimentally measured temperature dependence of the magnetic susceptibility,  $\chi$ , represented by solid dots, Motoyama *et al.* [84], and the dimer model,  $N_D = 2.0$  per formula unit, indicated by a line, as described in the text.

dimers  $N_D = 2.0$  per formula unit ( $g = 2.05$  along the  $a$  direction) and the intradimer exchange  $J = 130$  K. The deviation of  $\chi$  from the dimer model at high temperatures can be attributed to the contribution from the ladders. In the end, even the susceptibility method as a bulk measurement leads the way towards establishing the model of ordering in the chains.

### Inelastic neutron scattering and X-ray diffraction

Early inelastic neutron scattering (INS) experiments by Matsuda *et al.*, [92] directly investigated spin ordering in the parent compound  $\text{Sr}_{14}\text{Cu}_{24}\text{O}_{41}$ , at low temperatures ( $T = 8$  K). The observed spin excitations were interpreted by the authors with a model where two different types of antiferromagnetically coupled dimers exist, characterized by intradimer spin separation of two chain parameters and four chain parameters,  $2c_C$  and  $4c_C$ , respectively. Due to the complementarity of the spin and holes arrangements, in this model 6 holes appear for every 10 chain sites. The chain superstructural periodicity due to the complementary hole ordering, expected for this model, is equal to  $10c_C$ . More sensitive measurements of the same type, were performed also at the lowest temperatures, 5-20 K, by two independent groups of Eccleston *et al.*, [91] and Regnault *et al.*, [90]. These authors did not see any evidence of larger,  $4c_C$  dimers in their results. Their interpretation was based on a model with only  $2c_C$  AF dimers. Interdimer distance was found to be three chain parameters,  $3c_C$ , Fig. 1.23. Quantitatively, there is no difference to the previous model, since two dimers (as in the interpretation of the susceptibility results above) and 6 holes appear again for every 10 chain sites. The chain superstructure periodicity in this model is  $5c_C$ . Due to the low internal symmetry ( $5c_C = 2c_C$  intradimer +  $3c_C$  interdimer) of such superstructural motif, energy gained from creating the superstructure would probably be smaller than the frustration due to the chain subsystem's interaction with the ladder subsystem. That is, the observation of such a superstructure in X-ray diffraction measurements is ascribed to the interactions between the subsystems and not to the charge-order in chains, [82, 93].

Still, direct observation of the lattice distortion due to the complementary charge-order is necessary to confirm the AF dimer model. Indeed, X-ray diffraction (XRD) results for  $\text{Sr}_{14}\text{Cu}_{24}\text{O}_{41}$  directly point to structural change related to charge-order, Cox *et al.* [94]. These measurements were performed at 50 K. The observed periodicity was equal to 4 chain parameters. This observation is possible due to higher internal symmetry ( $4c_C = 2c_C$  intradimer +  $2c_C$  interdimer) of such superstructural motif. This result leads to the choice of the model with the chain hole count 5, Fig. 1.23. In this model 2.5 AF dimers would appear per 10 Cu sites.

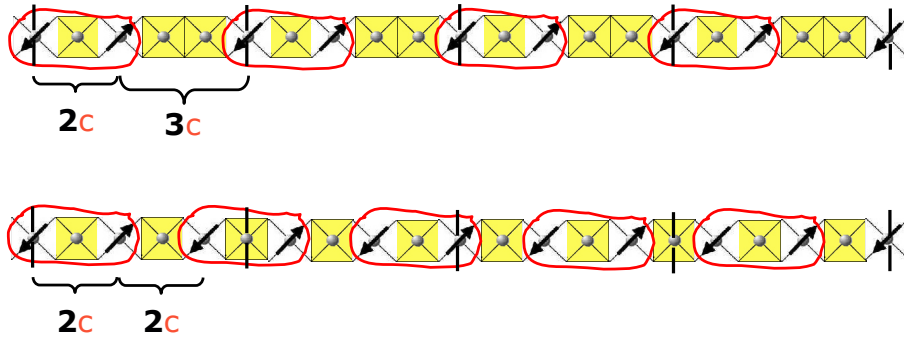


Fig. 1.23: Spin (red arrows) arrangement into the AF dimer (encircled) patterns with the complementary charge-order of the holes (yellow squares) for  $x = 0$  chains. The upper model, periodicity  $5c_C$ , chains hole count 6, is resulting from INS measurements at 5-20 K. The lower model, periodicity  $4c_C$ , chains hole count 5, is resulting from XRD measurements at 50 K.

We note the contradiction between the observed charge-order (by XRD) and spin ordering (by INS), *i.e.* chain hole counts of 5 and 6, respectively. However, the INS experiments were performed at lower temperatures than XRD. In order to resolve the contradiction we propose that the back-transfer of holes from the ladders to the chains occurs upon decrease in temperature below 50 K.

## NMR

The AF dimer model interprets the appearance of the spin gap in chains of  $\text{Sr}_{14-x}\text{Ca}_x\text{Cu}_{24}\text{O}_{41}$  materials as observed in susceptibility measurements [84]. In the AF dimer model intradimer exchange,  $J = 130$  K, may be related to the value of this gap [92]. NMR offers possibility of direct determination of the spin gap.  $^{63}\text{Cu}$  NMR signals for the ladder site can be separated from those for the chain site, since nuclei of these sites possess different quadrupole coupling. The initial  $^{63}\text{Cu}$  NMR measurements on polycrystalline samples by Kumagai *et al.* [95] addressed the issue of behavior of the spin-gap with increasing Ca-content  $x$ , for  $\text{Sr}_{14-x}\text{Ca}_x\text{Cu}_{24}\text{O}_{41}$ ,  $x = 0, 3, 6, 9$ . The spin-gap for the chains subsystem was found to be independent of  $x$ , with the value of 140 K. This value is well reproduced for  $x = 0$  in other studies: susceptibility, [89, 84], inelastic neutron scattering [88, 92, 91] and NMR [98, 96]. The same value is also found for  $x = 3.5$  by inelastic neutron scattering [97]. In Fig. 1.24, the temperature dependence of the spin-lattice relaxation rate  $1/T_1$  for the chains is shown for different materials of the q1D

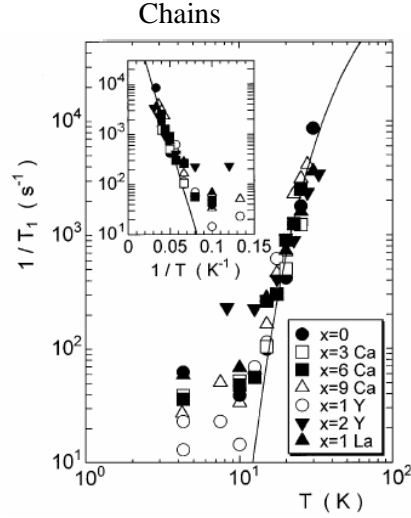


Fig. 1.24: The temperature dependence of the spin-lattice relaxation rate  $1/T_1$  for the chains is shown for different materials of the q1D cuprate family, and is most interesting for  $\text{Sr}_{14-x}\text{Ca}_x\text{Cu}_{24}\text{O}_{41}$ ,  $x = 0, 3, 6, 9$ . Full lines are fits to the activated behavior, established below 50 K. The activation energy is independent of  $x$ . From Ref. [95].

cuprate family [95]. From the activated behavior of  $1/T_1$ , it may be inferred that the spin-gap in the chains is fully opened below 50 K. Independence of  $x$  is also well documented.

The structure of NMR spectra also offers the possibility to analyze the temperature dependence of spin arrangement in chains. Takigawa *et al.* [98] performed  $^{63,65}\text{Cu}$  NMR/NQR measurements on single crystals of  $\text{Sr}_{14-x}\text{Ca}_x\text{Cu}_{24}\text{O}_{41}$ . Since holes ( $\text{Cu}^{3+}$  sites) and spins ( $\text{Cu}^{2+}$  sites) ordering is complementary, combination of methods sensitive to local magnetic fields and local electrical field gradients (EFG), seems to be well applied.

The first important result of Takigawa *et al.*, Fig. 1.25, left panel, is the observation of the chains  $^{63}\text{Cu}$  NMR spectrum center line splitting below  $T^*$  of 200 K. Inequality of Cu sites inferred from this result again suggests that the AF dimer pattern is being established in chains. Temperature dependence of the line shift, equal to the susceptibility  $\chi$  dependence, indicates that A sites are the AF dimer ones, *i.e.*  $\text{Cu}^{2+}$  sites. This is followed by the clear site distinction observed at low temperatures in the NQR spectrum, Fig. 1.25, right panel and the splitting of the B line below 50 K. A possible scenario to explain this splitting is that the dimers are separated by at least two nonmagnetic sites, which is an exact reproduction of the INS observed spin-pattern which requires for all 6 holes to be in the chains at the lowest

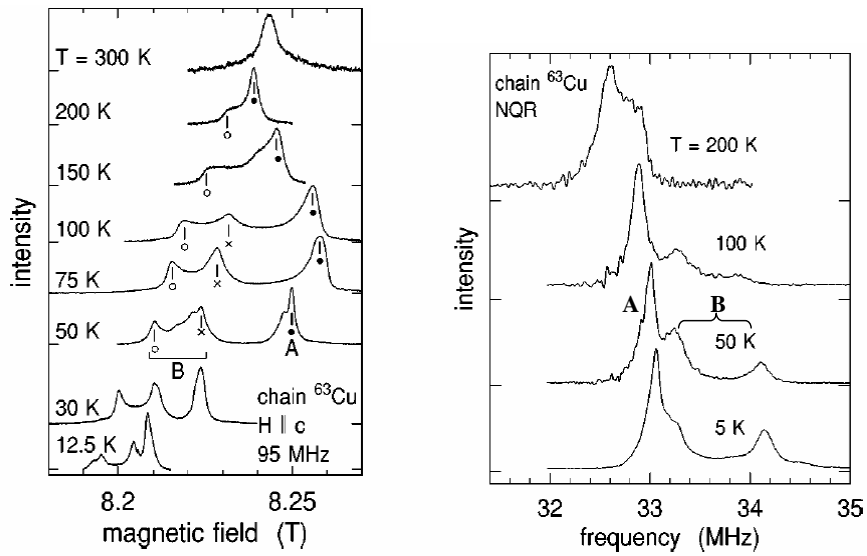


Fig. 1.25: Left panel: Temperature variation of the center line NMR spectrum at the chain  $^{63}\text{Cu}$  sites obtained at 95 MHz for  $H \parallel c$ . Right panel: Temperature variation of the NQR spectrum at the chain  $^{63}\text{Cu}$  sites. From Ref. [98].

temperatures, Fig. 1.23.

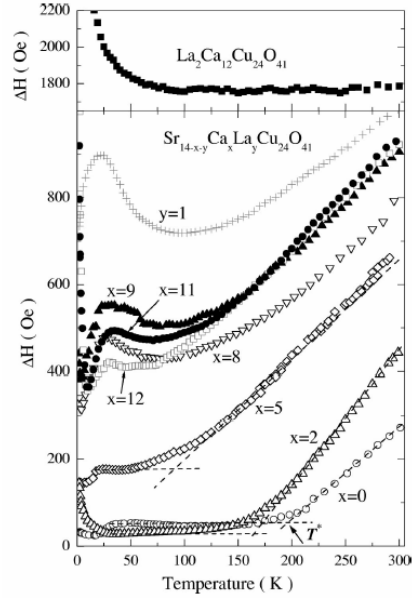


Fig. 1.26: Bottom panel: temperature dependence of the ESR linewidth  $\Delta H(T)$  of  $\text{Sr}_{14-x}\text{Ca}_x\text{Cu}_{24}\text{O}_{41}$  for various Ca contents, hole count  $\delta_h = 6$ . The topmost curve shows data for  $\text{La}_2\text{Sr}_{12}\text{Cu}_{24}\text{O}_{41}$ ,  $\delta_h = 5$ . The magnetic field has been applied along the  $c$  axis of the crystals. The dashed lines denote the constant and linear contributions to  $\Delta H(T)$ .  $T^*$ , defined as the crossing point of the dashed lines, is identified with the onset of long-range charge order in the chains. Top panel: the same for  $\text{La}_2\text{Sr}_{12}\text{Cu}_{24}\text{O}_{41}$ ,  $\delta_h = 4$ .  $T^*$  is not observed. From Ref. [99].

## ESR

Kataev *et al.* [99] have studied the electron spin resonance (ESR) of the  $\text{Cu}^{2+}$  ions in the chains, and found that the Cu-spin relaxation is appreciably influenced by the charge dynamics in the chains, resulting in a strong temperature dependence of the ESR linewidth  $\Delta H$  above a characteristic temperature  $T^*$ , Fig. 1.26. The crossover to a nearly temperature-independent line width  $\Delta H_0$  below  $T^*$  is identified with the onset of the long-range charge order associated with the AF dimer pattern order. With increasing Ca-content  $x$  this crossover shifts from about 200 K in  $\text{Sr}_{14}\text{Cu}_{24}\text{O}_{41}$  to 80 K for  $x = 5$ , indicating a rapid destruction of this order. For  $x=8$  the short-range order only remains, and persists shortly until for  $x > 11$  it is replaced by an AF long-range order, below 3.5 K [102, 100, 101].

**Conclusion: spin/charge arrangements in the chains**

The analysis of the experimental results, as found in literature, regarding the chain subsystem of  $\text{Sr}_{14-x}\text{Ca}_x\text{Cu}_{24}\text{O}_{41}$  leads to the conclusion that 2D spin ordering (AF dimer pattern) occurs in the chains, *e.g.* below  $T^* = 200$  K temperature for  $x = 0$ . The AF dimer pattern leads to the occurrence of spin-gap for chains, which (gap) is independent of Ca-substitution in  $\text{Sr}_{14-x}\text{Ca}_x\text{Cu}_{24}\text{O}_{41}$  materials. The AF dimer pattern is accompanied by the complementary 2D charge-order of the holes present in the chains. Due to this charge-order, the holes are well localized in the chains. From the difference in the XRD and INS results it can be concluded that chains hole count increases from 5 to 6, at least for the parent compound,  $x = 0$ , in the temperature range below 50 K and down to 5-20 K. This corresponds to NMR observation according to which spin-gap in the chains is only established below 50 K and to the observation of the line splitting in the NQR spectrum below the same temperature. While  $T^*$  is 200 K, these observations indicate that long-range order in chains of  $x = 0$  is fully established only below 50 K. Rapid destruction of long-range order occurs on Ca-substitution and for  $x=8$  the short-range order only remains.

## 1.2.6 Ladders subsystem

### Ladders spin-gap

While the chains subsystem showed somewhat unexpected gap in the spin excitation spectrum, the spin-gapped state of the ladder subsystem in  $\text{Sr}_{14-x}\text{Ca}_x\text{Cu}_{24}\text{O}_{41}$  was less unexpected. The theory predicted gapped spin-liquid state in the single ladder system. Indeed, such state was observed in the real materials, in the pure ladder compound  $\text{SrCu}_2\text{O}_3$ , as well as in the ladders subsystem of the composite compounds  $(\text{La, Sr, Ca})_{14}\text{Cu}_{24}\text{O}_{41}$ .

Imai *et al.* [96] performed  $^{17}\text{O}$  NMR measurements on  $x = 0$  and 3 materials. They have observed a transition from paramagnetic into the spin-gapped ground state of the ladders, at  $T^*(x = 0) \approx 200$  K and  $T^*(x = 3) \approx 140$  K.

Tagigawa *et al.* [98] performed  $^{63,65}\text{Cu}$  NMR measurements on  $x = 0$ . The observed spectral lineshapes indicated a transition in the ladders at similar  $T^*(x = 0) \approx 200$  K, Fig. 1.27. The center line attributed to the ladder sites shows a sharp single peak and no splitting, which occurs for chains due to charge-disproportionation. However, the satellite lines are broader and show temperature-dependent line shape below around 200 K.

The initial  $^{63}\text{Cu}$  NMR measurements of the spin-lattice relaxation rate  $1/T_1$  and of the Knight shift, on polycrystalline samples by Kumagai *et al.* [95], addressed the issue of behavior of the spin-gap with increasing Ca-content  $x$ , *i.e.* for  $\text{Sr}_{14-x}\text{Ca}_x\text{Cu}_{24}\text{O}_{41}$ ,  $x = 0, 3, 6, 9$ . The spin-lattice relaxation rate  $1/T_1$  for the ladders shows  $x$  dependence. In Fig. 1.28 it is shown that the activated behavior of  $1/T_1$  starts immediately below the room temperature and that different activation energies may be deduced for different  $x$ . Fig. 1.29 shows these results in comparison with the more recent NMR results for single crystals obtained by other groups [103, 98, 104]. The Ca-content dependence is qualitatively (and quantitatively for single crystals) the same in all studies. The gap decreases from 60 meV ( $\approx 600$  K) for  $x = 0$ , 50 meV at  $x = 2$ , 35 meV at  $x = 6$ , 27 meV at  $x = 8$ . Above  $x = 8$  it seems to saturate at 25-28 meV. On the contrary, the inelastic neutron scattering (INS) results, [97, 91, 105], do not indicate the Ca-content dependence. It is important to note that the difference in the behavior of NMR and INS gaps is, effectively, a difference in the observed gap values for  $x = 0$  and 2. The NMR results are obtained by fitting the data in temperature range from below 300 K down to 100 K, and INS results are obtained at temperatures below this range. Larger gaps for NMR than for INS for  $0 \leq x \leq 2$  materials may correspond to this temperature range mismatch.

Still, it is important to note that the spin-gap in ladders does not get

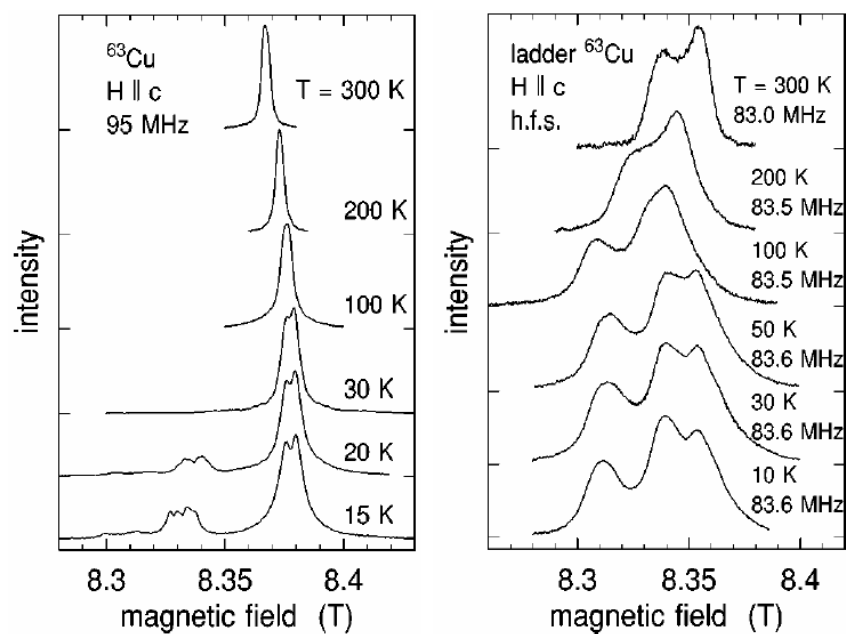


Fig. 1.27: Temperature variation of the high-field NMR spectrum at the ladder  $^{63}\text{Cu}$  sites of  $\text{Sr}_{14}\text{Cu}_{24}\text{O}_{41}$  with the magnetic field along the  $c$ -direction. Left panel: The center line of the ladder sites shows a sharp single peak. Right panel: The satellite lines are broader and show temperature-dependent line shape. From Ref. [98].

completely suppressed even for very high Ca-content,  $x = 12$ . This is noteworthy, since the presence of spin-gap is important in the mechanism which induces pairing of holes intrinsically doped into the ladders from the chains reservoir.

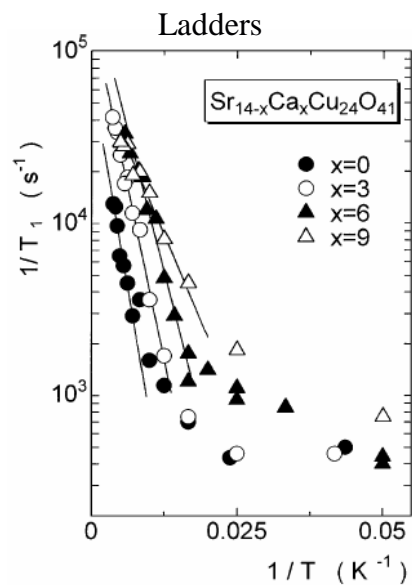


Fig. 1.28: The temperature dependence of the spin-lattice relaxation rate  $1/T_1$  for the ladders is shown for different materials of the q1D cuprate family, notably for  $\text{Sr}_{14-x}\text{Ca}_x\text{Cu}_{24}\text{O}_{41}$ ,  $x = 0, 3, 6, 9$ . Full lines are fits to the activated behavior. The activation energy decreases with  $x$ . From Ref. [95].

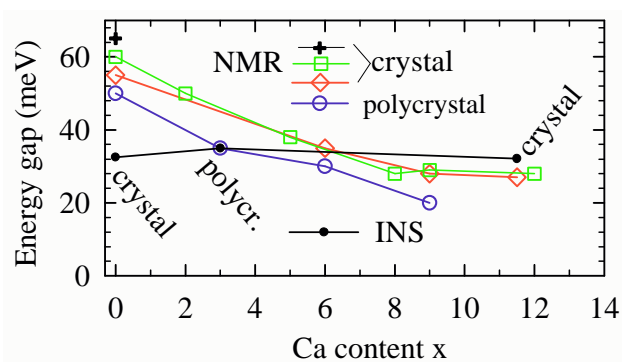


Fig. 1.29: The dependence of the spin-gap in  $\text{Sr}_{14-x}\text{Ca}_x\text{Cu}_{24}\text{O}_{41}$  for various Ca-contents  $x$ . The results are obtained by different groups (see text) using NMR or INS techniques. Some groups used single crystals, some polycrystalline samples. The spin-gap remains finite up to the high Ca- contents  $x = 12$ .

### Electrical transport in the ladders

As the holes in the reservoir in the chains seem to be well localized due to the spin AF dimer pattern and the complementary charge-order, the electrical transport paths must be found in the ladders. A comprehensive study of the anisotropic electrical resistivity on single crystals of  $\text{Sr}_{14-x}\text{Ca}_x\text{Cu}_{24}\text{O}_{41}$ ,  $x = 0, 3, 6, 11$  was performed by Motoyama *et al.* [84]. In Fig. 1.30  $\ln \rho$  vs.  $1/T$  plots are shown for the resistivity along the  $c$ - (parallel to the legs of ladders) and  $a$  axis (parallel to the rungs of ladders). All the compounds except  $x = 11$ , show a rapid increase in resistivity upon cooling - Arrhenius behavior of insulators. The value of  $a$ -axis resistivity,  $\rho_a$ , is larger than the  $c$ -axis resistivity,  $\rho_c$ , by one to two orders of magnitude. The anisotropic ratio,  $\rho_a/\rho_c$ , is not strongly dependent on  $x$ .

One should note that  $\text{Sr}_{14}\text{Cu}_{24}\text{O}_{41}$  is not highly insulating if compared with the Y-substituted compounds. As exposed before, nonisovalently substituted compounds have hole counts of less than 6, and what is more important, all holes are found in the chains, where they become very localized. Henceforth their low conductivity already at the room temperature.

The room temperature conductivity  $\approx 500 \Omega^{-1}\text{cm}^{-1}$ , seems to be close for various  $x$ , except that the conductivity increases slightly with Ca-substitution. This can not be quantitatively related to the ladders hole count results of Nücker *et al.* [76], *i.e.* with the fact that the hole count in this  $x$  range increases from 0.8 to 1.1 per ladder. Change in the activation energy, that is, its strong suppression is the most apparent in the resistivity results. In fact,  $x = 11$  material appears to be metallic down to 100, or even 70 K (red line in Fig. 1.31). Only below these temperatures, weakly activated behavior of the resistivity reappears for  $x = 11$ .

Most interestingly, the application of pressure, at these Ca-substitution levels, suppresses the remains of the insulating behavior and superconductivity is observed, Fig. 1.31. Indeed, after the remarkable theoretical prediction of superconductivity for the ladder materials and the initial experimental findings of Uehara *et al.* [69] ( $x = 13.6$ ,  $T_c = 12$  K,  $P_c = 3$  GPa) and Nagata *et al.* [107] ( $x = 11.5$ ,  $T_c = 6.5$  K,  $P_c = 4.5$  GPa), the SC phase was observed for all Ca-substitutions  $10 \leq x \leq 13.6$ . A comprehensive presentation of development of the SC state under pressure for various  $x$  was given by Motoyama *et al.* [106], Fig. 1.32. They have also presented the suppression of the insulating state and establishment of the metallic behavior, for  $\text{Sr}_{14}\text{Cu}_{24}\text{O}_{41}$  under pressure of 6.5 GPa, but, without occurrence of SC. It is intriguing that metallic behavior is not observed for  $x = 3, 6, 8$  at any pressure up to 8 GPa.

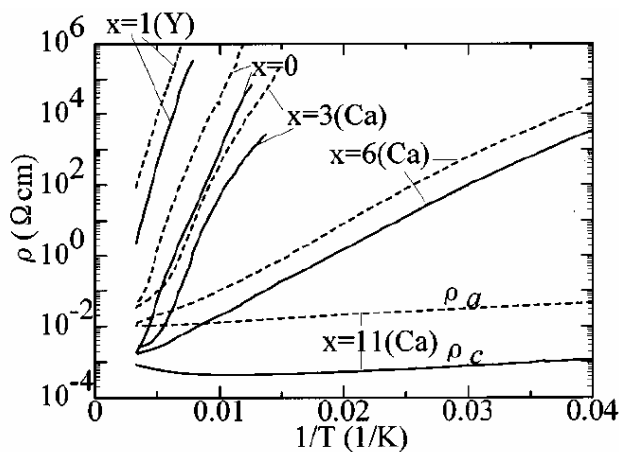


Fig. 1.30: The Arrhenius plots of the dc resistivity for  $\text{Sr}_{14-x}\text{Ca}_x\text{Cu}_{24}\text{O}_{41}$  and  $\text{Y}_1\text{Sr}_{13}\text{Cu}_{24}\text{O}_{41}$  along the  $c$ - and  $a$ -axis (solid and dashed curves, respectively). From Ref. [84].

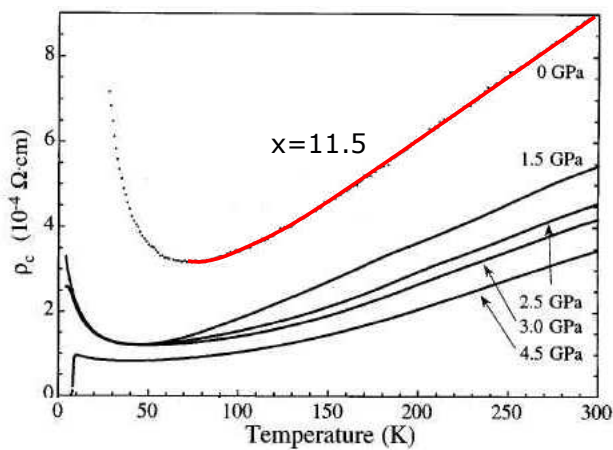


Fig. 1.31: Temperature dependence of the dc resistivity along  $c$ -axis under various pressures in  $x = 11.5$ . From Ref. [107].

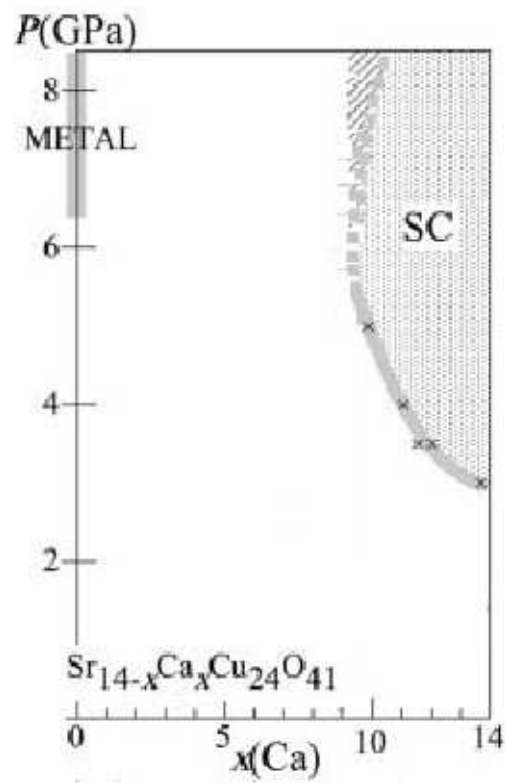


Fig. 1.32: The  $x - P$  phase diagram for  $\text{Sr}_{14-x}\text{Ca}_x\text{Cu}_{24}\text{O}_{41}$  by Motoyama *et al.* [106]. The SC phase is restricted at high pressures and for  $10 \leq x \leq 13.6$  and experimentally determined critical pressure  $P_c$  is plotted as cross marks.

### The relationship between the SC phase, and the spin-gap in the ladders

In this review we addressed the spin-gapped state of the ladders, as well as occurrence of superconductivity. The superconductivity is established under pressure at substitution levels where finite spin gap is observed in the studies without pressure. The important question is whether the ladders' spin-gap is suppressed or remains finite when the pressure is applied and superconductivity is established. Due to the experimental constraints this question has been studied on the local level by  $^{63}\text{Cu}$  or  $^{17}\text{O}$  NMR measurements by only two independent groups. First, Piskunov *et al.* [104] have performed experiments at pressure,  $p = 3.2 \text{ GPa} > p_c$ , which stabilizes SC. It has to be noted that those measurements were not done in the SC phase, but above 10 K. They have shown that pressure decreases the gap in the magnon excitations and stabilizes low-lying spin excitations. For comparison, they also present that, in  $x = 0$ , high pressure decreases the gap but does not introduce excitations. The appearance of the low-lying spin excitations is inferred from the contribution to the spin-lattice relaxation rate  $T_1^{-1}$ , which is linear in temperature below 30-40 K (Korringa-like). They conclude that the condition for the observation of superconductivity is the existence of zero-frequency spin fluctuations within the magnon gap. This condition is met only above critical pressure in heavily substituted compounds ( $10 \leq x \leq 13.6$ ).

Fujiwara *et al.* [108] also investigated  $x = 12$  material by the same method at 3.5 GPa, but they reached temperatures as low as 1.4 K. They confirmed the SC transition by the ac-susceptibility-like measurements. They observed Hebel-Slichter peak at  $T_{\text{SC}}$  in the temperature dependence of the spin-lattice relaxation rate  $T_1^{-1}$  vs.  $T$ . They also identified two excitation modes in the normal state. One gives rise to the activation-type or gapped component in  $T_1^{-1}$ , the other  $T$ -linear (Korringa) component linking directly with the superconductivity. Besides confirming the experimental situation as described by Piskunov *et al.*, Fujiwara *et al.* interpreted that the gapless component likely arises from free motion of holon-spinon bound states appearing due to the hole doping, and the pairing of two spins within two holon-spinons likely causes the superconductivity, Fig.1.33. The Hebel-Slichter peak indicates that no nodes appear in the SC gap. In this picture, superconductivity has an s-wave-like character, but only in the sense that a finite gap exists in the quasiparticle excitation.

The nature of insulating phase, related to the nature of electrical transport in the ladders and its suppression is one of the principal issues left unanswered at the end of this review. Characterizing the insulating phase and the relationship between the insulating phase, the SC phase and the

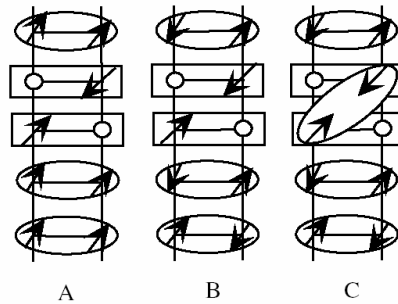


Fig. 1.33: (A) Illustration of spin and charge configuration at high temperatures. Ellipses show spin singlets on the rung. Some of them are in the triplet states at high temperatures. A rectangle implies the holon-spinon bound states. They move independently in the ladder. (B) Illustration at intermediate temperatures. A spin within the holon-spinon bound state is free and paramagnetic. All the spin pairs on the rungs are in the singlet state. (C) In the superconducting state. Two spins within the bound states form the pair. From Ref. [108]

spin-gap, that is, creating a phase diagram for the q1D cuprates is the focus of the research that will be presented in following chapters.

# 2 One-dimensional systems - theoretical overview

## 2.1 Phase diagram of weakly interacting 1D Fermi gas - the *g-ology* model

(TMTSF)<sub>2</sub>PF<sub>6</sub> - q1D material, highly conducting at the ambient temperature and showing highly anisotropic metallic-like conductivity down to very low temperatures is almost ideal material for applying the 1D interacting Fermi gas model. The prerequisite for the formation of such a molecular conductor is the charge delocalization. In (TMTSF)<sub>2</sub>PF<sub>6</sub> it occurs between the molecules on the TMTSF stack. The weak coupling limit is justified when the electron-electron interactions are smaller than the bandwidth  $4t$ , as occurs in TMTSF materials. The ground states (depending on the pressure) of (TMTSF)<sub>2</sub>PF<sub>6</sub> have been identified as  $2k_F$  SDW and triplet superconductivity.

Phase diagram and instabilities of 1D weakly interacting Fermi gas were successfully described by the *g-ology* model. This model contains the principal consequences of generalized, but weak, electron-electron interactions: the competition between the instabilities as well as 1D fluctuations, [50]. Depending on the coupling constants, *i.e.* wave vector of the interaction, various ground states may occur: singlet or triplet superconductivity and charge- and spin-density waves.

In a 1D system strong fluctuations, of either thermal or quantum origin, prevent long-range order at any temperature  $T \geq 0$ , [80, 1]. In the mean-field approximation these fluctuations are not taken into account, allowing for ordering at  $T > 0$ . In a real material, non-negligible interaction between the 1D structures will diminish the influence of the fluctuations and allow for ordering at  $T > 0$ . Therefore, the mean-field approach is useful to show that the competition between the superconducting and density-wave orders is the basic issue in q1D materials.

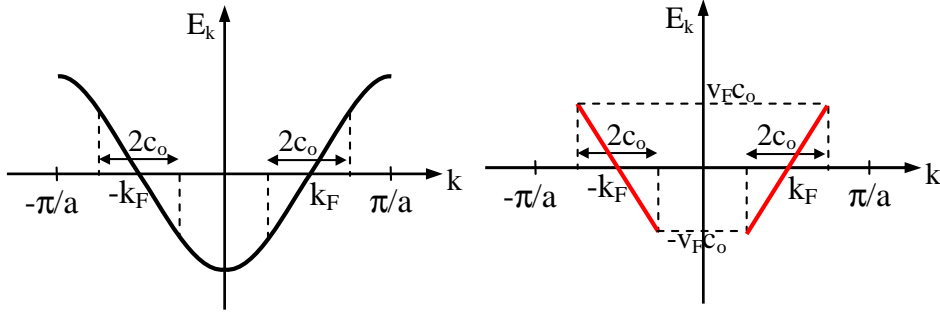


Fig. 2.1: Upper panel: Dispersion relation of a 1D Fermi (noninteracting electron) gas, 1DEG. Fermi surface is reduced to two points,  $k_F$ ,  $-k_F$ . Lower panel: Dispersion relation of a 1DEG linearized in the  $c_o$  (cut-off) neighbourhood of Fermi points.

The *g-ology* draws its name directly from the peculiarities of the perturbation theory in 1D. The model describes scattering processes, concerning states close to the FS, related by weak interactions and treated perturbatively, with respect to the Fermi liquid picture. Since the system of concern is 1D, FS is reduced to two points situated at  $-k_F$  and  $k_F$ . There are only 4 possible scattering processes and the respective coupling constants are indexed as  $g_1$ ,  $g_2$ ,  $g_3$  and  $g_4$ , hence the name for the model...

### 2.1.1 Noninteracting Hamiltonian

The Hamiltonian for the Fermi gas of non-interacting electrons is

$$H_0 = \sum_{\mathbf{k}, \alpha} E_{\mathbf{k}} c_{\mathbf{k}, \alpha}^{\dagger} c_{\mathbf{k}, \alpha} \quad (2.1)$$

where  $c_{\mathbf{k}, \alpha}^{\dagger}$  ( $c_{\mathbf{k}, \alpha}$ ) is creation (annihilation) operator of an electron with momentum  $\mathbf{k}$  and spin  $\alpha$ . The kinetic energy  $E_{\mathbf{k}}$  is usually measured with respect to the Fermi energy. Considering Bloch states as the non-interacting ground states, the momentum representation is the most appropriate for the weakly interacting system. The corresponding dispersion relation is illustrated schematically in Fig. 2.1, left panel.

Since, only the electrons lying near the Fermi surface play an important role in physical processes, the dispersion may be linearized around FS, Fig. 2.1, right panel. We note that there are two well-defined branches of the electron dispersion. The creation (annihilation) operators for the electrons belonging to the negative  $k$  branch are indexed  $b_{\mathbf{k}, \beta}^{\dagger}$  ( $b_{\mathbf{k}, \beta}$ ), while operators for the electrons belonging to the positive  $k$  branch are indexed  $a_{\mathbf{k}, \alpha}^{\dagger}$  ( $a_{\mathbf{k}, \alpha}$ ),

respectively. The spins are indexed  $\beta$  ( $\alpha$ ) for  $b$ - and  $a$ -branches, respectively. In terms of these operators, the free Hamiltonian is given by

$$H_0 = \sum_{\mathbf{k},\alpha} v_F(k - k_F) a_{\mathbf{k},\alpha}^\dagger a_{\mathbf{k},\alpha} + \sum_{\mathbf{k},\beta} v_F(-k - k_F) b_{\mathbf{k},\beta}^\dagger b_{\mathbf{k},\beta} \quad (2.2)$$

### 2.1.2 Interacting part of the Hamiltonian

The interactions in this model system, in general, are the Coulomb or the phonon mediated electron-electron interactions. The interaction is introduced by adding  $H_{int}$  term to the Hamiltonian, Eq. 2.2.

$$H_{int} = \sum_{\mathbf{k},\mathbf{k}',\mathbf{q},\alpha,\alpha'} U_{\mathbf{q}} c_{\mathbf{k}+\mathbf{q},\alpha}^\dagger c_{\mathbf{k}'-\mathbf{q},\alpha'}^\dagger c_{\mathbf{k}',\alpha'} c_{\mathbf{k},\alpha} \quad (2.3)$$

Working in momentum space means that interaction can be represented by the Fourier sum, with different momentum transfers  $\mathbf{q}$ , separating local and long-range parts. As already mentioned, there are only 4 scattering processes and each contributes by a separate part  $H_i$  to the interaction Hamiltonian.

$$\begin{aligned} H &= H_0 + H_{int} \\ H_{int} &= H_1 + H_2 + H_3 + H_4 \end{aligned} \quad (2.4)$$

The diagrams of these processes are shown in Fig. 2.2. In the diagrams solid lines denote electrons from the right,  $a$ -branch, whose momenta are positive. The dashed lines refer to the electrons from the opposite branch.

The first process corresponds to backward scattering of electrons, where the momentum transfer is  $q = 2k_F$ , Fig. 2.2 (a). This component contains the contribution of the short-range, effectively on-site interactions.  $g_1$  has a contribution from the Pauli principle or from the Coulomb repulsion  $U$  of two electrons found in the same orbital. The forward scattering component is characterized by momentum transfer  $q = 0$ , Fig. 2.2 (b), denoting long-range interactions. The diagram, Fig. 2.2 (c), corresponds to momentum transfer  $4k_F$ . It is not effective unless *Umklapp* occurs. Umklapp is active if the band is half-filled, since then the reciprocal lattice vector  $\mathbf{G}$  is equal to  $4k_F$  and thus cancels the scattering momentum transfer. This situation is realized in Fabre salts  $(\text{TMTTF})_2\text{X}$ , where electron-electron umklapp scattering is generated by the small Coulomb potential of the  $X$ -anions, *i.e.*  $g_3 \ll g_1, g_2$ , [109]. In these materials this situation leads to the dimerization of TMTTF molecules within the stack. For TMTSF compounds this dimerization is small, thus  $g_3$  is less important than in TMTTF compounds, [110]. In another possible

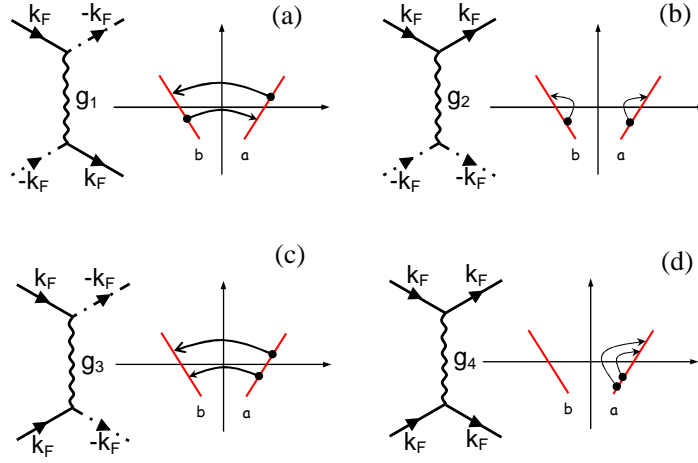


Fig. 2.2: Diagrams for possible scattering processes in the 1D interacting Fermi gas. They correspond to transfers between the dispersion branches. (a) Backward scattering,  $q = 2k_F$ . (b) Forward scattering,  $q = 0$ . (c) *Umklapp* scattering,  $q = 4k_F$ . (d) Another possible forward scattering process,  $q = 0$ .

forward scattering process, Fig. 2.2 (d), the particles are not transferred to the opposite branch and the momentum transfer is  $q = 0$ .

### 2.1.3 Instabilities in the 1D system

The aim of studying g-ology model is to determine what kind of instabilities, *i.e.* ground states, are likely to occur in the 1D system. The best way here is to calculate the response functions or generalized susceptibilities within linearized response. The response functions that are expected to be singular for a range of couplings given here are the ones of charge-density wave (CDW), spin-density wave (SDW), and singlet-superconductivity (SS) and triplet-superconductivity (TS). CDW or SDW instability is expected to occur for momentum transfer  $q = 2k_F$ , reflecting the singularity in the electron-hole (Peierls channel) bubble diagram at this wave-vector. SS or TS occurs, if the electron-electron (Cooper pair) bubble diagram is singular.

Using the response functions it is possible to rewrite interaction Hamiltonian, Eq. 2.4. The resulting Hamiltonian can be reduced in the mean-field approximation and diagonalized using Bogoliubov transformation. The order parameter appears as a gap  $\Delta$  opened at the Fermi surface

$$\Delta = 2E_F \exp\left(-\frac{1}{\lambda}\right) \quad (2.5)$$

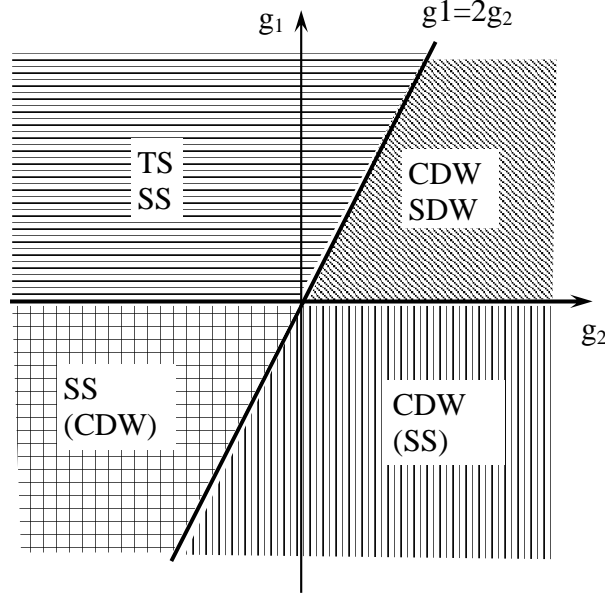


Fig. 2.3: Ground states occurring for q1D weakly interacting electron gas, calculated within the mean-field approximation. Only spin-independent couplings  $g_1, g_2$  are considered, and  $g_3$  is taken to be zero (non-half-filled band).

$g$ -ology parameters define  $\lambda$ . A finite gap  $\Delta_{\text{CDW}}$  is obtained for  $2g_1 - g_2 < 0$ . SDW ordering occurs for  $g_2 > 0$ , SS for  $g_1 + g_2 < 0$  and TS for  $g_1 - g_2 > 0$ . The full determination of the fluctuations which dominate at  $T = 0$  instead of the phase transition requires more advanced techniques than the mean-field approximation. The corresponding  $g_1, g_2$  "phase diagram" for all four types of fluctuation is given in Fig. 2.3. Superconducting and density wave fluctuations are separated by the line  $g_1 = 2g_2$ , while  $g_1 = 0$  separates singlet and triplet fluctuations. The main consequence of the umklapp  $g_3$  (half-filled band) is the formation of the gap in the  $q = 0$  charge-charge correlation function, *i.e.* the Mott localization. SDW (AF) is concomitantly favored over the  $2k_F$  CDW. Regarding the scope of this Thesis, a principal result, obtained from this diagram, is a suggestion of a boundary between superconducting and density-modulated ground state.

### Phenomenology of density waves

Nature of the pairing (Cooper or electron-hole channel) determines the response function, and thus the experimental phenomenology for a given electronic ground state. Density wave instabilities of 1DEG are due to electron-hole pairing, with either parallel or antiparallel spins, for SDW or CDW,

respectively. Density modulations of spin and charge are both defined by  $2k_F$  wave vector. When 3D couplings are added density waves are characterized by a metal-to-insulator transition (due to the opening of the energy gap at the Fermi level), accompanied by a drop in magnetic susceptibility. Susceptibility drop for SDW occurs only along the magnetic "easy" axis - *i.e.* the direction of the modulation amplitude. In the presence of the coupling between the electron and phonon systems the  $2k_F$  and  $4k_F$  electron CDWs are accompanied by the lattice distortion at the same critical vector. The  $2k_F$  SDW spin modulation is also accompanied by charge modulation with wave vector  $4k_F$ , [112]. These couplings allow for the direct observation of the modulations by X-ray diffuse scattering. Even for a negligible coupling between the electron and phonon systems electronic DWs may be observed by refinements of this experimental technique, [33, 34]. A difference between a "standard"  $2k_F$  CDW, which is accompanied by a Peierls lattice distortion, and a purely electron CDW depends on the adiabatic ratio  $E_F/\omega_{ph}$ , where  $E_F$  is the Fermi energy, and  $\omega_{ph}$  the frequency of the corresponding phonon. Peierls lattice distortion appear only in adiabatic limit, where  $E_F \gg \omega_{ph}$ , whereas in the nonadiabatic limit  $\omega_{ph} \gg E_F$  phonon mediates the nearly instantaneous attractive electron-electron interaction.

Finally, we note that coupled 1D electron-phonon systems primarily exhibit Peierls CDW ground state in which electronic density and lattice modulations are established concomitantly and are intimately related, [111]. A starting point for these systems is the 1D electron-phonon Hamiltonian. Such a CDW possesses long wavelength excitations - phasons which can couple to ac electric field and lead to interesting dynamical effects, see Sec. 2.4.

### 2.1.4 Weak coupling limit of the extended 1D Hubbard model

The *g-ology* Hamiltonian, Eqs. 2.2, 2.3, describes the 1D Fermi gas featuring weak interactions which can be treated perturbatively. It was demonstrated by Emery, [114] that the limit of strong interactions in the extended Hubbard model leads to the similar phase diagram in 1D as the weak-coupling model. Emery's approach starts from the Hubbard model, [113], which, in its simplest form, describes hopping  $t$ , between the nearest neighbour sites of the chain, labelled  $j$ , and Coulomb repulsion between the electrons of the opposite spin on the same site.

$$H = -t \sum_{j,\sigma} c_{j,\sigma}^\dagger c_{j+1,\sigma} + c_{j+1,\sigma}^\dagger c_{j,\sigma}$$

$$+ U \sum_{j,\sigma} c_{j,\sigma}^\dagger c_{j,\sigma} c_{j,-\sigma}^\dagger c_{j,-\sigma} \quad (2.6)$$

$c_{j,\sigma}^\dagger$  denotes the creation operator of an electron with spin  $\sigma$  in the Wannier state localized at the  $j$ th site. This model is exactly solvable in 1D. In the case of a half-filled band the ground state is antiferromagnetic insulator for any  $U > 0$ . Writing this Hamiltonian in the momentum representation

$$c_k = \frac{1}{\sqrt{N}} \sum_{i=1}^N \exp(-ikR_i) c_i \quad (2.7)$$

and linearizing the dispersion around  $\pm k_F$  (Fig. 2.1), a Hamiltonian of the *g-ology* form is obtained. All the couplings  $g_1, g_2, g_3, g_4$  will be equal, since they are all related to the single physical parameter  $U$  of the Hubbard Model. Thus,  $g_1 < 2g_2$ , and, according to *g-ology*, SDW and CDW are formed (Fig. 2.3). This is also consistent with the exact solution of the Hubbard model in 1D, which demonstrated that the ground state should be antiferromagnetic and insulating, [115].

In the next step, the inter-site (nearest-neighbor) interaction term  $V \sum_j n_j n_{j+1}$  is introduced, in addition to the on-site interaction term. The resulting Hamiltonian is referred to as extended Hubbard model (EHM). The introduction of  $V$  distinguishes between the values of *g-ology* couplings. The relation between the *g-ology* coupling parameters and the EHM parameters is the following:

$$\begin{aligned} U - 2V &\rightarrow g_1 \\ U + 2V &\rightarrow g_2 \\ U - 2V &\rightarrow g_3 \\ U + 6V &\rightarrow 2g_2 - g_1 \end{aligned} \quad (2.8)$$

As already mentioned  $g_3$  is important only when the band is half-filled. However, unlike here for EHM, the *g-ology* deals with  $g_3 \ll |g_1|, |g_2|$ , as in Bechgaard salts.

## 2.2 Strongly interacting 1D electron system

In the approach, which is more suitable for strongly non-conducting systems the Hubbard Hamiltonian (Hubbard 1963. [113]) with strong intra-atomic (on-site) interaction is used. The cuprate materials under study in this thesis have almost the same ambient temperature conductivity as (TMTSF)<sub>2</sub>-PF<sub>6</sub>. Still, these materials show insulating behavior almost everywhere (750 - 2 K, up to 6 GPa, depending on the material in question) throughout the phase diagram. Other properties, like the appearance of the spin-gap in the ladders subsystem and AF dimers and charge-order in the chains subsystem direct theoretical investigations towards using strong interactions, better suited for well localized systems. Structural elements of these materials, chains and (spin) ladders are very good realisations of different t-J models (drawn in particular from extended Hubbard model - EHM with strong interactions). These models suggest a competition of charge-density wave and superconducting ground states for ladders, the subsystem responsible for charge transport in Sr<sub>14-x</sub>Ca<sub>x</sub>Cu<sub>24</sub>O<sub>41</sub> materials. The exact nature (*e.g.* pairing symmetry) of these states is not established yet.

### 2.2.1 Strong coupling limit for cuprates

Electron Hamiltonian of the cuprate systems should incorporate terms related to oxygen orbitals. Therefore, in the standard approach, the following energy parameters are used:  $\varepsilon_p$ , energy of oxygen O2 $p_{x,y}$  orbitals and  $\varepsilon_d$ , energy of copper Cu3 $d_{x^2-y^2}$  orbitals. These orbitals form the CuO<sub>4</sub> square with three inequivalent oxygens ( $i=1,2,3$ ), Fig. 2.4. The physical situation depends on the splittings,  $\Delta_{pd}^{(i)} = \varepsilon_p^{(i)} - \varepsilon_d$ , and hybridization  $t_0$ , between these orbitals. In the strong coupling limit on-site (within the copper orbital) repulsive interaction  $U_d$  and the splittings  $\Delta_{pd}^{(i)}$  are considered to be much larger than effective hopping  $t$ , which is of the order of hybridization  $t_0$ . The ratio  $U/\Delta_{pd}^{(i)}$  determines the basic physical situation in the cuprates, [74].

When holes are transferred into the cuprate lattice they will be located either at Cu sites if  $U_d < \Delta_{pd}$  or in the oxygen orbitals if  $U_d > \Delta_{pd}$ . In the first case (Hubbard limit), O-sites are eliminated from the picture and the effective Hamiltonian describes hole motion on Cu-sites alone. In the opposite case (charge-transfer limit), which Zhang and Rice assumed for a cuprate layer, it is energetically favorable for doped holes to locate in oxygen orbitals surrounding the Cu-site, and form a singlet state with the hole in copper orbital. Again, they have shown that in this case a single band Hamiltonian describes the motion of this Zhang-Rice singlet through the lattice. Zhang

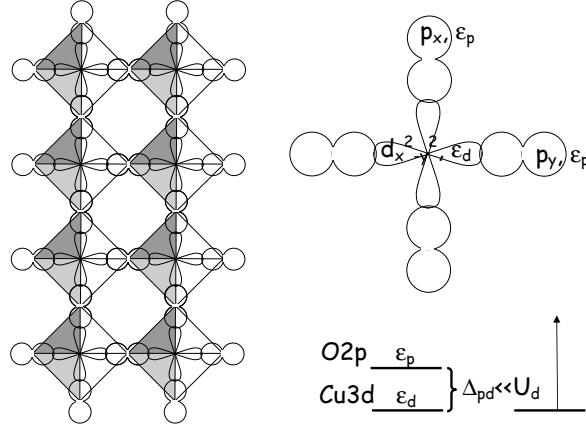


Fig. 2.4: Schematic diagram of the hybridization of the O hole ( $2p^5$ ) and Cu hole ( $3d^9$ ) within the  $\text{CuO}_4$  square. At oxygen sites only one of the two orbitals is shown. Energy level splitting is also denoted. The squares assembled into a ladder structure are shown.

and Rice started with a Hamiltonian for a 2D cuprate layer, Eq. 2.9, and it can be assumed that this model is also valid for the ladder lattice. That is, the hybridization term in their starting Hamiltonian contains the term  $t_0$  whose sign depends on the phases of the  $p_x$  ( $p_y$ ) and  $d_{x^2-y^2}$  wave functions, which depends on the exact lattice geometry. Two oxygen sites within the unit cell are not distinguished for brevity.

$$\begin{aligned}
H &= \sum_{j,\sigma} \varepsilon_d d_{j,\sigma}^\dagger d_{j,\sigma} + \sum_{l,\sigma} \varepsilon_p p_{l,\sigma}^\dagger p_{l,\sigma} \\
&+ U \sum_j d_{j,\uparrow}^\dagger d_{j,\uparrow} d_{j,\downarrow}^\dagger d_{j,\downarrow} \\
&+ \sum_{j,\sigma} \sum_{l \in j} t_0 d_{j,\sigma}^\dagger p_{l,\sigma} + \text{H.c.}
\end{aligned} \tag{2.9}$$

Here, vacuum is defined as filled  $\text{Cu}3d^{10}$  and  $\text{O}2p^6$  states. Operator  $d_{j,\sigma}^\dagger$  creates a hole in the  $\text{Cu}3d_{x^2-y^2}$  orbital and  $p_{l,\sigma}^\dagger$  in  $\text{O}2p_x$  ( $2p_y$ ) orbitals. At exactly half-filling and for  $t_0 = 0$ , each Cu-site is singly occupied ( $3d^9$ ), and all the O-sites are empty ( $2p^6$ ) in the hole representation. If  $t_0$  is finite but small (this happens at low doping in cuprates), the virtual hopping process involving the doubly occupied Cu-hole states produces a superexchange (AF) interaction between the neighbouring Cu holes. The Hamiltonian (hybridization term excluded), Eq. 2.9 reduces to spin- $\frac{1}{2}$  Heisenberg model on

the lattice of Cu sites:

$$H_S = J \sum \mathbf{S}_i \mathbf{S}_j \quad , \quad J = \frac{4t_0^4}{\Delta_{pd}^2 U_d} + \frac{4t_0^4}{2\Delta_{pd}^3} \quad (2.10)$$

As the formation of Zhang-Rice singlets is energetically favorable the above presented considerations lead to a possibility to map the Cu-O lattice close to half-filling, onto a lattice formed from only one kind of sites. When these sites are occupied physical situation is that one hole resides in CuO<sub>2</sub> unit cell and carries spin 1/2. In this, mapped lattice, effectively unoccupied sites, are those whose spin state is zero, as they are ZR singlets formed from the always present Cu 3d<sup>9</sup> hole and doped hole which locates in the oxygen orbitals 2p<sub>x</sub> (2p<sub>y</sub>). That is, Zhang and Rice replaced the hybridization term in Eq. 2.9, by an effective hopping Hamiltonian describing the motion of the ZR singlet

$$H_t = \sum_{i \neq j, \sigma} t_{ij} (1 - n_i, -\sigma) d_{i,\sigma}^\dagger d_{j,\sigma} (1 - n_j, -\sigma) \quad (2.11)$$

Noteworthy, the  $t$ - $J$  Hamiltonian composed from Eq. 2.10 and 2.11 in the charge-transfer limit taken by ZR, is equivalent to the effective Hamiltonian of the single band Hubbard model in the large  $U$  limit.

### 2.2.2 $t - J$ model for two-leg ladders

The model of two-leg ladders by Dagotto *et al.* [77, 73, 68], cartooned in the Sec. 1.2.6 (compare with Fig. 2.4) consists of two chains each described by a  $t$ - $J$  model. The chains are also coupled by  $t'$ - $J'$  interactions between them, Fig. 2.5. Note that three oxygens in the ladder are inequivalent and therefore  $t \neq t'$  and  $J \neq J'$ . This  $t$ - $J$ - $t'$ - $J'$  model considers hopping/coupling along the legs,  $t/J$  and along rungs of ladders  $t'/J'$ :

$$\begin{aligned} H &= J \sum_{i,\lambda=-1,1} \mathbf{S}_{i,\lambda} \cdot \mathbf{S}_{i+1,\lambda} + J' \sum_{i,\lambda=-1,1} \mathbf{S}_{i,\lambda} \cdot \mathbf{S}_{i,-\lambda} \\ &- t \sum_{i,\sigma,\lambda=-1,1} (c_{i,\lambda,\sigma}^\dagger c_{i+1,\lambda,\sigma} + \text{H.c.}) - t' \sum_{i,\sigma,\lambda=-1,1} (c_{i,\lambda,\sigma}^\dagger c_{i,-\lambda,\sigma} + \text{H.c.}) \end{aligned} \quad (2.12)$$

Hole creation operators  $c_{i,\sigma}^\dagger$  create ZR singlet at a given site. Physically, this site is mapped from CuO<sub>4</sub> square, as demonstrated for cuprate layer in the previous Section 2.2.1. The index  $\lambda$  denotes sites on the same rung, at one or at the other leg of the ladder. The index  $i$  indicates sites along the chains - that is, the legs of ladders.

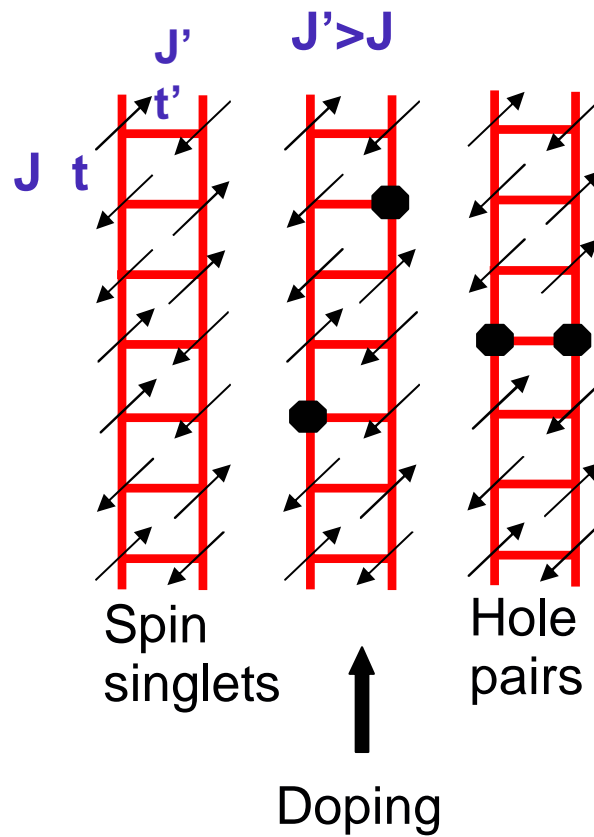


Fig. 2.5: Schematic definition of  $t$ - $J$ - $t'$ - $J'$  model. Hopping/coupling along the legs,  $t'$  and  $J'$  and along rungs of ladders  $t$  and  $J$  are denoted. The arrows denote occupied sites, spin 1/2, while open dots denote holes, which carry no spin due to formation of Zhang-Rice singlets. Suggested mechanism of hole-pairing in the two-leg ladders: When the coupling along the ladder rung  $J' > J$  is stronger than along the ladder legs, the ground state is a direct product of spin singlets appearing on the rungs. Doping individual holes to the ladder leads to destroying the singlets, which is energetically unfavorable. Therefore the holes tend to pair-up on the rungs.

In the large  $J'$  limit, at half filling, the ground state consists of a set of spin singlets in each rung of the ladder. There is a spin-gap in the spectrum of order  $J'$  which corresponds to creating a triplet in one of the rungs. When the system is doped with holes, it is energetically favorable to break as few rung singlets as possible. Therefore, every added pair of holes forms a bound state in a given rung, Fig. 2.5. To this bound state corresponds a pair-field operator

$$\Delta_i = \frac{1}{\sqrt{2}}(c_{i,\lambda,\uparrow}c_{i,-\lambda,\downarrow}) - (c_{i,\lambda,\downarrow}c_{i,-\lambda,\uparrow}) \quad (2.13)$$

The prediction of the gapped spin-liquid ground state was experimentally confirmed, for the q1D cuprate ladders materials, as shown in the Introduction Chapter, Sec. 1.2.6.

Finally, an important step is taken by recognizing that a subspace of rung singlets may be mapped to a linear chain. That is, each rung corresponds to a single site of this chain. The sites in this chain are either doubly occupied (mapped from the bound holes on the rung) or unoccupied (mapped from the two spins forming a rung singlet). In this subspace  $|U_{eff}| \propto J'$ , and the  $U_{eff} < 0$ , it is attractive. The analogy can be taken with the Hubbard model for a linear chain, see below Sec. 2.2.3 and Fig. 2.6. Therefore, as it was pointed out by Dagotto *et al.*, the ladder model away from half-filling (*i.e.* hole-doped) exhibits SC, or CDW, correlations. We note that the renormalized  $U_{eff}$  is probably smaller than  $t$  and that a weak coupling g-ology model may also be considered for describing ordering in the ladders. Dagotto *et al.* also checked numerically that binding energy of the pairs is negative for  $J'/J$  ratios in the range 0.4 – 4, and that the pairing correlations do occur immediately when  $J'$  is turned on. The balance between the SC and CDW depends on the parameters of the model and more generally on residual interactions between hole pairs, all of which is hard to predict theoretically, [50, 80, 77].

### 2.2.3 1D EHM in strong coupling limit

In order to clarify Dagotto's conclusion on the competition of SC and CDW in the spin ladders, we will schematically present the possible orderings in 1DEG of a single chain. EHM gives a particularly simple picture of the possible states of the system in the large- $U$  limit, in which  $t$  and  $V$  related terms are treated as perturbations, [116, 114]. It is not necessarily assumed that large  $U$  corresponds to any particular material, and for the present purpose it is merely a limit in which the theoretical properties of one-dimensional systems can easily be related to physically meaningful variables.

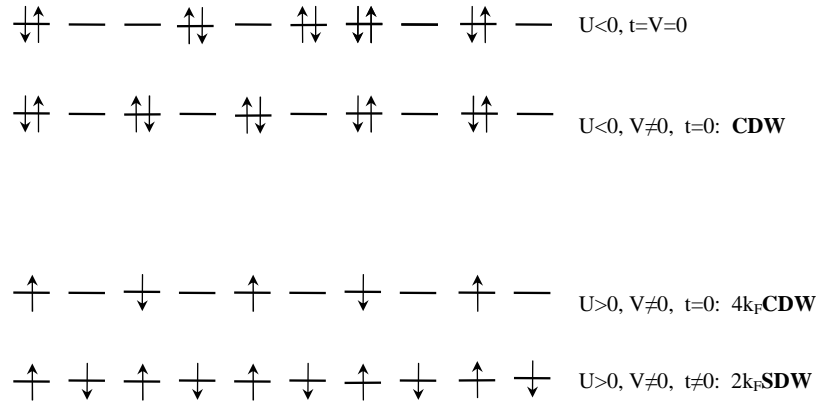


Fig. 2.6: Configurations of electrons, spin up,  $\uparrow$ , or spin down,  $\downarrow$  on a 1D chain when a strong on-site interaction is present,  $U \neq 0$ . For attractive  $U$ , and when inter-site interaction,  $V > 0$ , is included, a  $2k_F$  CDW is formed from electrons paired in singlets. For repulsive  $U$ , single electrons form a  $4k_F$  CDW at quarter filling. At half-filling, and with hopping allowed a  $2k_F$  SDW is formed.

### The on-site attraction, $U < 0$

The properties depend upon the sign of  $U$ . When this parameter is taken to be positive, it corresponds to the repulsion between the electrons of the opposite spin, occupying the same orbital. However, in strongly polarizable molecules, as well as in the Dagotto model, the direct Coulomb repulsion may be reduced, and the indirect interaction can lead to  $U < 0$ . The electrons of opposite spin form pairs, to take advantage of the on-site attraction. Molecular sites are either doubly occupied or unoccupied, Fig. 2.6. As mentioned above, this case is physically important here, since Dagotto's conclusion on the spin-ladders leads to the consideration of attractive  $U$ .

The ground state is very degenerate because the energy does not depend upon which sites are occupied. CDW states occur in an extreme form when there is an intersite repulsion  $V > 0$  but still no hopping  $t$ . To minimize the energy, the pairs are equally spaced, as shown in Fig. 2.6 for a half-filled band. The charge density varies periodically from 1 to 0 in the inter-site distance, so the wave vector is just  $2k_F$ . This is a possible ground state because the system is classical when  $t = 0$ . More realistically, when  $t \neq 0$ , the picture is not so static and there is a much smaller modulation of the charge density. Also, density modulation may be incommensurate to the inter-site distance, the electrons cannot be distributed so neatly amongst the sites. However, the wave vector  $2k_F$  always characterizes the CDW. This, standard CDW

is usually, due to non-negligible electron-phonon coupling, accompanied by lattice distortion at the same wave-vector  $2k_F$ . Although, it is in principle possible that a purely electronic CDW is observed, [33, 34].

For the case of inter-site attraction,  $V < 0$  singlet superconductivity can arise when hopping,  $t$ , is included. The electron pairs are bosons, bound in a singlet state, and it is possible that they become superfluid (and hence superconducting since they are charged) at low enough temperatures. Triplet superconductivity will not occur because the electrons are bound into singlet pairs before long-range triplet correlations can build up.

### The on-site repulsion, $U > 0$

Emery, [114] pointed out that in the strongly repulsive case,  $U > 0$ , for a half-filled band, when all sites are singly occupied, EHM can be mapped onto a spin-1/2 Heisenberg chain, with charges Mott-localized each on its site.

The  $2k_F$  SDW instability is clearly visualized for this case where only the spin degrees of freedom have to be considered. Virtual hopping produces an effective antiferromagnetic exchange interaction and the ground state has a modulation of the spin density, which is illustrated in Fig. 2.6. For weaker coupling and a different number of electrons, the state is more dynamic, but the wave vector is still  $2k_F$ .

CDW states can occur again in an extreme form when there is an intersite repulsion  $V > 0$ . In contrast to  $U < 0$  case, however, single electrons rather than pairs are equally spaced so the period of the CDW is halved and its wave vector is  $4k_F$ . This is so-called  $4k_F$  CDW or Wigner crystal in 1D. It manifests itself as a purely electronic CDW, not accompanied with any lattice distortions. This case is shown in Fig. 2.6 for a quarter-filled band, although the phase separation can occur as well [117]. Once again, hopping makes the CDW weaker and less static. It also mixes in doubly occupied sites and restores the Fermi sea, which may lead to an additional  $2k_F$  CDW periodicity.  $4k_F$  CDW is generated in *g-ology* picture for a quarter-filled band by strong interactions [110].

Although the above considerations were not assumed to correspond to any particular material, still it was shown that orderings of different nature occur also in the strong coupling limit.

## 2.3 Reexamined phase diagram of 1D EHM at half-filling

In q1D cuprates an important role is played by localized charges with strong electron-electron interaction. Still, Dagotto's considerations of the ordered phases in the ladders indicate a renormalized, but attractive  $U$  is responsible for ordering. Therefore a study of 1D EHM which covers both weak and strong-coupling limit of 1D EHM is presumably of importance for the cuprate ladders.

In the strong-coupling limit, Sec. 2.2.3, one can show that the model has two insulating phases, SDW phase and CDW phase, which are separated by a first-order transition line located at  $U \simeq 2V$ . In the weak-coupling limit g-ology analysis gives a continuous phase transition between the CDW and SDW phases also at  $U \simeq 2V$  or  $g_1 \simeq 0$ , Fig. 2.3. It is then natural to consider that, as the coupling constants are increased, the continuous-transition line changes into the first-order one at a tricritical point in the intermediate coupling regime, [118]. This phase diagram was reexamined both numerically, [119] and analytically. Second-order corrections to coupling constants were calculated to show that the bond-charge-density wave (BCDW, in which the Peierls dimerization occurs spontaneously) phase exists for weak couplings in between the CDW and SDW phases. SDW-BCDW and BCDW-CDW transitions are continuous and the two transition lines merge at a multicritical point into the first-order line  $U \simeq 2V$  separating the CDW and SDW phases, Fig. 2.7. Still, definitive results have been obtained only for effective, short-range Coulomb forces. Indications remained that the use of the effective interactions to approximate long-range forces occurring in strongly-correlated systems, does not yield the correct broken symmetry ground-state [121].

A closer inspection of Fig. 2.7 indicates that the BCDW phase occurs for  $V \simeq 0.4U$ . The possible scenario of the competition between BCDW and SC phase, in this parameter region was, very recently, proposed by Tsuchiizu and Suzumura, [120], in order to analyze the critical behavior for a single cuprate ladder in more detail. Here we just illustrate the further generalization of the EHM Hamiltonian, necessary to these authors to extend the understanding of the doped ladders. The EHM Hamiltonian generalized specifically for the two-leg ladders is split into hopping and on-(inter-)site interaction part,  $H = H_0 + H_{\text{int}}$ . The first part describes the hopping energies along and between the legs:

$$H_0 = -t_{\parallel} \sum_{j,\sigma,l} (c_{j,l,\sigma}^{\dagger} c_{j+1,l,\sigma} + \text{H.c.})$$

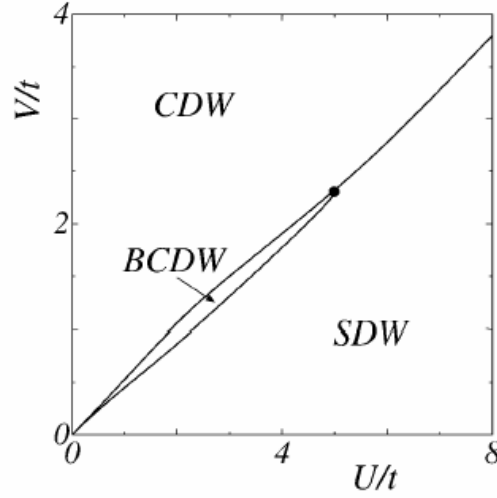


Fig. 2.7: Phase diagram of the extended Hubbard model at half-filling. CDW, SDW and BCDW denote, respectively, charge-, spin- and bond-charge-density wave ground states. The bicritical point is at  $(U, V) \simeq (5.0t, 2.3t)$ . From [118].

$$-t_{\perp} \sum_{j,\sigma} (c_{j,1,\sigma}^{\dagger} c_{j,2,\sigma} + \text{H.c.}), \quad (2.14)$$

where  $c_{j,l,\sigma}$  annihilates an electron of spin  $\sigma (= \uparrow, \downarrow)$  on the rung  $j$  and the leg  $l (= 1, 2)$ . The hopping along the rungs is the generalization compared to EHM. The Hamiltonian part  $H_{\text{int}}$  denotes interactions between electrons:

$$H_{\text{int}} = U \sum_{j,l} n_{j,l,\uparrow} n_{j,l,\downarrow} + V_{\parallel} \sum_{j,l} n_{j,l} n_{j+1,l} + V_{\perp} \sum_j n_{j,1} n_{j,2}, \quad (2.15)$$

where  $U$  represents on-site repulsion and  $V_{\parallel}$  ( $V_{\perp}$ ) represents nearest-neighbor repulsion along legs (rungs) of ladders, with  $n_{j,l,\sigma} = c_{j,l,\sigma}^{\dagger} c_{j,l,\sigma}$  and  $n_{j,l} = n_{j,l,\uparrow} + n_{j,l,\downarrow}$ .

For a complete description of the real material the authors also considered finite hole transfer  $\delta_h$  into the ladders. As can be found in Fig. 2.8 on-site repulsive interaction stabilizes  $d$ -wave-like SC state, while BCDW mixed with CDW is obtained due to nearest-neighbor repulsive interactions, with the transition close to  $V_{\perp}/U + V_{\parallel}/U \approx 0.4$ . The assumed hole transfer was  $\delta_h = 1.4$  per ladder, a value which corresponds well to the experiment, Sec. 1.2.4. The authors further emphasize that increasing hole transfer into the ladders reduces the effect of only  $V_{\parallel}$  and that the system exhibits a quantum phase transition into the  $d$ -wave-like (or rung-singlet) superconducting

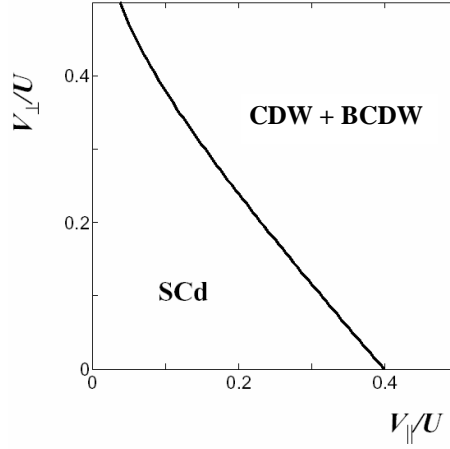


Fig. 2.8: The ground-state phase diagram of 1D EHM at half-filling, generalized for ladders, on the plane of  $V_{\parallel}/U$  and  $V_{\perp}/U$ , with  $U/t_{\parallel} = 2$ ,  $\delta_h = 1.4$ , and  $t_{\perp} = t_{\parallel}$ . From [120].

state. In Fig. 2.9  $m_t$ , the magnon excitation gap (spin gap) is shown *vs.* hole transfer. If  $m_t$  is regarded as the transition temperature, this depiction may be regarded as a phase diagram for doped cuprate ladders. The proposed phase diagram meets difficulties when applied to the real material, since there is no experimental evidence for the quantum critical point (QCP) between the CDW state and the SC state. In order to explain the discrepancy, the dimensionality effect and/or the disorder effect, smearing the QCP, has been suggested by the authors, [120]. We also note that  $U/t_{\parallel} = 2$  does not correspond well to a ratio obtained if standard values of  $U = 3.5 - 4$  eV for copper, and  $t_{\parallel} = 0.6$  eV, as calculated in Ref. [83], are taken. We also note that the hole transfer  $\delta_h \sim 4$ , shown to be necessary for SC, is much above the experimentally observed values, Sec. 1.2.4.

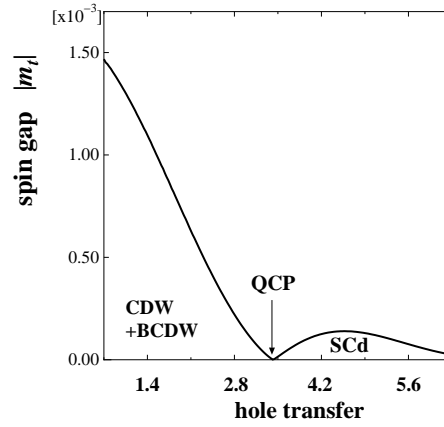


Fig. 2.9: The hole transfer dependence of the magnon spin gap  $m_t$  with  $U/t_{\parallel} = 2$ ,  $V_{\parallel}/U = V_{\perp}/U = 0.25$ , and  $t_{\perp} = t_{\parallel} = 1$ . CDW and BCDW denote, respectively, charge- and bond-charge- density wave ground states. SCd denotes d-wave-like superconducting state. QCP stands for quantum critical point. If  $m_t$  is regarded as the transition temperature, this depiction may be regarded as a phase diagram for doped cuprate ladders. From [120].

## 2.4 CDW phason response to ac field

### CDW – dynamics of the phase

The main features of a standard charge density wave (CDW) established in real material in the presence of electron-phonon coupling can be described with Fröhlich 1D electron-phonon Hamiltonian, [122].

$$H = \sum_{k,\sigma} \varepsilon_k c_{k,\sigma}^\dagger c_{k,\sigma} + \sum_q \hbar\omega_q (b_q^\dagger b_q + b_{-q}^\dagger b_{-q}) + \sum_{k,q,\sigma} g(k) c_{k+q,\sigma}^\dagger c_{k,\sigma} (b_q + b_{-q}^\dagger) \quad (2.16)$$

where  $c_{k,\sigma}^\dagger$  and  $b_q^\dagger$  are creation operators for 1D Bloch electron and a longitudinal phonon  $q$  with dispersions  $\varepsilon_k$  and  $\omega_q$  respectively, and  $g(k)$  is the electron-phonon coupling constant. In the mean-field theory in 1D, only the interaction with the phonon at  $Q = 2k_F$  is to be considered. Corresponding distortion of the lattice is described by a complex order parameter

$$\Delta e^{i\varphi} = g(2k_F) \langle b_{2k_F} + b_{-2k_F}^\dagger \rangle \quad (2.17)$$

where  $\Delta$  and  $\varphi$  are real. The displacement field of the lattice is given by

$$\langle b_{2k_F} + b_{-2k_F}^\dagger \rangle e^{2ik_F x} + c.c. = \frac{2\Delta}{g(2k_F)} \cos(2k_F x + \varphi) \quad (2.18)$$

That is, a charge modulation occurs in the system, accompanied by lattice distortion at similar wave-vector. Standard CDW appears below the so-called Peierls transition, [111]. The carriers condense below a gap  $2\Delta$ , in analogy with superconductivity. The condensate here, however, is formed by the electron-hole pairs of opposite spin, coming from the opposite sides of the Fermi surface, involving the wave vector  $2k_F$ .

The dynamics of this condensate is described in terms of a position- and time- dependent order parameter  $\Delta(x, t)$ . As  $\Delta(x, t)$  is complex, Eq. 2.17, both amplitude and phase fluctuations occur. These can be assumed to be decoupled and

$$\Delta(x, t) = (\Delta_0 + \delta) e^{i\varphi'} \quad (2.19)$$

where  $\Delta_0$  is the equilibrium order parameter, and  $\delta$  and  $\varphi'$  are the fluctuations from the equilibrium value. To lowest order in  $\delta$  and  $\varphi'$  the amplitude mode corresponds to  $2\Delta_0 + 2\delta$ , and the phase mode corresponds to  $2\Delta_0 i\varphi'$ .

The dispersion relations of these modes were evaluated by Lee, Rice and Anderson, [123]. While the amplitude mode has a gap, the phase mode is gapless (which was first pointed out by Fröhlich for an incommensurate DW); the  $q = 0$  translational mode corresponds to zero excitation energy, Fig. 2.10.

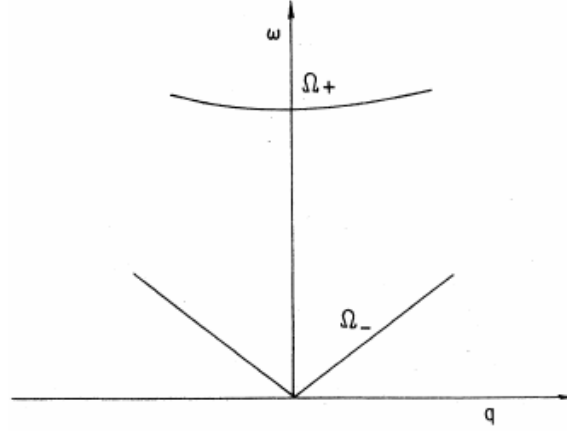


Fig. 2.10: Dispersion relation of CDW phase mode,  $\Omega_-$ , and of amplitude mode,  $\Omega_+$ .

The amplitude mode is expected to be Raman active, whereas phase mode carries a dipole moment, as it involves the motion of condensed electrons across the lattice background. Consequently, the  $q = 0$  phase mode carries a current. Experimentally, this mode is related to dc and ac conductivity of a CDW condensate. Therefore, most of the descriptions of dynamical collective phenomena of CDW are in terms of the dynamics of the phase only.

The Coulomb interchain interaction affects the phason mode dispersion, [124], [125]. The screened Coulomb singularity occurs in the second term of phason dispersion:

$$\omega_{ph}^2 \sim v_{ph}^2 q_{\parallel}^2 + \omega_L^2 \frac{q_{\parallel}^2}{q_{\parallel}^2 + q_{\perp}^2} \quad (2.20)$$

There are two limits. If the system as a whole is a dielectric, *i.e.* there are no uncondensed, free carriers, Coulomb interaction is screened when  $q_{\perp} < q_{\parallel}$  and the phason frequency is raised to a finite value  $\omega_{ph} \approx \omega_L$ . An instructive analogy may be drawn with electron gas where interactions raise the plasmon frequency to finite value. However, for  $q_{\perp} > q_{\parallel}$  phasons remain acoustic, *i.e.* we get  $\omega_{ph} \sim v_{ph} q_{\parallel}$ . In other words, CDW charge fluctuations can carry the Fröhlich supercurrent. The relative magnitude of  $q_{\perp}$ ,  $q_{\parallel}$  in the two limits relates to the periodic charge and lattice modulation being in-phase ( $q_{\perp} < q_{\parallel}$ ) or out-of-phase ( $q_{\perp} > q_{\parallel}$ ) on neighboring chains. If the system contains free carriers these may reduce  $\omega_L$  by screening the singularity in Eq. 2.20, but only at extremely large wavelengths.

Finally, in the real material, due to free carrier screening of Coulomb interactions, various interactions between CDW and underlying lattice remove

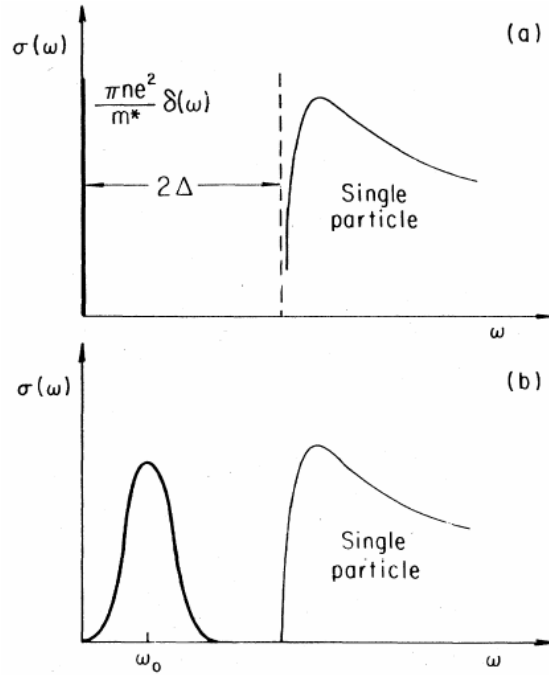


Fig. 2.11: Frequency-dependent response of the collective mode (a) without pinning,  $\omega = 0$  mode is infinitesimally narrow (b) with pinning and damping, a finite width pinned mode at finite frequency. The response at  $\omega > 2\Delta$  is due to free carrier excitations.

translational invariance and lead to pinning of the phase of the condensate. Such pinning is brought about by the local distortions of the condensate around pinning centers. Free carriers do not screen effectively at  $2k_F$ , so the pinning effects shift collective mode conductivity to finite – pinning frequency,  $\Omega_0$ , Fig. 2.11. This is the so-called *pinned* mode, observed in frequency dependent conductivity of standard CDW materials at 10 GHz or higher frequencies.

For modelling pinned mode, as observed within CDW phason response, a simple model satisfies. This is the so-called classical particle model. That is, CDW condensate is described as a classical particle performing damped oscillations in a harmonic, pinning potential. We note that the CDW is described with only one degree of freedom and that free carriers are not taken into account. The corresponding equation of motion is simply the equation for a forced, damped harmonic oscillator. The natural frequency of such a system is the pinning frequency,  $\Omega_0$ . Within the limit of small displacements, the potential term is simply  $\Omega_0^2 \varphi$ . Damping is taken to be weak  $\gamma_0$  and  $E$ , the applied ac field is harmonic.

$$\frac{d^2\varphi}{dt^2} + \gamma_0 \frac{d\varphi}{dt} + \Omega_0^2 \varphi = eE/m^* \quad (2.21)$$

$m^*$  is the effective mass of the CDW condensate, *i.e.* the mass of the classical particle representing it, while  $e$  stands for the electron charge. The nonuniform nature of pinning has been completely neglected in the above analysis, and this reflects as follows. This model in the above stated underdamped limit describes only the pinned mode and can not simultaneously describe the low-frequency (audio/radio) overdamped modes, as observed in the response of standard CDW materials. These modes can only be described in the strong damping limit of classical particle model.

### Littlewood's model of CDW phason response

Littlewood's exposition, [127], starts with Fukuyama, Lee and Rice, [128] model for CDW, which is more realistic than the classical particle one. The model by FLR of an incommensurate charge density wave (CDW) as a deformable medium has been successful in explaining many experimental results both qualitatively and quantitatively, [126]. In this model, the CDW is an elastic medium subject both to impurity pinning forces and an external drive force. Their model leads to an equation of motion

$$m^* \frac{d^2\varphi}{dt^2} + \gamma_0 \frac{d\varphi}{dt} - \kappa \nabla^2 \varphi + \sum_i V(\mathbf{r} - \mathbf{R}_i) \rho_0 \sin[\mathbf{Q} \cdot \mathbf{r} + \varphi(\mathbf{r})] = \rho_c E_z / Q_z \quad (2.22)$$

A sinusoidal CDW, characterized by a nesting vector  $\mathbf{Q}$ , corresponds to the charge density  $\rho(r) = \rho_c + \rho_0 \cos[\mathbf{Q} \cdot \mathbf{r} + \varphi(\mathbf{r})]$ . The FLR consider pinning of the phase  $\varphi$  by a random impurity potential  $V(\mathbf{r} - \mathbf{R}_i)$ .  $\kappa$  is the elastic modulus, which describes the elastic deformation of the phase due to pinning. Here it is assumed that CDW is free to oscillate only in the  $z$  direction of applied electric field,  $E_z$ .

We note that the term (of Hamiltonian corresponding to this equation of motion), which describes the interaction of charge density with the impurity potential, has the form

$$\begin{aligned} H_{imp} &= \sum_i \int d\mathbf{r} V(\mathbf{r} - \mathbf{R}_i) \rho(\mathbf{r}) \\ &= \sum_i V(\mathbf{Q}) \cos[\mathbf{Q} \cdot \mathbf{R}_i + \varphi(\mathbf{R}_i)] \end{aligned} \quad (2.23)$$

That is, the  $Q = 2k_F$  charge density modulation couples only to the respective Fourier component  $V(\mathbf{Q})$  of the impurity potential.

The general formulation is based on treating the interaction between CDW and free carriers within a two-fluid model, where the only interaction is that via an electromagnetic field. Total induced current is given by displacement and the conduction current, and CDW polarization current:

$$\mathbf{j}(\mathbf{r}, t) = \varepsilon \dot{\mathbf{E}} + \sigma \mathbf{E} + \rho_c \dot{u} \hat{\mathbf{z}} \quad (2.24)$$

Here,  $\dot{u} = \frac{\dot{\phi}}{Q_z}$  is the CDW velocity.  $\varepsilon$  and  $\sigma$  are the dielectric and conductivity tensors and for the harmonic field  $\dot{\mathbf{E}} = -i\omega \mathbf{E}$ , the complex conductivity tensor is defined as  $\tilde{\sigma} = \sigma(\mathbf{q}, \omega) - i\omega \varepsilon(\mathbf{q}, \omega)$ . Most CDW materials are anisotropic, and the conductivity tensor is accordingly approximated by the diagonal form  $\tilde{\sigma} = \tilde{\sigma}_\perp (\hat{\mathbf{x}} + \hat{\mathbf{y}})/\sqrt{2} + \tilde{\sigma}_z \hat{\mathbf{z}}$ . Here  $\tilde{\sigma}_z$  is conductivity in the best conducting direction, while  $\tilde{\sigma}_\perp$  is low conductivity in perpendicular directions.

The formulation is also based on the assumption of the linear response of the CDW. This leads to the linearization of the equation of motion, Eq. 2.22 about some static equilibrium state  $u_0(r)$ :

$$\sum_{q'} [G_0^{-1}(\mathbf{q}, \omega) \delta_{\mathbf{q}, \mathbf{q}'} + V(\mathbf{q} - \mathbf{q}')] u(\mathbf{q}', \omega) = \rho_c E_z(\mathbf{q}, \omega) \quad (2.25)$$

where the bare response function is

$$G_0^{-1}(\mathbf{q}, \omega) = -m^* \omega^2 - i\gamma_0 \omega + \mathbf{q} \cdot \boldsymbol{\kappa} \cdot \mathbf{q} \quad (2.26)$$

A formal solution to Eq. 2.25 is

$$u(\mathbf{q}, \omega) = \rho_c \sum_{q'} G_E(\mathbf{q}, \mathbf{q}'; \omega) E_z(\mathbf{q}, \omega) \quad (2.27)$$

Inserting this formal solution into Eq. 2.24 for the total current, and taking into account the anisotropy of the conductivity we get

$$[\sigma_{tot}(\mathbf{q}, \mathbf{q}'; \omega)]_z = \tilde{\sigma}_z \delta_{\mathbf{q}, \mathbf{q}'} - i\omega \rho_c^2 G_E(\mathbf{q}, \mathbf{q}'; \omega) \quad (2.28)$$

Last term is the CDW condensate conductivity, which due to the assumed anisotropy affects only the longitudinal component of conductivity,  $\tilde{\sigma}_z$ . The subscript  $E$  denotes that  $G_E$  is not any more the bare response function  $G_0^{-1}$ , but a response function to an external electric field  $G_E^{-1} = G_0^{-1} + V(\mathbf{q} - \mathbf{q}')$ .

### Uniform pinning

For illustrative purposes, a correspondence between this modelling and the classical particle model may be given if the pinning potential is taken as uniform,  $V(\mathbf{q}) = V_0\delta_{q,0}$ . Eq. 2.28 reduces to

$$\sigma_{tot}(0, \omega) = \sigma_z - i\omega\varepsilon_z - \frac{i\omega\rho_c^2}{G_0^{-1}(0, \omega) + V_0} \quad (2.29)$$

$\rho_c^2/(G_0^{-1}(0, \omega) + V_0)$  may be regarded as  $\varepsilon_{CDW}$ , the CDW contribution to the dielectric function. The collective CDW mode may be separated into longitudinal and transverse components.

The transverse mode  $q_z = 0, q_\perp \rightarrow 0$  may be obtained by finding the poles of total dielectric function. In this case, the single-particle  $\varepsilon_z$  is negligible since  $\varepsilon_{CDW}$  diverges, thus:

$$\begin{aligned} G_0^{-1}(0, \omega) + V_0 &= 0 \\ -m^*\omega_T^2 - i\gamma_0\omega_T &= -V_0 \end{aligned}$$

that is,  $\omega_T^2 = V_0/m = \Omega_0^2$ , the transverse mode frequency is the pinning frequency. Conductivity, Eq. 2.29 shows a weakly damped,  $\gamma_0$ , peak at  $\Omega_0$  frequency, as illustrated in Fig. 2.12.

The longitudinal mode  $q_\perp = 0, q_z \rightarrow 0$  may be obtained by finding zeros of the CDW dielectric function  $\varepsilon_z + \rho_c^2/(G_0^{-1}(0, \omega) + V_0)$ :

$$\begin{aligned} G_0^{-1}(0, \omega) + V_0 &= \rho_c^2/\tilde{\sigma}_z \\ m^*\omega_L^2 + i\gamma_0\omega_L &= V_0 - i\omega_L\rho_c^2/\tilde{\sigma}_z \end{aligned}$$

At high frequencies,  $\omega \gg \sigma_z/\varepsilon_z$  we have  $\tilde{\sigma}_z \sim -i\omega\varepsilon_z$ , and since the damping term may be neglected,  $\omega_L^2 = V_0/m + \rho_c^2/m^*\varepsilon_z$ . A very high  $\Omega_{pl} = \rho_c^2/m^*\varepsilon$  plasmon-like frequency, much above  $\Omega_0 = \sqrt{V_0/m}$  regulates the frequency of the longitudinal mode,  $\omega_L \approx \Omega_{pl}$ .

At low frequencies,  $\omega \ll \sigma_z/\varepsilon_z \rightarrow \tilde{\sigma}_z \sim \sigma_z$ , the damping term may be regarded as being enhanced  $i\gamma_0\omega_L + i\omega_L\rho_c^2/\sigma_z$ . That is, damping in this frequency range is regulated by free-carriers conductivity,

$$\gamma = \gamma_0 + \rho_c^2/\sigma_z \quad (2.30)$$

The longitudinal response develops a low-frequency, overdamped  $\gamma \gg \gamma_0$ , tail. It extends down to a frequency  $\tau_0^{-1} = \gamma/V_0 \approx \rho_c^2/(\sigma_z V_0)$ , as illustrated in Fig. 2.12. It is important to note that, in principle, such a purely longitudinal, low-frequency mode, can not be experimentally observed by spectroscopy

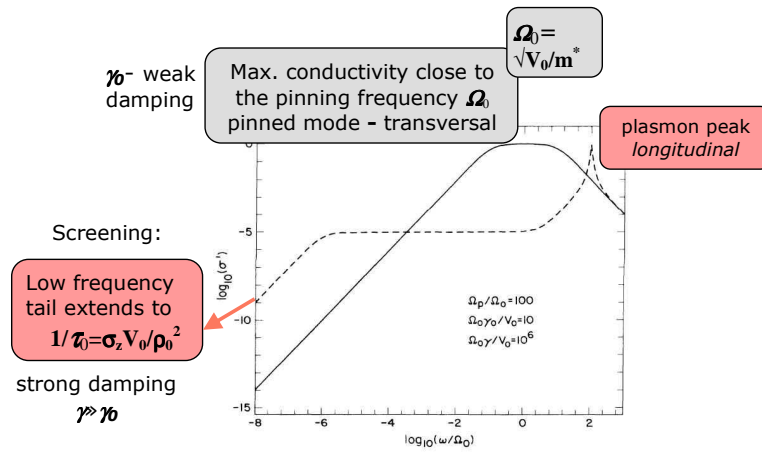


Fig. 2.12: The real part of the transverse component of collective conductivity  $\sigma'$  is shown by a solid line. The pinned mode, as a peak at  $\Omega_0$  is shown. The dashed line shows the real part of the longitudinal component of the collective conductivity (thus, not expected to be observable in the experiment). The high frequency plasmon peak is accompanied by an extra broad dispersion at low frequency,  $1/\tau_0$ .

techniques, since it exists only for zeros of the dielectric function. On the contrary, the low-frequency mode is experimentally observed, and consequently, this analysis has to be improved to account for this experimental fact.

### Nonuniform pinning

Pinned configurations and the local modes of oscillation of the CDW are disordered on a typical length scale  $\xi$  - Lee-Rice length. Below this scale the phase is considered constant. Therefore, we have focused at the CDW response to local field, through the response of local modes.

A convenient formulation for highlighting the influence of screening is obtained by constructing a local CDW response function  $G_\rho(\mathbf{q}, \mathbf{q}'; \omega)$  to a fixed external charge. This charge represents one of the free carriers existing in the real material. The local response calculation takes into account a disordered nature of CDW. Previously, the response to external electromagnetic field was given by  $G_E(\mathbf{q}, \mathbf{q}'; \omega)$ . The response function to a fixed external charge is calculated

$$G_\rho^{-1}(\mathbf{q}, \omega) = G_E^{-1}(\mathbf{q}, \omega) - i\omega\rho_c^2 R(\mathbf{q}, \omega) \quad (2.31)$$

An external current source is introduced  $j_{ext}(\mathbf{q}, \omega)$ . Electric field is calculated

$$E_z(\mathbf{q}, \omega) = [-i\omega\rho_c u(\mathbf{q}, \omega) + j_{ext}(\mathbf{q}, \omega)]R(\mathbf{q}, \omega) \quad (2.32)$$

where

$$R(\mathbf{q}, \omega) = \frac{q_z^2 - i\omega\mu_0\tilde{\sigma}_\perp}{q_\perp^2\tilde{\sigma}_\perp + q_z^2\tilde{\sigma}_z - i\omega\mu_0\tilde{\sigma}_\perp\tilde{\sigma}_z} \quad (2.33)$$

The skin depths  $\omega\mu_0\tilde{\sigma}_i$  are considered to be much larger than localization lengths of CDW  $\xi_\perp, \xi_z$ . Thus an electrostatic approximation can be made. This leads to the form of  $R(\mathbf{q}, \omega) = \tilde{\sigma}_z^{-1}[1 + (\tilde{\sigma}_\perp/\tilde{\sigma}_z)(q_\perp/q_z)^2]^{-1}$ . Now, if conductivity anisotropy is considered to be large

$$\xi_z/\xi_\perp < (\tilde{\sigma}_z/\tilde{\sigma}_\perp)^{1/2} \quad (2.34)$$

$R(\mathbf{q}, \omega) = 1/\tilde{\sigma}_z(\omega)$  assumes a simple form, and the local mode will appear essentially longitudinal ( $q_\perp = 0, q_z \rightarrow 0$ ) in character (contributing only to the conductivity in the best conductivity direction,  $\tilde{\sigma}_z$ ). In this case

$$G_\rho^{-1}(\omega) = G_E^{-1}(\omega) - i\omega\rho_c^2/\tilde{\sigma}_z(\omega) \quad (2.35)$$

The above expression is inverted and  $G_E$  (expressed through  $G_\rho$ ), that is necessary to calculate the experimentally measured conductivity, is obtained and inserted in Eq. 2.28. Accordingly, the longitudinal response is also expected to contribute in spectroscopy experiments, which, normally, should observe the conductivity only due to transverse modes. Mixing the character of the modes in CDW materials is essential for understanding spectroscopy results.

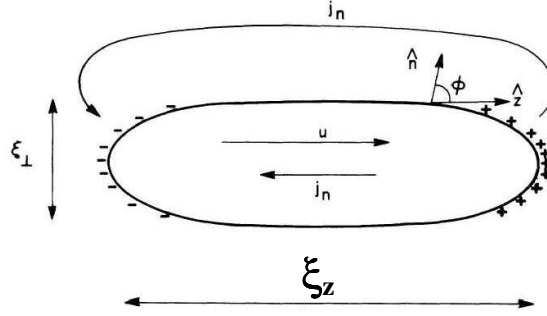


Fig. 2.13: The schematic picture of localized mode showing induced polarization charges (+, -) and normal current  $j_n$  backflow. A long-wavelength ( $q \rightarrow 0$ ) external field induces internal fields at a finite wavelength, comparable to  $\xi_z$  domain length scale. The local fields induce screening currents of free carriers, which dissipate energy.

Mixing of the mode character and the influence of conductivity anisotropy on the longitudinal character of local mode may be appreciated when the following is considered:

The local mode is considered as a local displacement  $u$ , of the CDW, over a region  $(\xi_\perp, \xi_z)$ , with  $u = 0$  outside this region. Within this length scale, the mode has a pinning energy  $V_0$ , and it responds to the average internal, local, field  $\langle E_z \rangle$ . The equation of motion is then

$$(-m^*\omega^2 - i\gamma_0\omega + V_0)u = \langle E_z \rangle \quad (2.36)$$

The determination of local field  $\langle E_z \rangle$  depends on the correction of external field for depolarization. Here, the local mode is regarded as polarized inclusion in a medium. In a case of elongated domain,  $\xi_\perp \ll \xi_z$ , the local field is equal to the external one. Thus the characteristic mode frequency is  $\Omega_0^2 = V_0/m^*$ , the frequency of the transverse, pinned, mode found for the uniform pinning case. For a different shape of the domain  $\xi_\perp > \xi_z$ ,  $\langle E_z \rangle = E_{ext} - P/\epsilon_z$ . Polarization  $P$  is given by  $\rho_c u$ , and the characteristic mode frequency is shifted to  $\tilde{\omega}^2 = V_0/m + \rho_c^2/m^*\epsilon_z$ , the frequency of the longitudinal mode,  $\omega_L^2$ , found previously for the uniform pinning case. Thus a disordered nature of CDW, and respective necessity to regard the local modes of CDW for different domains, has introduced mixing of the character of modes in a natural way.

## Results

Measured conductivity, as constructed above, contains single particle conductivity  $\tilde{\sigma}_z$  and also the CDW contribution of mixed character

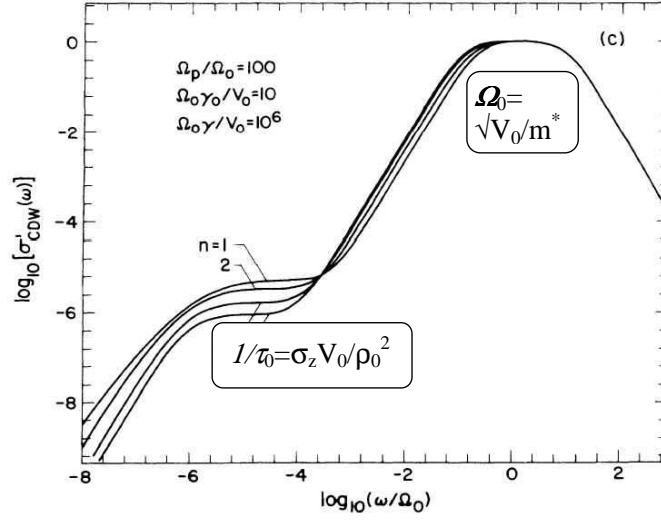


Fig. 2.14: The real part of the transverse component of conductivity  $\sigma'$ . The pinned mode, as a peak at  $\Omega_0$  is shown. The extra broad dispersion is found at lower frequencies, at  $1/\tau_0$ , related to the phonon overdamped tail from Fig. 2.19.

$$[\sigma_{meas}(\omega)]_z = \tilde{\sigma}_z - \frac{i\omega\rho_c^2 G_\rho(\omega)}{1 + i\omega\rho_c^2 G_\rho(\omega)/\tilde{\sigma}_z} \quad (2.37)$$

In order to study the effect of a distribution of modes, the CDW contribution is rewritten in terms of scaled variables.

$$\sigma_{CDW} = \frac{\rho_c^2}{\gamma_0} \frac{-i\omega\tau_0 I(\omega)}{1 + i\omega\gamma_1(\omega)I(\omega)} \quad (2.38)$$

where

$$\gamma_1(\omega) = \tau_0 [1 - i\omega\tau_0(\Omega_0/\Omega_{pl})^2]^{-1} \quad (2.39)$$

and

$$I(\omega) = \int_0^\infty dx g(x) [x - (\omega/\Omega_0)^2 - i\omega\tau - i\omega\gamma_1(\omega)]^{-1} \quad (2.40)$$

Two characteristic oscillation frequencies appear,  $\Omega_0$  and  $\Omega_{pl}$ , and two characteristic relaxation times ( $\tau_{bare} = \gamma_0/V_0$ ,  $\tau_0 = \rho_c^2/(\sigma_z V_0)$ ).  $g(x)$  is a model distribution of modes. For example, if the distribution of localized modes is taken to be a *delta*-function,  $g(x) = \delta(1-x)$ , the Eq. 2.29 is recovered—that is, the uniform pinning case occurs.

In Fig. 2.14, a narrow peak (pinned mode at  $\Omega_0$ ) due to coupling of external ac field to the transverse mode is shown. Bare damping  $\gamma_0$  (which

applies for transverse modes) probably has its origin in phason-phason or phason-phonon scattering processes.

There also appears an extra broad dispersion at  $1/\tau_0$  frequency. It is due to coupling of external ac field to the longitudinal screened mode. This break-down of selection rules corresponds to the longitudinal response mixing in the transverse one due to non-uniform pinning. That is, the tail of the plasmon from Fig. 2.12 mixes into the measured conductivity.

We note that  $\tau_0$  is proportional to the single particle conductivity  $\sigma_z$ , and for insulators it is expected to have the Arrhenius activation equal to the conductivity one. This is due to the external field inducing local field on the level of the length scale  $\xi_z$  of the local mode. These local fields induce screening currents of free carriers, which dissipate energy resistively, Fig. 2.13. It is precisely the resistive damping which appears in Eq. 2.30, for the uniform pinning case. The proportionality of conductivity and relaxation times  $\tau_0$  is well confirmed in various experiments on standard CDW materials, [129, 130, 131, 132].

Additional feature of this analysis is the relation between characteristic relaxation time  $\tau_0 = \rho_c^2/(\sigma_z V_0)$  and characteristic pinned mode frequency,  $\Omega_0 = \sqrt{V_0/m}$ . These two values, as well as  $\sigma_z$ , result from spectroscopy experiments on standard CDW materials, performed in a very broad frequency range. An expression for calculating the CDW condensate effective mass is given by Littlewood:

$$m^* = \rho_c^2/(\sigma_z \cdot \tau_0 \cdot \Omega_0^2) \quad (2.41)$$

Using this relationship, for example, Reagor *et al.* [133] estimated the effective mass for a standard CDW material  $(\text{TaSe}_4)_2\text{I}$  to be  $10^4$ . This value is, indeed, within the experimental limits of  $10^2$ – $10^4$  for CDW materials, [126]. Eventually, it is appropriate to note that Littlewood's model presents an important tool for connecting the experiment and theory. Our data will also be analyzed in this manner

# 3 Experimental techniques

## 3.1 $(\text{TMTSF})_2\text{PF}_6$

### 3.1.1 $(\text{TMTSF})_2\text{PF}_6$ samples and high pressure measurements protocol

We studied a nominally pure  $(\text{TMTSF})_2\text{PF}_6$  single crystal originating from a batch of high quality crystals. The high quality of the batch was proved in a study of quantum Hall effect (QHE) influence on the linear and non-linear resistivity tensor in magnetic field-induced spin density wave (FISDW) phases of  $(\text{TMTSF})_2\text{PF}_6$ , [11]. The crystal had a standard needle shape and dimensions  $3 \times 0.2 \times 0.1 \text{ mm}^3$ . The four annular contact geometry was used: gold was evaporated on the sample and the leads were attached with silver paste. The contact resistances were 2-3 Ohms. High quality of the crystal was confirmed by the resistivity ratio ( $\rho_{300K}/\rho_{min}$  of the order of 1000 ( $\rho_{min}$  is the minimum in resistivity just above the SDW transition)). All electrical transport measurements were performed along the needle  $\mathbf{a}$ -axis. Resistance measurements in the linear regime were done using the standard AC low frequency technique. In the linear regime, there should be no sample resistance dependence on the applied electric field and this was duly checked by using 1 and 10  $\mu\text{A}$  currents for measurements. High critical currents measurements were performed using a DC pulsed technique with 10  $\mu\text{s}$  short pulses and current amplitudes up to 100 mA. The pulse repetition period was 40 ms, *i.e.* 4000 times longer than the pulse. This is enough to avoid Joule heating of the sample even at the highest amplitudes of 100 mA. Non-heating was also checked by the shape of the pulse displayed on the oscilloscope. If heating effects were present when the highest non-pulsed currents were applied (0.3, 1 mA) then the SDW resistance just above  $T_{sc}$  should have lowered at increasing current. The inspection of Fig. 4.6, in the next Chapter, demonstrates that there is no difference in resistances measured in the SDW phase using currents from 0.001 to 1 mA.

The pressure cell was plugged on a Helium3 cryostat capable of reaching

0.35 K. Pt-100 and Lakeshore CarbonGlass 500 thermometers were used, as well as RuO<sub>2</sub> thermometer for the temperatures below 2 K.

Pressure was applied in a regular beryllium-copper cell, with silicon oil inside a Teflon cup as the pressure transmitting medium that would not freeze abruptly but solidify continuously. Consequently, reduced were the mechanical stresses and pressure shifts common to the freezing points of other liquids, which allowed numerous thermal cyclings of the same sample without notable cracks.

However, the drawback of such a technique is the requirement to change pressure only when the cell is warmed up to RT. For an accurate pressure determination, we used an InSb pressure gauge[134], located inside the cell close to the sample. The information from the pressure gauge can be also cross-checked by the phase diagram of (TMTSF)<sub>2</sub>PF<sub>6</sub> [10]. The InSb gauge was calibrated at RT against a manganine gauge establishing a linear pressure dependence of the InSb gauge resistance at a rate of 2.5%/kbar in a 6–12 kbar range.

Since the pressure could be changed at RT only, the measurements were conducted in 19 consecutive runs, (see Table 3.1, [135]). For all runs, after having applied the pressure at RT, cooling started immediately and continuously down to 0.35 K. The electrical transport measurements done, the sample was warmed back to RT and a subsequent increase or decrease of pressure was immediately applied before next cooling. The temperature sweep rates in cooling and warming did not exceed  $\pm 60$  K/h. The change of pressure at RT was checked by the resistance of the InSb gauge: for instance, a 0.8% increase in resistance corresponded to a 300 bar increment in pressure. Respective decrease of the sample resistance at a rate of 10%/kbar at RT was also used as a secondary pressure gauge. Additionally, the pressure coefficient of the InSb resistance measured at RT was equal to that measured at 6 K. Thus, we confirmed that all the pressure steps we made were measured by the InSb gauge with an accuracy of  $\pm 30$  bar.

The complete range of pressures applied and the chronological order of the experiment are found in Table 3.1. Starting in run #1, at a pressure  $p_1 = 6.8$  kbar, we were able to sweep a 4 kbar wide region with increments ranging from 300 to 100 bar. From run #1 to run #16, pressure was always increased in the same manner, except for a 1400 bar increment in the last run. From run #16 to run #17, we made a large pressure drop of  $2350 \pm 50$  bar. The value was calculated from the InSb resistance, later confirmed by the phase diagram of (TMTSF)<sub>2</sub>PF<sub>6</sub>. Therefore, the  $R$  vs.  $T$  curve for the run #17 was almost identical to the curve of the run #10 (both SDW,  $T_{\text{SDW}}$  and superconducting,  $T_{\text{SC}}$  transition temperatures were found identical within experimental errors). Small pressure increments for run #18 and #19

were again performed in the usual manner. Such a procedure allowed us to investigate the pressure domain 8.65–9.3 kbar with a pressure control that could not have been achieved in early studies.

RUN	pressure	$T_{\text{SDW}}$	$T_{\text{SC}}$
1	6.8	7.9	
2	7.1	7.1	
3	7.3	6.6	
4	7.5	6.2	
5	7.7	5.9	
6	7.85	5.6	
7	8.15	5.3	
8	8.35	4.7	
9	8.45	4.4	
10	8.65	3.8	1.18
17	8.65	3.8	1.18
11	8.75	3.5	1.19
18	8.9	2.85	1.21
12	8.95	2.85	1.21
13	9.1	2.45	1.21
19	9.2	1.8	1.21
14	9.3	1.4	1.21
15	9.6		1.195
16	11		1.106

Table 3.1: The complete range of pressures applied on the single crystal of  $(\text{TMTSF})_2\text{PF}_6$  studied in this work. Number of the run presents the chronological order of the experiment. The observed spin-density wave,  $T_{\text{SDW}}$  and superconducting,  $T_{\text{SC}}$ , transition temperatures are also given in the table.

## 3.2 (La, Sr, Ca)<sub>14</sub>Cu<sub>24</sub>O<sub>41</sub>

### 3.2.1 Samples and contacts preparation

The q1D cuprate single crystals were synthesized by the group of J. Akimitsu, T. Sasaki and T. Nagata from the Department of Physics, Aoyama-Gakuin University, Kanagawa, Japan. The q1D cuprate materials are prepared in two steps. Initially a stoichiometric mixture of dried powdered CaCO<sub>3</sub>, SrCO<sub>3</sub> (and/or La<sub>2</sub>O<sub>3</sub>) and CuO is prepared. This mixture may be melted, [71, 70], or calcined (heated and grinded) at high temperature [92], when a solid state reaction happens. This is the way polycrystalline samples are prepared. They are regrinded and sintered into polycrystalline rods, well shaped for floating zone recrystallization, which is a second step. Floating zone method is, basically, a recrystallization by local melting of the polycrystal. A melted zone (obtained by focusing high power light/heat source on the sample) is slowly moved along the crystal, thus allowing it to melt and slowly recrystallize. All these procedures have to be performed in the controlled atmospheres of either oxygen, hydrogen, or inert gasses, in order to control oxydation/reduction levels in the material. Actually, this sample preparation scheme is quite general in a broad field of transition metal oxides, [137]. X-ray diffraction (XRD) is used to check if the preparation procedure has provided single crystals. The obtained single crystals are quite large (*e.g.* 6mm diameter, 10 cm long) and may consist of several domains. Single crystal samples for transport measurements have to be cut away from these large crystals, Fig. 3.1.

The single crystal samples of q1D cuprates were between 3 and 5 mm long, with cross-sections of 0.2-0.4 cm<sup>2</sup>. Precision of the cut, *i.e.* the orientation of cut-away single crystal along the axes was also checked by XRD. The macroscopic crystal planes deviated from the crystallographic axes not more than the experimental error of the XRD equipment used, 1°-3°, [136].

For the dc resistivity measurements the four annular contact geometry was used. For the complex conductivity only two contacts had to be applied, covering the ends of the sample. This two contact geometry was necessary to avoid the influences from the stray capacitances of test-leads and cables, Fig. 3.1. Electrical contacts to the sample were obtained by a special DuPont 6838 silver paste applied directly on the surface and heated for one hour at 750 K in oxygen flow atmosphere. Thin gold leads (20 μm) were then pasted to the baked contact areas of the sample. Other methods of contact preparation were also tested, *e.g.* gold was evaporated onto the sample surface, or silver paste was applied without heating, or it was baked without oxygen flow atmosphere. Any of those impaired the possibility to measure the intrinsic sample properties. Even with the established contact preparation

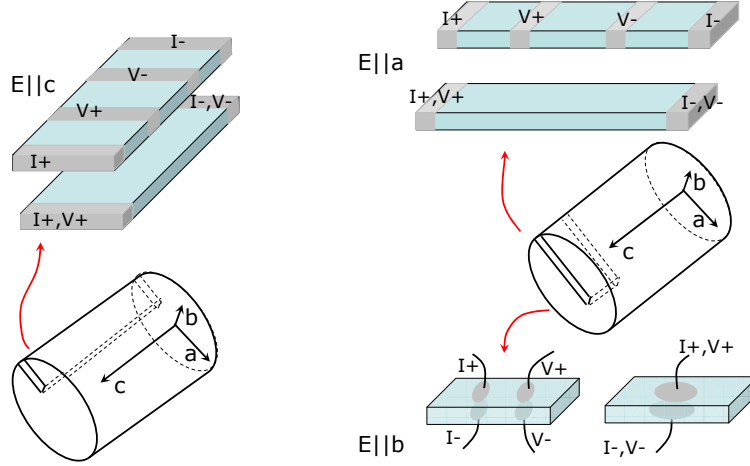


Fig. 3.1: Single crystal samples ( $5 \times 1 \times 0.2 \text{ mm}^3$ ) for transport measurements along  $c$ ,  $a$  or  $b$  axis were carefully cut away from a larger single crystal, designated as a cylinder. This larger single crystal was, after synthesis, confirmed by XRD to be single domain. Precision of the cut, *i.e.* the orientation of the cut-away single crystal along the axes was also confirmed by XRD. The macroscopic crystal planes deviated from the crystallographic axes not more than  $1^\circ$ - $3^\circ$ . Either four or two contacts were applied for dc resistivity or complex conductivity (LFDS) measurements, respectively .

method, the experimentalist should be ware of the possible artefacts: the room temperature resistivity of the material under study might be too high, the activation energies for resistivity might be strongly enhanced and strong nonlinear conduction effects might appear, as well. Furthermore, the complex conductivity measurements sometimes showed large capacitances where they should be negligible.

### 3.2.2 dc resistivity measurements

Measurements were performed in the temperature range 300 K - 2 K in a He-cryostat, where He-pumping was used for temperatures below 4.2 K. Pt-100 and Lakeshore CarbonGlass 500 thermometers were used. Temperatures above room temperature up to 750 K were reached in a simple thermostat (an oven) with an on-off temperature regulation. Pt/Pt-Rh10% thermocouple was used as a thermometer. Thermometry was calibrated properly thus the resistance *vs.* temperature curves measured in both of the setups joined smoothly. In a special case of La based compounds, we used a cryostat featuring a sample holder with the heating capability where temperatures up

to 400 K, [138], may be reached. Thus we avoided any possibility of artefacts due to the sample transfer from the thermostat to cryostat, which might have appeared exactly in the very temperature region we wanted to measure as carefully as possible. The results from all three setups coincided perfectly.

In this 2 K -700 K temperature range, measured resistances covered 14-15 orders of magnitude. Therefore, we had to use 4 different setups. For the low frequency lock-in setup, Stanford Research SR830 and Perkin-Elmer 7265 lock-ins were used for lowest resistances of 1 m $\Omega$ -1 k $\Omega$ . dc current source Keithley 220 and Keithley 182 nanovoltmeter were used in the range of 1  $\Omega$ -100 M $\Omega$ . These two setups are standard four probe methods. For higher resistances, two probe setups had to be used to avoid a time-constant problem. That is, the measured resistance,  $R$ , combined with the input capacitance ( $C \approx 5$  nF for the nanovoltmeter), defines a very long time constant  $RC$ . And when, as for four probe techniques, the current is applied the sample/voltmeter combination behaves as an RC circuit which takes a long time to charge, *e.g.*  $10 \times RC$ . So, the dc two probe technique for resistances up to 10-30 G $\Omega$  was used. That is, either Keithley 617 electrometer or Keithley 487 picoammeter, were used in V/I mode since here the voltage was applied and the current was measured. Also, these instruments have much higher input impedances than nanovoltmeters. Finally, for resistances up to 1 T $\Omega$  the most elaborate two probe ac technique was used. The ac voltage was sourced from the lock-in and applied to the sample. The resulting current was measured by the Stanford Research SR570 current preamplifier, and converted into a voltage read by a lock-in. One has to take care to measure at low enough frequency (down to 0.01 Hz), in order to stay below the low frequency dielectric modes of the sample.

In order to search for possible non-linear effects the resistance was also measured as a function of applied electrical field. These measurements were performed in four probe configuration, using a current source and a nanovoltmeter. Thus, a possible nonlinearity of the contact resistances was excluded.

In two contact measurement, contact resistances influenced the result. Measurements of the intrinsic sample resistivity are, therefore, performed in four contact configuration, to avoid the contact influence. In order to judge on the contact influence in the lowest temperatures region where measurements have to be performed in two probe configuration, we followed the procedure described below.

We have observed two different cases. For (Sr, Ca) materials measured with electric field,  $E$ , applied along a and b axis ( $E||a$ ,  $E||b$ ) and for all three directions for La substituted materials, both configurations gave practically identical results - indicating that the contact resistances were negligible in comparison to the sample bulk resistance. In the temperature region of in-

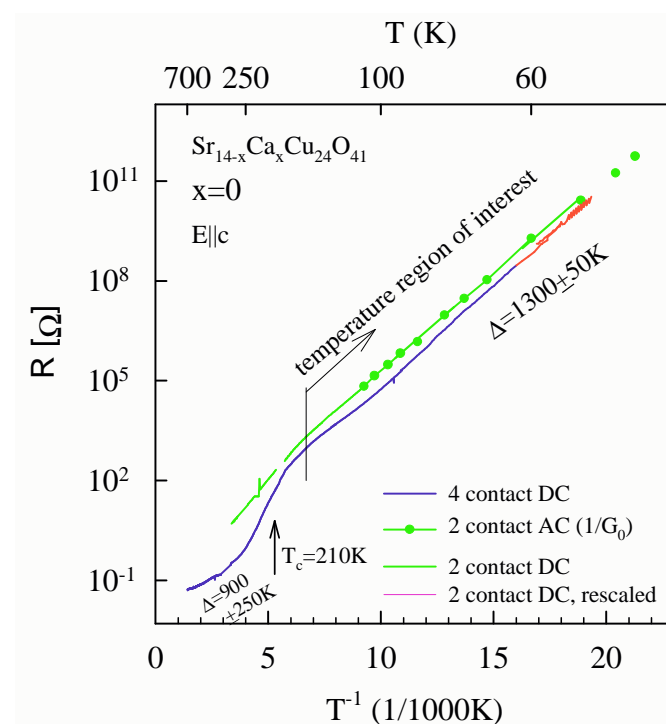


Fig. 3.2: Resistances for  $\text{Sr}_{14-x}\text{Ca}_x\text{Cu}_{24}\text{O}_{41}$ ,  $x = 0$  material along the most conducting  $c$  axis ( $E||c$ ). ac & dc two and dc four contact configuration results are compared. For all the methods in the temperature region of interest the same activation energies were obtained. Four contact dc reaches  $100\text{ M}\Omega$  (blue line), two contact dc  $30\text{ G}\Omega$  (green line) and two contact ac  $2\text{ T}\Omega$  (green dots). The red line represents two contact dc data rescaled to four contact dc, as an example.

terest, for (Sr, Ca) materials the two contact measurements along the most conducting  $c$  axis ( $E||c$ ) gave at least twice larger result when compared to the four contact measurements - implying that the contact resistance is comparable to the sample resistance. Therefore, the procedure is clarified in Fig. 3.2 for the example of  $\text{Sr}_{14-x}\text{Ca}_x\text{Cu}_{24}\text{O}_{41}$ ,  $x = 0$  material. First, we compare the resistance results in two (green line) and in four (blue line) probe configuration in the low temperature region where the resistances do not exceed  $100 \text{ M}\Omega$ . From both two & four contact measurements we find the same activation energies, *i.e.* the ratio between the two and four contact results is constant. We extrapolate on this and conclude that in the temperature region where the resistances exceed  $100 \text{ M}\Omega$  it is possible to rescale (red line) the results obtained in two contact configuration on to the results obtained in four contact configuration. We also note that two probe ac technique results (green circles) coincide perfectly with those from two probe dc technique, and as well, give the same activation energy to the lowest temperatures. Therefore, we conclude that two probe measurements provide results on the intrinsic properties of the material and that influences of contacts, if any, are negligible.

### 3.2.3 Complex conductivity measurements- low frequency dielectric spectroscopy (LFDS)

Complex conductivity is measured in two contact configuration from the room temperature down to 2 K in a He-cryostat. Thin coaxial cables (Lakeshore, diameter 1 mm, 50  $\Omega$ ) are used on the sample holder in order to minimize stray capacitances. In order to cover a large frequency and impedance range, two different methods were used to measure the frequency dependence of the complex conductance  $Y(\omega) = G(\omega) + iB(\omega)$ . At high frequencies (20 Hz–10 MHz) a Hewlett Packard 4284A and Agilent 4294A impedance analyzers were used. The high frequency limit  $F$  (in MHz) is determined by the cabling length  $L$  (1.5 meters for our cryostat). The rule of the thumb is  $FL < 15$  - basically, the wavelength should be much longer than the cabling length. At low frequencies (0.01 Hz–10 kHz) a set-up for measuring high-impedance samples was used. The ac voltage is applied to the sample. The current response of the sample is transformed to the voltage by a Stanford Research SR570 current preamplifier, and subsequently detected by a dual-channel digital lock-in, Stanford Research SR830. It is important to stress that we obtained the same results by using both methods in the frequency range 20 Hz–10 kHz where these methods overlap.

Concerning ac signal levels, higher voltages were carefully avoided in order to stay in the linear regime. We used either 20 or 50 mV, which resulted with electric fields on the sample of up to 200 mV/cm. For the cuprate materials under study the non-linear effects are almost negligible, 2-3 %, at the electric fields up to 10 V/cm, see Sec. 5.1. Thus, we consider this low enough levels, still giving strong enough signals.

Further, by taking into account the results of open-circuit measurements, we have assured that the stray capacitances do not influence the imaginary part of conductivity in the frequency window 0.01 Hz–10 MHz and in the temperature range of our study. Effectively, we subtracted the results of open-circuit measurement  $Y(\omega)_{open} = G(\omega)_{open} + iB(\omega)_{open}$  from the  $Y(\omega)$  results for the sample, [139]. This procedure removes background influences and improves the sensitivity of measurement. The background level of sample holder installed with coaxial cables is as small as  $C_b = B(\omega)_{open}/\omega = 0.45$  pF. Coaxial cores are signal pathways, while shields have to be interconnected as close as possible to the sample. This nullifies the cable capacitance. The observed background capacitance  $C_b$  is due to the unshielded pins to which the sample is attached.

From the real and imaginary parts of the conductance, Fig. 3.3, left panel, obtained after subtracting the background, the components of the dielectric

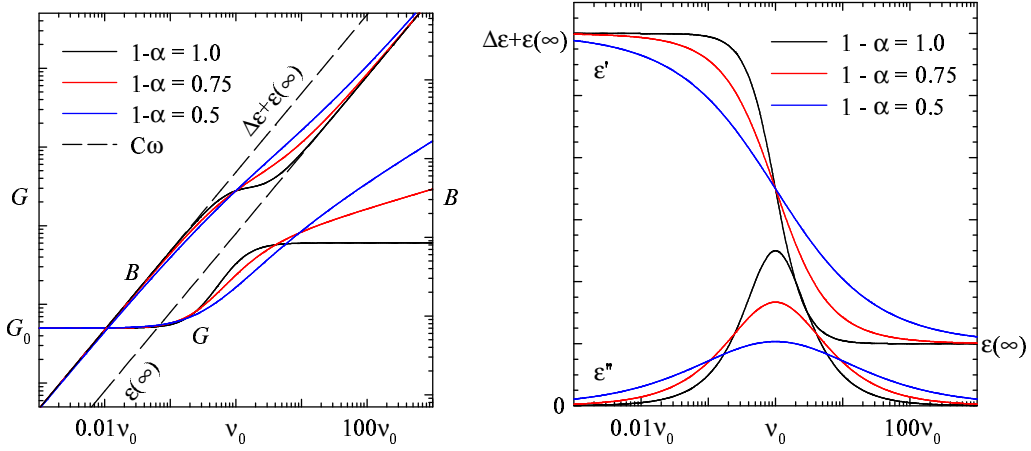


Fig. 3.3: Left panel: The typical forms of real,  $G$ , and imaginary,  $B$ , parts of the conductance which are eventually transformed into the real,  $\epsilon'$ , and imaginary,  $\epsilon''$ , parts of the dielectric function, according to Eqs. 3.2. Right panel: The typical forms of real and imaginary parts of the dielectric function, that can be described by Havriliak-Negami function, Eq. 3.3, for different  $1 - \alpha$  parameter values.

function were extracted using the relations

$$\epsilon_0 \epsilon'(\omega) = \frac{l}{S} \frac{B(\omega)}{\omega} \quad (3.1)$$

$$\epsilon_0 \epsilon''(\omega) = \frac{l}{S} \frac{G(\omega) - G_0}{\omega} \quad (3.2)$$

where  $\epsilon_0$  is the permittivity of vacuum, 8.858 pF/m.  $G_0$  is the dc conductivity obtained at low frequencies where  $G(\omega)$  is independent of  $\omega$ .  $\frac{l}{S}$  is the ratio between the sample length  $l$  (*i.e.* length between the contacts) and the cross section  $S$ . This ratio is called the aspect ratio.

The observed dielectric response can be well fitted by the phenomenological Havriliak-Negami (HN) function [140], Fig. 3.3. This is a generalized form of Debye function, widely used to describe the relaxation processes in disordered systems.

$$\epsilon(\omega) - \epsilon_{\text{HF}} = \frac{\Delta\epsilon}{1 + (i\omega\tau_0)^{1-\alpha}} \quad (3.3)$$

$\Delta\epsilon = \epsilon_0 - \epsilon_{\text{HF}}$  is the relaxation strength, and  $\epsilon_0$  and  $\epsilon_{\text{HF}}$  are the static and high frequency dielectric constant, respectively.  $\tau_0$  and  $1 - \alpha$  are the central relaxation time and the shape parameter which describes the symmetric

broadening of the relaxation time distribution function, respectively. The observed dielectric response in the frequency window of 0.01 Hz–10 MHz, for the various materials under study, was successfully fitted to a single HN mode. Measured data were fitted by using the least squares method in the complex plane [142, 143, 139]. Such an approach takes into consideration both real and imaginary part of the dielectric function while at the same time strongly improves the resolution if compared with the method in which the real and imaginary parts are treated separately, [141]. The complex plane method proved itself to be a powerful tool to resolve reliably a mode if it contributes to the measured capacitance with at least 0.5 pF. The capacitance measurement resolution is of the order  $\pm 0.01$  to 0.03 pF. For the aspect ratios (Eq.3.2) of the samples we worked with, 70-300/cm, 0.5 pF would amount to the minimum observable dielectric modes of 400-1500 with the resolution as good as  $\pm 10$ .

Since the complex conductivity has to be measured in 2 contacts, we need to judge on the contact influence. Firstly, we note that  $G_0$  low-frequency conductivities obtained here correspond perfectly to two contact dc resistivities - the activation energies are also the same, see Fig. 3.2. Secondly, the central relaxation time  $\tau_0$  obtained here behaves in an activated manner characterized by this same activation energy, see Chapter 5, Fig. 5.1. Therefore, we conclude that the contacts do not influence the intrinsic sample properties, despite being comparable to the bulk for the case of  $\text{Sr}_{14-x}\text{Ca}_x\text{Cu}_{24}\text{O}_{41}$  materials measured along  $c$  axis. In the case of (Sr, Ca) materials measured along  $a$  or  $b$  axis ( $E||a$ ,  $E||b$ ) and for all three directions for La substituted materials the contact resistances were anyhow negligible in comparison to the sample bulk resistance. As described before, if contact preparation failed, large capacitances may be observed in the temperature region where they should be negligible. In some cases, where the two contact measured resistivity was at least 3 times larger than the four contact one, an additional dielectric mode was observed. The latter effect is a known artefact due to poor contacts, [129].

We combine our dc/LFDS results with the quasi-optical microwave and far infrared (FIR) optical conductivity results obtained by the group of prof. M. Dressel and his coworkers B. Gorshunov, P. Haas and T. Rõõm at University of Stuttgart, Germany. The Stuttgart group utilized a coherent source quasi-optical spectrometer, for frequencies 5 to 25  $\text{cm}^{-1}$  (150-750 GHz), for direct measurements of  $\varepsilon'(\omega)$  and  $\varepsilon''(\omega)$ , [144]. From the far infrared (FIR) up to 10 000  $\text{cm}^{-1}$  the polarized reflection was determined by a Fourier transform spectrometer. Combined data sets were analyzed by the Kramers-Kronig relations in order to obtain the spectra of  $\varepsilon'(\omega)$ ,  $\varepsilon''(\omega)$ , and conductivity  $\sigma(\omega)$ .

# 4 Investigation of phase diagram of $(\text{TMTSF})_2\text{PF}_6$

In this work, an optimised pressure control (see Section 3.1) was used to investigate the critical region of the phase diagram (see Fig. 1.1) of  $(\text{TMTSF})_2\text{PF}_6$ , which features the phase boundary between the spin density wave, SDW, and superconducting state, SC. We have studied the pressure and temperature dependence of resistance and superconducting critical current, [135].

## 4.1 Experimental observations

### 4.1.1 Metallic state : $T > T_{\text{SDW}}, T > T_{\text{SC}}$

In Fig. 4.1a, we show the resistance *vs.* temperature below 20 K for a set of characteristic pressures from 6.8 to 9.2 kbar together with the data at 11 kbar where a direct metal-to-SC transition is observed. The temperature dependence of resistance in the metallic state (we concentrate on temperatures below 20 K) is quadratic, as expected when the electron scattering is dominated by electron-electron interactions, see Sec. 1.1.2, [27, 145].

We have noticed a shift of  $R$  *vs.*  $T$  curves by temperature independent resistance value after each pressure run (Table 4.1, see also Sec. 3.1), without any change of the actual temperature dependence. The resistance curves are usually shifted 0.1–0.2 m $\Omega$  upwards after each run (see caption of Fig. 4.1a). This effect is most clearly seen in the metallic state below 20 K since the absolute values of resistance (1–2 m $\Omega$ ) become then comparable to the offset. An example of this offset is shown in the inset of Fig. 4.1a. The two resistance curves result from run #10 and #17, *i.e.* they were measured at equal pressures, but with 7 runs performed in-between. The behaviour of run #17 can be made equal to the run #10 provided an offset of 2.5 m $\Omega$  is subtracted from resistance values of the earlier run #10. We tend to relate this effect to an increase of residual resistance due to a cumulative creation of defects after each temperature cycle. We will show later that such defects are not cracks,

RUN	pressure (kbar)	$T_{\text{SDW}}$ (K)	$T_{\text{SC}}$ (K)	$\Delta_{\text{SDW}}$ (K)	$R_{\infty}$ (m $\Omega$ )	$c$ vol%	$I_c$ (mA)
1	6.8	7.9		9.38	12.1	0.03	
2	7.1	7.1					
3	7.3	6.6					
4	7.5	6.2					
5	7.7	5.9					
6	7.85	5.6					
7	8.15	5.3		6.35	12.0	0.09	
8	8.35	4.7					
9	8.45	4.4		5.74	11.30	0.2	
10	8.65	3.8	1.18	5.56	10.60	0.3	
17	8.65	3.8	1.18				.001
11	8.75	3.5	1.19	5.58	8.772	0.36	
18	8.9	2.85	1.21	6.90	2.473	1.25	0.15
12	8.95	2.85	1.21	6.70	2.146	1.4	0.3
13	9.1	2.45	1.21	6.90	0.320	5	7
19	9.2	1.8	1.21	6.30	0.0452	17	35
14	9.3	1.4	1.21	6.80	0.0022	89	
15	9.6		1.195				
16	11		1.106			100	35

Table 4.1: The complete range of pressures applied on the single crystal of (TMTSF)<sub>2</sub>PF<sub>6</sub> studied in this work. The run number gives the chronological order of experiment. The observed spin-density wave,  $T_{\text{SDW}}$  and superconducting,  $T_{\text{SC}}$ , transition temperatures are given. The SDW activation energy,  $\Delta_{\text{SDW}}$ , asymptotic resistances,  $R_{\infty}$  and the volume proportion  $c$  (vol%) of the metallic phase when the sample is in coexistence region are obtained from the fits of  $R$  vs.  $T$  data to the corrected Arrhenius law, Eq. 4.3.  $I_c$  are critical currents for the suppression of SC phase.

as they would add junctions in the sample, that would be easy to detect in superconducting state. The added defects could be of point disorder nature of unknown origin. It should be noted that such phenomenon was previously unreported. Still, it can not be excluded from all the previous studies, since such extensive thermal cyclings were not performed before.

However, the metallic state resistance was the only feature influenced by extensive thermal cycling of the sample. The resistance values in the SDW state, which are orders of magnitude higher, were not influenced by the thermal cycling and we could not notice any influence on determination

of transition temperatures. Since the plot of resistance *vs.*  $T^2$  (see Fig. 4.1b) reveals the existence of quadratic temperature dependence below about 12 K with residual resistance increasing slightly after each pressure run, we have decided to use the residual resistance value obtained in the run #1 as the reference value, assuming that the sample was the least damaged in the first run, as compared to all subsequent runs. In so doing, we have noticed that the resistance is weakly pressure dependent at 20 K and becomes insensitive to pressure below 10 K in the investigated pressure domain.

#### 4.1.2 SDW region: $p < 8.6$ kbar, $T \lesssim T_{\text{SDW}}$

As the SDW region, we denote low pressure, low temperature region where the transition to SDW state is observed as a sharp increase of resistance (Fig. 4.2a) without any hysteretic behaviour when sweeping temperature up and down. The exact point of transition is defined as the temperature of the maximum of logarithmic derivative of resistance with respect to the inverse temperature,  $\partial(\ln R)/\partial(1/T)$  *vs.*  $T$ . In Fig. 4.2b, we show these maxima corresponding to the  $R$  *vs.*  $T$  curves above. Activation energy values,  $\Delta_{\text{SDW}}$ , are well defined inside broad temperature spans, especially for the pressures in this region, 6.8–8.45 kbar (Fig. 4.3). We note here that the asymptotic resistance at infinite temperature,  $R_{\infty}$ , remains constant in this pressure range, as expected in the standard semiconducting model.

#### 4.1.3 SC region: $p > 9.43$ kbar, $T \lesssim T_{\text{SC}}$

This pressure domain has been briefly investigated at two subsequently applied pressures (9.6 and 11 kbar). A direct transition from metallic to superconducting state has been observed, Fig. 4.4.  $T_{\text{SC}}$  was defined as the onset of resistance drop. These two pressures differ only in  $T_{\text{SC}}$ , which are  $1.195 \pm 0.005$  K and  $1.106 \pm 0.005$  K, respectively. The transitions are very narrow and no hysteresis has been observed at  $T_{\text{SC}}$ . The remaining shift of less than 3 mK observed between cooling and warming curves can be attributed to the finite speed of temperature sweep,  $\pm 1$  mK/s and the thermal inertia of the pressure cell. The mean pressure dependence  $\partial T_{\text{SC}}/\partial p \approx -0.07$  K/kbar is in agreement with the value already reported by Schulz *et al.* [51].

#### 4.1.4 Coexistence region: $8.6 < p < 9.43$ kbar

The coexistence region has been denoted as the regions of the phase diagram where both SDW and metallic (eventually SC) states clearly manifest. These

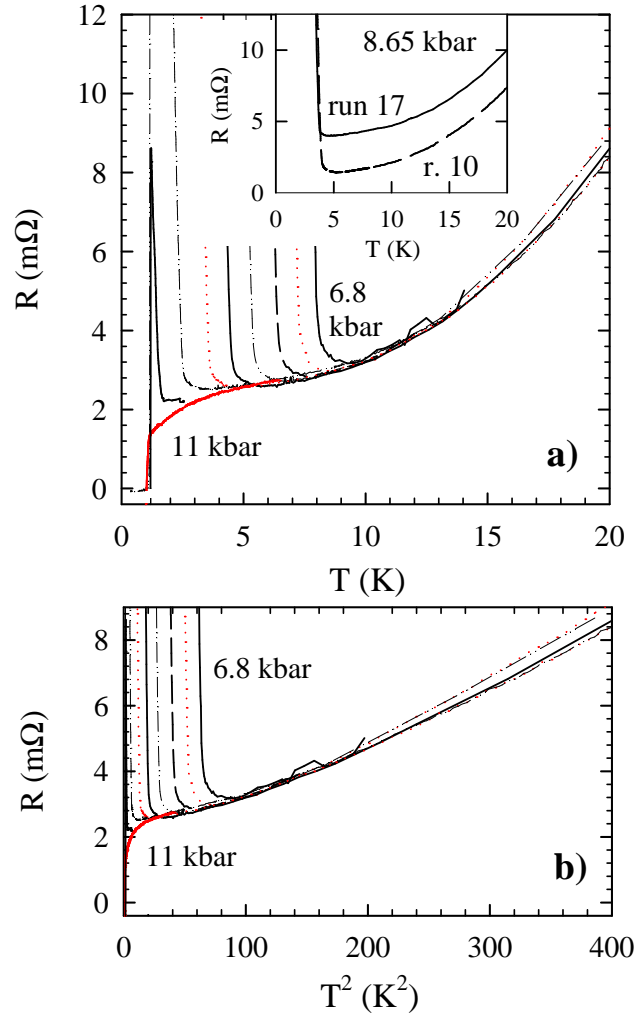


Fig. 4.1: (a) Resistance *vs.* temperature curves for the usual set of pressures (see legend in Fig. 4.2), the sharpness of transitions may be fully appreciated. In the inset: A detail of the minimum in the  $R$  *vs.*  $T$  curves. For runs 10 and 17, both measured at 8.65 kbar, residual resistance shift amounted to 2.5  $m\Omega$ . (b) Resistance *vs.* temperature squared curves for the given list of pressures. Low temperature behaviour approaches the  $T^2$  law of 3D metals.

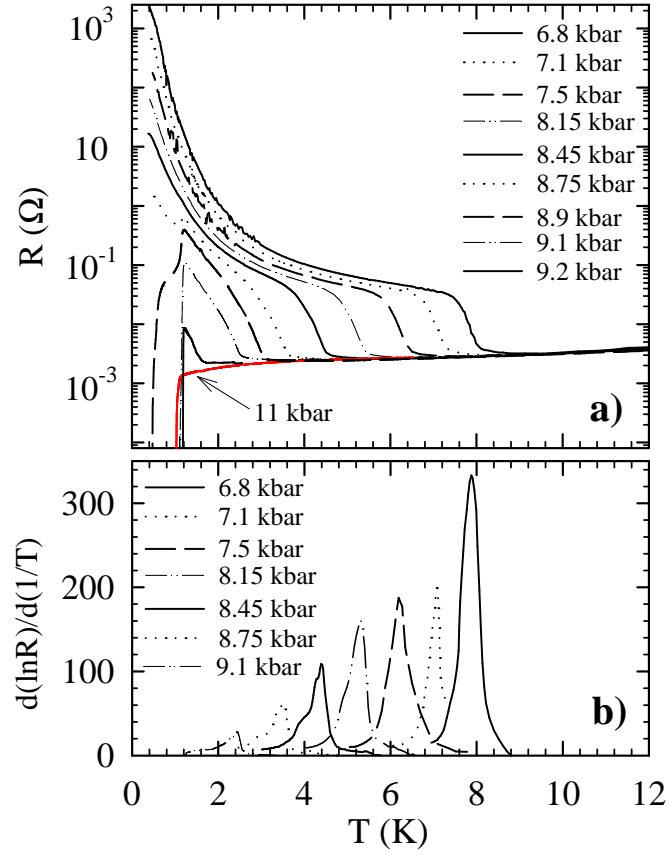


Fig. 4.2: (a) The logarithm of resistance *vs.* temperature in cooling, at different pressures. Above the SDW transition (step-like features), resistance decreases as expected for a metal. (b)  $T_{SDW}$  is defined as a peak in the derivative of logarithm of resistance over inverse temperature,  $\partial(\ln R)/\partial(1/T)$  *vs.* temperature,  $T$ .

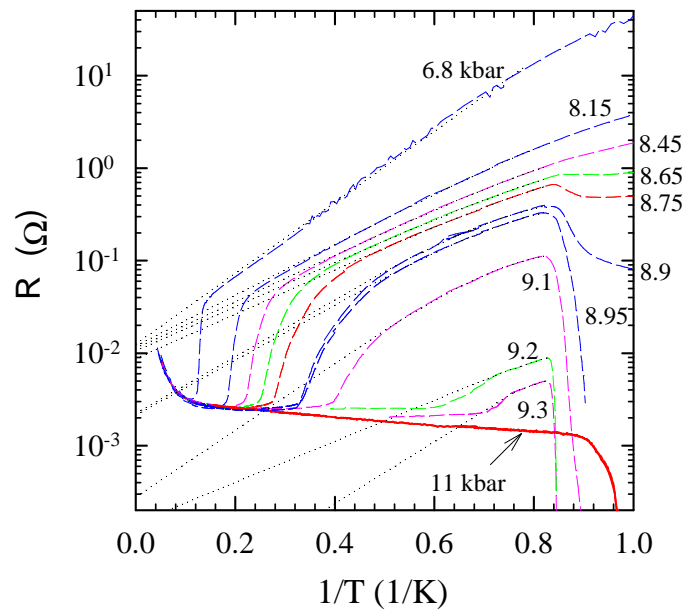


Fig. 4.3: The logarithm of resistance *vs.* inverse temperature for a given range of pressures, depicts behaviour in the SDW phase. Fits to the corrected Arrhenius law (dotted straight lines, Eq. 4.3) give the same asymptotic resistances  $R_\infty$ , for the curves inside pure SDW region. Inside the SDW/M region asymptotic resistances decrease by several orders of magnitude.

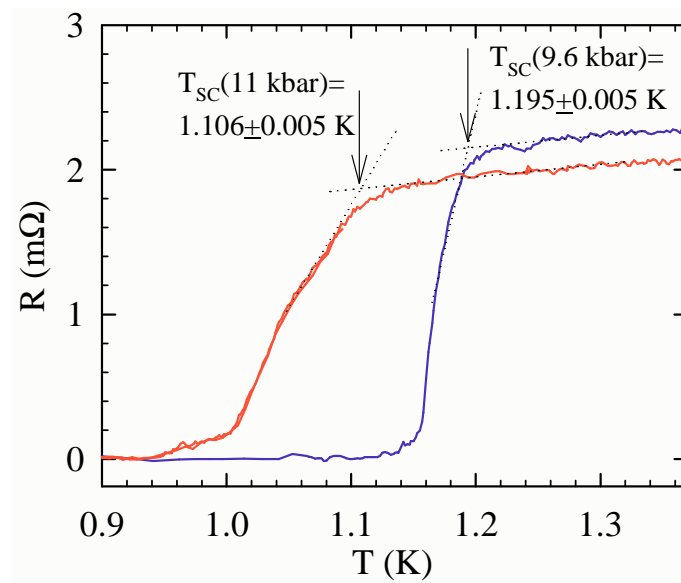


Fig. 4.4: Resistance *vs.* temperature for two pressures, where a direct transition from metallic to superconducting state has been observed.  $T_{SC}$  was defined as the onset of the resistance drop, the exact temperature being located where the dotted extrapolation lines cross (arrows). No hysteresis has been observed.

regions are denoted SDW/Metal and SDW/SC, respectively. Taking the advantage of good pressure control, we managed to investigate eight pressure points with the same sample in this narrow pressure range. They were measured in two groups of five and three consecutive runs (see Table 4.1). The second group was measured after a large pressure decrease. This decrease was precisely targeted to reproduce a point (8.65 kbar) in the lower end of the pressure range of interest. This provided a check for our capability of accurately controlling the pressure, but also an opportunity to investigate in more detail this pressure range in the usual manner by small pressure increments. As already noted, 8.65 kbar runs #10 and #17 gave almost identical  $R$  vs.  $T$  curves except for the residual resistance offset.

#### 8.6 < $p$ < 9.43 kbar, $T_{SC} \lesssim T \lesssim T_{SDW}$ : SDW/Metal

As shown in Fig. 4.5, a strong hysteretic behaviour is observed, in this pressure and temperature range, between cooling and warming resistance curves, suggesting an inhomogeneous electronic structure. This could be due to phase segregation, with the existence of metallic domains (Metal), in SDW background of strongly temperature dependent characteristics (size and relative disposition). This phase segregation region is denoted SDW/Metal, or SDW/M.

The extremal hysteretic resistance loop is recorded when the temperature sweep starts above  $T_{SDW}$ , reverses below  $T_{SC}$  and ends above  $T_{SDW}$  again. Different hysteretic loops appear when the temperature sweep is reversed between  $T_{SC}$  and  $T_{SDW}$  (see Fig.4.5a for a representative situation at 9.1 kbar).  $T_{SC}$  values determined from either cooling or warming curves are equal (Fig. 4.5b), within a few mK, as for the direct metal-to-SC transitions described above. It is quite interesting to note that a highly similar hysteretic behaviour of the thermopower was observed in the CDW state of (NbSe<sub>4</sub>)<sub>10</sub>I<sub>3</sub> [146].

#### 8.6 < $p$ < 9.43 kbar, $T \lesssim T_{SC}$ : SDW/SC

In the pressure range, where SDW transitions are still well defined,  $R$  vs.  $T$  curves are characterised by a sharp resistance drop at  $T = 1.2 \pm 0.01$  K. We start with a reasonable assumption that this feature is a manifestation of condensation of free-electron (M) domains into superconducting (SC) domains (while SDW domains remain unaltered). The SC domains could either percolate, and form large domains or, they could link, thanks to sufficiently narrow weak-links allowing for Josephson effect between them. Both mechanisms lead to zero resistance state. The following considerations will confirm

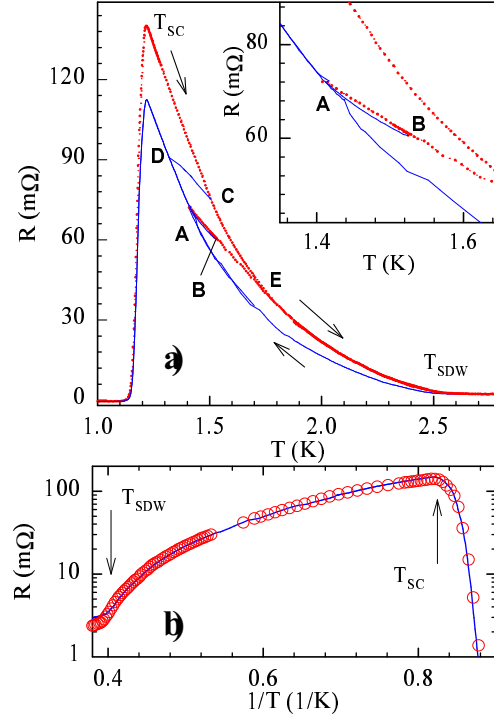


Fig. 4.5: a) Resistance *vs.* temperature at 9.1 kbar, inside the coexistence range. Solid and dotted lines denote cooling and warming, respectively. The extremal hysteretic loop is recorded when the temperature sweep starts from above  $T_{SDW}$ , then cooling continues through points A, D, through  $T_{SC}$ , and into superconducting state. Below, at least 1 K, the sweep may be reversed and warming proceeds through  $T_{SC}$ , C, E and back above  $T_{SDW}$  into the SDW phase. Different hysteretic loops appear when the temperature sweep is reversed between  $T_{SC}$  and  $T_{SDW}$ . Loop 1: cooled from above  $T_{SDW}$  to **A**, reversed, warmed to **E** and further to above  $T_{SDW}$ . Loop 2: warmed from below  $T_{SC}$  to **C**, reversed, cooled to **D** and further to below  $T_{SC}$ . Loop 3: cooled from above  $T_{SDW}$  to **A**, reversed, warmed to **B**, reversed, warmed to **A** and further to below  $T_{SC}$ . Inset: The position of point **B** is shown. b) Extremal curves  $\log R$  *vs.*  $1/T$  plot in cooling (solid line) and in warming (open points). The warming curve is rescaled by a factor defined by the ratio of peak resistance values from the upper panel. This rescaled warming curve coincides perfectly with the cooling one.

our starting assumption.

Initially, at  $p = 8.65$  kbar, the resistance drops to about 30% of the resistance which would be observed if an Arrhenius behaviour of the SDW state was extended below 1.2 K, Fig. 4.3. This drop occurs only if small (1 to 10  $\mu\text{A}$ ) measuring currents are used. For higher currents (100  $\mu\text{A}$ ), the resistance drop disappears and the usual Arrhenius behaviour is recovered. Then at 8.9 kbar, for the lowest currents, the resistance drops to zero (below our measurable limit of 0.001  $\text{m}\Omega$ ). At 8.9 kbar the resistance drop is suppressed concomitantly with the increase of current as shown in Fig. 4.6. Still, for the current of 1 mA, the resistance drop is far from being completely suppressed (it was not possible to use higher current in order to avoid the Joule heating of the sample, see Section 3.1). Generally, the detection of zero resistance at the lowest pressures inside the SDW/SC region requires the lowest measuring current and/or lowest possible temperatures.

As pressure is further increased to 9.1–9.3 kbar, a sharp drop of resistance to zero within 30–40 mK below the onset temperature is obtained regardless the weak amplitude of the current. In this pressure range, we used the pulse technique to determine the critical current,  $I_c$  without heating effects: at 9.1 kbar,  $I_c = 7$  mA, while at 9.3 kbar,  $I_c$  increased up to 30–40 mA as shown in Fig. 4.7. At 11 kbar, the critical current is of the same order of magnitude.

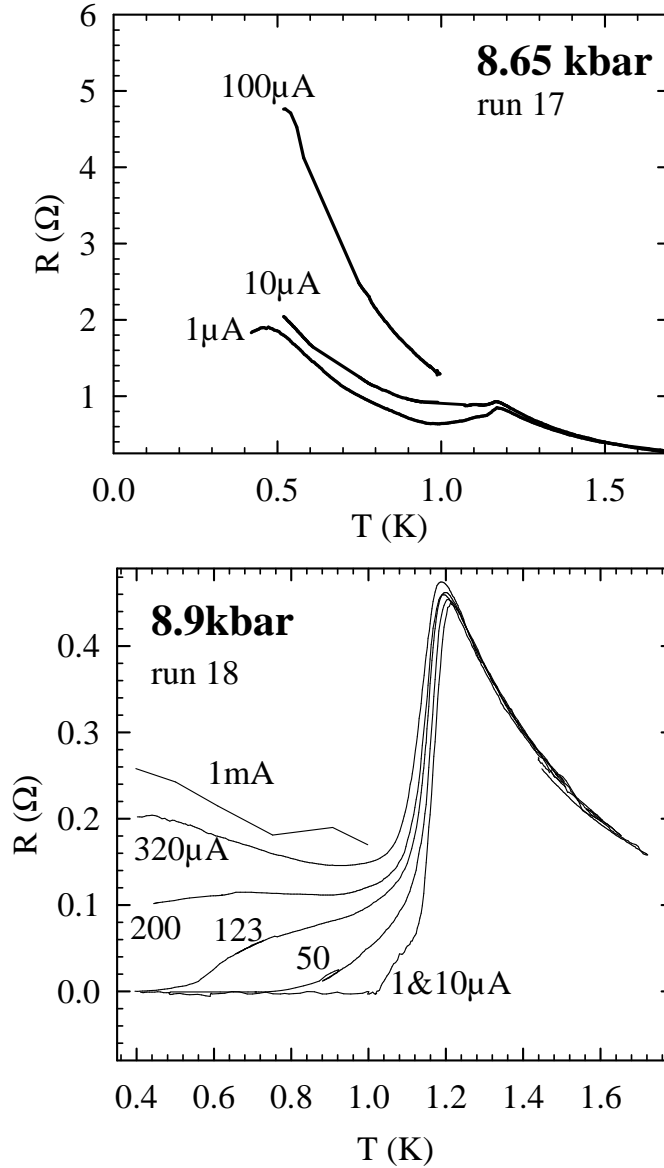


Fig. 4.6: Resistance dependence on the measurement current at 8.65 and 8.9 kbar. At 8.65 kbar, zero resistance is not observed even for the lowest currents. For high currents, the insulating behavior is fully recovered. At 8.9 kbar, zero resistance is reached for currents as high as  $123\mu\text{A}$  and it was not possible to suppress the resistance drop completely even with a 1 mA measurement current.

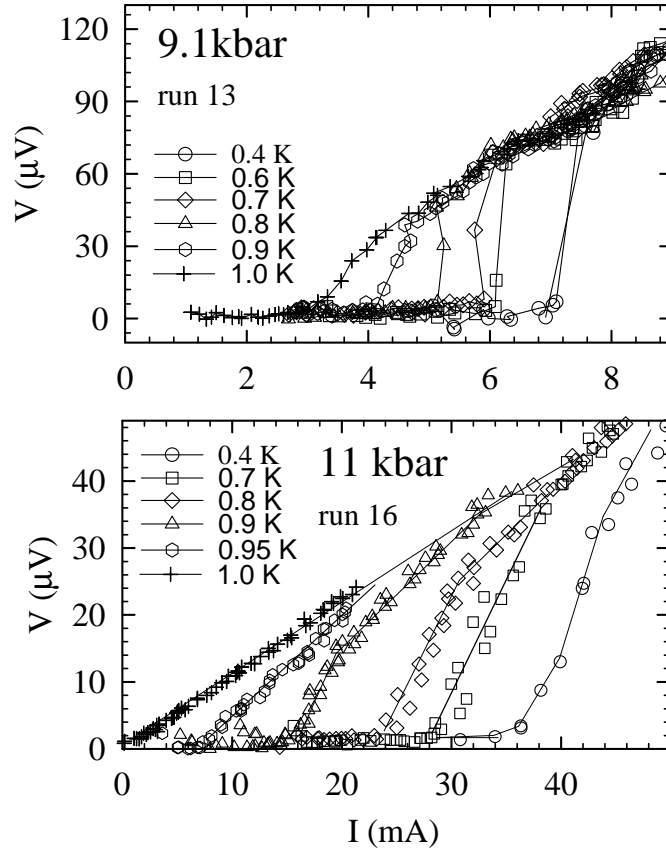


Fig. 4.7: Voltage-current,  $V$ - $I$  characteristics of the sample at various pressures. (a) At 9.1 kbar, at the lowest temperature of 0.4 K, the critical current ( $I_c = 7$  mA) is order(s) of magnitude higher than at only 0.2 kbar lower pressure. (b) At 11 kbar, the SC state is considered to be homogeneous and  $I_c$  reaches the maximum value of 35 mA.

### 4.1.5 Detailed $p, T$ phase diagram of (TMTSF)<sub>2</sub>PF<sub>6</sub>

An accurate determination of both transition temperature and pressure enables us to provide a precise  $T_{\text{SDW}}$  vs. pressure line, up to the critical point ( $p_c=9.43$  kbar, 1.2 K) where the suppression of SDW instability occurs and SC phase is fully established. That is, for all runs below  $p_c$ , we have observed well defined and narrow metal-to-SDW transitions. For pressures close to the critical point, the transitions are becoming broader as reported in [12] and [47]. The authors claimed that the transition broadening is prohibitive for an accurate study of the  $T_{\text{SDW}}$  vs. pressure phase boundary at pressures close to  $p_c$ . However, thanks to the good quality of our sample (RRR=1000, while RRR=10 in [12]), broadening was much lower, and this effect did not prevent the determination of transition temperatures even at pressures close to the critical point. This is a salient result of this work.

Our data combined with the study of Biškup *et al.* which have determined normal state-to-SDW transition temperatures in the range 1 bar to 7.5 kbar, allow to present a  $p, T$  phase diagram of (TMTSF)<sub>2</sub>PF<sub>6</sub> displayed in Fig. 4.8. The empirical formula, which takes into account the fact that  $p_c$  is found at  $T_{\text{SC}} = 1.2$  K, and not at  $T = 0$  K reads

$$T_{\text{SDW}}(p) = T_1 - [(T_1 - T_{\text{SC}}) * (p/p_c)^3] \quad (4.1)$$

Here,  $T_{\text{SC}}$  is the experimental value whereas  $T_1 = T_{\text{SDW}}(1\text{bar})$  and  $p_c$  are free parameters. Fits to Eq. 4.1 give best parameter values  $T_1 = 12.0 \pm 0.15$  K and  $p_c = 9.43 \pm 0.04$  kbar.  $T_1$  and  $p_c$  values correspond excellently to the experimental ones despite the fact that they were obtained as the only free parameters in the fit. It is also interesting to note that  $T_{\text{SDW}}$  pressure dependence seems to be a pure cubic one.

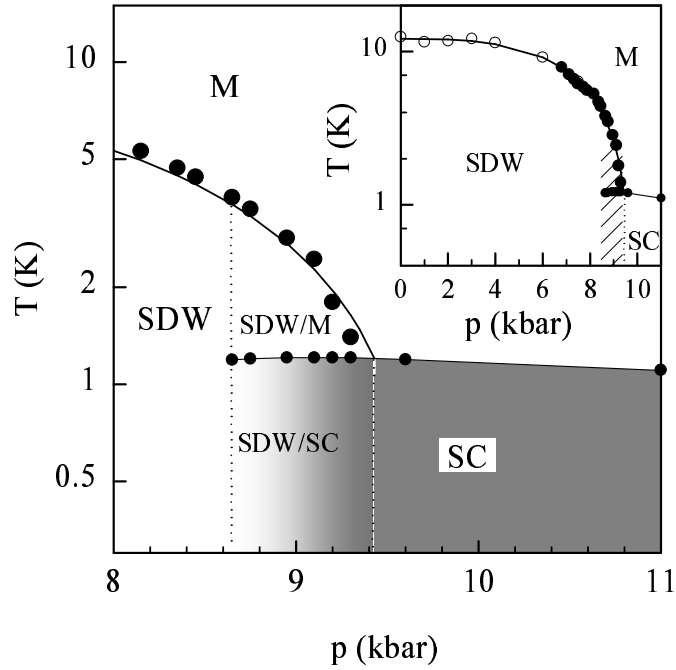


Fig. 4.8: High pressure–low temperature phase diagram of (TMTSF)<sub>2</sub>PF<sub>6</sub> material. SDW/M denotes the region where metallic, M, and SDW phases coexist inhomogeneously, below  $T_{\text{SDW}}$  line (large full points). Below  $T_{\text{SC}} = 1.20 \pm 0.01$  K line (small full points), this coexistence switches into the coexistence of SC and SDW phases. A gradient in shading (SDW/SC region) below  $T_{\text{SC}}$  denotes the increase in volume proportion of SC phase in the bulk sample. Inset: Our diagram is completed with data taken from Biškup *et al.* (open points). Solid curve is the fit to our empirical formula for  $T_{\text{SDW}}$  vs.  $p$  dependence (Eq. 4.1).

## 4.2 Quantification of domain fraction in co-existence region

There are several features in our experimental data substantiating the coexistence of phases, SDW/M above 1.2 K and SDW/SC below 1.2 K. Hysteresis presented in Fig. 4.5 is the primary, still only qualitative one. The other two features, besides evidencing for the coexistence, lead us to the possibility of quantification of the phases volume fraction in the bulk. Indeed, we consider the orders of magnitude change in the critical current, as presented in Figs. 4.6 and 4.7 directly proportional to the change in the effective cross-section taken up by superconducting domains for SDW/SC coexistence region. For the SDW/M region we intend to show that the change in the effective cross-section taken up by metallic domains may be incurred from the orders of magnitude change in resistance of the sample for pressures inside the 8.65 – 9.43 kbar region.

In the following, we assume that the sample in the inhomogeneous region behaves as a composite of two materials. We consider these two materials to have the properties of the sample at 11 kbar (pure SC ground state) and 6.8 kbar (pure SDW ground state) respectively.

### $T < T_{SC}$ : Quantification of SDW/SC domain fraction

At 11 kbar, the pressure is sufficiently far above the critical pressure to have a fully homogeneous state, metallic or SC, depending on temperature. It is emphasized by the measurements of the critical current from 0.4 to 1.0 K (Fig. 4.7b). That is, one may divide  $U/I$  for the highest currents, which completely suppress SC state, as to recover a resistance comparable to those measured above  $T_{SC}$  at the same pressure (values of order of  $m\Omega$ ). Obviously, high currents take the sample from purely superconducting state to a purely metallic state. We hereby conclude that superconductivity is here homogeneous through the whole cross-section of the sample with the critical current density of  $J_c = 200 \text{ A/cm}^2$ . Since  $T_{SC}$  is nearly constant in the whole pressure range of the inhomogeneous region, so should be the critical current density.

In the inhomogeneous region, we can model the sample as alternating SDW channels and superconducting channels. For simplification purposes only, the channels are assumed to extend longitudinally from one end of the sample to the other. A change of pressure is equivalent to a change of cross-section,  $c$ , of the SC channels and of the SDW channels,  $1 - c$ . We use crude approximation that  $c$  is temperature independent. In the inhomogeneous region, in the absence of weak links along the superconducting channels, the

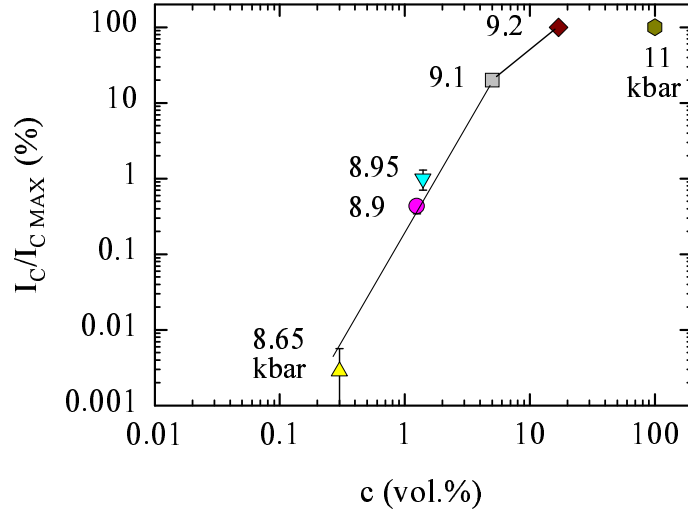


Fig. 4.9: Correlation between the critical current  $I_c$  at 0.4 K, in SDW/SC region and volume fraction  $c$  (vol.%) of metallic phase in the bulk sample, in the range  $T_{SC} < T < T_{SDW}$  in the SDW/M region. Values of  $I_c$  and  $c$  are given in Table 4.1.

SC fraction  $c$  of the sample cross-section is given by the respective  $I_c$  value divided by  $I_{cMAX} = 35$  mA measured at 11 kbar, in the pure SC state. Accordingly, at pressures in the inhomogeneous region, the critical current is lowered, *e.g.* at 9.1 kbar,  $I_c = 7$  mA (Fig. 4.7a). The respective values for different pressures are given in the Table 4.1.

The resistance recovered for currents above the critical value at 9.1 kbar is only 12 m $\Omega$ , *i.e.* about 25 times smaller than the resistance of sample just above  $T_{SC}$  at this same pressure (see Fig. 4.3). This feature can be ascribed to an electric field overcoming the field required for the depinning of SDW, which coexists with the restored metallic phase. Actually, we calculate the electric field to be of the order of 20 mV/cm at the measuring current of 7 mA ( $T = 1$  K) using the data for the 9.1 kbar pressure run. This electric field is about four times the value of the depinning field measured in (TMTSF)<sub>2</sub>PF<sub>6</sub> [27] or (TMTSF)<sub>2</sub>AsF<sub>6</sub>, [26] at ambient pressure. The conductivity at high currents is therefore the sum of sliding SDW conductivity (which still depends weakly on current) and the conductivity of *decondensated* free electrons in metallic domains.

**$T_{SC} < T < T_{SDW}$ : Quantification of SDW/M domain fraction**

The principle of additive conductivities leads us to another procedure, for quantification of the SDW/M domain fraction. We come back to the resistance curves and extract the metallic fraction,  $c$ , and SDW fraction,  $1 - c$ , from the resistance data in the  $T_{SC} < T < T_{SDW}$  temperature range. As for SDW/SC region, we model the sample as alternating insulating (SDW) channels and free electrons channels. The channels are, again, assumed to extend longitudinally from one end of the sample to the other. Thus, the fraction parameter  $c$  is related to effective cross-sections. Using this "rigid model", the Arrhenius law conductivity can be corrected as:

$$\sigma(T) = c\sigma_m + (1 - c)\sigma_{SDW} \quad (4.2)$$

In terms of the resistance we get:

$$1/R(T) = c/R_m + (1 - c)/R_{SDW} \quad (4.3)$$

where  $R_m$  is the resistance of a 100% metallic sample and  $R_{SDW} = R_\infty \exp(\Delta_{SDW}/T)$ . Fitting the experimental resistance data to Eq. 4.3 gave quite good fits as presented in Fig. 4.3 with the series of dotted lines. The fit parameters  $c$ ,  $\Delta_{SDW}$  and  $R_\infty$  are given in the Table 4.1. The observed decrease of  $R_\infty$  with pressure is a clear demonstration of increase of the metallic fraction of the sample. The observed evolution of  $\Delta_{SDW}$  with pressure is less clear. In pure SDW region it decreases with pressure, scaled with the transition temperature. Indeed  $2\Delta_{SDW} = 2.4T_{SDW}$ , although the BCS factor would be 3.52. Further, in the inhomogeneous SDW region, while  $T_{SDW}$  falls off,  $\Delta_{SDW}$  assumes more or less constant value. We attribute such a result to a rather large error in the fitting procedure since available data were from a very narrow temperature range,  $T_{SC} < T < T_{SDW}$ .

**Correlation of two quantification procedures**

Our study shows that the coexistence region extends over the 8.65 kbar–9.43 kbar range ( $\Delta p = 0.78$  kbar). Fig. 4.9 shows the correlation between two independent quantifications of non-SDW fraction  $c$ . These were obtained either by critical current measurements at 0.4 K, in SDW/SC region (y-axis,  $I_{cMAX} = 35$  mA), or by resistance measurements (x-axis,  $c$  from the corrected Arrhenius law) in  $T_{SC} < T < T_{SDW}$  range, in SDW/M region. The sample was modelled as alternating SDW channels and M or SC channels extending longitudinally from one end of the sample to the other. If this model was valid, a proportionality between the two independent quantifications of the non-SDW fraction would have been observed in the complete 8.65 kbar–9.43

kbar coexistence range. Since it was not the case, we suggested a plausible existence of two regions. In the higher inhomogeneous region (9.1–9.43 kbar), proportionality between two quantifications occurs. Here indeed, as modelled, SC domains extend from one end of the sample to the other and the critical current is proportional to volume fraction. In the lower inhomogeneous region (8.65–9.1 kbar), the Josephson junctions (or phase slip centers [147]) are present along the conducting channels in SDW/SC region. Therefore, the critical current is lowered disproportionately to volume fraction of the domains.

### 4.3 Phase segregation scenario

It is the experimental data which have imposed the search of an approach based on variational theory leading to an inhomogeneous phase with energy lower than that of homogenous states. In the following, we present the model developed by M. H eritier from Laboratoire de Physique des Solides, Orsay, France, [135]. He proposed a discussion of experimental data in the framework of the Fermi liquid picture, which is expected to be valid in this low temperature part of the phase diagram. The relative stabilities of different phases have to be studied: the metal, spin density wave and superconducting phase, but also all the possible regions where coexist either a SDW phase and a metallic phase, or, at lower temperature, a SDW phase and a superconducting one.

Our experimental data reveal (Section 4.1) the coexistence of two different phases, either SDW/Metal or SDW/SC, depending on the temperature. Presumably, this coexistence corresponds to a segregation in direct space and not in the reciprocal space. It is quite plausible that such a segregation is not produced on a microscopic scale ( $l \ll \xi$ , where  $\xi$  is the correlation length) or a mesoscopic scale ( $l \sim \xi$ ), but rather on a macroscopic scale ( $l \gg \xi$ ). The latter is much more favorable regarding the carrier localisation energy necessary to spatially confine the electrons, but also to interface energy necessary to create domain walls between different orders.

M. H eritier gives very simple and general arguments proving that, near enough to the critical line for the formation of an homogeneous SDW phase, a *spatially heterogeneous* phase has a lower free energy than the *homogeneous* SDW phase. The origin of such a phenomenon is due to the following essential physical features :

- The relevant quantity on which depends SDW order stability is  $t'_b$ . Applying a pressure increases  $t'_b$  and, therefore, SDW free energy  $F_m(t'_b)$ , up to a critical value  $t'^{**}_b$  at which homogeneous SDW phase disappears.

- The SDW stability decreases very strongly near  $t'_b{}^{**}$ . The slope of critical line is very large.
- The relevant quantity to stabilize the SDW phase near  $t'_b{}^*$  is  $b$ , the unit cell parameter along the  $y$ -direction. Indeed, increasing  $b$  strongly decreases  $t'_b$ , and, therefore, strongly lowers  $F_m(t'_b)$ .
- It is always favorable to create a heterogeneous phase : one part, the volume of which is  $(1-c)\Omega$ , has a cell parameter  $b + \delta b_1$  and is magnetic, with a lower magnetic free energy because of the higher  $b$  parameter ; the other part, the volume of which is  $c\Omega$ , is metallic and has a cell parameter  $b - \delta b_2$ , ( $\Omega$  is the total volume), which imposes  $\delta b_2/\delta b_1 = (1-c)/c$ . The latter relation implies the constant volume assumption which is considered in the present model. The elastic energy cost for such a deformation is, indeed, proportional to  $(\delta b)^2$  and, therefore of second order, while the deformation allows to gain a magnetic free energy proportional to the first order quantity  $\left(\frac{\partial F_m}{\partial t'_b}\right) \left(\frac{\partial t'_b}{\partial b}\right) \delta b$ . The larger the slope  $\left(\frac{\partial F_m}{\partial t'_b}\right)$ , the larger is free energy lowering.

The physical picture is as follows: at the homogeneous critical line the metallic and SDW phases are in equilibrium,  $c=1-c=1/2$ , Figs. 4.10, 4.11. For a pressure lower than the critical one, *i.e.*  $t'_b < t'_b{}^{**}$ , total free energy is lowered by the formation of macroscopic domains of metallic and of SDW character, respectively. For simplicity these domains are assumed to extend longitudinally from one end of the sample to the other. The metallic ones have a lower  $b$  parameter, and the SDW ones have a larger  $b$ . Elastic energy cost is

$$\begin{aligned} \Delta E_{elastic} &= (1-c)K(\delta b_1)^2 + cK(\delta b_2)^2 \\ &= \frac{1-c}{c}K(\delta b_1)^2 \end{aligned} \quad (4.4)$$

where  $K$  is an elastic constant. The magnetic free energy lowering, compared to the homogeneous phase free energy, is given by

$$\Delta F_m = (1-c) \left(\frac{\partial F_m}{\partial t'_b}\right) \left(\frac{\partial t'_b}{\partial b}\right) \delta b_1 - cF_m(t'_b) \quad (4.5)$$

This linear approximation is quite satisfactory because the derivative is quite large. By minimizing the total free energy  $\Delta F_{total} = \Delta E_{elastic} + \Delta F_m$  with respect to  $\delta b_1$  and  $c$ , we find that the stable phase is *heterogeneous*, with a

fraction  $c$  of metallic phase forming macroscopic metallic domains parallel to the  $a$ -axis:

$$c = \frac{1}{2} - \frac{2K \operatorname{sgn}(t'_b - t'^*_b) |F_m(t'_b)|}{\left(\frac{\partial F_m}{\partial t'_b}\right)^2 \left(\frac{\partial t'_b}{\partial b}\right)^2} \quad (4.6)$$

The free energy of the heterogeneous phase is given by

$$\Delta F_{total} = -\frac{1}{4} \frac{\left[ \frac{1}{4K} \left(\frac{\partial F_m}{\partial t'_b}\right)^2 \left(\frac{\partial t'_b}{\partial b}\right)^2 - F_m(t'_b) \right]^2}{\frac{1}{4K} \left(\frac{\partial F_m}{\partial t'_b}\right)^2 \left(\frac{\partial t'_b}{\partial b}\right)^2} < 0 \quad (4.7)$$

The fraction of metallic phase decreases as  $t'_b$ , *i.e.* as the applied pressure decreases and vanishes when:

$$\left| F_m(t'_b = t'_{b1}) \right| = \frac{1}{4K} \left(\frac{\partial F_m}{\partial t'_b}\right)^2 \left(\frac{\partial t'_b}{\partial b}\right)^2 \quad (4.8)$$

Here  $t'_{b1}$  is defined, Fig. 4.10, *i.e.* as the lower critical pressure for the formation of heterogeneous phase. For  $t'_b < t'_{b1}$ , the stable phase is a homogeneous SDW phase, Fig. 4.11.

In a symmetrical way, for a pressure higher than the critical pressure, *i.e.*  $t'_b > t'^{**}_b$ , total free energy is also lowered by the formation of described metallic and SDW domains. An expression quite similar to the case  $t'_b < t'^{**}_b$  can be obtained. Again, it is found that  $c = 1/2$  on the “homogeneous critical line” and increases with  $t'_b$ , *i.e.* with the applied pressure and goes to 1 when :

$$F_m(t'_b = t'_{b2}) = \frac{1}{4K} \left(\frac{\partial F_m}{\partial t'_b}\right)^2 \left(\frac{\partial t'_b}{\partial b}\right)^2 \quad (4.9)$$

which defines  $t'_{b2}$ , the upper critical pressure for the formation of an heterogeneous phase. For  $t'_b > t'_{b2}$ , the stable phase is an homogeneous metal.

In Fig. 4.10, it is schematically displayed the pressure dependence of magnetic condensation energy and the extent of the stability for the spatially inhomogenous phase. The energy of inhomogenous phase (continuous line) is lower than that of unstable homogenous phase (dashed line).

It should be stressed that the energy necessary to form domain walls between the metallic and magnetic domains was not taken into account. The energy necessary to localize the carriers within a domain was also not taken into account. Since the domains are believed to be macroscopic, the corresponding corrections should be quite small.

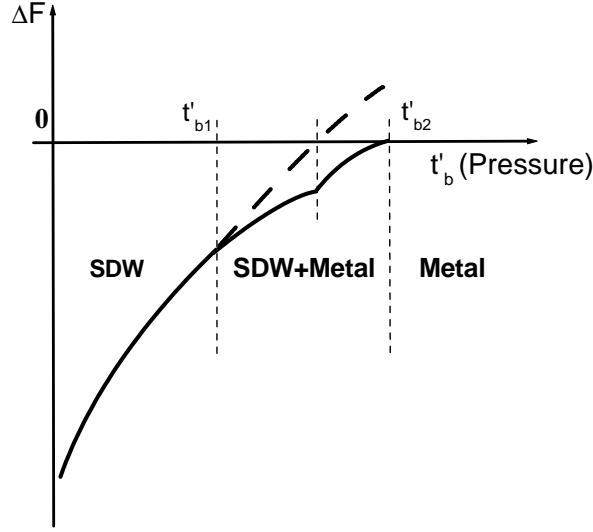


Fig. 4.10: Schematic behaviour of the free energy *vs.* nesting deviation parameter  $t'_b$  (x-axis). This parameter (being a measure of deviation from ideal nesting) corresponds well to the applied pressure.

Clearly, at lower temperatures, the macroscopic metallic domains should undergo a transition to a superconducting order, since the phase diagram exhibits a competition between magnetic and superconducting orders. Therefore, the formation of heterogeneous phase, with coexisting SDW and superconducting domains has to be investigated. Similar calculations can be done by including the superconducting phase free energy,  $F_s$ , assumed to be independent of  $t'_b$ . Such an approximation is certainly valid in the narrow pressure range considered here. No assumption will be made, neither on the physical mechanism inducing superconductivity, nor on symmetry of order parameter. It shall only be supposed that  $F_s$  is given by the usual mean field expression. As above, the total free energy is found to be lowered by the formation of heterogeneous phase, on both sides of the “homogeneous critical line”, with a volume  $c$  of superconducting domains and a volume  $(1 - c)$  of SDW domains.  $c$  vanishes for  $t'_b \leq t'_{b3}$ , where the lower critical value  $t'_{b3}$  is given by :

$$-F_m(t'_{b3}) = \frac{1}{4K} \left( \frac{\partial F_m}{\partial t'_b} \right)^2 \left( \frac{\partial t'_b}{\partial b} \right)^2 - F_s \quad (4.10)$$

Since  $F_s < 0$ , the coexistence region gets broader when the superconducting order grows as  $T \rightarrow 0$ . In the same way, in the superconducting region of the homogeneous phase diagram, the total free energy is lowered by the formation

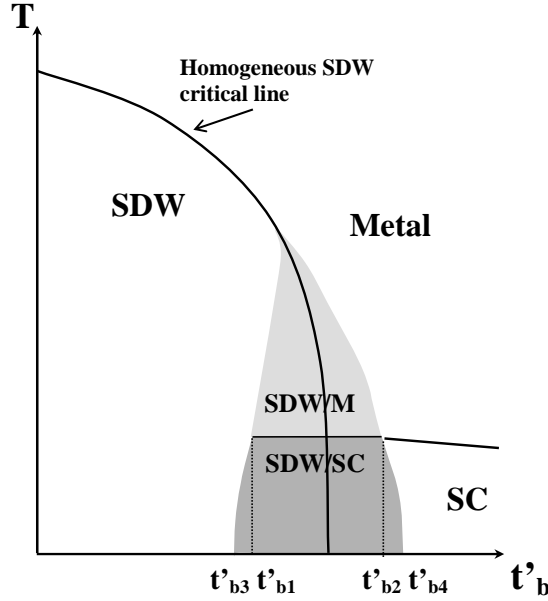


Fig. 4.11: Schematic phase diagram showing the inhomogeneous SDW/M and SDW/SC phases in the vicinity of critical border. The nesting deviation parameter  $t'_b$  corresponds well to applied pressure (x-axis).  $T$  stands for temperature.

of a fraction  $(1 - c)$  of SDW domains. On the “homogeneous critical line”,  $c = 1/2$  and increases when  $t'_b$  increases, up to an upper critical value  $t'_{b4}$ , given by ;

$$F_m(t'_{b4}) = \frac{1}{4K} \left( \frac{\partial F_m}{\partial t'_b} \right)^2 \left( \frac{\partial t'_b}{\partial b} \right)^2 + F_s \quad (4.11)$$

In order to explicitly calculate the critical lines, it is necessary to evaluate magnetic free energy  $F_m(t'_b)$ , together with the standard mean field expression for  $F_s$ . In principle [148], this allows a complete determination of critical lines  $c = 0$  and  $c = 1$ , which limit the stability of heterogeneous phase in the  $(T, t'_b)$  plane, or the  $(T, p)$  plane, correspondingly. A schematic illustration of the theoretical phase diagram is displayed in Fig. 4.11.

It should be emphasized that, within this model, pressure variation of the superconducting critical temperature  $T_c$  in the heterogeneous phase is not expected, exactly as we experimentally observed, Fig. 4.8. Nevertheless, it is expected that superconducting ordering increases the width,  $t'_{b4} > t'_{b2}$  and  $t'_{b3} < t'_{b1}$ , of the pressure range in which the heterogeneous phase is stable, because it lowers the total free energy, Fig. 4.11.

The maximum width of the stability region of heterogeneous phase is

obtained at zero temperature. We consider the following numerical values of the parameters entering the model :  $t'_b = 10K$ , see Sec. 1.1.4, [149][150];  $\frac{\partial t'_b}{\partial p} = 1K/\text{kbar}$ , [22][151], compare with Sec. 3.1;  $\frac{1}{b} \frac{\partial b}{\partial p} = 3 \cdot 10^{-3} \text{ kbar}^{-1}$ [152]. These values can be taken as typical. M. Héritier's model predicts a pressure range of stability of the heterogeneous phase of the order of 1 kbar. The agreement with our experiment (inhomogeneous region width, 0.8 kbar, Sec. 4.1.4) can be regarded as extremely good, if we consider the crudeness of the analysis.

#### 4.4 Discussion: DW and SC coexist in Bechgaard-Fabre salts (TM)<sub>2</sub>X

This new visit to the  $p, T$  phase diagram of (TMTSF)<sub>2</sub>PF<sub>6</sub> provides a better understanding of the boundary region between SDW and SC ground states. The experimental results suggest that a picture of coexisting SDW and SC macroscopic domains prevails in a narrow pressure domain of  $\approx 0.8$  kbar below critical pressure marking the establishment of an homogeneous SC ground state. In spite of a volume fraction of a SC phase strongly depressed at decreasing pressure in the coexistence regime we could not detect any significant change in  $T_{SC}$ . The early claim for the absence of SDW/SC coexistence in the vicinity of the critical pressure [46] based on the observation of an EPR response typical for the superconducting instability, can now be understood by the impossibility of the EPR technique to observe the very broad signal coming from the SDW domains.

M. Héritier developed a very simple model which, on the basis of quite general arguments, predicts the formation of a heterogeneous phase, in which coexist metallic and magnetic domains and, at lower temperatures, magnetic and superconducting domains. This result provides quite a plausible interpretation of data reported here. Obviously, the same kind of arguments might apply to other competing instabilities. What M. Héritier proposed is a variational theory saying that it is possible to find an inhomogeneous phase with free energy lower than the energy of homogenous phases (SDW or metal). As a variational constraint, constant total volume of the sample is taken. However, free energy lowering is not due to constraint. If the constraint is relaxed, the free energy of inhomogeneous state could still decrease and become even more stable than that of the homogenous state. However, in such a case, the model should rely very much on the detailed pressure dependence of the SDW condensation energy versus pressure.

It is important to point out that the coexistence region in the vicinity of SDW/SC boundary, reported here, is a feature of the respective region of

the generalized phase diagram of Bechgaard-Fabre salts, TM<sub>2</sub>X, and not just a particularity of (TMTSF)<sub>2</sub>PF<sub>6</sub> material. Recently, this phenomenon has been reported to arise in other members of this materials family. Only the applied pressures were larger, as to position the material in the proper region of generalized phase diagram. In the recently discovered superconductor of the TM<sub>2</sub>X family, (TMTTF)<sub>2</sub>PF<sub>6</sub>, the reentrance to SC was observed, under very high pressures 4.73 -5.26 GPa, below a metal-to-SDW transition, [7]. However, the extreme pressure conditions made a detailed study impossible. When a compound, (TMTTF)<sub>2</sub>BF<sub>4</sub>, with a smaller anion was chosen, the SDW-SC phase segregation was observed in the pressure range 33.5-37.5 kbar, Fig. 4.12, [153]. As in our study, the inhomogeneous coexistence has been established from critical current measurements. (TMTTF)<sub>2</sub>BF<sub>4</sub> results are in perfect correspondence with ours on (TMTSF)<sub>2</sub>PF<sub>6</sub> (see Fig. 4.3). Additionally, in the (TMTTF)<sub>2</sub>BF<sub>4</sub>, the upper critical field is shown to be large and pressure independent,  $H_{c2} = 2$  T, which certainly indicates the penetration of the field in the insulating regions in a similar way to Josephson vortices in layered superconductors. The observation of a large increase of the upper critical field  $H_{c2}$  is an immediate consequence of the existence of magnetic macroscopic domains in the superconducting phase. This had been reported long time ago by Greene and Engler for (TMTSF)<sub>2</sub>PF<sub>6</sub> [61] and Brusetti *et al.* for (TMTSF)<sub>2</sub>AsF<sub>6</sub> [47].

A similar situation may be encountered with the coexistence of two possible anion orderings, namely (1/2,1/2,1/2) and (0,1/2,1/2), in (TMTSF)<sub>2</sub>ReO<sub>4</sub> under pressure, detected by x-ray diffuse scattering [154]. We may anticipate that the coexistence domain will also be characterised by a segregation between metallic regions (associated to the (0,1/2,1/2) order) and (1/2,1/2,1/2) anion-ordered insulating regions [155]. A coexistence between SDW and SC orders has also been mentioned in this latter compound in the narrow pressure domain  $8 \pm 0.25$  kbar [155].

Finally, Duprat and Bourbonnais [157] have recently performed a calculation of the interference between SDW and SC channels using the formalism of renormalisation group at temperatures below the 1D-to-3D cross-over [158], in the presence of strong deviations to the perfect nesting. This calculation shows the possibility of reentrant superconductivity in the neighbourhood of the critical pressure and can explain the deviations of the  $\Delta/T_{\text{SDW}}$  ratio from the BCS ratio in the vicinity of critical pressure due to the non-uniform character of the SDW gap over the Fermi surface. Similar deviations are also obtained, for the same physical reason, in a simple mean field treatment by Gorkov, [156]. It is likely that merging the results of reference, [157] with the present coexistence model could improve the overall theoretical description.

As this Thesis was being completed, a study directly motivated by our

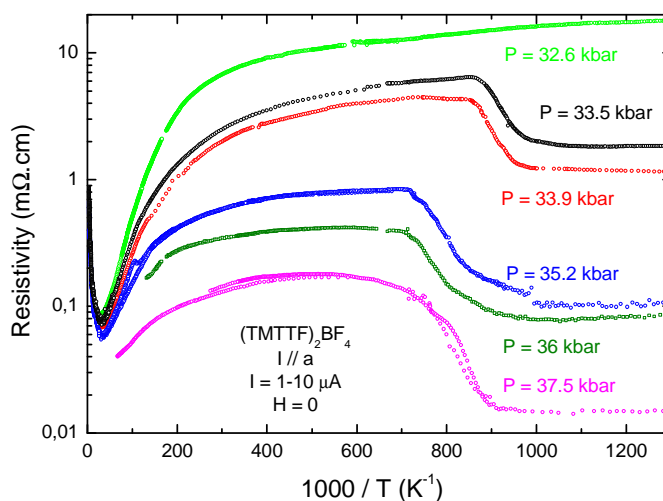


Fig. 4.12: Logarithm of the resistance *vs.* inverse temperature for (TMTTF)<sub>2</sub>BF<sub>4</sub> is shown, for the given range of pressures inside coexistence region. The metal-to-SDW transition, behavior to the corrected Arrhenius law inside the SDW/metal region and a transition to the SC state are depicted. In SC state, zero resistivity is obtained only for the highest pressures, indicating also SDW/SC coexistence. From Ref. [153].

experimental results was published by Podolsky *et al.*, [159]. The authors investigated competition between antiferromagnetism (SDW) and triplet superconductivity in q1D electron systems. They unified the two orders in an SO(4) symmetric framework and demonstrated the existence of such symmetry in one dimensional Luttinger liquids. SO(4) symmetry requires a first order transition between antiferromagnetic and unitary triplet superconducting phases, and a weakly first order transition between antiferromagnetic and normal (metallic) phases near the SO(4) symmetric point. The authors claim that this explains coexistence regions between superconducting and SDW phases, and between SDW and metallic phases, which were observed for (TMTSF)<sub>2</sub>PF<sub>6</sub> and other TM<sub>2</sub>X materials.

# 5 Investigation of phase diagram of $(\text{La, Sr, Ca})_{14}\text{Cu}_{24}\text{O}_{41}$

## 5.1 Evidence for CDW along legs of ladders in $\text{Sr}_{14}\text{Cu}_{24}\text{O}_{41}$

For  $\text{Sr}_{14-x}\text{Ca}_x\text{Cu}_{24}\text{O}_{41}$  materials the total hole count is  $\delta_h = 6$ . Approximately five of these holes are found in the chains subsystem, while approximately one is found to be transferred to the ladders subsystem, at least at higher temperatures. The holes in the ladders appears to be mobile and responsible for the electrical transport in  $\text{Sr}_{14-x}\text{Ca}_x\text{Cu}_{24}\text{O}_{41}$  materials. This initial presentation will address the parent compound of the  $\text{Sr}_{14-x}\text{Ca}_x\text{Cu}_{24}\text{O}_{41}$  family of materials -  $\text{Sr}_{14}\text{Cu}_{24}\text{O}_{41}$ . This is the only material in which there are no Sr/Ca substitutions, so the related disorder is minimal.

### 5.1.1 Correspondence of dc transport and LFDS

In Fig. 5.1 (bottom panel) we present the results of dc resistivity  $\rho_{dc}$  vs. inverse temperature,  $1/T$ , for  $\text{Sr}_{14}\text{Cu}_{24}\text{O}_{41}$ . The measurements were performed along the  $c$ -axis, that is, along the legs of ladders. The temperature range of measurement was from 750 K down to 50 K. We observed single particle electrical transport characterized by quite high RT conductivity of  $500 \Omega^{-1}\text{cm}^{-1}$ , confirming the existence of mobile holes transferred in the ladders. Also, we observed insulator-to-insulator phase transition, determined from a peak in the logarithmic derivative of resistivity. The peak in the derivative is centered at 210 K, characterized by full width at half maximum (FWHM) of 40 K. So, the insulator-to-insulator transition critical temperature is taken to be  $T_c = 210 \pm 20$  K. This transition is quite broad,  $\text{FWHM}/T_c = 20\%$ . It may be compared with  $(\text{TMTSF})_2\text{PF}_6$ , where  $T_{\text{SDW}} = 12 \pm 0.1$  K, and

$\text{FWHM}/T_c = 2\%$ , see Chapter 4 or Ref. [27]. The width of the transition that we observed in  $\text{Sr}_{14}\text{Cu}_{24}\text{O}_{41}$  indicates a certain level of intrinsic disorder in the nominally pure single crystal samples studied here. Both insulator phases, above and below the phase transition, are primarily characterized by well defined, but different, activation energies ( $\rho_{dc} \propto e^{\Delta/k_B T}$ ). In the high temperature (H.T.) phase activation energy  $\Delta_{\text{H.T.}} = 900$  K is lower than  $\Delta_{\text{L.T.}} = 1300$  K in the low temperature (L.T.) phase.

The frequency dependence of conductivity,  $\sigma'(\omega)$ , and the real,  $\varepsilon'(\omega)$ , and imaginary parts,  $\varepsilon''(\omega)$ , of the dielectric function, for a few selected temperatures, are displayed in Fig. 5.2. The radio-frequency relaxation is clearly observed as a peak in the  $\varepsilon''$  spectrum accompanied by a step-like decrease of  $\varepsilon'$ . These spectra can be described in terms of a generalized Debye expression (Sec. 3.2.3). Solid lines in Fig. 5.2 are fits to this formula:

$$\varepsilon'(\omega) + i\varepsilon''(\omega) = \Delta\varepsilon/[1 + (i\omega\tau_0)^{1-\alpha}]. \quad (5.1)$$

As already presented in more detail in Sec. 3.2.3,  $\Delta\varepsilon$  is the strength of the relaxation,  $\tau_0$  is a central relaxation time and  $1 - \alpha$  describes the symmetrical broadening of the relaxation times distribution. Temperature dependences of the relaxation parameters, for  $\text{Sr}_{14}\text{Cu}_{24}\text{O}_{41}$ , obtained from the fits are shown in Fig. 5.1.

As can be seen from Fig. 5.1, a dielectric mode of order of  $\Delta\varepsilon = 10^4$ - $10^5$  appears in the L.T. phase, below 110 K. It was not possible to use complex conductivity technique above 110 K for  $\text{Sr}_{14-x}\text{Ca}_x\text{Cu}_{24}\text{O}_{41}$ ,  $x=0$ , since the dielectric mode left the upper boundary of our experimental frequency window, see Section 3.2.3. An assumed behavior of  $\Delta\varepsilon$  for  $x=0$  is represented by a dashed line, based on that observed for  $x=3$  and 9, see Sec.5.3 and Refs. [160, 161]. That is, on decreasing temperature, a sharp growth of  $\Delta\varepsilon$  starts in the close vicinity of  $T_c$  and reaches the huge value of the order of  $10^4 - 10^5$  at  $T_c = 140$  K and  $T_c = 10$  K for  $x = 3$  and 9, respectively. These  $T_c$  values correspond perfectly to the temperature of the phase transition as determined in the dc resistivity measurements. Therefore, we can conclude that this perfect correspondence, between ac and dc results, is valid for  $x=0$  also, with  $T_c = 210$  K.

The dielectric mode is further characterized by  $1 - \alpha = 0.8$  parameter. That is, the distribution of the relaxation times is broader than Debye (Debye  $1 - \alpha = 1$ ). This distribution narrows towards a Debye one along with the decrease in the mode strength in the temperature range below 70 K. In the bottom panel of Fig. 5.1 both the central relaxation time  $\tau_0$  and the dc resistivity are shown. Again, a strong correspondence between dc and ac results has to be noted in that  $\rho_{dc} \propto \tau_0 \propto e^{\Delta_{\text{L.T.}}/k_B T}$  below  $T_c$ . The energy

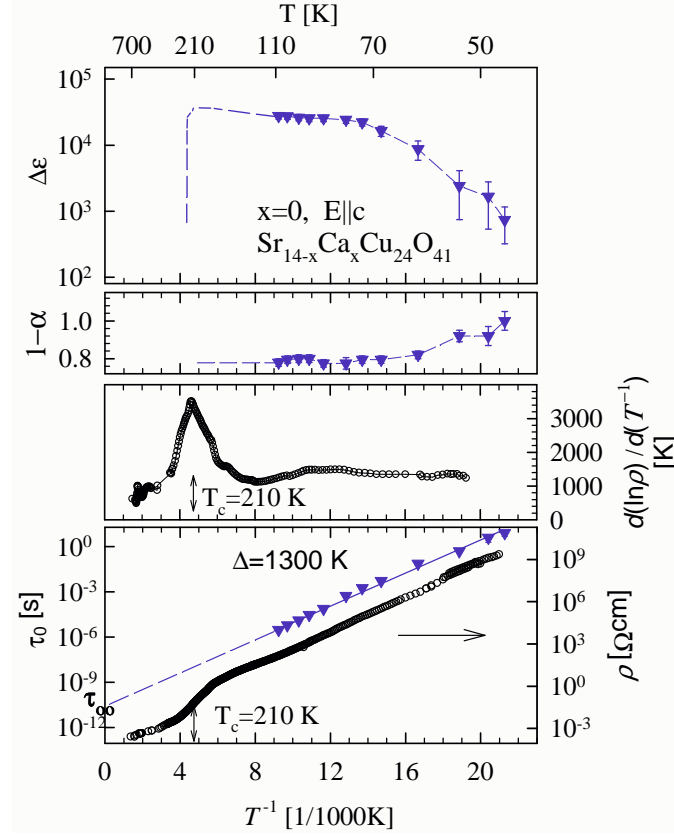


Fig. 5.1: dc and LFDS measurements for  $\text{Sr}_{14}\text{Cu}_{24}\text{O}_{41}$  are performed along the  $c$  axis. Inverse temperature  $1/T$  dependences of the dc resistivity and of the low-frequency dielectric relaxation parameters are shown, Eq. 5.1. Top panel: the strength  $\Delta\varepsilon$  of the dielectric relaxation. Assumed behavior of  $\Delta\varepsilon$  is represented by a dashed line. Second panel from the top: the parameter  $1-\alpha$  which describes the symmetrical broadening of the relaxation times distribution. At temperatures below 70 K, simultaneously with a decrease in  $\Delta\varepsilon$ ,  $1-\alpha$  increases towards 1 – the distribution becomes more Debye-like. Bottom panel: Both the central relaxation time  $\tau_0$  and the dc resistivity are thermally activated  $\rho_{dc} \propto \tau_0 \propto e^{\Delta_{L.T.}/k_B T}$  below  $T_c$  with an activation energy  $\Delta_{L.T.} \approx 1300$  K.  $T_c = 210 \pm 20$  K is determined from a peak in the logarithmic derivative of the resistivity, as presented in the second panel from the bottom. The dashed line in the bottom panel denotes the extrapolation of  $\tau_0$  to a high temperature value, the attempt time,  $\tau_\infty$ .

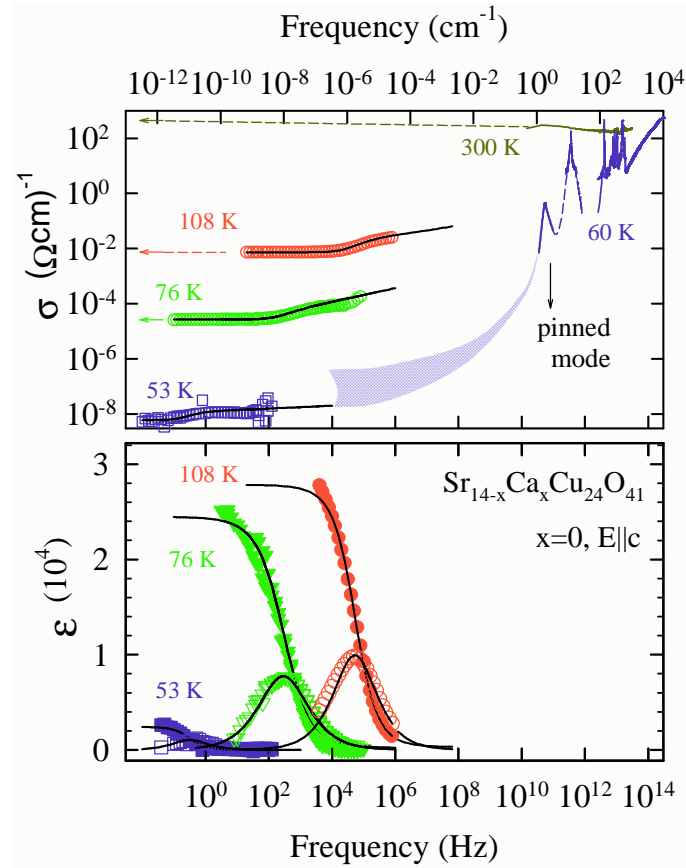


Fig. 5.2: Broad-band spectra for  $\text{Sr}_{14}\text{Cu}_{24}\text{O}_{41}$ , measured along the legs of ladders, *i.e.*  $c$  axis, at a few selected temperatures are shown. Conductivity, the real part -  $\sigma'$ , is shown in the upper panel and complex dielectric function is shown in the lower panel (imaginary  $\epsilon''$  and real  $\epsilon'$  parts, open and closed symbols, respectively). The full lines are from fits to the generalized Debye expression, Eq. 5.1. A mode in microwave range at  $1.8 \text{ cm}^{-1}$ , is detected by Kitano *et al.* [162]. The horizontal arrows on the left denote the dc conductivity. Decrease of the infrared conductivity (data by the Stuttgart group, [78]) at low temperatures corresponds to the opening of energy gap. Some phonon features become visible at the lowest temperatures. Shaded area, as a guide for the eye, connects the two frequency ranges.

gap  $\Delta_{L.T.} \approx 1300$  K has already been stated above. The dashed line in the bottom panel of Fig. 5.1 denotes the extrapolation of  $\tau_0$  to a high temperature value, the attempt time,  $\tau_\infty$ . The attempt time is of the order  $10^{-10}$ - $10^{-11}$  s, much larger than usual quasi-particle relaxation times of  $10^{-15}$  s.

Very large attempt time, along with the enormous strength of the dielectric mode (enormous dielectric constant) corresponds to a collective relaxation mechanism – the charge density wave (CDW) phason response to ac electric fields. The broad mode ( $1 - \alpha = 0.8$ ) indicates that the CDW is pinned in the random background potential. Standard feature of the CDW phason response is also the correspondence of the activation energy for the central relaxation time  $\tau_0$  with the dc resistivity one. Therefore, the low temperature energy gap  $\Delta_{L.T.} \approx 1300$  K is identified as the CDW gap,  $\Delta_{CDW}$  and the transition temperature  $T_c = 210 \pm 20$  K is identified as insulator-to-CDW phase transition temperature  $T_{CDW}$ .

An other feature of the CDW phason response to ac electric fields is the *pinned* mode, see Sec. 2.4. This mode is, in general, expected to appear in microwave/far-infrared range, [126]. We follow the assignment of the conductivity peak observed in the microwave range, at  $1.8 \text{ cm}^{-1}$  (see Fig. 5.2) to the CDW *pinned* mode, proposed by Kitano *et al.* [162, 163]. Also shown in Fig. 5.2 are quasi-optical microwave/FIR range ( $5$ - $10000 \text{ cm}^{-1}$ ) conductivity data for  $x=0$  material, taken from Ref. [78]. FIR range conductivity starts to decrease at temperatures lower than 240 K. This temperature agrees nicely with the CDW phase transition temperature  $T_{CDW} = 210$  K as determined from dc/LFDS. The FIR conductivity starts to decrease, below approximately  $2500 \text{ cm}^{-1}$ . The CDW gap value extracted from dc/LFDS measurements, corresponds well to the edge seen in the FIR conductivity spectra,  $\approx 900 \text{ cm}^{-1}$ .

While the above confirms standard CDW phason response is observed, the decrease in the dielectric mode strength below 70 K, deserves further elaboration. We suggest that this observation indicates a decrease in the effective number of holes condensing in the CDW in the ladders. Presumably, the holes from ladders back-transfer to the chains. This process was already proposed in Sec. 1.2.5, based on the inelastic neutron scattering and X-ray diffraction results for chains. In this manner, a contradiction is removed with the standard CDW phason model where temperature independent dielectric strength is expected.

## 5.1.2 Nonlinear conductivity

### CDW sliding conductivity

A standard feature of the CDW response to dc electric fields is the nonlinear, sliding conductivity, [126]. A very simple, "classical-particle" model, [164], accounts for a variety of experimental findings in standard CDW response both to dc and ac fields. This model assumes that the dynamics of the phase of the order parameter is important. The phase is regarded as a classical variable, and it is regarded to be uniform throughout the system. The phase couples directly to the pinning potential provided by inhomogeneities in the system. The electric-field-dependent conduction is a direct consequence of the depinning and consequential translational motion of the CDW condensate. Within the above classical-particle model, sliding CDW conductivity can not exceed the conductivity of an uncondensed system with an equal number of carriers. Here we note that, in 1954., in his model for superconductivity, Fröhlich envisioned that a condensate, being incommensurate to the lattice should be able to conduct freely if dc electric field is applied.

In a realistic system, the phase of the condensate is not uniform. Pinning potential may be due to commensurability between the CDW modulation and the lattice. Pinning may also be due to randomly distributed impurities or lattice defects. Here we distinguish two cases, weak and strong pinning. In the case of weak pinning, the density wave phase adjusts to impurity fluctuations, but is a constant over the length of Lee-Rice domains, [128] which contain many impurity sites. In the case of strong pinning, local distortions of the condensate are favored, where the phase is fully adjusted to obtain a maximum energy gain. Depinned CDW condensate motion is damped due to the back-flow of the free carriers, see Sec. 2.4. Thus, contribution of condensate sliding to conductivity is limited and related to the applied dc electric field. In the commensurate case, it appears that only  $N = 3$  commensurability is expected to be detected experimentally. For  $N = 2$ , the CDW order parameter becomes real, *i.e.* it has only amplitude, but no phase. Phason response is thus not expected. For  $N \geq 4$ , commensurability pinning is considered to be weaker than the impurity pinning.

dc electric field sufficient for depinning of the CDW is denoted *threshold field*,  $E_T$ .  $E_T$  is related to the energy barrier which has to be overcome for depinning of the condensate  $\mathbb{E}_{barrier} = e\rho_0(2\pi/\mathbf{Q})E_T$ , where  $\rho_0$  is carrier concentration and  $\mathbf{Q}$  is the CDW wave vector.  $\mathbb{E}_{barrier}$  is associated with the pinning potential  $V_0$ .

The threshold field for standard DW materials was observed to decrease with temperature decreasing away from the DW transition, [126]. This tem-

perature dependence for the case of impurity pinning was calculated by Maki, although for SDW, [27], but the arguments are general enough to be valid for CDW also. It was successfully applied to different samples of  $(\text{TMTSF})_2\text{-PF}_6$  material, where SDW is observed. At lower temperatures the threshold field assumes constant values for SDW materials, while for CDW it attains a minimum and starts to strongly increase with further decrease in temperature.

In general, for density waves, the experimentally observed thresholds correlate with the temperature scale. Therefore in  $(\text{TMTSF})_2\text{PF}_6$ , mV/cm thresholds are observed at temperatures of the order of 1-10 K. As standard CDW transition temperatures are an order of magnitude higher, the thresholds observed in standard CDW materials ( $\text{NbSe}_3$ ,  $\alpha\text{-TaS}_3$ ,  $\text{K}_{0.3}\text{MoO}_3$ ) are of the order of 0.1-1 V/cm when measured at temperatures around 100 K. Depending on the  $(\text{TMTSF})_2\text{PF}_6$  sample impurity contents, thresholds of the order of 5-30 mV/cm for weak and strong pinning, respectively, were found [27]. For a standard CDW material  $\alpha\text{-TaS}_3$  also, higher impurity content leads to the increase of threshold, up to 30 V/cm (see Fig. 5.5). In some cases, very high threshold fields may be related to commensurability pinning  $N = 3$ . As an example, we mention q1D organic material  $\text{Cu}(\text{DMe-DCNQI})_2$ , [165, 143] where commensurate CDW  $N = 3$  is established below  $\sim 50$  K. An important increase of the threshold field value, up to 130 V/cm was observed at 34 K. There, the CDW LRO is achieved in the whole bulk of the sample. A similar effect was observed in q1D organic material TTF-TCNQ when  $N = 3$  CDW is induced under pressure, [166].

### Contact quality influence on nonlinear conductivity in $\text{Sr}_{14}\text{Cu}_{24}\text{O}_{41}$

In order to check for the sliding conductivity in  $\text{Sr}_{14}\text{Cu}_{24}\text{O}_{41}$ , dc resistance,  $R$ , dependence on the applied electric field  $E$  was measured along the  $c$ -axis,  $E||c$ . As shown in Fig. 5.3, in the first and second stack of panels, we found that  $R$  does not deviate more than 2%, at the highest fields applied, 10 V/cm, from the low field value, (upper panel). A characteristic threshold electric field, above which the sliding conductivity starts, is not observed, as shown in the panels on the left, where  $R$  is shown *vs.*  $E$  on linear scale. The dashed boxes within the panels of Fig. 5.3 are blown-up and presented as the next lower panel. In this manner, we may follow  $R$  *vs.*  $E$  down to the smallest electric fields. Indeed, the negligibly small nonlinearity emerges from the noise background. In the panels on the right the resistance is shown *vs.* logarithm of the electric field. Presenting data in this manner illustrates how an apparent threshold field may be derived. In conclusion, no signs of the sliding mechanism were found.

In Fig. 5.3, in the third and fourth stack of panels, it is shown that a large nonlinearity occurred for the high quality sample where we used improper contact preparation method. However, the threshold was not observed, *i.e.* nonlinearity emerged immediately from the noise background. Since this is the four probe measurement, the observed nonlinearity is not due to the contacts *per se*. That is, contact nonlinearity does not enter the result. Still, since the contact resistances were at least order of magnitude higher than the sample bulk resistance, the improper current injection occurred, and also large unnested voltages were measured. This scenario was confirmed, when the proper contact application was performed and nonlinearity disappeared for this sample. As already explained above, in the panels on the right the resistance is shown *vs.* logarithm of the electric field.

Our results are apparently contradictory to those of Maeda *et al.* [168]. They claimed that sliding conduction by the q1D charge-ordered state ( $4k_F$  CDW) along the legs of ladders occurs in  $\text{Sr}_{14}\text{Cu}_{24}\text{O}_{41}$ . They derived threshold fields of the order of 0.5 V/cm in the temperature range 100 – 160 K, Fig. 5.4, left panel. Our inspection of the data presented by these authors indicated the following. If their data are presented *vs.* electric field shown on the linear, instead on the logarithmic scale, the behavior as we observed for a good contacts case (Fig. 5.3) is recovered. No threshold field may be derived. The nonlinearity emerges from the noise background. Conductivity deviates not more than 3-4%, at the highest fields applied, 4-5 V/cm, from the low field value. In our opinion this removes the contradiction. We regard that their data are consistent with ours.

Further, Blumberg *et al.* [167] reported also a sliding non-linear conductivity. That is, they claimed to observe a strong non-linear effect and to be able to derive a threshold field  $E_T = 0.2$  V/cm. By inspection of their data, shown in Fig. 5.4, right panel, we estimate that the nonlinear effect at twice the threshold field is of the order of 50%. For comparison we also note in their data that, already at 1 V/cm, conductivity increases for 100%, above the low field value. The nonlinearity of exactly this magnitude we obtained only for the sample where improper contact preparation method was applied. The resistance data of Blumberg *et al.* are also presented *vs.* electric field shown on the logarithmic scale. Here, we were not able to transform to the linear scale, and no precise comparison with our data was possible.

### Fröhlich conductivity and screening by free carriers

As shown in Fig. 5.4, right panel, Blumberg *et al.* also derived a second threshold,  $E_T^{(2)}$ . They relate this threshold to the crossover to a regime of free sliding, rigid condensate as envisioned by Fröhlich in 1954. in his model

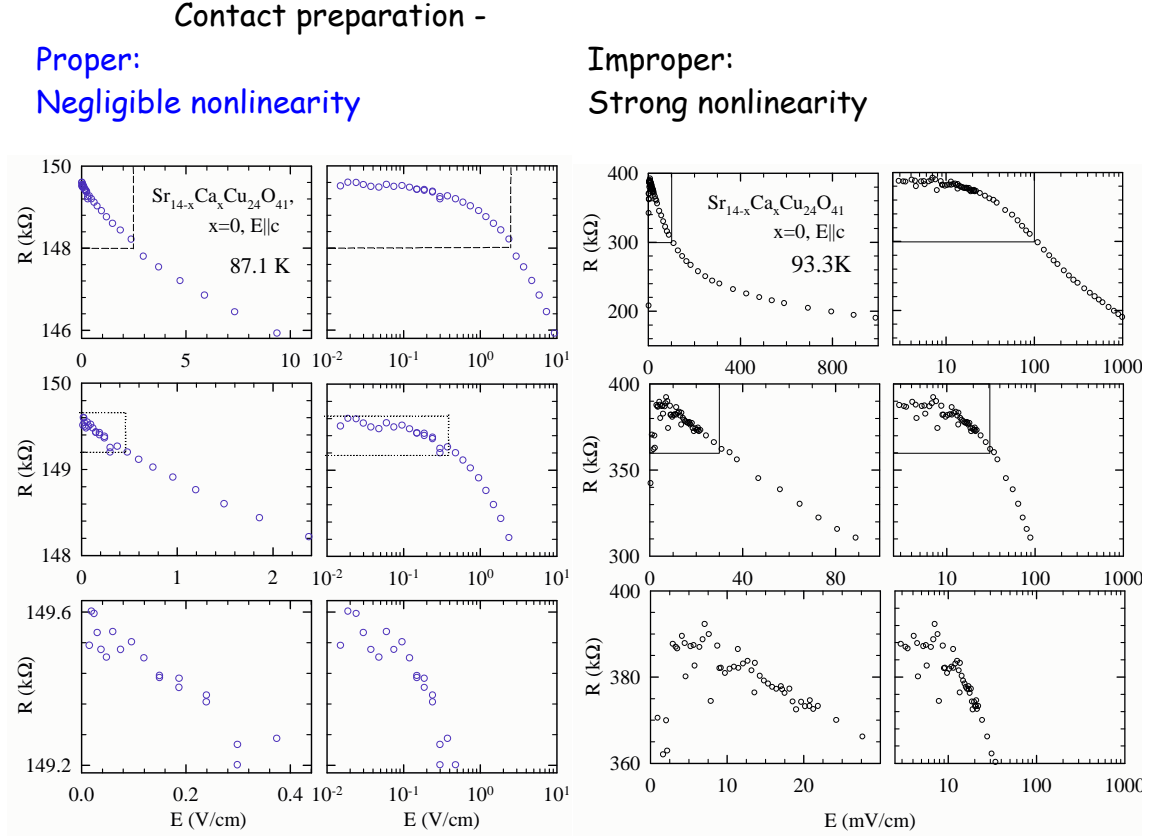


Fig. 5.3: Resistance *vs.* electric field applied along the *c*-axis, for  $\text{Sr}_{14-x}\text{Ca}_x\text{Cu}_{24}\text{O}_{41}$ . The results for different contact preparation cases (see Sec. 3.2) are shown either in the first and second stack or in the third and fourth stack of panels. In the first (third) stack, the electric field is shown on linear, and in the second (fourth) stack on logarithmic scale. From top to bottom the dataset is the same, for the respective cases, but the scale is being enlarged. This is denoted by the dashed boxes. For properly prepared contacts, a negligible nonlinearity, 2% at the maximum field of 10 V/cm, is observed. On the contrary, for improperly prepared contacts, a strong nonlinearity is observed - the conductivity doubled at the highest fields applied. Different apparent thresholds, depending on the scale, are derived in the second (fourth) stack of panels. In the first (third) stack of panels thresholds can not be derived. The apparent nonlinearity starts from the lowest fields - emerging from the noise background (bottom panel).

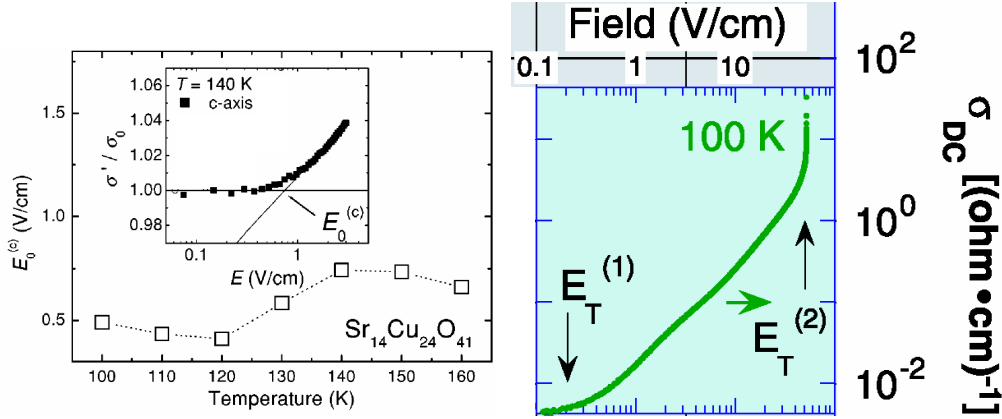


Fig. 5.4: Left panel: The threshold field  $E_0$  as a function of temperature. The authors, Maeda *et al.* [168], identified  $E_0$  as the onset of sliding conduction. The inset shows how  $E_0$  was derived from the nonlinear conductivity  $\sigma'$  normalized to low field conductivity value  $\sigma$ . Right panel: The strong nonlinear conductivity observed by Blumberg *et al.* [167] at 100 K. The authors identified thresholds  $E_T^{(1)}$  and  $E_T^{(2)}$  as the onset of sliding and Fröhlich conductivity, respectively.

of superconductivity. In Fröhlich model the screening effects of the free carriers are not taken into account. Therefore, in order to observe Fröhlich conductivity in a given material the screening has to be ineffective, [169]. Contrary to this, we observe that the screening is still well effective in  $\text{Sr}_{14}\text{Cu}_{24}\text{O}_{41}$  at 100 K. We infer this from the fact that both the central relaxation time,  $\tau_0$ , and dc resistivity,  $\rho_{dc}$ , show the same activated behavior from  $T_{CDW}$  down to the lowest temperatures, 45-50 K. In Littlewood's model (Sec. 2.4) it was shown that this  $\tau_0 \propto \rho_{dc}$  behavior is due to the CDW relaxation damped by the free-carriers, which flow around the pinned CDW and produce screening currents. Therefore we conclude that for  $\text{Sr}_{14}\text{Cu}_{24}\text{O}_{41}$  the screening is still effective at 100 K and thus no Fröhlich conduction may be observed.

### Relation of $\Delta\varepsilon$ and $E_T$

In the classical particle model for CDW, the dielectric strength  $\Delta\varepsilon$  is related to the threshold electric field  $E_T$  for the nonlinear conduction.

$$\varepsilon_0 \Delta\varepsilon E_T = \frac{Me}{\pi ab} \quad (5.2)$$

The term on the right side represents the number of chains (or other 1D structures, ladders or stacks) per cross-section area.  $a$  and  $b$  are the lattice

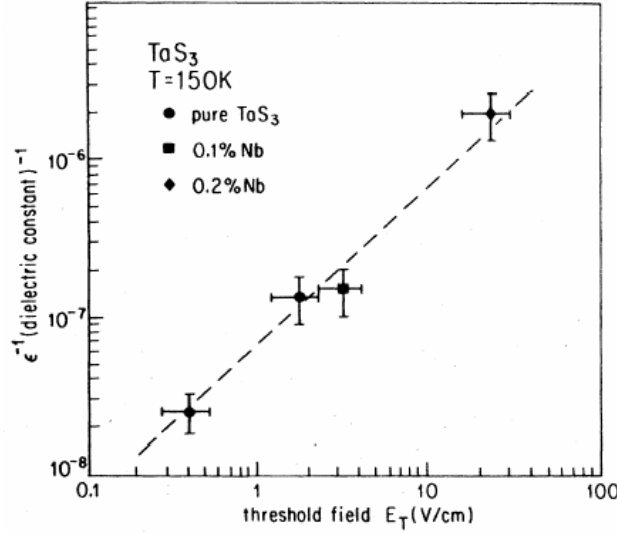


Fig. 5.5: Inverse low-frequency dielectric constant  $\epsilon^{-1}$  (4 MHz) vs. threshold field  $E_T$  in *o*-TaS<sub>3</sub> alloys at 150 K. From Ref. [170]

parameters, and  $M$  is the number of carriers per unit cell.  $e$  is the electron charge of  $1.6 \times 10^{-19}$  C.

The relation given by Eq. 5.2 was experimentally confirmed to be valid for a standard CDW material, *o*-TaS<sub>3</sub>, Wu *et al.*, [170]. For *o*-TaS<sub>3</sub> samples, disordered due to alloying with NbS<sub>3</sub>, Wu *et al.* observed a much smaller  $\Delta\epsilon \approx 10^5$  than in the pure material and correspondingly enhanced sliding threshold of 30 V/cm, Fig. 5.5. This material presents a CDW transition at about 200 K and the studies of nonlinearity were done at 150 K. Therefore, it is well suited for comparison with CDW in Sr<sub>14</sub>Cu<sub>24</sub>O<sub>41</sub>. For Sr<sub>14</sub>Cu<sub>24</sub>O<sub>41</sub>, an intrinsically disordered material, characterized by even lower  $\Delta\epsilon \approx 3 \times 10^4$ , an even higher threshold might be extrapolated, at least 100 V/cm.

An estimate for  $E_T$  in Sr<sub>14</sub>Cu<sub>24</sub>O<sub>41</sub> based on the observed dielectric strength  $\Delta\epsilon$ , may also be given directly, using Eq. 5.2. Here it is necessary to remind that only holes transferred into ladders are mobile, condense into CDW and enter this calculation, see Sec. 1.2.6. One hole transferred per ladder equals 4 mobile holes per one approximate superstructure cell, since this cell contains 4 formula units, Fig. 1.12 and 1.13. Therefore, we set  $M=4$ . The cross-section of the superstructure cell, perpendicular to ladders is  $a \cdot b \approx 150 \text{ \AA}^2$ . This direct calculation leads to an even higher estimate for  $E_T$  of the order  $10^3$  V/cm, obviously much above the maximum applied field of 10 V/cm. For *o*-TaS<sub>3</sub>, this direct calculation also gave an order of magnitude higher estimates compared to the values obtained in the experiment, [126]. A good

quantitative agreement was obtained for the SDW material (TMTSF)<sub>2</sub>PF<sub>6</sub> at 2–3 K, with  $M = 1/2$ ,  $a \cdot b \approx 100 \text{ \AA}^2$ ,  $\Delta\varepsilon \approx 3 \times 10^9$  and  $E_T \approx 5 - 10 \text{ mV/cm}$ , [27, 44].

We also refer here to the threshold field  $E_T = 0.2 \text{ V/cm}$  derived by Blumberg *et al.* for Sr<sub>14</sub>Cu<sub>24</sub>O<sub>41</sub>. They also observed radio-frequency dielectric mode of dielectric strength  $\Delta\varepsilon \approx 4 \times 10^6$ . That is, two orders of magnitude stronger than the mode we observed. Using this comparison and relying on Eq. 5.2, *i.e.* on the proportionality  $E_T \propto \Delta\varepsilon^{-1}$  we estimate that in our case the threshold field should be two orders of magnitude higher, around 20 V/cm. This value is two times above our experimental limit. In this manner we may conclude that an apparent contradiction between Blumberg *et al.* and ours data, is removed. We also note that the  $\tau_0$  they observed were for a magnitude larger, as expected for higher quality samples. Here, we might conclude that the samples studied by Blumberg *et al.* were of significantly higher quality. However, the response they observed is much broader ( $1 - \alpha = 0.6$ ), which indicates a higher level of randomness in the impurity distribution.

### 5.1.3 Standard features of CDW ground state in Sr<sub>14</sub>Cu<sub>24</sub>O<sub>41</sub>

#### Response to dc fields

A standard feature of the CDW phason response to dc fields is sliding conductivity. However, we have not observed sliding conductivity and the related threshold electric field. We suggest that sliding conductivity is not observed due to the too small electric fields (up to 10 V/cm) applied in this study. Presumably due to the sample quality dependence, the threshold field was above the experimental limit in our study. We can anticipate two possible origins for a very large  $E_T$ . Either, it is due to the strong pinning to randomly distributed centers resulting from intrinsically disordered structure of Sr<sub>14</sub>Cu<sub>24</sub>O<sub>41</sub>. Or, it is possible that CDW in Sr<sub>14</sub>Cu<sub>24</sub>O<sub>41</sub> is commensurate with  $N = 3$  and thus strongly pinned to the ladders lattice background.

Such, presumably very large, threshold field also correlates with relatively small observed dielectric strength of the radio-frequency dielectric mode, see Fig. 5.5. The relation between  $E_T$  and  $\Delta\varepsilon$ , Eq. 5.2, is modelled within a simple classical particle model of CDW, [126].

### Response to ac fields - $m^*$ calculation

The two signatures of the CDW phason response to ac fields are observed in  $\text{Sr}_{14}\text{Cu}_{24}\text{O}_{41}$ . The radio-frequency mode is activated down to the lowest temperatures measured, 45-50 K. The *pinned* mode was identified at  $1.8 \text{ cm}^{-1}$  by Kitano *et al.* [162, 163]. The ac response that is observed in  $\text{Sr}_{14}\text{Cu}_{24}\text{O}_{41}$  is extremely reminiscent, phenomenologically, of the CDW phason response in most well-known 1D compounds like  $\text{K}_{0.3}\text{MoO}_3$ ,  $\text{NbSe}_3$ ,  $\text{TaS}_3$ , and  $(\text{TaSe}_4)_2\text{I}$  [126].

As we discuss next, this holds qualitatively as well as quantitatively. We will describe the dynamical response of  $\text{Sr}_{14}\text{Cu}_{24}\text{O}_{41}$  utilizing a standard theory for CDW systems as presented in Sec. 2.4. The pinning frequency  $\Omega_0$  is related to the radio-frequency mode central relaxation time  $\tau_0$  and to dc conductivity  $\sigma_z$  measured along the *c*-axis. This relationship, as shown below, allows us to estimate the effective mass  $m^*$ :

$$m^* = \frac{e^2 \rho_0}{\sigma_z \tau_0 m_0 \Omega_0^2} \quad (5.3)$$

Below we describe the variables used in this calculation.

$\Omega_0 = 0.34 \times 10^{12} \text{ [rad/s]} (1.8 \text{ cm}^{-1})$  - CDW pinning frequency, [162].

$\sigma_z \text{ [}\Omega^{-1}\text{m}^{-1}\text{]}$  - conductivity along the *c*-axis at selected temperatures, taken from our experiment, Fig. 5.2. Longitudinal conductivity was calculated by multiplying the inverse of the resistance  $1/R_4 \text{ [}\Omega^{-1}\text{]}$  with the sample aspect ratio,  $\frac{l}{S} = 3000 \text{ m}^{-1}$ .

$\tau_0 \text{ [s]}$  - central relaxation time, at selected temperatures, taken from our experiment, Fig. 5.1.

$\rho_0 = 1 \times 10^{27} \text{ [m}^{-3}\text{]}$  - carrier concentration, inferred from crystal and electronic structure of  $\text{Sr}_{14-x}\text{Ca}_x\text{Cu}_{24}\text{O}_{41}$ . In this calculation we assumed one hole per ladder. That is, 4 mobile holes reside in the ladders per approximative superstructure unit cell, Sec. 1.2.6).

$m^*$  - the effective mass  $m^*$  is just the multiplication factor which multiplies electron mass  $m_0 = 9.1 \times 10^{-31} \text{ [kg]}$ .

The calculated effective mass values, for a few selected temperatures, are shown in the Table 5.1. The pinning frequency and carrier concentration are temperature independent. Only the product  $\sigma_z \tau_0$  introduces temperature variation in the calculated values of  $m^*$ . We take  $m^* \approx 100$  value as a temperature average, since effective mass is considered to be temperature

x=0

$T$	$\sigma_z \tau_0$	$m^*$
108 K	$12.5 \times 10^{-7}$	80
68 K	$10 \times 10^{-7}$	100
53 K	$5 \times 10^{-7}$	200

Table 5.1:  $T$  is temperature in Kelvin. The selected temperatures cover the range where the dielectric response measurements were done.  $\sigma_z \tau_0 [\Omega^{-1} \text{m}^{-1} \text{s}]$  is a product of dc conductivity  $\sigma_z$  and  $\tau_0$  central relaxation time, resulting from measurements along the  $c$ -axis. The values of these parameters may also be read from Figs. 5.1 and 5.2.

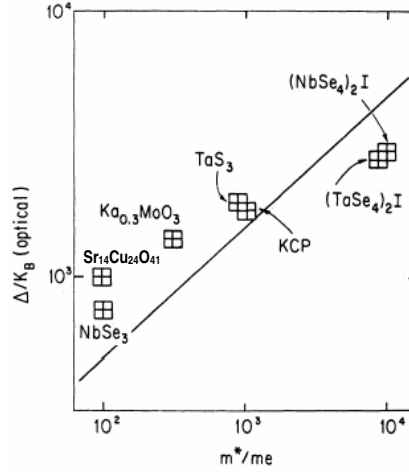


Fig. 5.6: Effective mass  $m^*$  vs. the activation energies and  $\Delta_{\text{CDW}}$  for various standard CDW compounds. Our result for  $\text{Sr}_{14}\text{Cu}_{24}\text{O}_{41}$  is also shown. The solid line represents the relation  $m^* \propto \Delta_{\text{CDW}}^2$ . From Ref. [126]

independent [126]. The value for the effective mass for  $\text{Sr}_{14}\text{Cu}_{24}\text{O}_{41}$  material calculated here should be compared to the standard  $m^* = 1$  for SDW [37] or to the standard  $m^* = 10^2 - 10^4$  for CDW [126]. As can be found from Fig. 5.6 the range of the CDW effective mass values is related to the values of the CDW energy gap. Values of  $m^* \approx 100$  and  $\Delta_{\text{CDW}} = 1300$  K situate  $\text{Sr}_{14}\text{Cu}_{24}\text{O}_{41}$  material close to the standard CDW materials presented in Fig. 5.6. Any discrepancies are easily attributed to the fact that relation  $m^* \propto \Delta_{\text{CDW}}^2$  is controlled by the value of the electron-phonon coupling constant, which is weak, compared to electron-electron interaction, in  $\text{Sr}_{14}\text{Cu}_{24}\text{O}_{41}$ .

### 5.1.4 Conclusions

In dc electrical transport we observed a transition to a low-temperature insulating state below  $T_c = 210$  K characterized by the activation energy  $\Delta = 1300$  K. We presented evidence that this transition corresponds to a charge-density wave formation along the ladders, the subsystem responsible for charge transport, in q1D cuprate  $\text{Sr}_{14}\text{Cu}_{24}\text{O}_{41}$ . While the *pinned* mode was previously reported in the microwave frequency range, in the radio frequency range we observed thermally activated mode, characterized by similar activation energy as dc transport. Quasi-coherent microwave and FIR measurements also corresponded to these results, [78, 160]. We estimated the effective mass of CDW condensate to be  $m^* \approx 100$ , within the range of values for standard CDW materials. Although sliding conductivity was not observed in this study, we note independent reports of nonlinear conductivity. The apparent contradiction is presumably due to different quality of samples. This is a known influence in studies of q1D materials. Our results confirm the theoretical prediction, that a competing CDW ground state exists in q1D cuprates in addition to superconductivity.

However, we note that some issues remain: the observed CDW occurs below an insulator-to-insulator transition, indicating strong electron-electron interaction in the ladders subsystem. These strong interactions are probably necessary to render the non-metallic phase at high temperatures. It is interesting to note that below the transition the activation energy increases, from  $\Delta_{H.T.} = 900$  K to  $\Delta_{CDW} = 1300$  K. This difference may be regarded as being due to the additional, "CDW proper" gap opening. This only remotely reminds of the standard metal-to-insulator transition occurring in the standard CDW materials. We also note that the spin-gap is 2–3 times smaller than the CDW gap. For a standard CDW material this is not observed. Instead, the gaps in spin and charge sector open concomitantly and they are of the same size.

## 5.2 Localization of holes in chains of $\text{La}_y\text{Sr}_{14-y-x}\text{Ca}_x\text{Cu}_{24}\text{O}_{41}$

An understanding is necessary on the nature of the spin/charge state and in particular on the charge dynamics in the chain subsystem of nonisovalently substituted compounds  $\text{La}_y\text{Sr}_{14-y-x}\text{Ca}_x\text{Cu}_{24}\text{O}_{41}$ , which possess a reduced hole count,  $\delta_h = 6 - y$ . We remind that for  $\delta_h \leq 5$  compounds all holes reside in the chains. No ordering of any kind has been reported for these compounds. In order to clarify the mechanism of the charge transport, we have studied  $\text{La}_3\text{Sr}_3\text{Ca}_8\text{Cu}_{24}\text{O}_{41}$  and  $\text{La}_{5.2}\text{Ca}_{8.8}\text{Cu}_{24}\text{O}_{41}$ . These particular compounds are characterized by low hole counts  $\delta_h = 6 - 3 = 3$  and  $\delta_h = 6 - 5.2 = 0.8$ , respectively. Our dc resistivity and low frequency dielectric spectroscopy results cover a broad frequency range from dc to 1 MHz. The compounds have been studied in a wide temperature range from 750 K to 35 K, [171].

### 5.2.1 dc conductivity indicates hopping charge transport mechanism

In Fig. 5.7 we present for  $\text{La}_3\text{Sr}_3\text{Ca}_8\text{Cu}_{24}\text{O}_{41}$  and  $\text{La}_{5.2}\text{Ca}_{8.8}\text{Cu}_{24}\text{O}_{41}$  compounds the dc conductivity measured along the  $c$ -axis, *i.e.*, along the chains, as a function of temperature. The compounds will also be denoted as  $\text{La}_3$  and  $\text{La}_{5.2}$ , respectively.

That is, for  $\text{La}_{5.2}$  and  $\text{La}_3$ , above respective  $T_c = 330$  K and 300 K, the dc conductivity follows a simple activation behavior  $\sigma_{dc}(T) \approx \exp(-2\Delta/T)$ . The activation energies  $2\Delta = 4200$  K and 3200 K were observed for  $\text{La}_{5.2}$  and  $\text{La}_3$ , respectively. The fits to the simple activation behavior are depicted by solid lines in the insets. As directly seen from the  $\log \sigma_{dc}(T)$  *vs.*  $T^{-1/2}$  plot, presented in the main panels of Fig. 5.7, below  $T_c$  down to 50-35 K the conductivity perfectly follows Mott's variable-range hopping (VRH) behavior

$$\sigma_{dc}(T) = \sigma_0 \exp \left[ - (T_0/T)^{\frac{1}{1+d}} \right] \quad (5.4)$$

with the dimensionality of the system  $d = 1$ . That is, the fits to this law appear as straight lines in the main panels, where the horizontal scale is the inverse square-root of temperature.  $T_c$  is determined by the crossing of extrapolated fitting curves, with the error bar of  $\pm 15$  K.

These results clearly demonstrate the hopping mechanism of charge transport in one dimension; at  $T_c$  it crosses over from nearest-neighbor hopping to variable-range hopping. The cross-over temperature  $T_c$  is given by  $T_c = \Delta/(2\alpha c)$  [172, 173]. Here the energy of sites near the Fermi energy

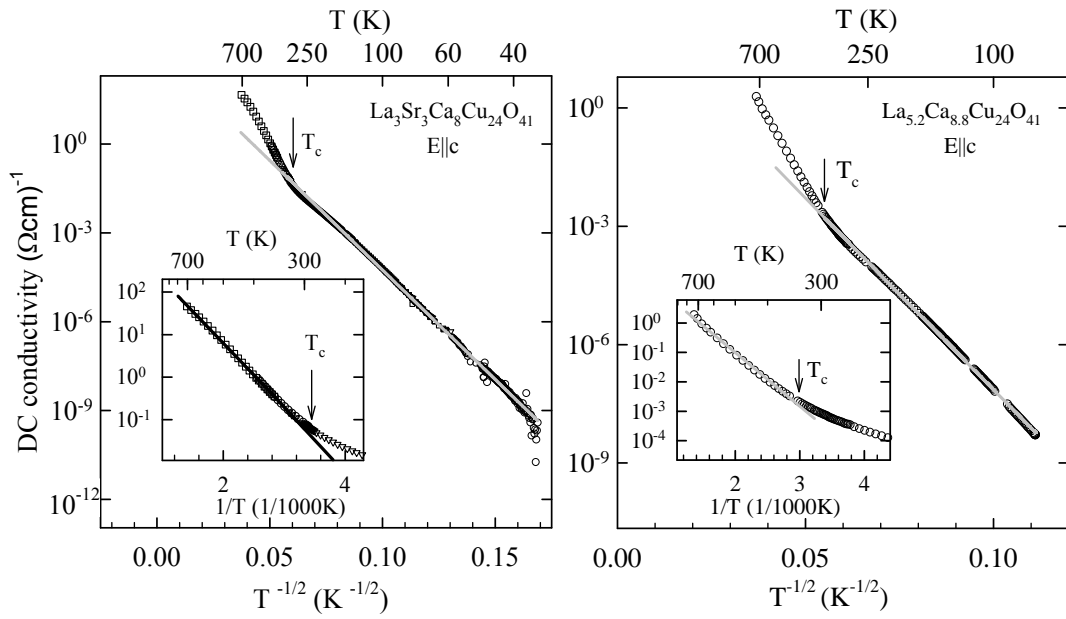


Fig. 5.7: dc conductivity  $\sigma_{dc}$  of  $\text{La}_3\text{Sr}_3\text{Ca}_8\text{Cu}_{24}\text{O}_{41}$  and  $\text{La}_{5.2}\text{Ca}_{8.8}\text{Cu}_{24}\text{O}_{41}$  along the  $c$ -axis vs.  $T^{-1/2}$ . Above respective  $T_c = 300$  K and 330 K,  $\sigma_{dc}$  follows a simple activation behavior, which indicates the nearest-neighbor hopping charge transport mechanism (full lines in the insets). Below  $T_c$  the behavior  $\sigma_{dc} \propto \exp(T^{-1/2})$  is observed (full lines in the main panels) corresponding to the regime of variable-range hopping in one dimension.

available for hops, has an uniform distribution in the range  $-\Delta$  to  $+\Delta$ , the  $c$  is the distance between the nearest Cu chain sites and  $\alpha^{-1}$  is the localization length. By using respective  $\Delta = 1600 - 2100$  K and  $c = 2.77\text{\AA}$ , we find  $\alpha^{-1} \approx 1\text{\AA}$ . The values of the VRH activation energies for  $\text{La}_{5.2}$  and  $\text{La}_3$ ,  $T_0^{exp} = 5 \cdot 10^4$  K and  $T_0^{exp} = 2.9 \cdot 10^4$  K, respectively, are obtained from the fit of our data to Eq. 5.4. These values are very close to those expected theoretically for  $\text{La}_{5.2}$  and  $\text{La}_3$ :  $T_0^{th} = 8\Delta c\alpha \approx 4.6 \cdot 10^4$  K and  $T_0^{th} = 8\Delta c\alpha \approx 3.5 \cdot 10^4$  K, respectively.

### 5.2.2 Frequency dependent measurements also indicate hopping transport mechanism

For brevity, we present the results only for  $\text{La}_3\text{Sr}_3\text{Ca}_8\text{Cu}_{24}\text{O}_{41}$  compound. The features of the frequency dependent conductivity observed for  $\text{La}_{5.2}\text{Ca}_{8.8}\text{Cu}_{24}\text{O}_{41}$  correspond well, and lead to the same conclusions as the results for  $\text{La}_3\text{Sr}_3\text{Ca}_8\text{Cu}_{24}\text{O}_{41}$ .

Fig. 5.8 demonstrates the conductivity  $\sigma(\nu, T)$  spectra of  $\text{La}_3\text{Sr}_3\text{Ca}_8\text{Cu}_{24}\text{O}_{41}$  over a broad frequency range for different temperatures. Our LFDS results are more instructive when combined and analyzed with the quasi-optical microwave and far infrared optical conductivity results in the  $6\text{-}350\text{ cm}^{-1}$  range, taken from Ref. [171].

As confirmed by our fit (see below), the kinks in  $\sigma(\nu, T)$  on the left side of the lowest-frequency phonon are of electronic (non-phonon) origin and we assign this contribution to the hopping of holes in the chains. Excluding the phonon component, the electronic conductivity can be expressed as the sum of two terms

$$\sigma(\nu, T) = \sigma_{dc}(T) + A(T) \cdot \nu^s \quad s \approx 1 \quad (5.5)$$

where  $\sigma_{dc}(T)$  is given by Eq. 5.4. We note that the frequency independent behavior is found in the radio-frequency range for all temperatures (open symbols in Fig. 5.8). Similar dependences have been observed in a variety of disordered systems [174]. The frequency-dependent component  $\sigma_{ac}(\nu, T) = A(T) \cdot \nu^s$  is found to contain a temperature dependent prefactor  $A(T)$ . The cross-over frequency  $\nu_{co}$  from the frequency independent to the frequency dependent conductivity can be estimated from the condition that the ac hopping length has to be smaller than the dc hopping length in order that  $\sigma_{ac}(\nu, T)$  overcomes  $\sigma_{dc}(T)$  [172]. For one-dimensional VRH, the dc hopping length is given by  $R_0 = (\Delta c/2\alpha T)^{1/2}$ , and the ac hopping length is  $R_\nu = \frac{1}{2}\alpha \ln(\nu_{ph}/\nu_{co})$ , where the attempt frequency  $\nu_{ph}$  depends on the electron-phonon interaction. Assuming  $\nu_{ph} \approx 10^{12}\text{ s}^{-1}$ , we find for the cross-over frequency  $\nu_{co}$  the values  $0.15\text{ cm}^{-1}$ ,  $0.015\text{ cm}^{-1}$  and  $0.0006\text{ cm}^{-1}$  for  $T = 300$

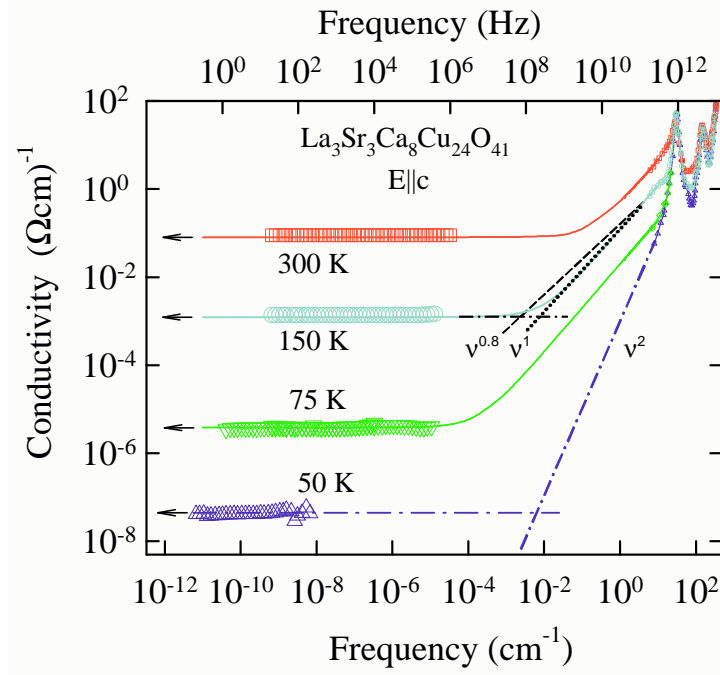


Fig. 5.8: Broad conductivity spectra combined from our dc/LFDS results and microwave/FIR results taken from Ref. [171]. Spectra are obtained for  $\text{La}_3\text{Sr}_3\text{Ca}_8\text{Cu}_{24}\text{O}_{41}$  along the  $c$ -axis at selected temperatures. Hopping conduction of the form  $\nu^s$ ,  $s \approx 1$ , is found between 6 and 20  $\text{cm}^{-1}$  for  $T \geq 75$  K, while a featureless, frequency independent behavior is found in the radio-frequency range for all temperatures. The arrows denote the dc values. The full lines are fits to Eq. 5.5. A pure power law contributions with  $s = 0.8$  and 1 are shown for  $T = 150$  K by a dashed and dotted line, respectively. At 50 K only a  $\nu^2$  contribution (dashed-dotted line) due to the low-energy phonon tail is observed.

K, 150 K and 75 K, respectively. These values coincide nicely with those obtained when the  $\nu^s$  fits in  $6 - 20 \text{ cm}^{-1}$  range are extrapolated to lower frequencies (Fig. 5.8). In particular, the choice of the exponent  $s = 1$  appears to be the most appropriate. For example, at  $T = 150 \text{ K}$  we find  $\nu_{co} \approx 0.0027 \text{ cm}^{-1}$  and  $0.013 \text{ cm}^{-1}$ , for  $s = 0.8$  and  $1$ , respectively. Experimentally we are not able to distinguish between the  $\nu^{0.8}$  and  $\nu^1$  dependences due to relatively narrow frequency range in which  $\sigma \sim \nu^s$  behavior is detected. At  $T \leq 50 \text{ K}$  the hopping vanishes because the charge carriers are frozen out, and we observe only the  $\nu^2$  contribution to the conductivity associated with the low-energy phonon (Lorentzian) tail.

### 5.2.3 Hopping transport is due to localized holes in chains

We now comment on the hopping transport found in the chains of  $\text{La}_3\text{Sr}_3\text{Ca}_8\text{Cu}_{24}\text{O}_{41}$ , as well as  $\text{La}_{5.2}\text{Ca}_{8.8}\text{Cu}_{24}\text{O}_{41}$ , in comparison with disordered non-crystalline insulators. Firstly, for the latter compounds the value of the exponent in Eq. 5.4 is commonly found to be  $1/4$ , corresponding to hopping in 3 dimensions; it becomes  $1/2$  if electron-electron interaction plays a role [175]. However, electron-electron interactions are expected to have a significant impact on the correlated many-electron hopping, only when the temperature  $T$  is larger than  $T_0$ , which is far from experimental range since  $T_0 = 2.9 - 5 \cdot 10^4 \text{ K}$ , [172, 176]. The situation is different for systems consisting of parallel chains of finite length where small disorder leads to weakly localized states [177]. This model gives the temperature exponent  $1/2$  as found in our experiment. We conclude that the exponent  $1/2$  confirms the one-dimensional nature of the electronic structure of chains in  $\text{La}_y\text{Sr}_{14-y-x}\text{Ca}_x\text{Cu}_{24}\text{O}_{41}$ , which is in accord with the crystallographic structure [70, 71]. Secondly, the obtained values for  $T_0$  indicate the standard regime of the VRH where the hopping distance  $R_0 = (\Delta c/2\alpha T)^{1/2}$  is larger than the localization length  $\alpha^{-1}$ ; the extremely small  $\alpha^{-1} \approx 1 \text{ \AA}$  shows that the system is far from the metal-insulator transition. Following the usual interpretation of the VRH law, from  $T_0 = 16\alpha^3/n(E_F)$  we find the electronic density of states at the Fermi level  $n(E_F) \approx 5.5 \cdot 10^{24} \text{ eV}^{-1}\text{cm}^{-3}$ . Finally, a straightforward consequence of the observed VRH conduction is that its extrapolation indicates a zero conductivity at  $T = 0$ , in accord with the theory developed for disordered non-crystalline insulators.

Generally, a frequency-dependent conductivity varying as  $A(T) \cdot \nu^s$ , where  $s \approx 1$ , does not necessarily imply hopping conduction [172]. However, we suggest that dc VRH conduction as well as the power-law ac conduction are

attributed to the same set of localized states near the Fermi level. The value of the exponent close to one indicates that the observed ac conductivity is due to phonon-assisted hops between spatially distinct sites similarly to the dc contribution, and not to the photon absorption for which  $s \approx 2$  is usually found [172]. Note that we did not find the latter in the whole measured frequency range, despite the theoretical prediction that with increasing frequency there is a cross-over from the regime dominated by phonon-assisted  $\sigma_{\text{hopping}} \approx \nu^s$ ,  $s \leq 1$  to that dominated by photon-assisted conduction which varies as  $\nu^s$ ,  $s \approx 2$ . The conductivity observed at 50 K, which follows a  $\nu^2$  behavior, is in our case simply a phonon tail, and is not due to hopping.

#### 5.2.4 A comparison between $\text{Sr}_{14-x}\text{Ca}_x\text{...}$ and $\text{La}_y\text{Sr}_{14-y-x}\text{Ca}_x\text{...}$ materials

At this point, we compare the electrical transport properties observed for  $\text{La}_y\text{Sr}_{14-y-x}\text{Ca}_x\text{Cu}_{24}\text{O}_{41}$  and for  $\text{Sr}_{14}\text{Cu}_{24}\text{O}_{41}$  material. Also a reference on the results for other  $\text{Sr}_{14-x}\text{Ca}_x\text{Cu}_{24}\text{O}_{41}$  materials will be necessary, [171, 160].

Firstly, we note that, in contrast to  $\text{Sr}_{14}\text{Cu}_{24}\text{O}_{41}$ , in  $\text{La}_y\text{Sr}_{14-y-x}\text{Ca}_x\text{Cu}_{24}\text{O}_{41}$  materials no signature of the CDW phason response to dc and ac electric fields is found. In addition to a featureless radio-frequency response, we also did not observe electric-field dependence of dc conductivity up to 25 V/cm, in the temperature range 326 K- 50 K. Finally, no signature of the pinned mode in the microwave frequency range was found for  $\text{La}_y\text{Sr}_{14-y-x}\text{Ca}_x\text{Cu}_{24}\text{O}_{41}$  materials.

Secondly, we analyze and compare in more detail the dc conductivity results, as presented in Fig. 5.9 for  $\text{La}_3$  and  $\text{La}_{5.2}$  along the ones for  $\text{Sr}_{14}\text{Cu}_{24}\text{O}_{41}$ . Very different RT resistivities have to be noted: 1400, 13 and  $0.002 (\Omega\text{cm})^{-1}$ , respectively. Inspection of the logarithmic derivatives, presented in the lower panel, allows quantification of differences in the observed conductivity temperature dependences. For  $\text{Sr}_{14}\text{Cu}_{24}\text{O}_{41}$  high temperature insulating phase and low temperature CDW phase are characterised by well defined activation energies, and a phase transition in between, observed as a peak in the logarithmic derivative. For  $\text{La}_y\text{Sr}_{14-y-x}\text{Ca}_x\text{Cu}_{24}\text{O}_{41}$  materials, no transition is observed, only a crossover from nearest-neighbor hopping behavior at high temperatures, where an activation energy can be defined, to a VRH behavior below respective crossover temperatures  $T_c \approx 300 - 330$  K.

In Fig. 5.10 we compare the dc transport parameters, *i.e.* RT resistivity, activation energy and crossover/transition temperature for  $\text{La}_y\text{Sr}_{14-y-x}\text{Ca}_x\text{Cu}_{24}\text{O}_{41}$  and  $\text{Sr}_{14-x}\text{Ca}_x\text{Cu}_{24}\text{O}_{41}$  materials. The data for another nonisovalently substituted material  $\text{Y}_1\text{Sr}_5\text{Ca}_8\text{Cu}_{24}\text{O}_{41}$ , hole count  $\delta_h = 5$ , by Mo-

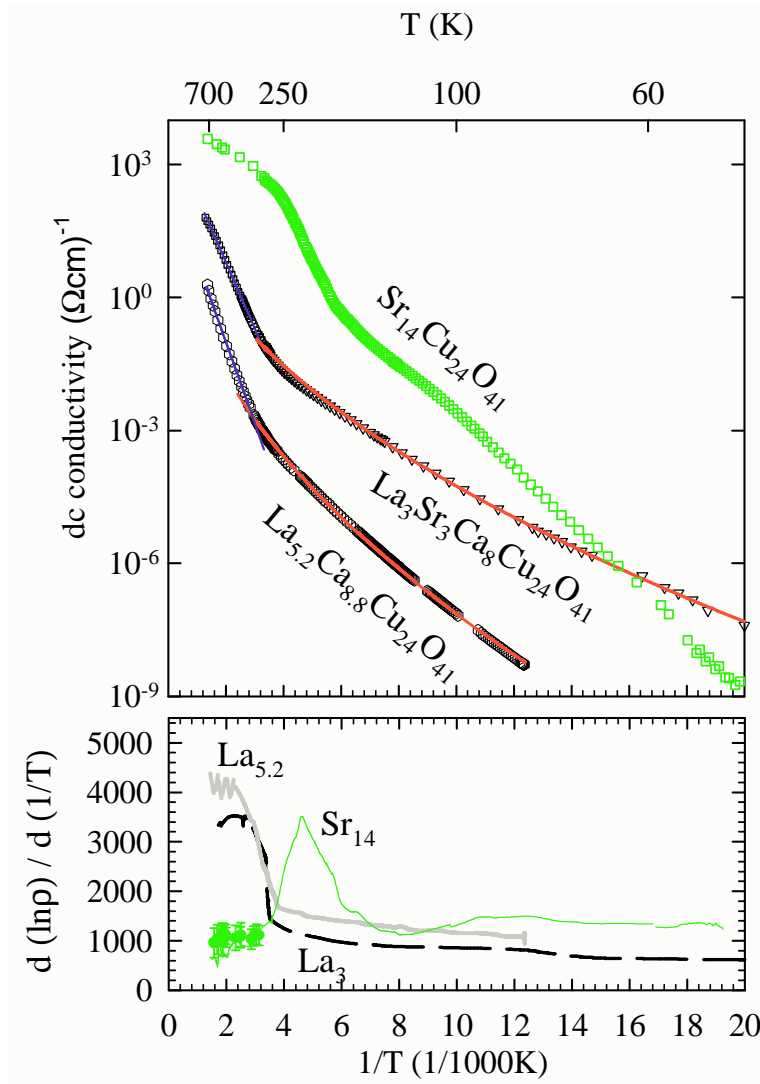


Fig. 5.9: Upper panel: dc conductivity  $\sigma_{dc}$  of  $\text{La}_3\text{Sr}_3\text{Ca}_8\text{Cu}_{24}\text{O}_{41}$  and  $\text{La}_{5.2}\text{Ca}_{8.8}\text{Cu}_{24}\text{O}_{41}$  compared to the one for  $\text{Sr}_{14}\text{Cu}_{24}\text{O}_{41}$ , along the  $c$ -axis, *vs.* inverse temperature. Solid, weakly curved lines are fits to Mott's VRH law, Eq. 5.4. Lower panel: corresponding logarithmic derivatives clarify the differences between the behavior of nonisovalently substituted compounds, denoted  $\text{La}_3$  and  $\text{La}_{5.2}$  and the parent compound, denoted  $\text{Sr}_{14}$ . For  $\text{Sr}_{14}$  well defined activation energies, in the high, 900 K, and especially in the low temperature insulating phase, 1300 K, may be found, with the phase transition observed as a peak in the logarithmic derivative at 210 K. On the contrary, for La-substituted materials only a change in the slope is observed for  $\text{La}_{5.2}$  and  $\text{La}_3$  at respective crossover temperatures, 330 K and 300 K. At high temperatures, well defined activation energies of 4200 K and 3200 K, respectively are found. Activation behavior changes over to a VRH law behavior for  $\text{La}_{5.2}$  and  $\text{La}_3$ , with characteristic energies  $5 \cdot 10^4$  K and  $2.9 \cdot 10^4$  K, respectively.

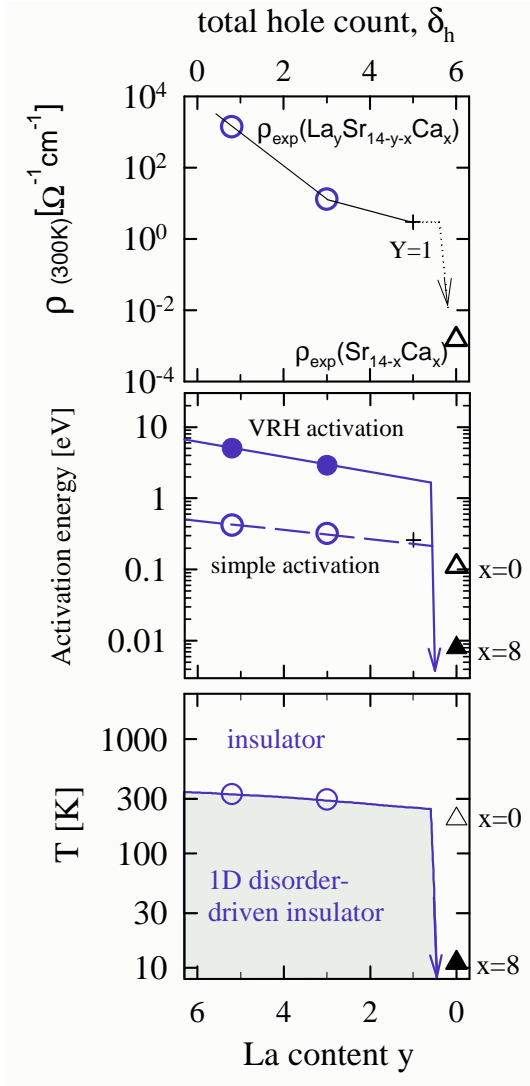


Fig. 5.10: dc electrical transport data for  $\text{Y}_1\text{Sr}_5\text{Ca}_8\text{Cu}_{24}\text{O}_{41}$  by Motoyama *et al.*, [84], crosses, complements our data for  $\text{La}_3\text{Sr}_3\text{Ca}_8\text{Cu}_{24}\text{O}_{41}$ ,  $\text{La}_{5.2}\text{Ca}_{8.8}\text{Cu}_{24}\text{O}_{41}$ , circles. These are compared to  $\text{Sr}_{14}\text{Cu}_{24}\text{O}_{41}$  and  $\text{Sr}_6\text{Ca}_8\text{Cu}_{24}\text{O}_{41}$ , denoted with triangles and also as  $x=0$ ,  $x=8$ , respectively. The La(Y) content corresponds to hole count,  $\delta_h = 6 - y$ . Upper panel: RT resistivity for  $\delta_h \leq 5$  is at least three orders of magnitude higher than for  $\text{Sr}_{14-x}\text{Ca}_x\text{Cu}_{24}\text{O}_{41}$  materials. Middle panel:  $\delta_h \leq 5$  materials may be characterized by simple activation, or by VRH activation energy, above and below the crossover temperature, respectively. These energies are higher than the activation energy of  $x=0$ , either in the high temperature insulating phase or in CDW. The energy difference is pronounced for  $x=8$ . Lower panel: The denoted temperatures for  $\text{La}_3$  and  $\text{La}_{5.2}$  are only crossover temperatures where a change occurs in the hopping transport mechanism. They do not correspond (vertical arrow) to CDW transition temperatures for  $x=0$ ,  $x=8$ .

toyama *et al.*, [84] complete the picture. The symbols on the right side,  $x=0$  and  $x=8$  denote the parent compound  $\text{Sr}_{14}\text{Cu}_{24}\text{O}_{41}$  and isovalently substituted  $\text{Sr}_6\text{Ca}_8\text{Cu}_{24}\text{O}_{41}$ , respectively. Comparison with the latter member of  $\text{Sr}_{14-x}\text{Ca}_x\text{Cu}_{24}\text{O}_{41}$  family is important, since Ca-content in this material is similar to Ca-content of presented La(Y) substituted materials. That is, if we set  $y$  to 0 in  $\text{La}_y\text{Sr}_{14-8-y}\text{Ca}_8\text{Cu}_{24}\text{O}_{41}$  we get  $x=8$  material.

In the upper panel, it is important to note that for materials where  $\delta_h \leq 5$  it is not possible to account for the resistivity decrease by a mere increase in the hole number. Also, the localization length  $\alpha^{-1} \approx 1\text{\AA}$  is quite similar for both  $\text{La}_{5.2}$  and  $\text{La}_3$ , while their RT resistivity differs for two orders of magnitude. Regardless of this observation, the most important result shown in this figure is that RT resistivities of materials where  $\delta_h \leq 5$  are at least three orders of magnitude higher than for materials  $\delta_h = 6$ . This difference is denoted by a vertical arrow.

In the middle panel and lower panel we note that the energy and temperature scales are different for the two families of materials. For  $x=0$  the difference is not pronounced as for  $x=8$  material, which has an order of magnitude lower energy/temperature scale. We note that La-content, which changes the number of holes dramatically, has only a minor influence on energy/temperature parameters in  $\delta_h \leq 5$  materials. On the contrary, Ca-content in  $\delta_h = 6$  materials has a major influence on energy/temperature scale. This occurs despite the fact that the redistribution of holes between the ladders (one hole in  $x=0$ ) and chains (five holes in  $x=0$ ) is minimal upon Ca-substitution. The difference in the influence of La-content and Ca-content and the respective hole count on the energy/temperature scales between  $\delta_h \leq 5$  and  $\delta_h = 6$  materials is denoted by vertical arrows, separating these families of materials.

### 5.2.5 Conclusions

The investigations of the frequency and temperature dependent conductivity yield clear evidence that nonisovalently substituted  $\text{La}_3\text{Sr}_3\text{Ca}_8\text{Cu}_{24}\text{O}_{41}$  and  $\text{La}_{5.2}\text{Ca}_{8.8}\text{Cu}_{24}\text{O}_{41}$  are insulators with hopping transport along the chains. At microscopic scale, we propose that strong local distortions of the chains due to irregular coordination of  $\text{La}^{3+}$ ,  $\text{Sr}^{2+}$  and  $\text{Ca}^{2+}$  ions [70, 71] induce a non-periodic potential in which holes reside. The VRH conductivity can be then viewed as a result of distorted distribution of microscopic conductivities, as predicted in Anderson localization theories. Therefore, copper-oxygen chains in nonisovalently substituted  $\text{La}_y\text{Sr}_{14-y-x}\text{Ca}_x\text{Cu}_{24}\text{O}_{41}$  can be considered as a one-dimensional system in which disorder, associated with random distribution of holes, causes the Anderson localization. We assume that the chain subsystem behaves as a one-dimensional disorder-driven insulator for the whole range of La-substituted materials, *i.e.* for the whole range of hole counts  $0 \leq \delta_h < 6$ .

Featuring at least three orders of magnitude higher resistivity at RT, the charge transport in  $\text{La}_y\text{Sr}_{14-y-x}\text{Ca}_x\text{Cu}_{24}\text{O}_{41}$  was ascribed to a hopping mechanism in the chain subsystem - a different one than the transport in a gapped insulator  $\text{Sr}_{14}\text{Cu}_{24}\text{O}_{41}$  (hole count  $\delta_h = 6$ ). This confirms our assumption from Sec. 5.1- that the charge transport in  $\text{Sr}_{14-x}\text{Ca}_x\text{Cu}_{24}\text{O}_{41}$  is due to the mobile holes residing in the ladders. This also yields a definite evidence that CDW in  $\text{Sr}_{14}\text{Cu}_{24}\text{O}_{41}$  is established in the ladders, as we suggested [160, 167].

While no ordering is observed for the chains in  $\text{La}_y\text{Sr}_{14-y-x}\text{Ca}_x\text{Cu}_{24}\text{O}_{41}$ , for the chains in  $\text{Sr}_{14}\text{Cu}_{24}\text{O}_{41}$  it was previously shown that a charge gap opens due to the charge order (CO) related to spin-ordering according to the antiferromagnetic dimers pattern. Note that the CO is established in the chains concomitantly with the CDW phase in the ladders. Thus, a possibility is revealed for the existence of a phase transition in the phase diagram of  $(\text{La,Sr,Ca})_{14}\text{Cu}_{24}\text{O}_{41}$  compounds. We propose that the disordered chains subsystem  $0 \leq \delta_h < 6$  crosses over into a charge-ordered gapped insulator at  $\delta_h = 6$ . However, the way how the transport switches from the chains to the ladders in  $5 < \delta_h < 6$  range is still an open issue. Is there a phase transition from La-substituted to La-free materials and how the phase diagram of the former merges with the one of the latter should be resolved by further experiments on materials with very low La content, which corresponds to  $\delta_h \lesssim 6$ .

### 5.3 Suppression of CDW, in ladders of $\text{Sr}_{14-x}\text{Ca}_x\text{Cu}_{24}\text{O}_{41}$ , by Ca-substitution, $x=0, 3, 6, 8, 9, 11.5$

Superconductivity is established at pressures above 3 GPa in the isovalently substituted compounds  $\text{Sr}_{14-x}\text{Ca}_x\text{Cu}_{24}\text{O}_{41}$ . It is only observed for high Ca-content materials,  $10 \leq x \leq 13.6$ , [106]. We have shown for the parent compound  $\text{Sr}_{14}\text{Cu}_{24}\text{O}_{41}$ ,  $x=0$ , that CDW is established in the ladders, where mobile holes are found. These findings confirm theoretical suggestions that, due to the quasi one-dimensional nature of ladders, a CDW may compete with the occurrence of superconductivity in the hole-doped ladder system. Obviously, upon Ca-substitution, CDW has to give way to SC ground state.

Here we present the results of our further investigation, which addressed the Ca substituted materials,  $\text{Sr}_{14-x}\text{Ca}_x\text{Cu}_{24}\text{O}_{41}$ ,  $x=0, 3, 6, 8, 9, 11.5$ . We intended to clarify the question of the competition (or balance?) between the two ground states for all  $\text{Sr}_{14-x}\text{Ca}_x\text{Cu}_{24}\text{O}_{41}$  materials. We performed two different sets of experiments. Firstly, we extended the picture obtained for  $\text{Sr}_{14}\text{Cu}_{24}\text{O}_{41}$  by measuring  $\text{Sr}_{14-x}\text{Ca}_x\text{Cu}_{24}\text{O}_{41}$  compounds of different Ca-contents  $x \neq 0$ . Secondly, we also studied the transport anisotropy for different  $x$  materials.

#### 5.3.1 dc transport $E||c$ , $0 \leq x \leq 11.5$

In Fig. 5.11 we present the results of dc resistivity  $\rho_{dc}$  vs. inverse temperature  $1/T$ , in comparison for all the compounds under study,  $x=0, 3, 6, 8, 9, 11.5$ . The symbol  $E||c$  denotes measurements along the  $c$ -axis, that is, along the legs of ladders. The temperature range of measurement was from 750 K down to 2 K. All the materials show comparable and high RT conductivities in the range  $300\text{--}1200 \Omega^{-1}\text{cm}^{-1}$ , Table 5.2, confirming the existence of mobile holes transferred in the ladders.

The energy gaps become, Table 5.2, larger when going from high temperatures into the CDW phase, indicating that an additional gap opens for  $0 \leq x \lesssim 6$ , Fig. 5.11. While in the standard CDW, a transition from the metallic state to the insulating state is observed due to the opening of an energy gap [126], in the present case the transport in the high temperature (H.T.) phase is already non-metallic. We explain this by electron-electron interactions within the ladders, leading towards a Mott-insulator. As far as CDW ground state observed in  $\text{Sr}_{14-x}\text{Ca}_x\text{Cu}_{24}\text{O}_{41}$  is concerned, we suggest that it might fall between the two well defined limits of charge order: the CDW order of itinerant charges and the charge order (CO) of localized

charges.

The transition broadens substantially with increasing  $x$ , as reflected by an increase of the transition width and a decrease of the peak height of  $d(\ln \rho)/d(T^{-1})$  plotted in the lower left panel of Fig. 5.11. The broadening might be attributed to disorder introduced by Ca-substitution; a well known effect in quasi-1D compounds [27]. For  $x=8, 9$ , Fig. 5.11,  $\Delta_{CDW}$  is strongly suppressed, when compared with  $\Delta_{H.T.}$ , which is here 2-3 times higher. Therefore, in the logarithmic derivative only a step-like feature appears. The width of the step we consider analogous to the width of the peak at half maximum (FWHM) for  $x=0, 3, 6$ , see Sec. 5.1.1. That is, the transition broadening is further documented, since the relative width of the step (normalized to the respective temperature scale) for  $x=8, 9$  is larger than FWHM divided by respective  $T_c$  for  $x=0, 3, 6$ .

Correspondingly to CDW gap, transition temperature decreases from 210 K for  $x = 0$  to 7 K for  $x = 9$ , as denoted by arrows in Fig. 5.11. For  $x=11.5$  at a crossover temperature  $T_{co} = 6.5$  K  $\rho_{dc}$  activation energy changes, from  $\Delta_{H.T.} = 22$  K to  $\Delta_{L.T.} = 5$  K. The ratio  $2\Delta_{L.T.}/3.52T_{co} = 0.4$  is much lower than one. And we note that for  $x=0, 3, 6, 8, 9$ , where we identify CDW transition the ratio is  $2\Delta_{CDW}/3.52T_c \approx 3$ . In a mean-field theory like BCS this ratio should be one, and in the real q1D systems it is usually enhanced above one. Therefore, we can not consider that  $T_{co}$  for  $x=11.5$  corresponds to a phase transition.

c-axis	$\sigma(300\text{K})$ ( $\Omega\text{cm}^{-1}$ )	$T_c$ (K)	$\delta T_c/T_c$	$\Delta_{CDW}$ (K)	$\Delta_{H.T.}$ (K)
$x=0$	500	210	0.1	$1300 \pm 50$	$900 \pm 250$
$x=3$	400	140	0.3	$1100 \pm 50$	$800 \pm 100$
$x=6$	300	55	0.4	$300 \pm 40$	$280 \pm 60$
$x=8$	600	11	0.35	$80 \pm 10$	$160 \pm 20$
$x=9$	1200	7	0.4	$30 \pm 5$	$100 \pm 20$
$x=11.5$	1000	$T_{co} = 6.5$			

Table 5.2: dc transport parameters for  $\text{Sr}_{14-x}\text{Ca}_x\text{Cu}_{24}\text{O}_{41}$  materials: RT conductivity, CDW transition temperature, relative transition width, CDW activation energy, and high temperature insulating phase activation energy.

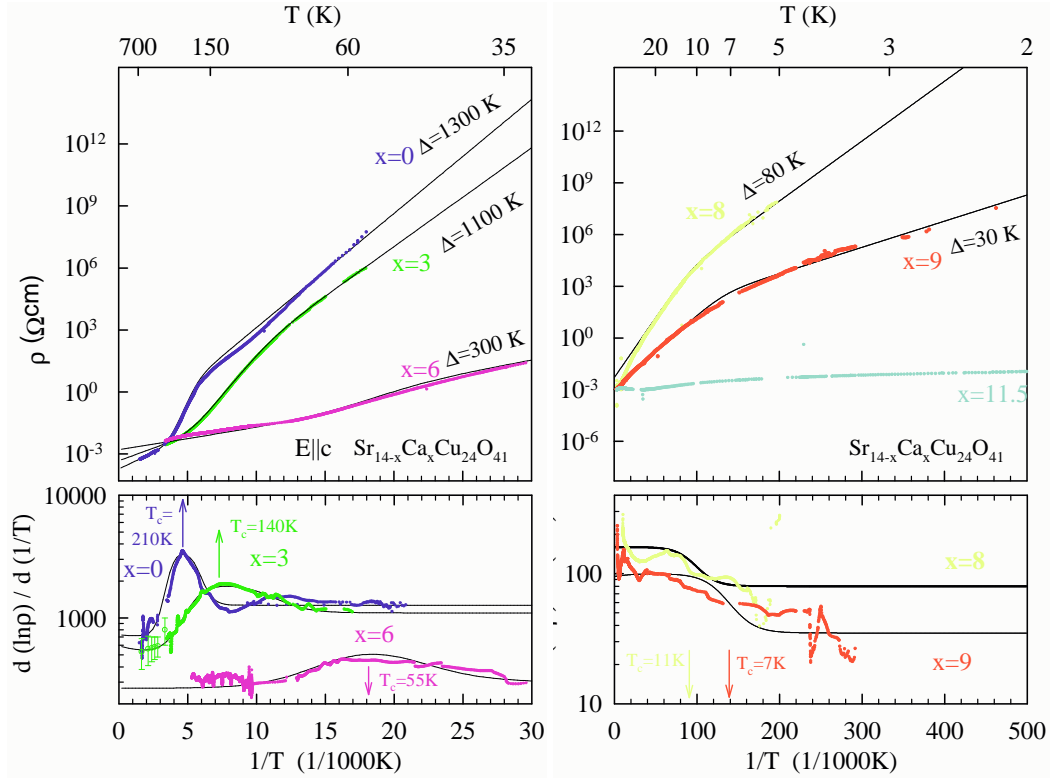


Fig. 5.11: The dc resistivity is activated  $\rho_{dc} \propto e^{\Delta_{CDW}/k_B T}$  below  $T_c$  with activation energies  $\Delta_{CDW}$  denoted. The high temperature phase is also characterized by a well defined activation energy  $\Delta_{H.T.}$ . For  $x=0, 3, 6$   $\Delta_{H.T.}$  is lower than  $\Delta_{CDW}$  and transition temperature  $T_c$  can be determined from a peak in the logarithmic derivative of the resistivity. For  $x=8, 9$   $\Delta_{H.T.}$  becomes 2-3 times higher than  $\Delta_{CDW}$  and in the logarithmic derivative only a step-like feature appears. For  $x=11.5$  there is no transition to CDW phase. At a crossover temperature  $T_{co} = 6.5$  K only  $\rho_{dc}$  activation energy changes, from 22 K to 5 K. In all panels the full lines guide the eye.

### 5.3.2 ac response $E||c$ , $0 \leq x \leq 9$

In the frequency range 0.01 Hz - 1 MHz the spectra of the dielectric function were obtained from the complex conductance measured at  $2 \text{ K} < T < 200 \text{ K}$ . All measurements were done along the crystallographic  $c$ -axis of high-quality single crystals.

A specific analysis of the radio-frequency complex conductance allowed to follow-up the CDW dielectric response through the respective phase transition temperature ranges for  $x=3, 6, 8, 9$  materials. It was not possible for  $x=0$  since the feature which allowed this analysis was out of the frequency window. This analysis will be demonstrated for  $x=3$ . In the left panels of Fig. 5.12 normalized,  $\frac{G-G_0}{G_0}$ , real part of the conductivity,  $G$  vs. frequency is shown.  $G_0$  stands for low-frequency, equal to dc, conductivity, see Sec. 3.2. The imaginary part of the conductivity,  $B$  is also shown at several temperatures. What is particular is, that at temperatures 150 K and 159 K, the CDW dielectric mode has left the frequency window.  $G$  remains constant within the frequency window, while the contribution to the static dielectric constant is still observed as *tails* in  $B$ . As  $B$  is proportional to the frequency, the static dielectric constant may be extracted from this proportionality,  $\epsilon_0 = B/\omega$ . Corresponding  $\epsilon'$  tails are shown in the right panel where real,  $\epsilon'$ , and imaginary,  $\epsilon''$ , parts of the dielectric function are shown. Naturally, central relaxation time  $\tau_0$  and the shape parameter  $1 - \alpha$  can not be extracted in this manner (see Fig. 5.17). At lower temperatures, where the mode is inside the frequency window these two parameters are extracted along  $\Delta\epsilon$  by a standard procedure described in Sec. 3.2, as for  $x = 0$ .

A pronounced dielectric relaxation is observed for all compositions  $x=3, 6, 8$  and  $9$ , as well as for  $x=0$  (see also Fig. 5.2) providing evidence for the CDW formation [78, 160]. In Fig. 5.12, right panel, we show for  $x=3$ , the screened loss peak ( $\epsilon''$ ) centered at  $\tau_0^{-1}$ , which moves toward lower frequencies and smaller amplitudes with decreasing temperature. The main features of this relaxation do not qualitatively change on Ca-substitution, for  $0 \leq x \leq 9$ : the dielectric strength  $\Delta\epsilon = \epsilon_0 - \epsilon_{HF} \approx 5 \times 10^4$ , the symmetric broadening of the relaxation-time distribution given by  $1 - \alpha \approx 0.8$ , and the central relaxation time  $\tau_0$ , which closely follows a thermally activated behavior in a manner similar to the dc resistivity;  $\tau_0(T) \propto \rho(T)$  (see also Fig. 5.1).

Our results clearly demonstrate that a phase transition to the CDW ground state is strongly suppressed by Ca-substitution. This demonstration is based on the strong correspondence between dc resistivity and LFDS results. In Fig. 5.13 this is depicted for three representative Ca-contents  $x$ . On decreasing temperature, a sharp growth of  $\Delta\epsilon$  starts in the close vicinity of  $T_c$  and reaches the huge value of the order of  $10^4 - 10^5$  at  $T_c = 140 \text{ K}$  and

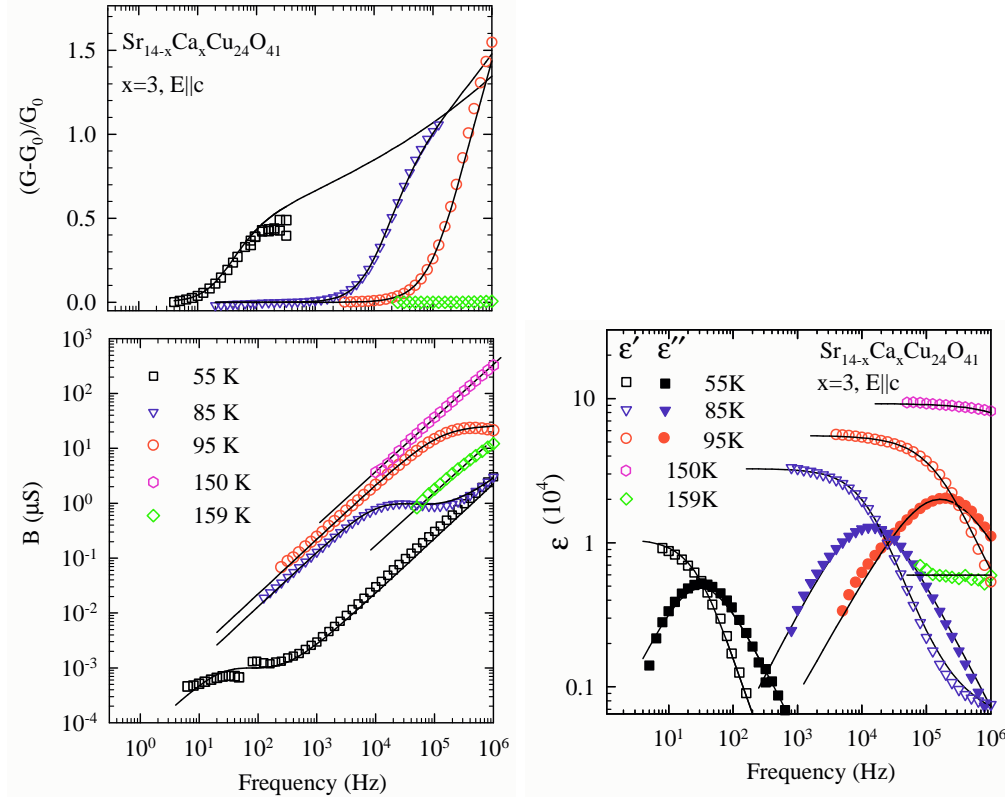


Fig. 5.12: Left panels: LFDS data analysis for the example of  $x=3$ . Normalized,  $\frac{G-G_0}{G_0}$ , frequency-dependent real part of the conductivity, is shown in the upper left panel. In the lower left panel the imaginary part of the conductivity,  $B$  is also shown at several temperatures. The *tails* at 150 K and 159 K are due to the dielectric strength of the dielectric modes appearing at frequencies above the experimental frequency window. Right panel: Corresponding real and imaginary parts of the dielectric function as a function of frequency. The full lines are from fits by the generalized Debye expression:  $\epsilon(\omega) - \epsilon_{HF} = \Delta\epsilon/[1 + (i\omega\tau_0)^{1-\alpha}]$ . The full lines in the *tails* at 150 K and 159 K simply denote the dielectric strength of the modes existing above the experimental frequency window.

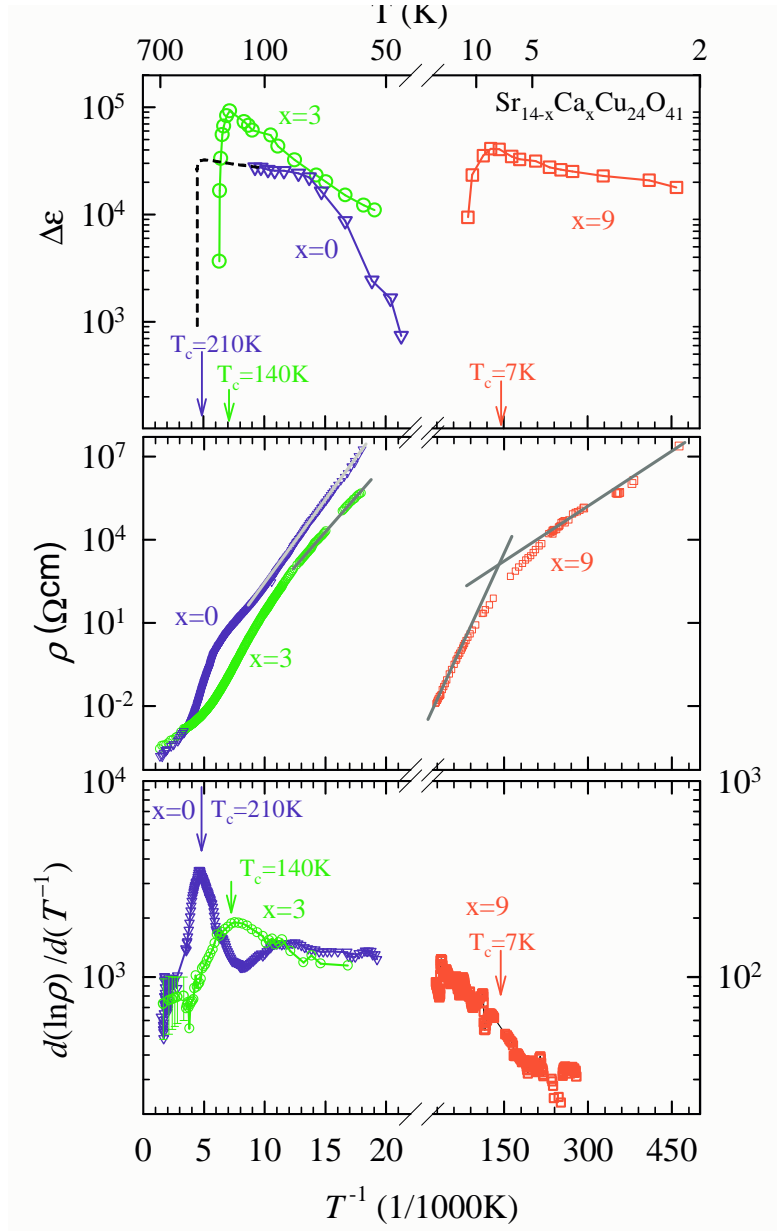


Fig. 5.13: Temperature dependence of the dielectric strength  $\Delta\varepsilon$  of the CDW radio-frequency related mode (upper panel) and dc resistivity  $\rho$  (middle panel) in  $\text{Sr}_{14-x}\text{Ca}_x\text{Cu}_{24}\text{O}_{41}$  for three representative Ca-contents  $x$ . dc and LFDS measurements are performed along the  $c$  axis. The arrows indicate the CDW phase transition temperature  $T_c$ , as determined from the logarithmic derivative of the resistivity, presented in the lowest panel. The temperatures where  $\Delta\varepsilon$  attains maximum, correspond perfectly to these  $T_c$ , for the respective material. In the upper panel the full lines guide the eye, while in the middle panel the lines represent fits by Arrhenius functions. An assumed behavior of  $\Delta\varepsilon$  for  $x = 0$ , based on that observed for  $x = 3$  and  $9$ , is represented by a dashed line.

$T_c = 7$  K for  $x = 3$  and  $9$ , respectively. These  $T_c$  values perfectly correspond to the temperature of the phase transition as determined in the dc resistivity measurements, indicated by pronounced peaks at  $T_c$  in the derivative of the resistivity. The overall decrease of  $\Delta\varepsilon$  below  $T_c$  for  $x=0$  is substantial. This issue was already addressed in Sec. 1.2.5 and 5.1.1. We suggested that a back-transfer of holes from ladders to chains starts below 70 K. Based on the decrease of  $\Delta\varepsilon$ , this assumption may be extended for  $x=3$ . It has to be noted that the decrease becomes much less pronounced for  $x=9$ , indicating a minor, if any back-transfer for this material.

Finally, we comment on the Stuttgart group microwave/FIR results [78, 160]. The conductivity decreases below approximately  $2500 \text{ cm}^{-1}$  for  $x = 0$  and  $3$ , and around  $25 \text{ cm}^{-1}$  for  $x = 9$ , which we associate with the opening of the CDW gap. This decrease is only observed for  $x=0$ ,  $x=3$  and  $x=9$  at temperatures lower than 240 K, 150 K and 20 K, respectively. These temperatures nicely agree with the CDW phase transition temperature  $T_c$  as determined from dc and LFDS (Fig. 5.13). Moreover, the CDW gap values  $\Delta_{CDW}$  extracted from these measurements ( $1300 \text{ K} \approx 900 \text{ cm}^{-1}$ ,  $1100 \text{ K} \approx 750 \text{ cm}^{-1}$  and  $30 \text{ K} \approx 20 \text{ cm}^{-1}$ , for  $x=0$ ,  $3$  and  $9$ , respectively) correspond well to the edges seen in the optical conductivity spectra.

### 5.3.3 Features of CDW phason response in $\text{Sr}_{14-x}\text{Ca}_x\text{Cu}_{24}\text{O}_{41}$ , $0 \leq x \leq 9$ , $E||c$

As shown above, the CDW phason response to ac electric fields is qualitatively similar for all  $0 \leq x \leq 9$ . Below, we summarize additional similarities.

Firstly, we note that the dc field dependence was consistent for all  $0 \leq x \leq 9$ . That is, it featured only a negligible nonlinearity for the representative Ca-contents  $x=3,9$ , similarly to the one described before for  $x=0$  - no sliding conductivity was observed. For  $x=3,9$  as well as for  $x=0$ , the applied electric fields reached  $10 \text{ V/cm}$ , see Sec. 5.1.2.

Secondly, we note that besides for  $x=0$ , the pinned mode was detected for  $x=3$ , but not for  $x=9$ , [163]. The latter may be due to the screening by the larger number of free carriers in this compound. Since we observe the screened temperature-dependent response in the radio-frequency range centered at  $\tau_0^{-1}$  (see Fig. 5.12), which represents a fingerprint of the CDW phason response, see Sec. 2.4, for  $x=0$  all the way up to  $x=9$ , we can safely assume that the pinned mode always exists around  $\Omega_0 \approx 1.8 \text{ cm}^{-1}$ . Using the same analysis as in Sec. 5.1.3, and assuming that the number of holes remains close to 1 in the ladders of  $0 \leq x \leq 9$ , we estimate the effective mass  $m^* \approx 100$ . There is basically no dependence on temperature or Ca content

for  $x$  between 0 and 9.

Thirdly, we identified an additional feature of the CDW phason response in complex conductivity results for the whole range of materials  $0 \leq x \leq 9$ . It is based on the observation of non-negligible high frequency dielectric constant,  $\varepsilon_{HF}$ . This is observed in LFDS measurements as the contribution to the real part of the dielectric function above the CDW radio-frequency mode, *e.g.* at 1 MHz. That is,  $\varepsilon_{HF}$  contains the dielectric strength of pinned mode, as well as single-particle contributions with modes in the optical frequency range. All these contributions are not expected to be above  $\varepsilon_{HF} \approx 10$ . For the aspect ratios of the samples under study,  $\varepsilon_{HF}$  of this magnitude would be below measurable limit. Contrary to this, we observed measurable  $\varepsilon_{HF}^{exp}$  as given in Table 5.3. We compare the experimental values with the theoretical ones  $\varepsilon_{HF}^{th}$ , calculated according to an expression relating the plasma frequency,  $\Omega_{plasma}$ , and the energy gap characterizing the 1D system,  $\Delta$ , [37]:

$$\varepsilon_{HF}^{th} = 1 + \frac{1}{6} \frac{\Omega_{plasma}^2}{\Delta^2} \quad (5.6)$$

We note from Table 5.3 that the best correspondence is obtained when calculating with  $\Delta_{H.T.}$ , and not  $\Delta_{CDW}$ . Although, if  $\varepsilon_{HF}^{exp}$  is assumed to be the dielectric strength of the (CDW) pinned mode, then  $\Delta_{CDW}$  should be a better choice. In any case, we suggest that the observed  $\varepsilon_{HF}^{exp}$  confirms the existence of pinned mode for higher Ca-contents, which existence was only assumed for  $x=9$ , see just above.

c-axis	$\Omega_{plasma}$ (eV)	$\Delta_{CDW}$ (K)	$\varepsilon_{HF}^{th}$	$\Delta_{H.T.}$ (K)	$\varepsilon_{HF}^{th}$	$\varepsilon_{HF}^{exp}$
$x=0$	0.5	1300	4	900	8	< 10
$x=3$	0.7	1100	9	800	16	< 10
$x=6$	0.8	300	150	300	150	$100 \pm 100$
$x=8$	0.87	80	2500	160	600	$500 \pm 100$
$x=9$	0.9	30	15000	100	1500	$800 \pm 100$

Table 5.3:  $\Delta_{CDW}$ ,  $\Delta_{H.T.}$ : CDW(H.T.) gap from dc resistivity and/or LFDS.  $\Omega_{plasma}$ : plasma frequency from optical measurements by Osafune *et al.*, [75].  $\varepsilon_{HF}^{exp/th}$ : the observed and theoretically calculated values of high frequency dielectric constant.

## 5.4 Evidence for anisotropic CDW in ladder planes

Following the study of  $\text{Sr}_{14-x}\text{Ca}_x\text{Cu}_{24}\text{O}_{41}$  compounds of different Ca-contents  $x \neq 0$ , we also studied the transport anisotropy for different  $x$  materials. In particular, when discussing the suppression of the CDW ground state in  $\text{Sr}_{14-x}\text{Ca}_x\text{Cu}_{24}\text{O}_{41}$ , the dimensionality and its relation to the Ca-substitution (or pressure) is important. Our intention was to resolve whether the nesting arguments have to be taken into account. Resolving the issue for CDW ground state would certainly clarify the picture for the competing SC state.

All experiments were conducted on high-quality single crystals along the three crystallographic axis:  $c$ - (along the ladder legs),  $a$ - (along the ladder rungs) and  $b$ - (perpendicular to the ladder planes). The dc resistivity and ac complex conductivity of  $\text{Sr}_{14-x}\text{Ca}_x\text{Cu}_{24}\text{O}_{41}$  ( $x=0, 3, 6, 8, 9$  and  $11.5$ ) were investigated in the temperature range  $2 \text{ K} < T < 700 \text{ K}$ .

### 5.4.1 dc transport $E||c$ , $E||a$ , $E||b$ , $0 \leq x \leq 11.5$

We compare the dc transport properties of  $\text{Sr}_{14-x}\text{Ca}_x\text{Cu}_{24}\text{O}_{41}$  along all three directions. Fig. 5.14 reveals for three representative Ca-contents  $x=0, 3, 9$  that the phase transition temperatures  $T_c$ , when measured along the  $c$ - and  $a$ -axis, are equal in value and have the same dependence on Ca substitution, Table 5.4. The same holds for the energy gaps in the high temperature phase above  $T_c$  and in the CDW ground state, which both are isotropic. The energy gaps become larger when going from high temperatures into the CDW phase, indicating that an additional gap opens for  $x \lesssim 6$ , as discussed in Sec. 5.3.1. The substantial transition broadening with increasing  $x$ , observed for measurements along the ladder legs is also observed along the ladder rungs, with similar transition widths, Fig. 5.14. The above results and correspondences are also found for  $x=6, 8$  compounds, not shown in Fig. 5.14. For  $x=11.5$  (where no CDW transition occurs) the  $a$ -direction dc transport properties of the insulating phase were similar to the previously shown for the  $c$ -direction, Table 5.4.

While dc transport within the ladder ( $c, a$ ) plane shows a set of properties similar for both directions, the dc resistivity along the third,  $b$ -direction, perpendicular to the ladder planes shows a distinct behavior, Table 5.4, Fig. 5.14. Different activation energies are observed, and no phase transition is registered. For  $x=3, 9$ , indeed, we observe a single activation in the whole temperature range. For  $x=0$  the activation energy is larger at high temperatures than any of the observed for the  $c, a$  plane and changes over

below 170 K to a twice lower value. The simple activation process observed for the  $b$ -direction indicates that the charge transport perpendicular to the ladder planes probably happens via nearest-neighbor hopping, as expected between disordered chains. Particularly, the large  $\Delta$  for  $x=0$ , changing over to a smaller one, Table 5.4, reminds of the hopping transport mechanism we observed along disordered chains of  $\text{La}_y\text{Sr}_{14-y-x}\text{Ca}_x\text{Cu}_{24}\text{O}_{41}$  compounds, Fig. 5.9, Sec. 5.2.1. We finish the exposition for the  $b$ -direction by concluding that the CDW certainly does not develop a long range order in 3D for any  $x$ .

Finally, a word is in order to comment the issue of the CDW phase transition temperature and the in-plane extent of the CDW order. The peak in  $d(\ln \rho)/d(T^{-1})$  is a clear sign of the phase transition and we can safely assume that the long-range-order is established below  $T_c$  in the ladder plane ( $c,a$ ) for  $x \lesssim 6$ . In contrast to that, for  $x=8, 9$ , only a change in the slope is observed in the resistivity, for both in-plane directions, indicating that the CDW order, with only a finite in-plane correlation length, is established.

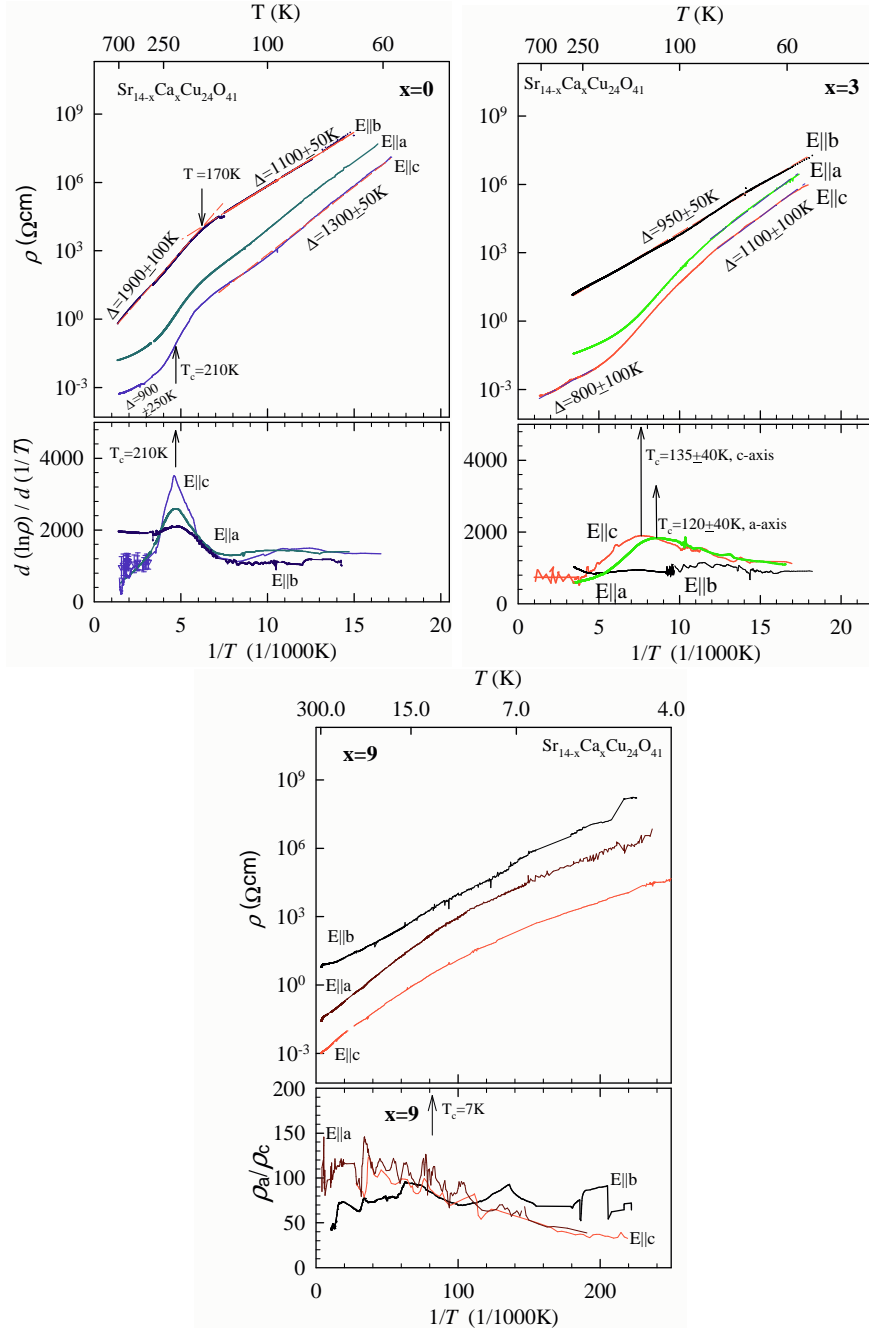


Fig. 5.14: dc resistivity data for three representative compositions  $x=0, 3, 9$ , measured along three directions, is shown in the upper panels. Corresponding logarithmic derivatives of the resistivity for all directions are shown in the lower panels. In the  $a$ - and  $c$ -direction (see Sec. 5.3.1), a peak for  $x=0, 3$  (or a step for  $x=9$ ) in  $d(\ln \rho)/d(T^{-1})$  indicates that CDW order is established (only a short-range one for  $x=9$ , see text). For the  $b$ -direction no such features - *i.e.* no ordering is observed.  $\rho_{dc}$  is thermally activated and the activation energies (denoted in the upper panels) are isotropic in the ( $c, a$ ) ladder plane, both in CDW and HT insulating phases. Different activation energy is observed perpendicular to the ladder plane, in  $b$ -direction. For  $x=3, 9$  this activation energy is constant in the temperature range of study, while for  $x=0$  a crossover is observed at 170 K.

	$\sigma_{RT}$ (S/cm)	$T_c$ (K)	$\Delta_{CDW}$ (K)	$\Delta_{H.T.}$ (K)	$\rho_i/\rho_j$ 300K	$\rho_i/\rho_j$ CDW	$\Delta\varepsilon_{max}$ at $T_c$	$\Delta\varepsilon_c/$ $\Delta\varepsilon_a$
$x=0$ c-axis	500	210	$1300 \pm 50$	$900 \pm 250$			$3 \times 10^4$	7.5
a-axis	17	210	$1300 \pm 50$	$800 \pm 300$	$\rho_a/\rho_c$ 30	$\rho_a/\rho_c$ 15	$4 \times 10^3$	
b-axis	0.03	$T_{co}$ 170	$\Delta_{L.T.}$ $1100 \pm 50$	$1900 \pm 100$	$\rho_b/\rho_c$ 10000	$\rho_b/\rho_c$ 300	no mode	
$x=3$ c-axis	400	140	$1100 \pm 50$	$800 \pm 100$			$1 \times 10^5$	2.5
a-axis	27	120	$1100 \pm 50$	$800 \pm 300$	$\rho_a/\rho_c$ 10	$\rho_a/\rho_c$ 3	$4 \times 10^4$	
b-axis	0.01	—	$950 \pm 50$	$950 \pm 50$	$\rho_b/\rho_c$ 40000	$\rho_b/\rho_c$ 15	no mode	
$x=6$ c-axis	300	55	$300 \pm 40$	$280 \pm 60$			$9 \times 10^4$	—
a-axis	70	55	$300 \pm 40$	$360 \pm 60$	$\rho_a/\rho_c$ 4	$\rho_a/\rho_c$ 5	—	
$x=8$ c-axis	600	11	$80 \pm 10$	$160 \pm 20$			$5 \times 10^4$	$\infty$
a-axis	54	11	$80 \pm 10$	$160 \pm 20$	$\rho_a/\rho_c$ 10	$\rho_a/\rho_c$ 12	no mode	
$x=9$ c-axis	1200	7	$30 \pm 5$	$100 \pm 20$			$4 \times 10^4$	$\infty$
a-axis	40	7	$30 \pm 5$	$100 \pm 20$	$\rho_a/\rho_c$ 30	$\rho_a/\rho_c$ 150	no mode	
b-axis	0.1	—	$70 \pm 10$	$70 \pm 10$	$\rho_b/\rho_c$ 10000	$\rho_b/\rho_c$ 30000	no mode	
$x=11.5$ c-axis	1000	$T_{co}$ 6.5	$\Delta_{L.T.}$ 5	$\Delta_{H.T.}$ 22		$\rho_i/\rho_j$ H.T.	no mode	
a-axis	1000	6.5	5	22	$\rho_a/\rho_c$ 10	$\rho_a/\rho_c$ 50	no mode	

Table 5.4: dc transport parameters for  $Sr_{14-x}Ca_xCu_{24}O_{41}$  materials, measured in all three directions: room temperature conductivity, CDW transition temperature, CDW activation energy, high temperature insulating phase activation energy, anisotropy at 300K, anisotropy in CDW phase. For comparison LFDS data, *i.e.* the maximum values of dielectric strength, for the *c*- and *a*-directions, where the dielectric dispersion was observed, are shown. The ratio of maxima,  $\Delta\varepsilon_c/\Delta\varepsilon_a$ , can be correlated with the dc anisotropy  $\rho_a/\rho_c$ .

### 5.4.2 ac response $E||c$ , $E||a$ , $0 \leq x \leq 9$

Fig. 5.15 shows the conductivity spectra in a broad frequency range measured along the ladder rungs,  $E||a$ , for three representative Ca-contents  $x=0,3,9$ . For  $x=0,3$ , as well as for  $x=6$ , not shown, a strong temperature dependent relaxation of the dielectric function  $\varepsilon(\omega) = \varepsilon' + i\varepsilon''$  is found, as seen in the insets. Our dc/LFDS data are combined with microwave/FIR data obtained by Stuttgart group, taken from Ref. [161].

Fits by the generalized Debye expression Eq. 5.1 yield the main parameters of this relaxation: the dielectric strength  $\Delta\varepsilon = \varepsilon_0 - \varepsilon_{HF} \approx 10^3$ , the symmetric broadening of the relaxation-time distribution given by  $1 - \alpha$ , and the central relaxation time  $\tau_0$ . These fits are shown as solid lines in the Insets of Fig. 5.15. Also, we show the corresponding Cole-Cole plots which relate  $\varepsilon'$  and  $\varepsilon''$  components, confirming that the quality of fits, and the reliability of the data, is equal for the results obtained along the ladder rungs and the ladder legs direction, Fig. 5.16.

In Fig. 5.17, for the representative compound  $x=3$ , we compare the main parameters from measurements along the ladder legs and along the ladder rungs. Qualitatively similar results were obtained for  $x=0$  and 6. While the dielectric strength along the rungs is an order of magnitude smaller than the one observed along the legs (for  $x=0$ , see Fig. 5.16), the thermally activated behaviors are almost identical for both directions, lower panel, Fig. 5.17. The activation energy is similar to that of the dc conductivity in the CDW phase, Table 5.4. The dielectric response sets in below the phase transition temperatures  $T_c=210$  K ( $x=0$ ), 140 K ( $x=3$ ), and 55 K ( $x=6$ ) in the same manner as found along the ladder legs. That is, the dielectric strength  $\Delta\varepsilon$  reaches maximum at the same temperatures for both the  $a$ - and the  $c$ -axis. The width of the relaxation in both directions is similar,  $1 - \alpha \approx 0.8$ .

These result suggests that the same mechanism, *i.e.* the screening of a CDW phason due to Coulomb interaction [125], is responsible for the ac properties in both directions of  $\text{Sr}_{14-x}\text{Ca}_x\text{Cu}_{24}\text{O}_{41}$ , along the ladder legs and along the ladder rungs. For higher Ca content  $x=8$  (not shown here) and  $x=9$  the analogy breaks down since no such dispersion is detected for  $E||a$  down to 4.2 K, Fig. 5.15, 5.16.

In the third direction ( $E||b$ ), we find no signature of a CDW-related dielectric response at any Ca-substitution. Two compositions  $x=0$  and 3 have been studied in detail. A completely featureless radio-frequency conductivity is observed, as for  $\text{La}_y\text{Sr}_{14-y-x}\text{Ca}_x\text{Cu}_{24}\text{O}_{41}$  compounds. Indeed, as in dc, ac measurements show similarity between the transport along the disordered chains of  $\text{La}_y\text{Sr}_{14-y-x}\text{Ca}_x\text{Cu}_{24}\text{O}_{41}$  materials and the transport perpendicular to the ladder planes in  $\text{Sr}_{14-x}\text{Ca}_x\text{Cu}_{24}\text{O}_{41}$ .

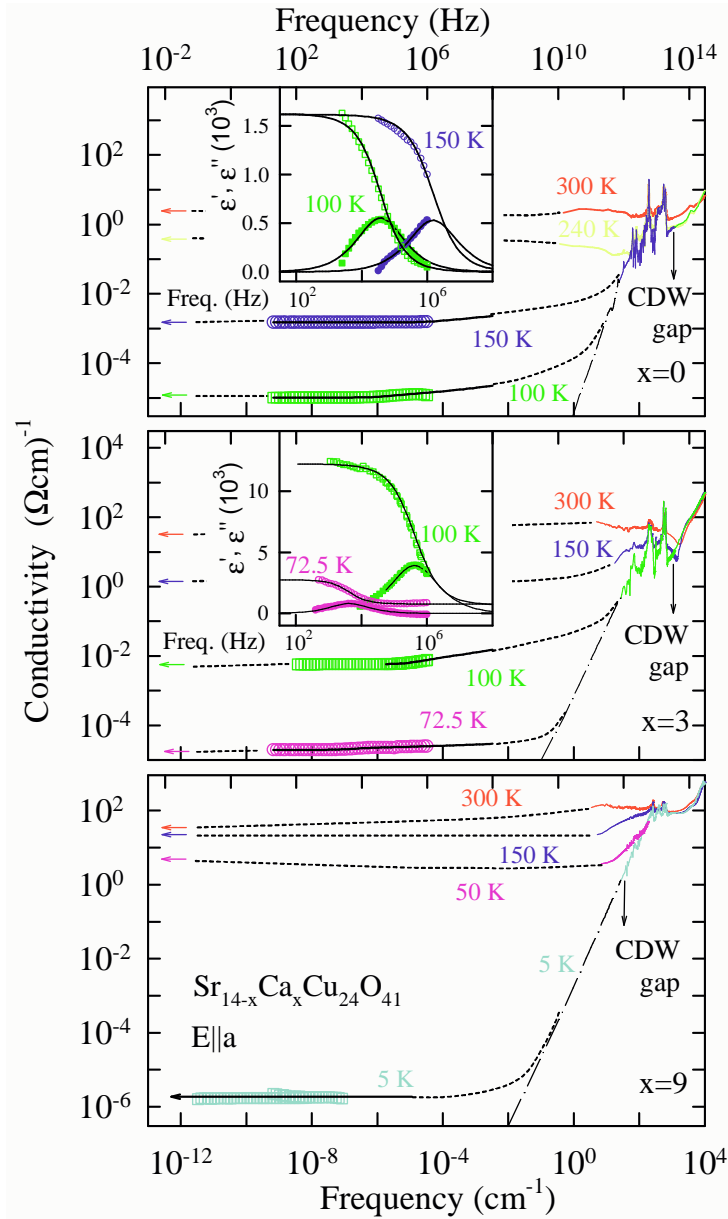


Fig. 5.15: Broad-band spectra of conductivity and complex dielectric function (real  $\epsilon'$  and imaginary  $\epsilon''$  parts) of  $\text{Sr}_{14-x}\text{Ca}_x\text{Cu}_{24}\text{O}_{41}$  along the  $a$  crystallographic axis for Ca contents  $x=0, 3$  and  $9$  at a few selected temperatures. Strong temperature dependent dispersion of  $\epsilon'$  and  $\epsilon''$  (insets, the full lines are from fits to the generalized Debye expression, Eq. 5.1), seen also as smooth increase in the conductivity spectra, is a fingerprint of the screened CDW collective response. This response is observed at all  $T < T_c$  for  $x=0$  and  $3$ , but not for  $x=9$ . Decrease of the infrared conductivity at low  $T$  corresponds to the opening of an energy gap. At the lowest  $T$  only the lowest-frequency phonon tail is seen and represented with the dash-dot  $\nu^2$  line. Infrared conductivity data are taken from Ref. [161]. The arrows denote the dc conductivity. Dotted lines are guides to the eye.

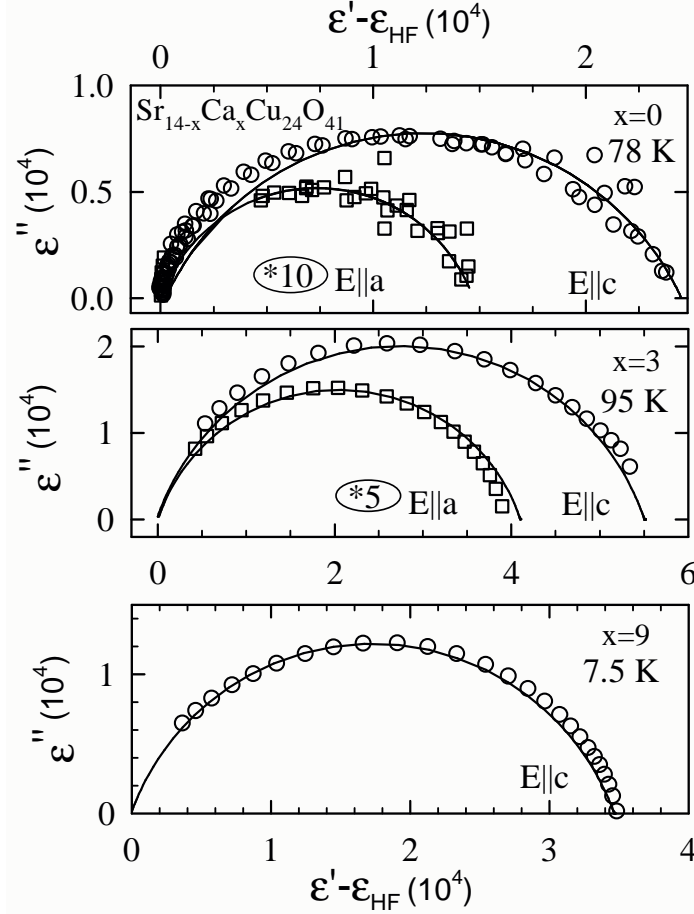


Fig. 5.16: Representative Cole-Cole plots of the dielectric dispersion which occurs due to the anisotropic collective CDW response of  $\text{Sr}_{14-x}\text{Ca}_x\text{Cu}_{24}\text{O}_{41}$  for  $x=0$  (upper panel) and  $x=3$  (middle panel) measured along the ladder legs,  $E||c$  and rungs,  $E||a$ . Note that plots for the response along the  $a$ -axis are blown-up 10 ( $x=0$ ) and 5 ( $x=3$ ) times. The plot for  $x=9$  is also shown (lower panel). Significantly, no dispersion in the  $a$ -direction was observed. Full lines are from fits to the generalized Debye expression, Eq. 5.1. The intersections of the arcs with  $\varepsilon' - \varepsilon_{HF}$  axes indicate the values of  $\Delta\varepsilon$ .

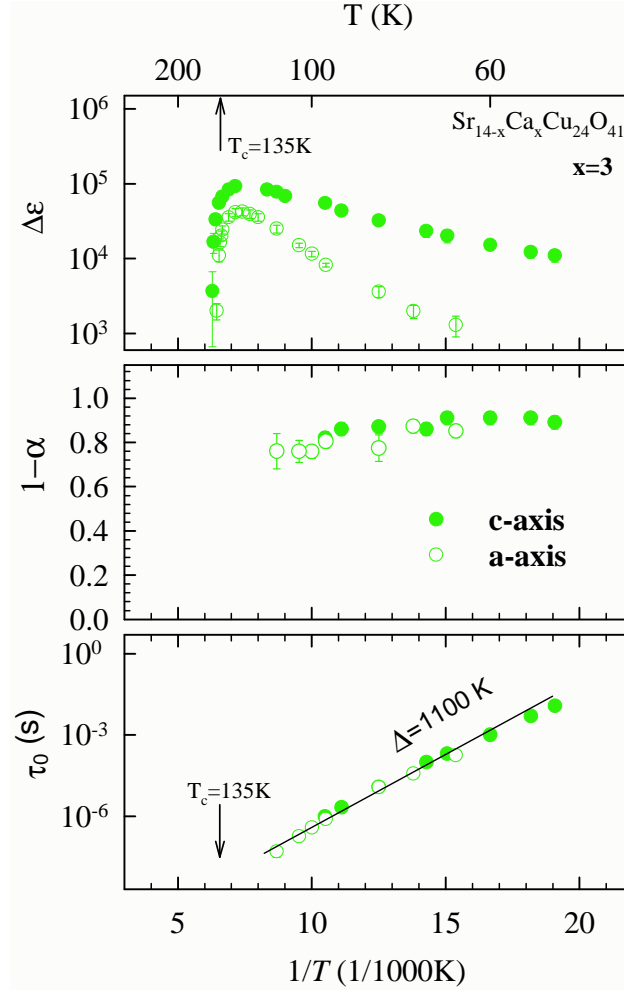


Fig. 5.17: Radio-frequency dielectric relaxation parameters for representative compound  $x=3$ , obtained for ac field applied along the  $c$ - and  $a$ -axis. Upper panel: the strength  $\Delta\varepsilon$  of the dielectric relaxation. The maximum value of  $\Delta\varepsilon$  is found at the same temperature, for both directions. This temperature coincides to  $T_c$  determined from a peak in the logarithmic derivative of the dc resistivity, Fig. 5.14. Middle panel: the parameter  $1-\alpha$  which describes the symmetrical broadening of the relaxation times distribution is the same for both directions. Lower panel: the central relaxation time  $\tau_0$  is the same for both directions.  $\tau_0$  is thermally activated  $\tau_0 \propto e^{\Delta_{CDW}/k_B T}$  below  $T_c$ , with an activation energy  $\Delta_{CDW} \approx 1100$  K equal to dc resistivity activation energy.

In Fig. 5.15, we combine our results with microwave/FIR spectra (in the range 5-10 000  $\text{cm}^{-1}$ ) taken from Ref. [161]. The energy gap associated with the CDW formation is also seen in the infrared spectra for  $E||a$  (arrows in Fig. 5.15), where the conductivity at the lowest frequencies decreases upon cooling. The estimated gap values for different  $x$  correspond well to those determined from the activated dc resistivity both for  $E||a$  and  $E||c$ , Table 5.4. The phonon bands become less pronounced for higher Ca contents  $x$  due to screening by free carriers. At low T only a  $\nu^2$  contribution (Fig. 5.15, dash-dot line) of the low-energy phonon wing is observed.

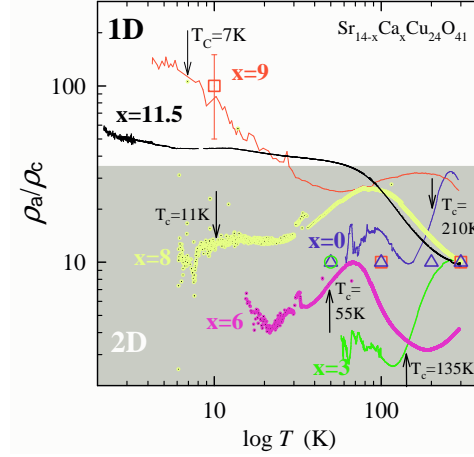


Fig. 5.18: Temperature dependence of the conductivity anisotropy  $\sigma_c/\sigma_a$  of  $\text{Sr}_{14-x}\text{Ca}_x\text{Cu}_{24}\text{O}_{41}$  for different Ca contents  $x$ . Lines and symbols stand for dc and ac (FIR range,  $50\text{ cm}^{-1}$ ) anisotropy, respectively:  $x=0$  (blue line, triangles),  $x=3$  (green line, circles),  $x=6$  (magenta line),  $x=8$  (yellow line),  $x=9$  (red line, squares). The higher and lower anisotropy regimes, denoted as 1D and 2D, are shown in the respective white and grey backgrounds. Anisotropy data may also be found in the Table 5.4

### 5.4.3 Dimensionality *vs.* $x$ - correspondence of dc and ac results

The conductivity ratio  $\sigma_c/\sigma_a = \rho_a/\rho_c$  shown in Fig. 5.18 characterizes the anisotropy of the system within the ladder plane. At all temperatures the anisotropy is of the order of 10 for Ca contents  $x \leq 8$ , indicating a dimensionality of the ladder subsystem close to 2D, Table 5.4. For  $x=9$  the strong rise of the anisotropy below 40 K, most pronounced in the CDW phase, reveals a cross-over into the 1D regime, which develops for high Ca contents at low temperatures. 1D regime seems to be a low temperature feature, since also for  $x=11.5$ , where no CDW is established, the anisotropy is enhanced in the insulating phase at low temperatures. It is also worth noting that the anisotropy in the CDW dielectric strength reflects the dc anisotropy. As shown in Table 5.4,  $\rho_a/\rho_c$  values in CDW phase correlate with  $\Delta\varepsilon_c/\Delta\varepsilon_a$  for  $x=0, 3$ . Also, for  $x=9$  where no mode is observed in the ladder rungs direction ( $\frac{\Delta\varepsilon_c}{\Delta\varepsilon_a} = \infty$ ),  $\rho_a/\rho_c$  is very large, as commented above.

#### 5.4.4 Within $(c,a)$ ladder plane CDW develops 2D LRO

In a 1D metal one expects the development of a CDW only along the chain axis. Hence the existence of the loss peak as the signature of the screened phason relaxation in the perpendicular direction (along the ladder rungs) is completely unexpected, [127]. On the other hand, due to interchain coupling the DW nesting vector is  $Q(2k_F, \pi/b)$ , see Sec. 1.1.3 for the case of  $(\text{TMTSF})_2\text{PF}_6$ . Thus  $Q^{-1}$  is not parallel to the chain axis. When the interchain coupling is due to finite overlaps  $t_\perp$  (and not to interchain Coulomb interactions - page 77) the charges condensed in the DW have a degree of freedom in the overlap direction. According to this line of reasoning, the DW phason response might occur for an ac electric field applied perpendicular to the chains.

However, until now, the phason screened dielectric relaxation was only observed for ac electric field applied along the best conductivity axis of the quasi-1D compounds. In our best knowledge, so far, there was no attempt to measure it along the less conductivity axes. In  $\text{Sr}_{14-x}\text{Ca}_x\text{Cu}_{24}\text{O}_{41}$  we find that the radio-frequency loss peak centered at  $\tau_0^{-1}$  decays Arrhenius-like for both directions  $E||c$  and  $E||a$ ; these are well established features to characterize the CDW phason screened response, Sec. 2.4. On the other hand, CDW phason pinned mode was not observed for direction  $E||a$ . We suggest that the pinned mode frequency is raised along  $a$ -direction, due to dc-anisotropy. Mode at such raised frequency could not have been observed in the microwave measurements along  $a$ -axis, reported by Kitano *et al.*, [162], in which the upper bound of the frequency window was 100 GHz. Our reasoning is based on Littlewood's model, Sec. 2.4, where  $\tau_0^{-1}$ ,  $\sigma_{dc}$  and pinning frequency  $\Omega_0$  are related. Since  $\tau_0^{-1}$  are the same for both  $c$ - and  $a$ -directions, we get:  $\Omega_0^2(a) = \Omega_0^2(c) \times [\sigma_{dc}(c)/\sigma_{dc}(a)]$ . Taking  $\Omega_0(c) = 1.8 \text{ cm}^{-1}$  [162] and  $\sigma_{dc}(c)/\sigma_{dc}(a) \approx 10$ , we calculate the pinning frequency of the CDW along the ladder rungs ( $a$ -axis)  $\Omega_0(a) \approx 5 \text{ cm}^{-1}$  (=150 GHz).

The dielectric strength of the loss-peak found along the  $a$ -axis is about 10 times smaller than the one observed along the  $c$ -axis, which corresponds to the single-particle conductivity anisotropy, Table 5.4. Most interestingly, for the  $x=9$  compound the large dc anisotropy,  $\sigma_{dc}(c)/\sigma_{dc}(a) \geq 100$ , indicates a highly 1D nature at low T when the CDW state is established; in this case the screened phason relaxation is only observed along the  $c$ -axis.

In brief, our findings indicate that a CDW in the  $(c,a)$ -ladders plane develops 2D long-range order. In addition, based on the observed anisotropic phason-like dispersion we may extrapolate from the standard phason response model in 1D, to a 2D model of phason dispersion.

## 5.5 Discussion: Competing and coexisting ground states in ladders and chains

### 5.5.1 Phase diagram for ladders

Fig. 5.19 summarizes our results on the charge transport along the ladders in  $\text{Sr}_{14-x}\text{Ca}_x\text{Cu}_{24}\text{O}_{41}$ . We identified an insulator-to-insulator phase transition. The low-temperature phase for all  $0 \leq x \leq 9$  was identified to be the charge density wave ground state. A strong decrease of the CDW phase transition temperature  $T_c$  and the CDW single-particle gap  $\Delta_{CDW}$  induced by Ca-substitution is striking. Concomitant broadening of the transition was also observed. The high-temperature (HT) phase features insulating behavior, in opposition with a metallic behavior normally observed above standard DW transitions. The HT phase activation energy,  $\Delta_{H.T.}$ , is smaller or comparable to  $\Delta_{CDW}$  for  $x \lesssim 6$ . For higher Ca-contents the HT phase shows 2-3 times larger activation energy than CDW. Also, HT insulating phase persists at Ca-substitution levels,  $x=11.5$ , but only below 80 K, while CDW is suppressed already for  $x>9$ . The insulating behavior for  $10 \leq x \leq 13.6$  can be suppressed under pressure. The applied pressure of 3-6 GPa, recovers metallic behavior, and superconductivity sets in at low temperature. Superconducting transition temperature  $T_{SC}$  reaches a maximum value of 12 K under pressure of 4 GPa, [69, 106, 107]. It is useful to note that for  $x = 0$  pressure of 6.5 GPa removes the CDW phase and suppresses insulating HT phase. However, no superconductivity is observed down to lowest temperatures, [106].

Fig. 5.19 also correlates our results with the results for gapped spin-liquid ground state in the ladders. While CDW-gap is strongly suppressed with Ca-substitution, spin-gap persists almost unchanged (30 meV) up to Ca-content  $x=12$ . The CDW phase transition temperature  $T_c$ , coincides only for  $x=0,3$  with the crossover temperature  $T^*$ , which separates the high temperature paramagnetic regime from the spin-liquid ground state. The NMR results by Piskunov *et al.*, [104], indicate that the spin-gap is opened for  $x=12$  below 100 K. This result implies that  $T^*$  line deviates from  $T_c$  behavior for  $x > 2$  and remains at about 100 K for all  $x$  up to  $\sim 12$ .

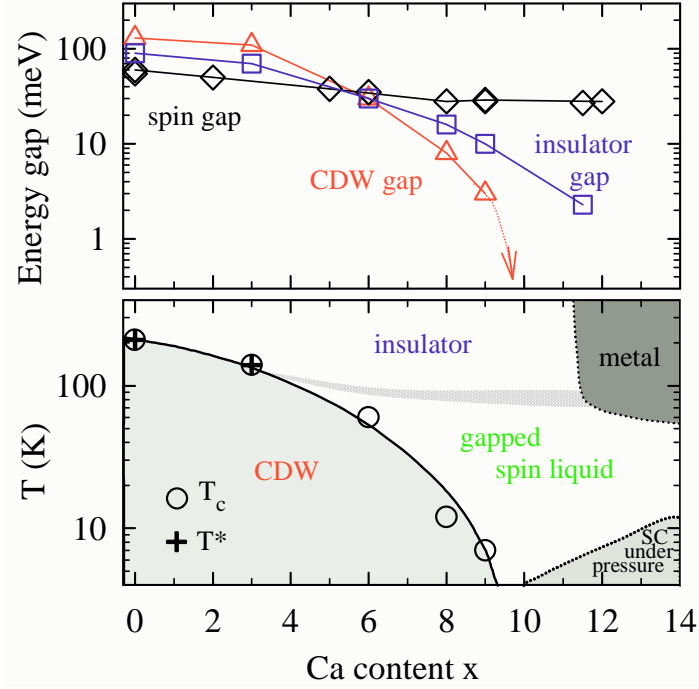


Fig. 5.19: Upper panel: Dependences of the energy scales in the ladders of  $\text{Sr}_{14-x}\text{Ca}_x\text{Cu}_{24}\text{O}_{41}$  on the calcium content. CDW gap  $\Delta_{CDW}$  (triangles) is the largest scale at low contents,  $x < 6$ . The spin gap (diamonds) in the ladders,  $\Delta_{spin}^{ladders}$ , is also shown (data from Fig. 1.29). It can be considered Ca-content independent (Sec. 1.2.6). The high temperature phase features insulating behavior with well defined activation energy  $\Delta_{H.T.}$ , squares. Lower panel: Qualitative phase diagram for  $\text{Sr}_{14-x}\text{Ca}_x\text{Cu}_{24}\text{O}_{41}$  as a function of Ca-content. The CDW phase is determined by the CDW critical temperature  $T_c$  (open circles), which coincides with the paramagnetic – spin-gapped phase crossover-temperature  $T^*$  (crosses) [96, 178] for  $x=0, 3$ . As the spin-gap persists unchanged up to  $x=12$ ,  $T^*$  is also not significantly suppressed, as denoted by a broad diffuse line [104]. Above 50 K and for  $x > 11$  HT phase features metallic behavior [84]. Superconducting phase appears for  $10 \leq x \leq 13.6$ , below 12 K, under pressures above 3 GPa [106].

### 5.5.2 Origin of HT insulating phase and CDW ground state and mechanism that governs their suppression

In the following, we first address the issue of origin of HT insulating phase. We assume the existence of a conducting band for the holes residing in ladders, so Fermi wave vector  $2k_F$  can be defined. Within the description of Zhang-Rice singlet we find that hybridization between O2p and Cu3d levels allows for derivation of a single-band effective Hamiltonian, [74]. Within this model a given site, *i.e.* a  $\text{CuO}_4$  square, may either contain an unpaired electron with spin 1/2 (which resides on the  $\text{Cu}^{2+}$  ion) or the site may be empty when the Zhang-Rice singlet forms (a hole within the O2p orbitals of the square is strongly bound to  $\text{Cu}^{2+}$  ion, due to hybridization). No double occupancy is allowed. In the present case for ladders, we note that hole number is very low, 1 hole per 7 rungs. Thus, the ladder band is very close to half-filling,  $f = 1/2$ , with one unpaired spin 1/2 electron at almost every site. In the case of  $\text{Sr}_{14-x}\text{Ca}_x\text{Cu}_{24}\text{O}_{41}$ ,  $2k_F = 2\pi f/c_L$ , where  $c_L = 3.9\text{\AA}$  is the ladder lattice parameter. We get  $1/k_F \approx 2.5\text{\AA}$ .

In the Drude model the mean free path  $\Lambda$  for the ladders is calculated from the RT conductivity:

$$\sigma = \frac{4e^2}{h} \frac{z}{ab} \Lambda$$

where  $a$  and  $b$  are the other two lattice parameters and  $z = 4$  is the number of ladders per unit cell cross-section,  $ab$ . We get  $\Lambda \approx 1\text{\AA}$ .

Ioffe and Regel, [182], argued that as the extent of disorder increases in a metallic system, there was a limit to metallic behavior; when the quasi-particle mean free path  $\Lambda$  becomes less than its de Broglie wavelength  $2\pi/k_F$ , coherent metallic transport would not be possible. Thus, the Ioffe-Regel criterion for occurrence of insulating behavior is

$$k_F \Lambda < 2\pi$$

Based on the Ioffe-Regel criterion, Mott proposed that a metal-insulator (M-I) transition must occur when the disorder is sufficiently large that Ioffe-Regel criterion is satisfied. In recognition of Anderson's early work on disorder induced localization, Mott called this M-I transition the "Anderson transition". In other words, a system of noninteracting electrons turns into an Anderson localized insulator, as increasing disorder causes the localization of the Bloch wave functions, [181].

In cuprate ladders, at RT,  $\Lambda \approx 1\text{\AA}$  is quite smaller than  $2\pi/k_F \approx 15\text{\AA}$ . This certainly indicates that insulating behavior of cuprate ladders might be,

at least partially, attributed to Anderson localization. However, an Anderson insulator is not expected to cross-over to metallic state under pressure - contrary to what is observed in ladders. We note that organic 1D materials like  $(\text{TMTSF})_2\text{PF}_6$  also feature  $k_F\Lambda < 2\pi$ . However, unlike insulating cuprate ladders discussed here, these organics show metallic conductivity even at highest temperatures. They belong to so-called bad metals, which besides having a "too short" mean free path also fail to exhibit resistivity saturation, [183].

On the other hand, in a clean 1D metallic system, at half-filling  $f = \frac{1}{2}$ , as the electron interaction  $U$  is switched on, a gap arises in the energy spectrum and the system turns into a Mott or charge-ordered insulator, [180]. Since the band-filling in the cuprate ladders is close  $f = \frac{1}{2}$  and the on-site Coulomb repulsion is  $U = 3-4\text{eV}$  ( $U/4t > 1$ ), Mott localization seems to be a plausible origin of the insulating phase at high T, as well as of CDW ground state.

A word is in order on the equivalency of Ca-substitution and pressure effects on the lattice parameters of  $\text{Sr}_{14-x}\text{Ca}_x\text{Cu}_{24}\text{O}_{41}$ , [70, 71, 179]. The inter-layer lattice parameter  $b$  is the most susceptible, at room temperature it decreases for 6-8 %, either by Ca-substitution from  $x=0$  to  $x=13$ , or under 8 GPa for  $x=0$ . Corresponding changes of the intra-layer ladder parameters  $a$  and  $c$  are small,  $\approx 1\%$ . Importantly, this also shows that the dimensionality of the ladder subsystem does not change, in accord with our electrical transport anisotropy data at high temperature.

We can now address the issue of mechanism which might govern the suppression of the HT insulating phase and CDW ground state. Firstly, the hole transfer increases upon Ca-substitution, [76, 75]. Presumably it increases also under pressure, as the pressure and Ca-substitution influence the crystallographic parameters in the same manner. Higher hole count in the ladders increases the deviation from half-filling and moves the system towards metallic state. Secondly, the Ca-substitution or pressure decrease the ladder parameters  $a$  and  $c$ , and correspondingly increase wave-function overlaps in the ladder plane. Consequently, localization might be also removed by decreasing  $U/4t$ .

As for the CDW suppression, we first point out that the worsened nesting induced by Ca-substitution can not cause the CDW suppression since the anisotropy in the ladder plane does not change. Therefore, we can apply similar arguments to discuss the suppression of CDW. CDW phase is clearly less robust than HT phase since Ca-substitution  $x > 9$  is enough to suppress it fully. In analogy with HT phase, we consider for CDW phase suppression the effects of band-filling deviation and of increase of overlaps in the ladder plane (*i.e.* decrease of  $U/4t$ ). In addition, a decrease of the  $b$ -parameter might be expected to influence the inter-site Coulomb repulsion  $V$ . These

effects must come into play together with the influence of disorder.

A rapid CDW suppression might be attributed to a disorder introduced by Ca-substitution at Sr sites, which is indicated by broadening of the CDW phase transition with Ca-substitution. We remind that, at microscopic scale, strong local distortions of the ladders due to irregular coordination of  $\text{Sr}^{2+}$  and  $\text{Ca}^{2+}$  ions [70, 71] occur by Ca-substitution. Also, reducing the  $b$  parameter increases disorder in the ladder layer through increased coupling with the chain layer.

We also note the work of Tsuchiizu and Suzumura, [120] where the suppression of CDW (and the appearance of SC phase) was parametrized by the decrease in the ratio of intersite (nearest-neighbor)  $V$  and on-site  $U$  interactions within the extended Hubbard model for the doped ladder. Their results for the ladders also correspond to the results for a 1D chain where also a decrease in  $V/U$  ratio induces transition from CDW to SC phase, [80]. Also, they relate  $V$  with band-filling deviation (hole transfer).

### 5.5.3 Correspondence of phase diagrams of ladders and chains

To emphasize the influence of coupling between the subsystems we construct the phase diagram for ladders and the phase diagram for chains in  $\text{Sr}_{14-x}\text{Ca}_x\text{Cu}_{24}\text{O}_{41}$ , Fig. 5.20. These phase diagrams feature a high degree of correlation between the two subsystems. Both 2D CDW long-range order in the ladders and 2D charge-order (CO) in the chains crosses over to a short range order for  $x \gtrsim 6$ . The latter persists shortly and fully vanishes for  $x \gtrsim 11$ . Complexity is added through the features of the spin-sector. AF dimer pattern (AFD) in the chains is intimately related to the CO and shows the same  $x$  dependence. For high Ca-contents, *i.e.*  $x \gtrsim 11$ , it is replaced by antiferromagnetic (AF) order at low temperatures. In contrast, the gapped spin-liquid ground state in the ladders is more robust and persists up to  $x = 13.6$ . Moreover, it remains finite even when SC state is established under pressure. It is not known if AF order in the chains persists under pressure when SC is established in the ladders. This possibility poses the question of concepts, which may result from the coexistence of superconductivity and magnetism, but in different subsystems of a composite material.

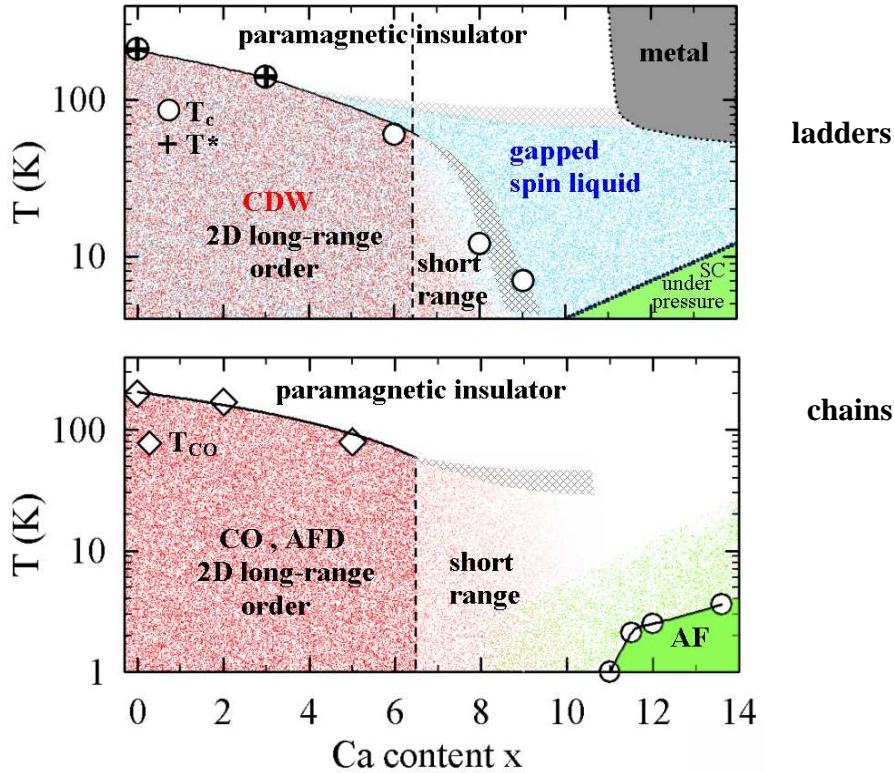


Fig. 5.20: The correspondence between the phase diagrams for ladders and chains is emphasized. The diagrams present the data for both charge and spin sector. Upper panel (ladders): charge-density wave 2D LRO is established below  $T_c$ , circles. The crossover from the LRO to short range order is denoted by phasing out of the red background. The gapped spin liquid (blue background) exists below  $T^*$  denoted by crosses and also by a broad diffuse line. It persists even for  $x$ , where superconductivity is established under pressure (green). Lower panel (chains): The crossover to a 2D ordering at the same  $T_{co}$  for the charge and spin-sectors is due to complementarity between the arrangement of the spins and holes in the chains. Destruction of LRO is again denoted by dephasing the red background. AF dimer pattern is replaced by an AF long-range order for  $x > 11$  (green).

### 5.5.4 Nature of CDW ground state in ladders

Our result that a phason-like dispersion (seen as broad screened relaxation modes) exists along both the rungs and legs of ladders indicates that the ground state in the ladders of  $\text{Sr}_{14-x}\text{Ca}_x\text{Cu}_{24}\text{O}_{41}$  is not of the standard CDW type. The collective excitations of this charge order are similar to a long wave excitation of CDW phason. However, further experiments have to clarify whether such a (anisotropic) dispersion is a unique feature of the charge order in ladders or whether it is common to quasi-2D systems with charge order. While in principle we do not see a reason why a CDW formed in a system of coupled chains would not respond in perpendicular direction, this question deserves a more elaborate theoretical consideration.

Further,  $\text{Sr}_{14-x}\text{Ca}_x\text{Cu}_{24}\text{O}_{41}$  ladders are, as expected for cuprate materials, a strongly coupled system. Indeed, experimental observations suggest that strong electron-electron interaction gives rise to a Mott-localized high temperature phase. In the same manner, the ground state might be the charge ordered state of partially localized charges. That is, CDW in the ladders might fall between the two well defined limits of charge order: the CDW order of itinerant charges and the charge order of localized charges. However, as stated above the collective excitations are similar to CDW and even the condensate effective mass  $m^* \approx 100$  is within the range of values (although in the lower limit) for a standard CDW with non-negligible electron-phonon coupling.

Discussing the nature of the broken symmetry ground states in a 1D half-filled band with arbitrarily long-range Coulomb interaction Mazumdar and Campbell [121] started by pointing out that nesting arguments should not be applied since there is no single-particle (band) picture for nonzero correlations. Still, they obtained inequalities based on the arbitrarily strong Coulomb parameters, which defined the parameter space for the existence of broken symmetry states. One of these inequalities leads to, and is consistent with, the CDW/SDW boundary obtained in the continuum limit (valid for weak coupling) of the extended Hubbard model. Exactly at this boundary, using weak coupling approach (g-ology) Tsuchiizu *et al.*, [120] have shown that a bond-CDW (BCDW) phase exists in between CDW and SDW. Using the same approach they also investigated the doped two-leg Hubbard ladder and provided a qualitative phase diagram where a BCDW (p-wave: angular momentum  $l = 1$ ) coexists with CDW (s-wave: angular momentum  $l = 0$ ) for strong nearest-neighbor repulsion and gives way to d-wave-like SC. This phase diagram is highly similar with the experimental phase diagram of cuprate ladders. Study by Schollwöck *et al.*, [184] of a doped two-leg ladder used the approach applicable for arbitrary interaction strength. They

obtained a ground state for the ladder where CDW coexists with a d-wave-like density wave (angular momentum  $l = 2$ ). The ground state in the ladders might be the one of these exotic charge-ordered phases. However, there is no theoretical prediction about collective excitations in such a phase and how they should respond to applied dc and ac fields.

It is useful to compare experimental results for a material where the CO, occurring due to localization and strong coupling is well documented, with those for  $\text{Sr}_{14-x}\text{Ca}_x\text{Cu}_{24}\text{O}_{41}$  ladders. One example is the charge order associated with a  $4k_F$  CDW - Wigner crystal ground state due to electron-electron interactions, established in the q1D material, Fabre salt  $\text{TMTTF}_2\text{AsF}_6$  [185]. A fingerprint of CO: a charge disproportionation was detected in NMR measurements by Chow *et al.*, [186]. In contrast to that, no signature of charge disproportionation has been detected in NMR measurements in the ladders of  $\text{Sr}_{14-x}\text{Ca}_x\text{Cu}_{24}\text{O}_{41}$ , Fig. 1.27, [98].

The CO transition in  $\text{TMTTF}_2\text{AsF}_6$  was also detected from a divergence in the dielectric strength at  $T_{co}$ . The results for  $\text{TMTTF}_2\text{AsF}_6$ , Fig. 5.21, show no temperature dependence in the position of the peak of the  $\varepsilon'(\omega)$ . This indicates a temperature-independent central relaxation time. Thus, such a relaxation can not be due to CDW phason response, but it could be related to short-wavelength excitations of CDW, like solitons, or charged-domain walls, [143]. On the contrary, ac field response of the ladders shows the central relaxation time thermally activated in the same manner as the dc conductivity.

We also compare,  $1/\varepsilon'$ , the inverse of the real part of the dielectric function for  $\text{TMTTF}_2\text{AsF}_6$  and for ladders of  $\text{Sr}_{14-x}\text{Ca}_x\text{Cu}_{24}\text{O}_{41}$ ,  $x=3$ , measured in the  $c$ - and  $a$ -directions. It was observed for  $\text{TMTTF}_2\text{AsF}_6$  that  $1/\varepsilon'$  in the vicinity of  $T_c$  follows the Curie law  $1/\varepsilon' \propto 1/|T_{co} - T|$ . On the contrary,  $1/\varepsilon'$  in the ladders does not show the same behavior, Fig. 5.22.

Therefore, we conclude that ground state established in the ladders of  $\text{Sr}_{14-x}\text{Ca}_x\text{Cu}_{24}\text{O}_{41}$  is not similar to the well documented charge-order observed in  $\text{TMTTF}_2\text{AsF}_6$ .

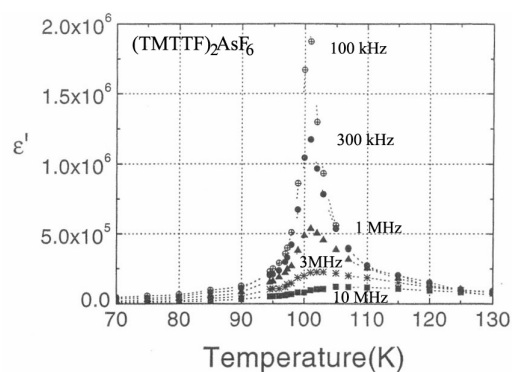


Fig. 5.21: Temperature dependence of the real part of the dielectric function for  $\text{TMTTF}_2\text{AsF}_6$  at various frequencies. From Ref. [185].

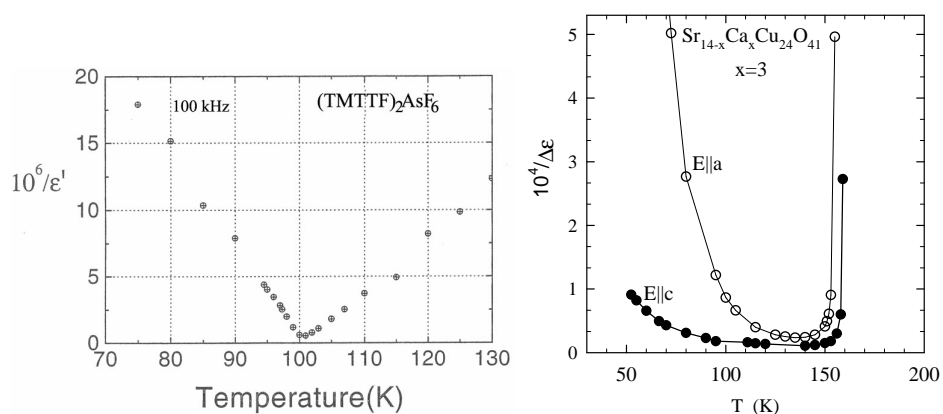


Fig. 5.22: Temperature dependence of the inverse of the real part of the dielectric function for  $\text{TMTTF}_2\text{AsF}_6$  (left panel, from Ref. [185]) and  $\text{Sr}_{14-x}\text{Ca}_x\text{Cu}_{24}\text{O}_{41}$ ,  $x=3$ ,  $c$ - and  $a$ -directions, measured at 100 kHz (right panel).

### 5.5.5 Superconductivity in the ladders

Finally, we address briefly the SC ground-state established for  $10 \leq x \leq 13.6$  and under high pressure, 3-6 GPa, below 12 K. We discuss this SC ground state in relation to Dagotto's model for superconductivity in ladders. In this model, singlet pairing interaction in the ladder rung acquired the role of renormalized, attractive  $U_{eff}$  for the ladder projected onto a 1D chain. In other words - the spin-gap has still to be observed in the metallic state just above SC transition - as, indeed, is the case, [104, 108]. In this line of reasoning the absence of SC, while the spin-gap is observed when  $x=0$  is rendered metallic under pressure, is intriguing. The observation of low-lying spin-excitations within the spin-gap for  $x=12$ , under pressure where SC sets in, and the absence of these for  $x=0$  resolves the issue. However, this indicates that SC arises only when a large enough density of carriers appears at the Fermi level, which contradicts Dagotto's model. Observation of Hebel-Slichter peak, [108], in NMR spin-lattice relaxation rate at  $T_{SC}$  also indicates that a finite gap exists in the quasiparticle excitation for all wave vectors (directions). This s-wave-like character also contradicts d-wave-like SC suggested by Dagotto. Fujiwara *et al.* suggest that SC state is not established by hole-pairing on the same rung, but on the neighboring ones.

In the end of the exposition of our results and the respective discussions, we note that the nature of charge-density wave is intricately related with the nature of superconductivity in  $\text{Sr}_{14-x}\text{Ca}_x\text{Cu}_{24}\text{O}_{41}$  compounds. Whether these ground states are unconventional and of non-s-wave symmetry, as theoretically expected, is not clear yet. Further research is needed to clarify these issues.

# 6 Summary and Concluding Remarks

This study of quasi-one-dimensional materials has concentrated on understanding and improving the experimental phase diagrams. Especially, the competition and/or coexistence of superconductivity and density-wave phases was addressed by studying the charge transport properties. q1D materials from two different families were studied: single chain  $(\text{TMTSF})_2\text{PF}_6$ , from the family of organic Bechgaard-Fabre charge-transfer salts and  $(\text{La, Sr, Ca})_{14}\text{Cu}_{24}\text{O}_{41}$ , composite chain/ladder cuprates. While research interest in the q1D cuprates is relatively new, the research on Bechgaard-Fabre salts continues for the last 25 years. In the generic phase diagram of Bechgaard-Fabre salts there are still uninvestigated regions and thus they may still be regarded as new materials. Also, any work on other q1D materials is much more instructive if it is compared to the results obtained on the representative compound of the family,  $(\text{TMTSF})_2\text{PF}_6$ .

A detailed study of dc resistivity and superconducting critical currents in the high pressure region (6.8-11 kbar) of  $(\text{TMTSF})_2\text{PF}_6$  phase diagram was performed, with a control of the pressure which could not be achieved in the early studies. A narrow pressure region, 8.65 - 9.43 kbar, was determined where SDW/metal and SDW/SC coexisted. That is, below metal-to-SDW transition parts of the sample remained metallic. Eventually, when the temperature is lowered below 1.2 K the metallic parts undergo metal-to-SC transition. The volume proportion,  $c$  (vol%) of the metallic (and/or SC phase) was increasing with pressure in the coexistence region. At a given pressure, two estimates for  $c$  (vol%) were obtained. The nonlinear correlation of the estimates indicated two different regimes. In the higher inhomogeneous region (9.1–9.43 kbar), domains (or percolated paths) span the length of sample. In the lower inhomogeneous region (8.65–9.1 kbar) Josephson junctions (or phase slip centers) are present along the conducting channels in the SDW/SC region. Similar coexistence phenomena were recently observed in other members of  $(\text{TM})_2\text{X}$  family, as well as in the layered organic  $\kappa$ -(BEDT-TTF) $_2\text{X}$

compounds.

A very simple coexistence model was proposed, based on a variational theory calculation. It indicated that it is possible to find an inhomogeneous phase with a free energy which is lower than the energy of the homogeneous phases (SDW or metal). It explains fairly well our experimental findings. On the other hand, some other, microscopic models, explain our results only qualitatively.

For q1D cuprates the strong coupling limit applies, on the contrary to  $(\text{TMTSF})_2\text{PF}_6$ , where the weak-coupling is appropriate. When discussing the competition/coexistence of DW and SC in the q1D cuprates of the formula  $\text{A}_{14}\text{Cu}_{24}\text{O}_{41}$  (A=Sr, Ca, La, Y...) phase diagram, the theoretical approach is more difficult and not well developed. Two families were investigated,  $\text{Sr}_{14-x}\text{Ca}_x\text{Cu}_{24}\text{O}_{41}$  materials where exist 6 holes per formula unit, one out of which resides in the ladders for  $x = 0$  material, while Ca-substitution increases this hole count slightly. We also studied  $\text{La}_y\text{Sr}_{14-y-x}\text{Ca}_x\text{Cu}_{24}\text{O}_{41}$  materials, where exist  $6 - y$  holes, all residing in the chains.

We have shown the dc and ac charge transport in the chains of  $\text{La}_y\text{Sr}_{14-y-x}\text{Ca}_x\text{Cu}_{24}\text{O}_{41}$  is due to hopping of holes. While the chain subsystem in  $\text{La}_y\text{Sr}_{14-y-x}\text{Ca}_x\text{Cu}_{24}\text{O}_{41}$  materials behaves as a one-dimensional disorder-driven insulator, a 2D charge-order occurs in the chain subsystem of  $\text{Sr}_{14-x}\text{Ca}_x\text{Cu}_{24}\text{O}_{41}$  ( $T^* = 200$  K for  $x=0$ ). This charge-order is intimately related to the spin-ordering according to AF dimers (AFD) pattern, showing the same  $T^*$  vs.  $x$  dependence. 2D CO and AFD pattern in the chains cross over to a short range order for  $x \gtrsim 6$ . For  $x \gtrsim 11$ , AFD pattern is replaced by AF order at low temperatures.

On the other hand, in  $\text{Sr}_{14-x}\text{Ca}_x\text{Cu}_{24}\text{O}_{41}$ , holes transferred to the ladders are mobile and responsible for the electrical transport. This is strongly supported by the observation that RT resistivity of  $\text{La}_y\text{Sr}_{14-y-x}\text{Ca}_x\text{Cu}_{24}\text{O}_{41}$  materials, where transport occurs in the chains, is at least three orders of magnitude larger than for  $\text{Sr}_{14-x}\text{Ca}_x\text{Cu}_{24}\text{O}_{41}$ .

The way how the transport switches from the chains in La-substituted to the ladders in La-free materials, is still an open issue. Is there a phase transition and how the phase diagram of the former merges with the one of the latter should be resolved by further experiments on materials with very low La content, in the hole count  $\lesssim 6$  range.

The studies of charge transport in  $\text{Sr}_{14-x}\text{Ca}_x\text{Cu}_{24}\text{O}_{41}$  were performed for  $x=0, 3, 6, 8, 9, 11.5$ . For the parent compound,  $\text{Sr}_{14}\text{Cu}_{24}\text{O}_{41}$ , in dc resistivity an insulator-to-insulator transition at  $T_c = 210$  K was observed. The low temperature insulating phase was identified as charge density wave (CDW) with CDW single-particle gap  $\Delta_{\text{CDW}} = 1300$  K. That is, the fingerprints of CDW phason response to ac electric fields, which is a collective relaxation

mechanism, were observed. As the first, a narrow phason mode, *pinned* mode, was previously found in the microwave frequency range. As the second, by low-frequency dielectric spectroscopy (LFDS) we observed a broad thermally activated mode in radio-frequency range. From these results we estimated CDW condensate mass to be  $m^* \approx 100$ , a value which is within the range reported for standard CDW materials. Quasi-coherent microwave and FIR measurements also corresponded with the identification of CDW phase.

However, dc electric field dependent, sliding conductivity was not observed in our study of CDW phase in  $\text{Sr}_{14}\text{Cu}_{24}\text{O}_{41}$ . On the contrary, independent groups reported different observations of nonlinear conductivity. We suggest that this apparent contradiction might be due to different quality of studied single crystals. In our study, it might be that, due to too low electric fields applied, CDW sliding was not detected. This uncertainty could be resolved by further experiments on samples from different batches.

Further, the dc and ac transport anisotropy study within the ladder ( $c, a$ ) plane of  $\text{Sr}_{14}\text{Cu}_{24}\text{O}_{41}$  showed a set of properties similar for both directions. The phase transition temperatures  $T_c$ , when measured along the  $c$ -axis and  $a$ -axis, are equal in value and the same holds for the  $\Delta_{\text{CDW}}$ . The ac properties in both ladder plane directions correspond to the CDW phason response. Along the perpendicular,  $b$ -direction, a distinct behavior with different activation energies, and no phase transition, is registered. In addition, no signature was found of a CDW-related dielectric response. This indicates that the charge transport perpendicular to the ladder planes probably happens via nearest-neighbor hopping, as expected between disordered chains.

For  $\text{Sr}_{14-x}\text{Ca}_x\text{Cu}_{24}\text{O}_{41}$ ,  $0 < x \leq 9$ , a strong decrease with Ca-substitution, of the CDW phase transition temperature, with concomitant transition broadening, and the CDW single-particle gap, was observed (for  $x=9$ ,  $T_c=7$  K,  $\Delta_{\text{CDW}} = 30$  K). For  $x=11.5$  no ordering was found. As well as for the parent compound  $x=0$ , the anisotropy study of dc and ac transport for  $0 < x \leq 9$  showed a set of properties similar for both ladder plane directions. Only for  $x=8,9$  the CDW phason relaxation was not detected for  $E||a$  down to 4.2 K. Again, as for  $x=0$ , the transport in the perpendicular direction ( $E||b$ ), was of a distinctive, presumably hopping character. The ( $c, a$ ) plane anisotropy in the CDW dielectric strength reflected the dc anisotropy, as  $\rho_a/\rho_c$  values in CDW phase correlate with  $\Delta\varepsilon_c/\Delta\varepsilon_a$  for  $x=0, 3$ . For  $x=9$  where no mode is observed in the ladder rungs direction ( $\frac{\Delta\varepsilon_c}{\Delta\varepsilon_a} = \infty$ ),  $\rho_a/\rho_c = 150$  is very large only in the low temperature region, indicating a highly 1D nature.

The dc and ac transport anisotropy results imply that CDW develops in the ( $c, a$ )-ladders plane with a 2D long-range order (LRO), which crosses over to a short range order for  $x \geq 6$ . We note, that at the same Ca-substitution levels, the CO in the chains changes over from 2D LRO to a short range

one. For  $x \leq 11.5$ , both CDW and CO disappear from the respective phase diagram. Such a correlated behavior stresses an interplay between the ladders and the chains.

The high temperature (HT) phase, existing above the CDW phase, is characteristic for the insulating behavior occurring in spite of high RT conductivity ( $\approx 500$  S/cm, very similar to those of metallic  $(\text{TMTSF})_2\text{PF}_6$ ). The insulating HT phase persists up to  $x=11.5-12$ , while the CDW is suppressed already for  $x > 9$ . The HT phase activation energy,  $\Delta_{\text{H.T.}}$ , is smaller or comparable to  $\Delta_{\text{CDW}}$  for  $x \lesssim 6$ . For higher Ca-contents the HT phase shows 2-3 times larger activation energy than CDW.

Complexity is added in the description of the ladders through the features of the spin-sector. The ground state of the ladders is a gapped spin-liquid. The spin-gap ( $\Delta_{\text{spin}}^{\text{ladders}} = 350$  K) is almost independent of Ca-substitution and persists for  $x=12$ , unlike the CDW gap. The magnitudes of the two gaps are very different: for  $x=0$ ,  $\Delta_{\text{spin}}^{\text{ladders}}$  is 2-3 times smaller than the CDW gap, while for  $x=9$ , the spin-gap is an order of magnitude larger.

Above 3 GPa in  $\text{Sr}_{14-x}\text{Ca}_x\text{Cu}_{24}\text{O}_{41}$ ,  $10 \leq x \leq 13.6$ , the pressure suppresses the insulating HT phase, recovering metallic behavior before superconductivity is established. The spin-gap is not removed by the application of pressure, at least up to 3.5 GPa. Surprisingly, the low-lying spin excitations are observed within the spin-gap. These observations raise the question on the nature of SC phase. Apparently, the SC possesses an s-wave character, in the meaning that a finite gap exists in the quasiparticle excitations. On the other hand, theoretical considerations suggested d-wave symmetry, although the lack of rotational symmetry of the ladders prevents an exact symmetry classification.

It is not known whether AF order in the chains for  $x > 11$  persists under pressure when SC is established in the ladders. This possibility raises the question about concepts, which may stem from the coexistence of superconductivity and magnetism, but in the different subsystems of a composite material.

Finally, the origin of the HT insulating phase and CDW ground state in the ladders and the mechanism for their suppression is given. As the HT insulating phase is suppressed under pressure, and metallic behavior recovered, Anderson localization is excluded as the main origin of the insulating behavior. Since the band-filling in the cuprate ladders is close to  $f = \frac{1}{2}$  and the on-site Coulomb repulsion is  $U = 3 - 4\text{eV}$  ( $U/4t > 1$ ), Mott localization seems to be a plausible origin of the HT insulating phase. This phase is removed under Ca-substitution/pressure either by the deviation from half-filling (which might be induced by even slight hole transfer into the ladders) or by an increase in intraladder overlap integrals, when  $U/4t$  decreases. We

note here the equivalency of Ca-substitution and pressure effects. As the anisotropy in the ladder plane is not affected by Ca-substitution/pressure, the worsened nesting can not cause the CDW ground state suppression. Still, CDW phase is clearly less robust and, while similar arguments as for HT phase, can be applied for CDW suppression, the influence of disorder must also come into play. Disorder in the ladders is introduced by Ca-substitution at Sr-sites, but also by an increase in coupling with the chain layer. The latter changes the intersite Coulomb repulsion  $V$ , which might also influence the stability of the CDW phase.

Our observation of anisotropic CDW phason-like response in the ladder, and the fact that the cuprates are a strongly coupled system indicated that the CDW ground state in the ladders is not of the standard type. In particular, more work is needed to clarify, whether the anisotropic phason-like dispersion is a unique feature of the charge order in the ladders, or whether it is common to quasi-2D systems with charge order. CDW in the ladders might fall between the two well defined limits of charge order: the CDW order of itinerant charges and the charge order of localized charges. The ground state in the ladders might be the one of the exotic charge-ordered phases, characterized by non-s-wave like pairing. However, there is no theoretical prediction about collective excitations in such phases and how they should respond to applied dc and ac fields.

In the end, the nature and the suppression of charge-density wave in the ladder planes is intertwined with the scenario for superconductivity in the ladders of  $\text{Sr}_{14-x}\text{Ca}_x\text{Cu}_{24}\text{O}_{41}$  compounds. The question remains whether these states are unconventional and further research is needed to clarify these issues

# Bibliography

- [1] D. Jérôme, in *Organic Conductors: Fundamentals and Applications*, ed. by J. P. Farges, (Marcel Dekker, Inc., New York, 1994).
- [2] S. Lefebvre, P. Wzietek, S. Brown, C. Bourbonnais, D. Jérôme, C. Mézière, M. Fourmigué and P. Batail, *Phys. Rev. Lett.* **85**, 5420 (2000).
- [3] N. D. Mathur *et al.* , *Nature* **394**, 39 (1998).
- [4] J. Orenstein and A. J. Millis, *Science* **288**, 468 (2000); M. Maple, *Journal of Magnetism and Magnetic Materials* **177**, 18 (1998).
- [5] V. J. Emery, *Synthetic Metals* **13**, 21 (1986).
- [6] H. Ito, T. Ishiguro, M. Kubota and G. Saito, *J. Phys. Soc. Jpn.* **65**, 2987 (1996).
- [7] H. Wilhelm, D. Jaccard, R. Duprat, C. Bourbonnais, D. Jérôme, J. Moser, C. Carcel, and J. M. Fabre, *Eur. Phys. J. B* **21**, 175 (2001).
- [8] S.-C. Zhang, *Science* **275**, 1089 (1997).
- [9] S. Nagaosa, *Science* **275**, 1078 (1997).
- [10] D. Jérôme, *Science* **252**, 1509 (1991).
- [11] T. Vuletić, C. Pasquier, P. Auban-Senzier, S. Tomić, D. Jérôme, K. Maki and K. Bechgaard, *Eur. Phys. J. B* **21**, 53 (2001).
- [12] N. Biškup, S. Tomić and D. Jérôme, *Phys. Rev. B* **51**, 17972 (1995).
- [13] A. Hinchliffe and H. J. Soscún Machado, *Int. J. Mol. Sci.* , **1**, 39 (2000).
- [14] K. Bechgaard, *JACS* **103**, 2440 (1981).; K. Bechgaard, C. S. Jacobsen, K. Mortensen, H. J. Pedersen and N. Thorup, *Solid State Commun.* **33**, 1119 (1980).

- 
- [15] N. Thorup, G. Ringdorf, H. Soling and K. Bechgaard, *Acta Cryst. B* **37**, 1236 (1981).
- [16] J. F. Kwak, J. E. Schirber, P. M. Chaikin, J. M. Williams, H.-H. Wang, L. Y. Chiang, *Phys. Rev. Lett.* **56**, 972 (1986).
- [17] T. Ishiguro, K. Yamaji and G. Saito, *Organic Superconductors* (Springer Berlin, 1998).
- [18] P. M. Chaikin, *J. Phys. I France* **6**, 1875 (1996).
- [19] C. Bourbonnais and D. Jérôme, in *Advances in Synthetic Metals, page 206*, edited by P. Bernier, S. Lefrant and G. Bidan (Elsevier, 1999).
- [20] C. Bourbonnais and D. Jérôme, cond-mat/9903101.
- [21] D. Jérôme, A. Mazaud, M. Ribault and K. Bechgaard, *J. Physique Lettres* **41**, L-95 (1980).
- [22] P. M. Grant, *J. Physique Colloque* **44**, C3-847 (1983).
- [23] C. S. Jacobsen *et al.*, *Phys. Rev. Lett.* **53** 194 (1984).
- [24] T. Takahashi, Y. Maniwa, H. Kawamura and G. Saito, *J. Phys. Soc. Jpn.* **55**, 1364 (1986).
- [25] D. Jérôme and H. J. Schulz, *Adv. Phys.* **31**, 299 (1982).
- [26] O. Traetteberg, G. Kriza, C. Lenoir, Y.-S. Huang, P. Batail and D. Jérôme, *Phys. Rev. B* **49**, 409 (1994).
- [27] S. Tomić, J. R. Cooper, W. Kang, D. Jérôme and K. Maki, *J. Phys. I France* **1**, 1603 (1991).
- [28] K. Mortensen, Y. Tomkiewicz and K. Bechgaard, *Phys. Rev. B* **25**, 3319 (1982).
- [29] J. M. Delrieu, M. Roger, Z. Toffano, A. Moradpour and K. Bechgaard, *J. Physique (France)* **47**, 839 (1986).
- [30] J. B. Torrance, H. J. Pedersen and K. Bechgaard, *Phys. Rev. Lett.* **49** 881 (1982).
- [31] L. P. Le *et al.*, *Europhys. Lett.* **15**, 547 (1991); and *Phys. Rev. B* **48**, 7284 (1993).

- [32] A. W. Overhauser, Phys. Rev. **167**, 691 (1968).
- [33] J. P. Pouget and S. Ravy, J. Phys. I France **6**, 1501 (1996).
- [34] J. P. Pouget and S. Ravy, Synthetic Metals **85**, 1523 (1997).
- [35] K. Ichimura, M. Kobayashi, K. Nomura, T. Hanajiri, J. Yamada, S. Nakatsuji and H. Anzai, Synthetic Metals **120**, 897 (2001).
- [36] S. Kagoshima, Y. Saso, M. Maesato, R. Kondo, T. Hasegawa, Solid State Commun. **110**, 479 (1999).
- [37] G. Grüner, *Density Waves in Solids* (Addison-Wesley, Reading, MA, 1994).
- [38] S. Tomić, J. R. Cooper, D. Jérôme and K. Bechgaard, Phys. Rev. Lett. **62**, 462 (1989).
- [39] G. Kriza, G. Quirion, O. Traetteberg, W. Kang and D. Jérôme, Phys. Rev. Lett. **66**, 1922 (1991); E. Barthel, G. Kriza, G. Quiron, P. Wzietek, D. Jérôme, J. B. Christensen, M. Joergensen and K. Bechgaard, Phys. Rev. Lett. **71**, 2825 (1993).
- [40] T. Takahashi, Y. Maniwa, H. Kawamura, K. Murata and G. Saito, Synth. Metals **19**, 225 (1987).
- [41] J. C. Lasjaunias, K. Biljaković, F. Nad', P. Monceau and K. Bechgaard, Phys. Rev. B **72**, 1283 (1994).
- [42] M. Basletic, B. Korin-Hamzic and K. Maki, Phys. Rev. B **65**, 235117 (2002).
- [43] B. Korin-Hamzic, M. Basletic and K. Maki, Europhys. Lett. **59**, 298 (2002).
- [44] T. Vuletić, D. Herman, N. Biškup, M. Pinterić, A. Omerzu, S. Tomić and M. Nagasawa, J. Phys. IV **9**, Pr10–275 (1999).
- [45] G. Mihaly, Y. Kim and G. Grüner, Phys. Rev. Lett. **66**, 2806 (1991); **67**, 2713 (1991).
- [46] L. J. Azevedo, J. E. Schirber, J. M. Williams, M. Beno and D. Stephens, Phys. Rev. B **30**, 1570 (1984).
- [47] R. Brusetti, M. Ribault, D. Jérôme and K. Bechgaard, J. Physique **43**, 801 (1982).

- [48] M. Nagasawa, T. Sambongi, K. Nomura and H. Anzai, *J. Phys. (Paris) Colloq.* **3**, C2-49 (1993).
- [49] G. Montambaux, in *Low-Dimensional Conductors and Superconductors*, page 233, edited by D. Jérôme and L. G. Caron (Plenum Press, New York, 1987).
- [50] J. Sólyom, *Adv. Phys.* **28**, 201 (1979).
- [51] H. J. Schulz, D. Jérôme, M. Ribault, A. Mazaud and K. Bechgaard, *J. Physique Lettres* **279**, L51 (1981).
- [52] R. L. Green *et al.*, *Mol. Cryst. Liq. Cryst.* **79**, 173 (1982); M. Y. Choi *et al.*, *Phys. Rev. B* **25**, 6208 (1982); S. Bouffard *et al.*, *J. Phys. C* **15**, 2951 (1982).
- [53] L. C. Hebel and C. P. Slichter, *Phys. Rev.* **113**, 1504 (1959).
- [54] K. Andres *et al.*, *Phys. Rev. Lett.* **45**, 1449 (1980).
- [55] P. Garoche, R. Brusetti, D. Jérôme and K. Bechgaard, *J. Physique Lettres* **43**, L-147 (1980).
- [56] S. Belin and K. Behnia, *Phys. Rev. Lett.* **79**, 2125 (1997).
- [57] I. J. Lee, M. J. Naughton, G. M. Danner, and P. M. Chaikin, *Phys. Rev. Lett.* **78**, 3555 (1997); I. J. Lee, P. M. Chaikin, and M. J. Naughton, *Phys. Rev. B* **62**, R14669 (2000).
- [58] A. M. Clogston, *Phys. Rev. Lett.* **9**, 266 (1962).
- [59] M. Takigawa, H. Yasuoka and G. Saito, *J. Phys. Soc. Jpn.* **56**, 873 (1987).
- [60] I. J. Lee, S. E. Brown, W. G. Clark, M. J. Strouse, M. J. Naughton, W. Kang and P. M. Chaikin, *Phys. Rev. Lett.* **88**, 017004 (2002).
- [61] R. L. Green and E. M. Engler, *Phys. Rev. Lett.* **45**, 1587 (1980).
- [62] S. Tomić, D. Jérôme, P. Monod and K. Bechgaard, *J. Physique Lettres* **43**, L839 (1982).
- [63] K. Yamaji, *J. Phys. Soc. Jpn.* **51**, 2787 (1982).
- [64] K. Yamaji, *J. Phys. Soc. Jpn.* **56**, 1841 (1987).

- [65] Y. Hasegawa and H. Fukuyama, J. Phys. Soc. Jpn. **55**, 3978 (1986).
- [66] K. Yamaji, J. Phys. Soc. Jpn. **52**, 1361 (1983).
- [67] K. Machida and T. Matsubara, J. Phys. Soc. Jpn. **50**, 3231 (1981).
- [68] E. Dagotto, Rep. Prog. Phys. **62**, 1525 (1999).
- [69] M. Uehara, T. Nagata, J. Akimitsu, H. Takahashi, N. Mori and K. Kinoshita, J. Phys. Soc. Jpn. **65**, 2764 (1996).
- [70] T. Siegrist, L. F. Schneemeyer, S. A. Sunshine, J. V. Waszczak and R. S. Roth, Mat. Res. Bull. **23**, 1429 (1988).
- [71] E. M. McCarron, M. A. Subramanian, J. C. Calabrese and R. L. Harlow, Mat. Res. Bull. **23**, 1355 (1988).
- [72] T. M. Rice, S. Gopalan and M. Sigrist, Europhys. Lett. **23**, 445 (1993).
- [73] E. Dagotto and T. M. Rice, Science **271**, 618 (1996).
- [74] S.-C. Zhang and T. M. Rice, Phys. Rev. B **37**, R3759 (1988).
- [75] T. Osafune, N. Motoyama, H. Eisaki and S. Uchida, Phys. Rev. Lett. **78**, 1980 (1997).
- [76] N. Nücker, M. Merz, C. A. Kuntscher, S. Gerhold, S. Schuppler, R. Neudert, M. S. Golden, J. Fink, D. Schild, S. Stadler, V. Chakarjian, J. Freeland, Y. U. Idzerda, K. Conder, M. Uehara, T. Nagata, J. Goto, J. Akimitsu, N. Motoyama, H. Eisaki, S. Uchida, U. Ammerahl and A. Revcolevschi, Phys. Rev. B **62**, 384 (2000).
- [77] E. Dagotto, J. Rieira, and D. Scalapino, Phys. Rev. B **45**, 5744 (1992).
- [78] B. Gorshunov, P. Haas, T. Rõõm, M. Dressel, T. Vuletić, B. Korin-Hamzić, S. Tomić, J. Akimitsu and T. Nagata, Phys. Rev. B **66**, 060508(R) (2002).
- [79] K. Ishida, K. Kitaoka, Y. Tokunaga, S. Matsumoto, K. Asayama, M. Azuma, Z. Hiroi and M. Takano, Phys. Rev. B **53**, 2827 (1996).
- [80] V. J. Emery, *Highly Conducting One-Dimensional Solids*, page 247, edited by J. Devreese, R. Evrard, and V. van Doren (Plenum, New York, 1979).
- [81] Z. Hiroi, J. Solid State Chem. **123**, 223 (1996).

- [82] O. Milat, G. Van Tendeloo, S. Amelinckx, M. Mehbod and R. Deltour, *Acta Cryst. B* **48**, 618 (1992); T. Fukuda, J. Mizuki and M. Matsuda, *Phys. Rev. B* **67**, 012104 (2003); Comment by: S. van Smaalen, *Phys. Rev. B* **67**, 026101 (2003).
- [83] M. Arai and H. Tsunetsugu, *Phys. Rev. B* **56**, R4305 (1997).
- [84] N. Motoyama, T. Osafune, T. Kakeshita, H. Eisaki and S. Uchida, *Phys. Rev. B* **55**, R3386 (1997).
- [85] Y. Mizuno, T. Tohyama and S. Maekawa, *J. Phys. Soc. Jpn.* **66**, 937 (1997).
- [86] M. Kato, K. Shiota and Y. Koike, *Physica C* **258**, 284 (1996).
- [87] S. Uchida, T. Ido, H. Takagi, T. Arima, Y. Tokura and S. Tajima, *Phys. Rev. B* **43**, 7942 (1991).
- [88] M. Matsuda and K. Katsumata, *Phys. Rev. B* **53**, 12201 (1996).
- [89] S. A. Carter, B. Batlogg, R. J. Cava, J. J. Krajewski, W. F. Peck, Jr., and T. M. Rice, *Phys. Rev. Lett.* **77**, 1378 (1996).
- [90] L. P. Regnault, J. P. Boucher, H. Moudden, J. E. Lorenzo, A. Hiess, U. Ammerahl, G. Dhalenne, and A. Revcolevschi, *Phys. Rev. B* **59**, 1055 (1999).
- [91] R. S. Eccleston, M. Uehara, J. Akimitsu, H. Eisaki, N. Motoyama, and S. Uchida, *Phys. Rev. Lett.* **81**, 1702 (1998).
- [92] M. Matsuda, K. Katsumata, H. Eisaki, N. Motoyama, S. Uchida, S. M. Shapiro and G. Shirane, *Phys. Rev. B* **54**, 12199 (1996).
- [93] O. Milat, private communication
- [94] D. E. Cox, T. Iglesias, K. Hirota, G. Shirane, M. Matsuda, N. Motoyama, H. Eisaki and S. Uchida, *Phys. Rev. B* **57**, 10750 (1998).
- [95] K. Kumagai, S. Tsuji, M. Kato, and Y. Koike, *Phys. Rev. Lett.* **78**, 1992 (1997).
- [96] T. Imai, K. R. Thurber, K. M. Shen, A. W. Hunt and F. C. Chou, *Phys. Rev. Lett.* **81**, 220 (1998).
- [97] R. S. Eccleston, M. Azuma and M. Takano, *Phys. Rev. B* **53**, R14721 (1996).

- [98] M. Takigawa, N. Motoyama, H. Eisaki and S. Uchida, Phys. Rev. B **57**, 1124 (1998).
- [99] V. Kataev, K.-Y. Choi, M. Grüninger, U. Ammerahl, B. Büchner, A. Freimuth and A. Revcolevschi, Phys. Rev. B **64**, 104422 (2001).
- [100] S. Ohsugi, K. Magishi, S. Matsumoto, Y. Kitaoka, T. Nagata and J. Akimitsu, Phys. Rev. Lett. **82**, 4715 (1999).
- [101] T. Nagata, H. Fujino, J. Akimitsu, M. Nishi, K. Kakurai, S. Katano, M. Hiroi, M. Sera and N. Kobayashi, J. Phys. Soc. Jpn. **68**, 2206 (1999).
- [102] M. Isobe, M. Onoda, T. Ohta, F. Izumi, K. Kimoto, E. Takayama-Muromachi, A. W. Hewat and K. Ohoyama, Phys. Rev. B **62**, 11667 (2000).
- [103] K. Magishi, S. Matsumoto, Y. Kitaoka, K. Ishida, K. Asayama, M. Uehara, T. Nagata and J. Akimitsu, Phys. Rev. B **57**, 11533 (1998).
- [104] Y. Piskunov, D. Jérôme, P. Auban-Senzier, P. Wzietek and A. Yakubovsky, Phys. Rev. B **69**, 014510 (2004).
- [105] S. Katano, T. Nagata, J. Akimitsu, M. Nishi and K. Kakurai, Phys. Rev. Lett. **82**, 636 (1999).
- [106] N. Motoyama, H. Eisaki, S. Uchida, N. Takeshita, N. Mori, T. Nakanishi and H. Takahashi, Europhys. Lett. **58**, 758 (2002).
- [107] T. Nagata, M. Uehara, J. Goto, N. Komiya, J. Akimitsu, N. Motoyama, H. Eisaki, S. Uchida, H. Takahashi, T. Nakanishi and N. Mori, Physica C **282-287**, 153 (1997).
- [108] N. Fujiwara, N. Mori, Y. Uwatoko, T. Matsumoto, N. Motoyama and S. Uchida, Phys. Rev. Lett. **90**, 137001 (2003).
- [109] S. Barišić and S. Brazovskii, *Recent Developments in Condensed Matter Physics, Vol. 1, p. 327*, ed. by J. T. Devreese (Plenum, New York, 1981).
- [110] V. J. Emery, R. Bruinsma and S. Barišić, Phys. Rev. Lett. **48**, 1039 (1982).
- [111] R. E. Peierls, *Quantum Theory of Solids*, (Oxford University, New York/London, 1955).
- [112] A. Virosztek and K. Maki, Phys. Rev. B **37**, 2028 (1988).

- [113] J. Hubbard, Proc. R. Soc. A **276**, 238 (1963).
- [114] V. J. Emery, Phys. Rev. B **14**, 2989 (1976).
- [115] E. H. Lieb and F. Y. Wu, Phys. Rev. Lett. **20**, 1445 (1968).
- [116] K. V. Efetov and K. I. Larkin, Soviet Phys. JETP, **42**, 390 (1975).
- [117] K. Uzelac, J. Phys. C: Solid State Phys. **19**, L441 (1986).
- [118] M. Tsuchiizu and A. Furusaki, Phys. Rev. Lett. **88**, 056402 (2002).
- [119] M. Nakamura, J. Phys. Soc. Jpn. **68**, 3123 (1999); Phys. Rev. B **61**, 16 377 (2000).
- [120] M. Tsuchiizu and Y. Suzumura, cond-mat/0311534.
- [121] S. Mazumdar and D. K. Campbell, Phys. Rev. Lett. **55**, 2067 (1985).
- [122] H. Fröhlich, Proc. R. Soc. A **223**, 296 (1954).
- [123] P. A. Lee, T. M. Rice and P. W. Anderson, Phys. Rev. B **14**, 703 (1974).
- [124] S. Barišić, Mol. Cryst. Liq. Cryst. **119**, 413 (1985); S. Barišić, *Electronic properties of inorganic materials with quasi-one-dimensional structures, Part 1, page 1*, edited by P. Monceau (Reidel, Dordrecht/Boston/Lancaster, 1986).
- [125] A. Bjeliš, in *Applications of Statistical and Field Theory Methods to Condensed Matter*, edited by D. Baeriswyl *et al.* (Plenum Press, New York, 1990).
- [126] G. Grüner, Rev. Mod. Phys. **60**, 1129 (1988).
- [127] P. B. Littlewood, Phys. Rev. B **36**, 3108 (1987).
- [128] H. Fukuyama, P. A. Lee, Phys. Rev. B **17**, 535 (1978); P. A. Lee, T. M. Rice, Phys. Rev. B **19**, 3970 (1979).
- [129] R. J. Cava, R. M. Fleming, P. Littlewood, E. A. Rietman, L. F. Schneemeyer and R. G. Dunn, Phys. Rev. B **30**, 3228 (1984).
- [130] R. J. Cava, R. M. Fleming, R. G. Dunn and E. A. Rietman, Phys. Rev. B **31**, 8325 (1985).

- [131] R. J. Cava, P. Littlewood, R. M. Fleming, R. G. Dunn and E. A. Rietman, *Phys. Rev. B* **31**, 2439 (1986).
- [132] R. M. Fleming, R. J. Cava, L. F. Schneemeyer, E. A. Rietman and R. G. Dunn, *Phys. Rev. B* **33**, 5450 (1986).
- [133] D. Reagor, S. Sridhar, M. Maki and G. Grüner, *Phys. Rev. B* **32**, 8445 (1985).
- [134] M. Kończykowski, M. Baj, E. Szafarkiewicz, L. Kończewicz and S. Porowski, *High Pressure and Low Temperature Physics*, page 523, edited by C. W. Chu and I. A. Woollam (Plenum Press, New York, 1978).
- [135] T. Vuletić, P. Auban-Senzier, C. Pasquier, S. Tomić, D. Jérôme, M. Héritier and K. Bechgaard, *Eur. Phys. J. B* **25**, 319 (2002).
- [136] O. Milat, unpublished.
- [137] I. Tanaka and H. Kojima, *Nature*, **337**, 21 (1989).
- [138] M. Prester and I. Živković, unpublished.
- [139] M. Pinterić, T. Vuletić, S. Tomić and J. U. von Schütz, *Eur. Phys. J. B* **22**, 335 (2001).
- [140] S. Havriliak and S. Negami, *J. Polym. Sci. C* **14**, 99 (1966).
- [141] S. Tomić, N. Biškup, M. Pinterić, J. U. von Schütz, H. Schmitt and R. Moret, *Europhys. Lett.* **38**, 219 (1997).
- [142] M. Pinterić, M. Miljak, N. Biškup, O. Milat, I. Aviani, S. Tomić, D. Schweitzer, W. Strunz and I. Heinen, *Eur. Phys. J. B* **11**, 217 (1999).
- [143] M. Pinterić, T. Vuletić, M. Lončarić, S. Tomić and J. U. von Schütz, *Eur. Phys. J. B* **16**, 487 (2000).
- [144] G. Kozlov and A. Volkov, *Topics in Applied Physics* **74**, Millimeter and Submillimeter Wave Spectroscopy of Solids, ed. G. Grüner (Springer-Verlag, Berlin, 1998).
- [145] L. P. Gor'kov, *J. Phys. I France* **6**, 1697 (1996).
- [146] A. Smontara, K. Biljaković, J. Mazuer, P. Monceau and F. Lévy, *J. Phys. Cond. Matt.* **4**, 3273 (1992).

- [147] M. Tinkham, *Introduction to superconductivity, Chap.11* (McGraw-Hill, New York, 1996).
- [148] G. Montambaux, Phys. Rev. B **38**, 4788 (1988).
- [149] G. Montambaux, M. Héritier and P. Lederer, J. Phys.: Condens. Matter **19**, L293 (1986).
- [150] M. Héritier, G. Montambaux and P. Lederer, J. Physique Lettres **45**, 943 (1984).
- [151] L. Ducasse, M. Abderrabba, J. Hoarau, M. Pesquer, B. Gallois and J. Gaultier, J. Physique Colloque **47**, C19-3805 (1986).
- [152] B. Gallois *et al.*, Mol. Cryst. Liq. Cryst. **148**, 279 (1987).
- [153] C. Pasquier, P. Auban-Senzier, T. Vuletić, S. Tomić, M. Héritier and D. Jérôme, J. Phys. IV **12**(9), Pr9-197 (2002).
- [154] R. Moret, S. Ravy, J. P. Pouget and R. Comes, Phys. Rev. Lett. **57**, 1915 (1986).
- [155] S. Tomić and D. Jérôme, J. Phys.: Condens. Matter **1**, 4451 (1989).
- [156] L. P. Gor'kov and A. G. Lebed', J. Physique Colloque **44**, C3-1531 (1983).
- [157] R. Duprat and C. Bourbonnais, Eur. Phys. J. B **21**, 219 (2001).
- [158] V. J. Emery, J. Physique Colloque **44**, C3-977 (1983).
- [159] D. Podolsky, E. Altman, T. Rostunov, and E. Demler, cond-mat/0403406.
- [160] T. Vuletić, B. Korin-Hamzić, S. Tomić, B. Gorshunov, P. Haas, T. Rõõm, M. Dressel, J. Akimitsu, T. Sasaki and T. Nagata, Phys. Rev. Lett. **90**, 257002 (2003).
- [161] T. Vuletić, T. Ivek, B. Korin-Hamzić, S. Tomić, B. Gorshunov, P. Haas, M. Dressel, J. Akimitsu, T. Sasaki and T. Nagata, submitted to Phys. Rev. Lett. (2004).
- [162] H. Kitano, R. Isobe, T. Hanaguri, A. Maeda, N. Motoyama, M. Takaba, K. Kojima, H. Eisaki and S. Uchida, Europhys. Lett. **56**, 434 (2001).

- [163] H. Kitano, R. Inoue, A. Maeda, N. Motoyama, K. Kojima, H. Eisaki and S. Uchida, *Physica C* **341-348**, 463 (2000).
- [164] G. Grüner, A. Zawadowski and P. M. Chaikin, *Phys. Rev. Lett.* **46**, 511 (1981).
- [165] T. Vuletić, M. Pinterić, M. Lončarić, S. Tomić and J. U. von Schütz, *Synth. Metals* **120**, 1001 (2001).
- [166] R. C. Lacoë, J. R. Cooper, D. Jérôme, F. Creuzet, K. Bechgaard and I. Johanssen, *Phys. Rev. Lett.* **58**, 262 (1987).
- [167] G. Blumberg, P. Littlewood, A. Gozar, B. S. Dennis, N. Motoyama, H. Eisaki, and S. Uchida, *Science* **297**, 584 (2002).
- [168] A. Maeda, R. Inoue, H. Kitano, N. Motoyama, H. Eisaki and S. Uchida, *Phys. Rev. B* **67**, 115115 (2003).
- [169] P. B. Littlewood, *Solid State Commun.* **65**, 1347 (1988).
- [170] Wei-yu Wu, L. Mihály and G. Grüner, *Solid State Commun.* **55**, 663 (1985).
- [171] T. Vuletić, B. Korin-Hamzić, S. Tomić, B. Gorshunov, P. Haas, M. Dressel, J. Akimitsu, T. Sasaki and T. Nagata, *Phys. Rev. B* **67**, 184521 (2003).
- [172] N. F. Mott and E. A. Davis, *Electronic Processes in Non-crystalline Solids* (Oxford University, London, 1971).
- [173] Z. G. Yu and X. Song, *Phys. Rev. Lett.* **86**, 6018 (2001).
- [174] J. C. Dyre and T. B. Schröder, *Rev. Modern Physics* **72**, 873 (2000).
- [175] F. Ladieu and M. Sanquer, *Ann. Phys. (Paris)* **21**, 267 (1996).
- [176] M. L. Knotek and M. Pollack, *Phys. Rev. B* **9**, 664 (1974).
- [177] V. K. S. Shante and C. M. Varma, *Phys. Rev. B* **8**, 4885 (1973).
- [178] K. R. Thurber, K. M. Shen, A. W. Hunt, T. Imai and F. C. Chou, *Phys. Rev. B* **67**, 094512 (2003).
- [179] S. Pachot, P. Bordet, R. J. Cava, C. Chailout, C. Darie, M. Hanfland, M. Marezio and H. Takagi, *Phys. Rev. B* **59**, 12048 (1999).

- 
- [180] N.F.Mott *Metal-Insulator Transitions* (Taylor and Francis, London, 1990).
- [181] P. W. Anderson, Phys. Rev. **109**, 1492 (1958).
- [182] A. F. Ioffe and A. R. Regel, Prog. Semicond. **4**, 237 (1960).
- [183] V. J. Emery and S. A. Kivelson, Phys. Rev. Lett. **74**, 3253 (1995).
- [184] U. Schollwöck, S. Chakravarty, J. O. Fjaerestad, J. B. Marston and M. Troyer, Phys. Rev. Lett. **90**, 186401 (2003).
- [185] F. Nad', P. Monceau, C. Carcel and J. M. Fabre, J. Phys.: Condens. Matter **12**, L435 (2000).
- [186] D. S. Chow, F. Zamborszky, B. Alavi, D. J. Tantillo, A. Baur, C. A. Merlic and S. E. Brown, Phys. Rev. Lett. **85**, 1698 (2000).

# List of publications

- [1 ] N. Biškup, **T. Vuletić**, D. Herman, S. Tomić, M. Nagasawa and K. Bechgaard. Low Frequency Dielectric Response in Spin Density Wave Phase of Bechgaard Salts. *Synth. Metals* **103**, 2052 – 2053 (1999).
- [2 ] **T. Vuletić**, D. Herman, N. Biškup, M. Pinterić, A. Omerzu, S. Tomić and M. Nagasawa. Single-particle and spin-density wave charge dynamics in  $(\text{TMTSF})_2\text{PF}_6$  and  $(\text{TMTSF})_2\text{AsF}_6$ : A comparative overview. *J. Phys. IV* **9**(10), Pr10–275–Pr10–277 (1999).
- [3 ] M. Pinterić, **T. Vuletić**, M. Lončarić, S. Tomić and J. U. von Schütz. Low frequency dielectric spectroscopy of the Peierls-Mott insulating state in the deuterated copper-DCNQI systems. *Eur. Phys. J. B* **16**(3), 487–493 (2000).
- [4 ] S. Tomić, M. Pinterić, **T. Vuletić**, J. U. von Schütz and Dieter Schweitzer. Low-frequency dielectric spectroscopy of commensurate density waves. *Synth. Met.* **120**, 695–698 (2001).
- [5 ] **T. Vuletić**, M. Pinterić, M. Lončarić, S. Tomić and J. U. von Schütz. Non-ohmic electrical transport in the Peierls-Mott state of deuterated copper-DCNQI systems. *Synth. Met.* **120**, 1001–1002 (2001).
- [6 ] **T. Vuletić**, C. Pasquier, P. Auban-Senzier, S. Tomić, D. Jérôme, K. Maki and K. Bechgaard. Influence of quantum Hall effect on linear and nonlinear conductivity in the FISDW states of the organic conductor  $(\text{TMTSF})_2\text{PF}_6$ . *Eur. Phys. J. B* **21**, 53 – 60 (2001).
- [7 ] M. Pinterić, **T. Vuletić**, S. Tomić and J. U. von Schütz. Complex low-frequency dielectric relaxation of the charge-density wave state in the  $(2,5(\text{OCH}_3)_2\text{DCNQI})_2\text{Li}$ . *Eur. Phys. J. B* **22**, 335–341 (2001).
- [8 ] **T. Vuletić**, P. Auban-Senzier, C. Pasquier, S. Tomić, D. Jérôme, M. Héritier and K. Bechgaard. Coexistence of Superconductivity and

- Spin Density Wave orderings in the organic superconductor  $(\text{TMTSF})_2\text{PF}_6$ .  
Eur. Phys. J. B **25**, 319–331 (2002).
- [9 ] B. Gorshunov, P. Haas, T. Rõõm, M. Dressel, **T. Vuletić**, B. Korin-Hamzić, S. Tomić, J. Akimitsu and T. Nagata. Charge Density Wave formation in  $\text{Sr}_{14}\text{Cu}_{24}\text{O}_{41}$ . , Phys. Rev. B **66**, 060508(R) (2002).
- [10 ] S. Tomić, **T. Vuletić**, M. Pinterić and B. Korin-Hamzić. Modalities of self-organized charge response in low dimensional systems. J. Phys. IV **12**(9), Pr9–211–214 (2002).
- [11 ] C. Pasquier, P. Auban-Senzier, **T. Vuletić**, S. Tomić, M. Héritier and D. Jérôme. Coexistence of superconductivity and spin density wave orderings in Bechgaard and Fabre salts. J. Phys. IV **12**(9), Pr9–197–200 (2002).
- [12 ] **T. Vuletić**, B. Korin-Hamzić, S. Tomić, B. Gorshunov, P. Haas, M. Dressel, J. Akimitsu, T. Sasaki and T. Nagata. Variable-range hopping conductivity in the copper-oxygen chains of  $\text{La}_3\text{Sr}_3\text{Ca}_8\text{Cu}_{24}\text{O}_{41}$ . Phys. Rev. B **67**, 184521 (2003).
- [13 ] **T. Vuletić**, B. Korin-Hamzić, S. Tomić, B. Gorshunov, P. Haas, T. Rõõm, M. Dressel, J. Akimitsu and T. Nagata. Suppression of the charge-density wave state in  $\text{Sr}_{14}\text{Cu}_{24}\text{O}_{41}$  by calcium doping. Phys. Rev. Lett. **90**, 257002 (2003).
- [14 ] M. Pinterić, **T. Vuletić** and S. Tomić. Properties of Mott-Peierls insulating phase in deuterated copper-DCNQI systems. Proceedings of 39th international conference on microelectronics, devices and materials, MIDEM 2003, 231–236 (2003).
- [15 ] M. Pinterić, **T. Vuletić**, M. Lončarić, K. Petukhov, B. Gorshunov, J. U. von Schütz, S. Tomić and M. Dressel. MottPeierls phase in deuterated copper-DCNQI systems: a comprehensive study of longitudinal and transverse conductivity and ageing effects. J. Phys.: Condens. Matter **15**, 7351–7364 (2003).
- [16 ] **T. Vuletić**, T. Ivek, B. Korin-Hamzić, S. Tomić, B. Gorshunov, P. Haas, M. Dressel, J. Akimitsu, T. Sasaki and T. Nagata. Anisotropic charge modulation in ladder planes of  $\text{Sr}_{14-x}\text{Ca}_x\text{Cu}_{24}\text{O}_{41}$ . submitted to Phys. Rev. Lett. (2004); cond-mat/0403611